STABLE ISOTOPE AND TRACE ELEMENT FRACTIONATION AND IMPLICATIONS FOR CHEMICAL WEATHERING RATES

BY

NICOLE M. FERNANDEZ-FRANZAN

DISSERTATION

Submitted in partial fulfillment of the requirements
for the degree of Doctor of Philosophy in Geology
in the Graduate College of the
University of Illinois at Urbana-Champaign, 2020

Urbana, Illinois

Doctoral Committee:

Assistant Professor Jennifer L. Druhan, Chair and Director of Research
Professor Thomas M. Johnson
Professor James Best
Research Associate Professor Robert Sanford

Abstract

Application of stable isotopes and trace-element environmental tracers offers a promising approach in characterizing the underlying geochemical and hydrological processes giving rise to observed chemical weathering rates. Yet, to fully leverage these geochemical tools a better understanding of the fundamental mechanisms driving observed signatures is essential. This dissertation builds upon our current knowledge of stable isotope and trace element fractionation in low temperature, terrestrial environments through a combination of highly constrained laboratory experiments, geochemical models, and field analyses. Through this research, the extent of water–rock interactions and rate dependence of stable isotope and trace element fractionation during secondary mineral formation (a key fractionation pathway in weathering systems) is investigated. Further, the potential of stable Si isotopes to complement concentration – discharge relationships is explored through the development of a global dataset of silicon stable isotope–discharge relationships encompassing different lithologies and climates. Major findings from this thesis can be summarized as follows. First, metal stable isotopes and trace elements appear to be dependent on a variety of physio-chemical properties such as mineral surface area, solid to fluid ratios, and fluid solute compositions. Second, silicon, calcium, and strontium stable isotopes and germanium, strontium trace element ratios show a common, broadly consistent relationship between reaction rate and fractionation. Finally, the Si stable isotopes of stream water as a function of discharge are found to be sensitive to site-specific hydrogeochemical processes and are effective tracers of weathering intensity.

Acknowledgments

I am extremely grateful for all the support that I have received during the course of this PhD journey. I really don't think I would have made it without the help of my family, friends, and colleagues who have been there every step of the way and have always kept encouraging me to continue forward, even in those moments when I felt at my lowest. A PhD is really a collective effort in the end, and I couldn't have done it without you all!

First and foremost, I would like to express my sincere gratitude towards my partner and future wife who has been a foundation for me over the past 3 years and has the magical ability to always put any situation (no matter how big or small) in perspective. I love your French calm and how patient you have been with me, even during those times where I worked until 3am or had to work during weekends or during our vacation time. I know it wasn't always easy for you, but you were always understanding and supportive. For that, I thank you from the bottom of my heart. J'ai de la chance de t'avoir dans ma vie et de partager le reste de notre vie ensemble. Merci mon amour, je t'aime profondément.

I would like to also thank my mom, dad, and brother for all their support over the years both in sports and academically and dealing in general with all my crazy ideas and energy. Ma famille française, je vous remercie de tout mon cœur. Belle maman et beau papa merci de m'avoir accueilli chaleureusement dans la famille comme votre deuxième fille. Thank you to my close friends Julia Cisneros, Olivia Thurston, Carole Tan, Maguette Tall, and Morgane and Guillaume Corbisé (and of course my nephews, Théo et Nathan) as well as my friends from IPGP – Paul Floury, Marie Kußner, Sylvain Pasquet, Jean

Marçais, Quentin Charbonnier, Alida Perez-Fodich (and Francisco), Charlotte Le Traon and UIUC– Jia, Mahta, Naomi, Haley, Georgia, Peggy, Jenna, and many others.

I would also like to thank my advisor Jennifer Druhan for mentoring me over the past 8 years since I was an undergraduate and being patient throughout this whole experience. I would like to also thank my labmates, Yuchen Liu, Gabby Davila Ordonez, Matt Bizjack, Jia Wang, Mahta Gholizadeh, Max Giannetta, and Jon Golla for all their help and mutual support over the past 5 years. Thank you to all my friends and colleagues at IPGP: Pascale Louvat, Jérome Gaillardet, Julien Bouchez, Lou Derry, Laëticia Faure, Laure Meynadier, Jean-Louis (Bibi) Berk, Catherine Chauvel, and everyone else in the G2E équipe; also thanks to my collaborators in CAGE Elsa Amsellem, Mike Antonelli, Zhengbin Dang, Jessica Dallas, Thibaud Sontag, Barthélémy Julien; Pierre Burckel and everyone else I had the privilege to meet and talk with over the course of my 3 years at IPGP. Finally, thank you to my committee members, Jim Best, Tom Johnson, and Rob Sanford, Lana Holben, and all the other members of the UIUC geology faculty for all their help, guidance, and fruitful conversations over the course of my time at Illinois.

This thesis is based upon work supported by the National Science Foundation Graduate Research Fellowship Program under Grant No. DGE -1144245 and by the Chateaubriand Fellowship of the Office for Science & Technology of the Embassy of France in the United States.

TABLE OF CONTENTS

LIST OF FIGURES…….. vii
LIST OF TABLES……..... ix
CHAPTER 1: *Preface*……. 1
CHAPTER 2: *Silicon isotopic re-equilibration during amorphous silica precipitation and implications for isotopic signatures in geochemical proxies*…….…..... 13
2.1 INTRODUCTION…….. 13
2.2 METHODS……... 18
2.3 RESULTS…….. 28
2.4 DISCUSSION…….. 32
2.5 SUMMARY AND CONCLUSIONS……... 64
CHAPTER 3: *A first look at Ge/Si partitioning during amorphous silica precipitation and implications for Ge/Si as a tracer for silicate weathering*……..... 66
3.1 INTRODUCTION…….. 66
3.2 METHODS……... 73
3.3 RESULTS…….. 81
3.4 DISCUSSION……..... 85
3.5 CONCLUSIONS…….. 101
CHAPTER 4: *Silicon isotope – discharge relationships in small catchments spanning different climates and lithologies*……..... 103
4.1 INTRODUCTION……. 103
4.2 SITE DESCRIPTIONS……. 108
4.3 METHODS……..... 118
4.4 RESULTS/DISCUSSION……..... 124
4.5 CONCLUSIONS…….. 171
CHAPTER 5: *Addressing the potential of self-consistent $\delta^{44}Ca$, $\delta^{88/86}Sr$, and Sr/Ca partitioning during calcite precipitation: An experimental and modeling study*……..... 174
5.1 INTRODUCTION……. 174
5.2 METHODS……. 189
5.3 RESULTS...……..... 195
5.4 DISCUSSION……..... 207
5.5 CONCLUSIONS…….. 255
CHAPTER 6: *Summary*……. 257
REFERENCES……..…… 262
APPENDIX A Mass-dependent fractionation…….. 312
APPENDIX B Influence of surface area on solubility…….. 313
APPENDIX C Mineral–fluid interaction depth approximation …….. 315
APPENDIX D Solving for the instantaneous partition coefficient (K_d^{inst}) from the Rayleigh-distillation derivation (Tang et al., 2008) ……..…….. 320

APPENDIX E Storm event C–Q and R–Q relationships for each site…….. 322
APPENDIX F Calcite precipitation experiments with no pH-drift control…….. 344

LIST OF FIGURES

Figure 2.1 Dissolved silica concentration and stable isotope timeseries…..……. 30
Figure 2.2 Conceptual model of isotope behavior during precipitation.……..…….. 37
Figure 2.3 Rayleigh model predictions……...…….…….. 40
Figure 2.4 Apparent fractionation factors as a function of precipitation rate…..…….. 44
Figure 2.5 Transient model simulations…….…….. 49
Figure 2.6 Sensitivity analyses of time interval, T, for high SA case…….……..... 52
Figure 2.7 Amorphous silica surface thickness accumulation through time....……..... 54
Figure 2.8 Transient model results of solid phase Si stable isotope composition…….....……..... 55
Figure 3.1 Dissolved SiO_2, Ge/Si, and $\delta^{30}Si$ timeseries……....…..... 82
Figure 3.2 Fluid $\delta^{30}Si$ vs Ge/Si……..……....…..... 84
Figure 3.3 K_D^{inst} vs. log R_p for Ge/Si partitioning during am.silica formation……..... 87
Figure 3.4 Trace model Ge/Si simulations under a conservative Ge scenario..... 91
Figure 3.5 k_f^{Ge} vs. K_{sp}^{Ge} parameter space for trace model benchmarking..... 92
Figure 3.6 Trace model Ge/Si simulations for a Ge incorporation scenario..... 93
Figure 3.7 Fluid $\delta^{30}Si$ vs. Ge/Si relationships extended out to longer timescales..... 99
Figure 4.1 Storm event hydrographs…….…..…..…..... 128
Figure 4.2 Flow duration curves…….…….... 129
Figure 4.3 Box-and-Whisker plots and histograms of dissolved Si concentrations and $\delta^{30}Si$……..... 132
Figure 4.4 DSi (C) and $\delta^{30}Si$ (R)–discharge (Q) relationships within catchments…….... 136
Figure 4.5 Conceptual digram of DSi and $\delta^{30}Si$ variability as a function of discharge……..…….... 138
Figure 4.6 Stream DSi vs $\delta^{30}Si$ as a function of discharge across sites…….……..... 144
Figure 4.7 Stream $\delta^{30}Si$ vs. DSi across sites…….…..... 148
Figure 4.8 Rayleigh distillation model…...…….…….. 151
Figure 4.9 Stream $\delta^{30}Si$ vs. Ca*/Si ratios and Mg*/Na vs. Ca*/Na relationships..... 155
Figure 4.10 Chemical weathering vs. denudation rates and stream $\delta^{30}Si$ sensitivity to weathering intensity……..…….…..... 158
Figure 4.11 Comparison of storm event $\delta^{30}Si$ and weathering intensity with global observations……...……..……..... 160
Figure 4.12 Secondary clay control on stream $\delta^{30}Si$ signatures...……..……..... 163
Figure 4.13 Testing possible vegetation control on stream $\delta^{30}Si$ signatures……..... 169
Figure 5.1 Isotopic zoning during calcite growth…….……..……..... 180
Figure 5.2 Field and experimental Sr/Ca ratios…….……..…..... 183
Figure 5.3 Closed system sparging setup……...…….……..……... 190
Figure 5.4 Ca batch experimental results.……...…….……..……... 196
Figure 5.5 Sr batch experimental results.……...…….…….. 203

Figure 5.6 Fluid $\delta^{44/40}$Ca, $\delta^{88/86}$Sr, and Sr/Ca covariation……..... 206
Figure 5.7 Rp^{inst} vs. $Rp^{cumul.}$ relationship.……...…….……..... 211
Figure 5.8 Sr uptake and release rates and their co-variation with precipitation rate..... 218
Figure 5.9 $\Delta^{44/40}$Ca as a function of precipitation rate.……..... 226
Figure 5.10 $\Delta^{88/86}$Sr and K_D as a function of precipitation rates……..... 229
Figure 5.11 $\Delta^{44/40}$Ca, $\Delta^{88/86}$Sr, and $K_{D,Sr}$ cross correlations.……..... 234
Figure 5.12 CrunchTope model simulations for Ca stable isotopes…..……..... 240
Figure 5.13 Trace model simulations for Sr incorporation batch experiments..... 243
Figure 5.14 Trace model simulations for Sr release batch experiments……..... 245
Figure 5.15 Trace model simulations of fluid Sr/Ca partitioning during Sr uptake…….…... 247
Figure 5.16 Multi-tracer model simulations for $\delta^{44/40}$Ca, Sr/Ca, and $\delta^{88/86}$Sr fractionation during calcite growth…….…. 252
Figure A.1 Silicon three-isotope plot for mass-dependent fractionation …….….. 312
Figure C.1 Unit cell of quartz (modified from Nejad et al., 2017).……...…….…... 315
Figure C.2 Rayleigh distillation curves of δ^{30}Si isotopic evolution as a function of the fraction of aqueous Si precipitated as amorphous silica ……...…….…..... 317
Figure E.1 Box-and-whisker plots of seawater-corrected major cations of flood events…….…….…... 341
Figure E.2 Silhouette analysis for KMeans clustering….…….…... 342
Figure F.1 pH variability and influence on the attainment of equilibrium .....…….... 344
Figure F.2 Influence of pH drift on fluid Ca stable isotopes…….…… 345

LIST OF TABLES

Table 2.1 Initial experimental conditions for amorphous silica precipitation batch runs..... 20
Table 2.2 Results of amorphous silica precipitation batch experiments.....……. 27
Table 2.3 Transient model input parameter values..……..……... 48
Table 2.4 Fluid interaction depths into amorphous silica……..... 58
Table 3.1 Germanium data for amorphous silica precipitation experiments……..…….. 83
Table 3.2 Initial conditions for the Ge trace element batch model……..……..…….. 89
Table 4.1 Catchment characteristics…….….. 117
Table 4.2 Storm event characteristics…….…..... 123
Table 4.3 Storm event silicon chemistry characteristics…..……..... 134
Table 4.4 Power-law relationships between DSi and discharge ($C=aQ^b$) ……..... 147
Table 5.1 Initial conditions for calcite precipitation experiments.……..... 191
Table 5.2 Free drift calcite precipitation experimental results…...……..... 197
Table 5.3 Ca, Sr stable isotopes and Sr/Ca ratios for free drift calcite precipitation experiments…….…….. 199
Table 5.4 Initial conditions for CrunchTope simulations…….……... 239
Table 5.5 Crunch and multi-tracer model trace element and stable isotope input parameters..…….…….. 255
Table B.1 Calculated surface area corrected amorphous silica solubility concentrations (S′, **eq. B.1**) at 20°C for all three amorphous silica batch experiments spanning a range of surface areas..... …….…….. 313
Table C.1 High surface area batch experimental data used for the Mavromatis et al. (2016, 2017) mineral-fluid interaction depth calculation…….…….…….. 318
Table E.1 Stream water major cation chemistry corrected for atmospheric input…..…. 322
Table E.2 Stream Si concentrations and stable isotope ratios……..…….…….. 333

Chapter 1

Preface

Over 250 years ago Antoine Laurent Lavoisier first described carbonic acid (Lavoisier, 1774). This was followed by the seminal work of J.J Ebelmen in 1845, building on the idea of atmospheric CO_2 dissolving into water as a driver for complex water–rock interactions (i.e. silicate and carbonate weathering) that play a dual role in both regulating Earth's climate over geologic time and producing the "Critical Zone" that serve as the foundation for Earth's biosphere. From the seminal work of Albrecht and Ourisson, 1971 and Berner et al. (1983) onwards, global chemical weathering rates and the primary controls on overall dissolved solute fluxes though watersheds around the world have been a principle focus of Earth science research over the past 35 years.

Unprecedented global warming trends (IPCC, 2018), project increases in extreme flooding though the 21st century (Hirabayashi et al., 2013; Donat et al., 2016; Alfieri et al., 2017), and anthropogenic stresses on the world's watersheds and river networks as a result of pollution, damming, logging, urbanization, and other activities (Best, 2019) threaten to destabilize biogeochemical cycles vital to the sustainability of local ecosystems, water quality, and the roughly 8 billion people who inhabit the Earth's surface. Thus, it is critical now more than ever that we address quantitatively how global weathering rates and the ecosystems that they sustain will adapt to a rapidly changing climate. This is ultimately an effort to develop and validate novel forecasting models (i.e. Goddéris and Brantley, 2019) to better anticipate our increasingly volatile future.

Despite concerted efforts by the weathering research community, we are still a long way away from obtaining accurate estimates of global chemical weathering rates.

Highly constrained laboratory experiments attempting to constrain weathering rates yield values that are orders of magnitude faster than what is observed in the field (White and Brantley, 2003). Even among the field determined weathering rates themselves, there is substantial variability and ambiguity as a result of uncertainties in the dissolved solute concentrations, river discharge measurements, and contributions from multiple weathering sources like silicate, carbonate, and evaporite lithologies (Li and Yang, 2010; Bouchez and Gaillardet, 2014). In addition to this inherent uncertainty, dissolved solute and river discharge are also known to vary spatiotemporally. Thus, depending on the spatial resolution of the geochemical and hydrologic data available, field weathering rates can range considerably from study to study for a given watershed (Neal et al., 2012) or across basins of differing size (Moon et al., 2014).

Such fundamental limitations in our capabilities to characterize hydro-chemical dynamics at the watershed scale prevents us from accurately quantifying chemical weathering rates across scales. These complex natural environments represent underdetermined systems where the solute flux measured at a river outlet can represent an infinite number of possible combinations of chemical reactions (i.e. primary mineral dissolution, secondary mineral formation, adsorption, ion exchange, and others) and transport processes (i.e. advection, dispersion, diffusion, and mixing). Thus, we are limited by an inability to fully isolate and quantify a unique set of contributions to overall over all chemical weathering rates driving dissolved solute generation and export out of a given watershed.

Geochemical tracers in addition to solute concentrations are thus necessary independent constraints, which reduce the degrees of freedom in a given hydrogeochemical system. The weathering research community is increasingly leveraging metal stable isotopes (i.e. Li, B, Sr, Mg, Ca, Si, and others) and (trace)elemental

ratios (Sr/Ca, Ge/Si, Li/Na, B/Na, and others) for these purposes. The advantage in using these tracers is that they are highly sensitive to the principal secondary weathering reactions –namely, secondary mineral formation, plant uptake, and adsorption – that exert a large control on observed solute fluxes. Each of these individual reactions has a characteristic shift in either the isotope or trace element ratio that serves as a fingerprint, allowing these processes to be easily identified and quantified. These changes in relative abundance can be directly quantified through either a fractionation factor (stable isotopes) or partition coefficient (trace elements) and distinctions in these fractionation factors/partition coefficients allow us to identify and isolate aspects of the chemical weathering reaction network contributing to observed solute fluxes. The development and application of a suite of such "mid-mass" stable isotope and (trace)elemental environmental tracers has significantly advanced our understanding of catchment and large river basin dynamics (an excellent review on this can be found in Weiderhold et al., 2015). Their increasing popularity has recently motivated the development of a new generation of reactive transport models capable of monitoring the evolution of these tracers through time and space (ex. CrunchTope, Druhan et al., 2019; Druhan and Winnick, 2019). Hence, these environmental tracers offer substantial promise in the pursuit of accurate estimates of chemical weathering rates and the processes that underlie them.

Thus, we stand to substantially improve our ability to analyze the terrestrial weathering zone through more accurate, quantitative understanding of the behavior of these tracers as they are partitioned through these systems. At present, a key issue is the substantial disparity between "laboratory derived" and "field observed" fractionation factors (Bouchez et al., 2013) observed across multiple mid-mass isotope systems. This is in a manner analogous to the earlier observations of disparity in chemical weathering

rates. Thus, in order to fully leverage these geochemical tools, we must pursue an improved understanding of elemental and isotopic partitioning under conditions relevant to dynamic weathering environments.

This outstanding need serves as underlying motivation for my thesis: To bridge the gap between laboratory/model and field scale observations through improved understanding of the underlying fractionation mechanisms driving (trace)elemental ratios and isotopic signatures in natural weathering environments. My thesis represents a first step into a rapidly growing field that will form the foundation of my future scientific career. I utilize a combination of laboratory experiments, numerical models, and field analyses to address essential research questions that correspond to three central themes, partitioned into four chapters in this thesis:

(1) *Do the physical properties of a weathering system such as mineral surface area and solid to fluid ratios influence weathering tracer signatures and their interpretation as geochemical proxies?*

(2) *Does there exist a common, broadly consistent relationship between reaction rate and fractionation that can describe the behavior of multiple weathering tracers (i.e. metal stable isotopes and (trace)elemental ratios) simultaneously within the same system?*

(3) *At the catchment scale, do weathering tracers record dissolved solute dynamics as a function of discharge? Can they provide new insight into the variety of reaction pathways and fluid residence times that aggregate into observed dissolved fluxes?*

To begin to address these broad research questions, I have focused specifically on stable isotope and elemental ratio tracers related to silicate and carbonate weathering. The reason for this is because silicate and carbonate weathering are the predominant chemical weathering pathways on the Earth's surface. Further, silicate and carbonate weathering represent distinct timescales where silicates are generally considered to

weather slowly (on geologic timescales) and carbonates are known to weather fast (on 100 to 1000-year timescales). Thus, studying silicate and carbonate weathering reactions allows us to observe how these environmental tracers evolve within different systems and across a broad range of reaction timescales. The silicate weathering tracers considered in thesis are silicon stable isotopes ($\delta^{30/28}$Si), a well-known tracer in the weathering community (see Frings et al., 2016 for a review), and Ge/Si, a under-utilized trace element tracer that has tremendous promise as a silicate weathering (Mortlock and Frohlich, 1987; Kurtz et al., 2002) and biological (Wiche et al., 2018) tracers. The carbonate tracers considered in the thesis were Ca ($\delta^{44/40}$Ca) and Sr ($\delta^{88/86}$Sr) stable isotopes and Sr/Ca trace element ratios. These tracers are mainly used in the carbonate community as paleoproxies to characterize marine environments (Fantle, 2010; Fantle and Griffith, 2019) but have slowly begun to be more frequently utilized for terrestrial weathering systems (Schmidtt et al., 2012; Fantle and Tipper, 2014; Fantle, 2019; Griffith et al., 2020). Up until recently, there have only been a handful of studies across the silicate and carbonate weathering communities that have considered using multiple tracer approaches to probe reaction and transport processes driving catchment solute dynamics (Tipper et al., 2006, 2008, 2012; Pogge von Strandmann et al., 2012, 2014; and others). I suggest that we are missing a critical opportunity in this regard as metal stable isotopes and trace elemental ratios are potentially powerful complements to one another. Using stable isotopes and trace elements in tandem takes advantage of the fundamental differences in their chemical properties that allow for them to trace different sources and geochemical reactions that would otherwise be missed if only a single tracer was applied. Importantly, if these tracers are self-consistent and share common fractionation mechanisms then we would possess the outstanding capability of being able to predict the evolution of several

proxies simultaneously and, thus, obtain novel insight into the various sources and water–rock interactions occurring simultaneously within a given system. In Chapters 3 through 5, I develop experiments, numerical simulations, and field analyses to demonstrate that using a multi-tracer approach is both feasible (in that we have a common theoretical framework capable of describing these various tracers) and advantageous.

In this thesis, I have focused primarily on the formation of secondary minerals (i.e. secondary phases that are produced out of oversaturated solutions). In natural weathering systems these solids form as a result of primary mineral dissolution and represent a ubiquitous influence on the evolution environmental tracers through the Critical Zone. There are several reasons to justify this emphasis. First, secondary mineral formation is a fundamental process in soil formation in the weathering zone, sequestering dissolved solutes generated in the subsurface and thereby locking them into the overlying regolith and soil. Second, along the same lines, secondary mineral formation dictates the proximity of the weathering system to equilibrium with respect to mineral dissolution and, thus, controls how much dissolved solute is generated and ultimately exported out of a given watershed. Third, and most importantly, secondary mineral formation is a major fractionation pathway for both metal stable isotopes and trace elements in weathering environments. Thus, focusing primarily on secondary mineral formation serves a dual purpose in that an improved understanding of the fractionating signatures of their formation provides insight into their contribution to overall solute fluxes and, further, allows us to improve upon pre-existing theoretical frameworks for stable isotope and trace element fractionation (Watson, 1996; DePaolo, 2011; Druhan et al., 2013). In Chapters 2, 3, and 5, I interrogate the evolution of silicate and carbonate weathering tracers during amorphous silica and calcite precipitation, two common

secondary phases in silicate and carbonate weathering zones, through combined laboratory experiments and numerical geochemical modeling. Chapter 4 scales up from laboratory experiments where the growth of multiple secondary silicate phases (such as clays and (hydr)oxides) operates in tandem with other fractionating pathways (like plant uptake) to produce the silicon stable isotope signatures of field scale systems. Specifically, I explore the relationship between these isotope ratios and discharge during flood events (characterized by rapid changes in river discharge over a short period of time) across a global network of catchments.

Within this overarching context a summary of chapters and what will be investigated throughout the remainder of the dissertation is presented below.

Chapter 2: Silicon isotopic re-equilibration during amorphous silica precipitation and implications for isotopic signatures in geochemical proxies

In this chapter, I explore how water–rock interactions and mineral surface area influence isotopic signatures archived during secondary silicate formation. It is already well established that mineral surface area affects the rates of chemical reactions. However, this influence of surface area on stable isotope fractionation has yet to be fully recognized. Certainly, there must be an indirect relationship through the control surface area exerts on reaction rate, and the resulting extent of stable isotope fractionation. However, I argue that the balance between mineral surface area and observed isotope ratios of the surrounding fluid reflects a more direct linkage. Stable isotope signatures generated during secondary mineral formation have been hypothesized to "re-equilibrate" or "reset" as a function of the surface area and depth into the mineral surface that the surrounding fluid can access once active growth has ceased. This is the basis for the 'recrystallization' effects studied at length in marine diagenesis settings (Fantle, 2015; Gorski and Fantle, 2017; Huber et al., 2017; and others). Yet thus far, this relationship has

yet to be incorporated into a generalized modeling framework for stable isotope fractionation in "free-drift", dynamic systems. In this study I evaluated the timing and extent of silicon isotopic re-equilibration during amorphous silica (opal) formation through a series of laboratory experiments supported by multi-component numerical modeling. Amorphous silica precipitation experiments were conducted over a range of surface areas and solid to fluid ratios at 20°C and near neutral pH for a period of 30 days. These experiments show for the first-time evidence that surface area exerts a first order control on the extent of isotopic re-equilibration following secondary mineral precipitation.

Chapter 3: A first look at Ge/Si partitioning during amorphous silica precipitation and implications for Ge/Si as a tracer for silicate weathering

This chapter builds off of Chapter 2, leveraging samples from the same experiments used to investigate silicon stable isotope ($\delta^{30}Si$) fractionation to develop a germanium trace element dataset. This allows for us to examine for the first time how Ge/Si ratios behave during secondary amorphous silica formation under highly constrained laboratory conditions and whether they can be modeled using the same rate parameters as silicon isotopes. Germanium (Ge) is considered a "pseudo isotope" of silicon, readily substituting for Si within silicate minerals. Thus, underlying mechanisms for Ge trace element partitioning between a fluid and growing mineral should be analogous to stable silicon isotope fractionation and it is widely observed that the Ge/Si ratios of secondary minerals and fluids are distinct in natural systems (Mortlock and Frohlich, 1987; Kurtz et al., 2002, 2012; Lugolobi et al. 2010). However, unlike $\delta^{30}Si$, Ge is much less developed at this point in both experimental and field-scale studies. This is highlighted by the fact that very little kinetic and thermodynamic data exists for Ge

partitioning in secondary silicate minerals in general and none is currently available for amorphous silica. Hence, this study represents the first experimental dataset of its kind for Ge partitioning during secondary amorphous silica precipitation. Given that Ge/Si is a less developed system than $\delta^{30}Si$, I leveraged these proxies in tandem and challenged myself with modeling both tracers based on the same reaction rates.

This project involved collaboration with colleagues at both the Institut de Physique du Globe de Paris (IPGP) in France and at Cornell University where Ge concentrations were measured. This study is currently in preparation to be submitted for publication.

Chapter 4: Silicon isotope-discharge relationships in small catchments spanning different climates and lithologies

This study transitions from the laboratory experiments and numerical models described in Chapters 2 and 3 to consider field scale silicon stable isotope behavior within low order streams. It is well known that stream solute concentrations and discharge rates are highly coupled and integrate a multitude of different reaction pathways, water sources, and fluid residence times (Evans and Davies, 1998; Hornberger et al., 2001; Godsey et al., 2009, 2019). Thus, as suggested above, measured solute fluxes within streams can provide key insight into the hydrogeochemical controls within the weathering zone of landscapes (what we call the "Critical Zone"). The vast majority of such concentration (C) – discharge (Q) relationships are based on long-term monitoring and often give the appearance that solute concentrations are invariant even over many orders of magnitude differences in flow rates (termed "chemostatic" behavior; Godsey et al., 2009, 2019). In this study, I seek to probe beneath this "chemostatic" behavior using silicon stable isotopes as a complement to solute concentrations. Further, I investigate the extent to which short timescale extreme storm or flooding events can offer a window into

watershed transport and geochemical relationships that remain masked under annual or monthly observational frequencies.

Toward these goals, I developed the first large-scale dataset of stable silicon isotopes (Si R) – discharge (Q) relationships using over 150 stream samples collected from storm events across seven low order and headwater catchments spanning different lithologies, climates, and vegetation. This research is part of the a cross CZO (Critical Zone Observatory) international project called SAVI (Science Across Virtual Institutes) that involves collaboration between French (OZCAR), Canadian (Hakai Institute), and American Critical Zone networks. I worked with many collaborators throughout this project including Dr. Julien Bouchez and Dr. Jérôme Gaillardet at IPGP whom I have had a longstanding partnership with over the past three years of my PhD, Dr. Lou Derry at Cornell Unversity, Dr. Jon Chorover at the University of Arizona, and Ian Giesbrecht at the Hakai Institute and Simon Fraser University. The results from this study are currently in preparation to be submitted for publication.

Chapter 5: Addressing the potential of self-consistent $\delta^{44}Ca$, $\delta^{88/86}Sr$, and Sr/Ca fractionation during calcite precipitation: An experimental and modeling study

In Chapter 5 the scope shifts to Ca, Sr stable isotopes and Sr/Ca trace element behavior during calcite precipitation under "free-drifting" (i.e. varying saturation state) conditions that characterize terrestrial weathering environments. The goal of this chapter is to test the same hypotheses of contemporaneous stable isotope and trace element fractionation subject of a common mineral formation rate as achieved for amorphous silica precipitation. Where the silicate studies were based on a more simplistic and slower system, these carbonate tracers occur within characteristically fast and relatively complex secondary carbonate formation conditions. Unlike amorphous silica, calcite precipitation

kinetics and growth mechanisms are dynamic and highly sensitive to parameters such as pH, atmospheric CO_2 and carbonate alkalinity. Thus, the question becomes, are silicate and carbonate tracers capable of sharing similar fractionation mechanisms despite operating over drastically different timescales and contributing factors? For instance, do mineral properties such as surface area still exerts a first order control on tracer partitioning or are these effects diminished by distinct chemical factors that drive secondary calcite precipitation?

To address these questions, I ran a series of calcite precipitation batch experiments over a range of surface areas (0.0026 to 0.057 m^2 g^{-1}) and starting initial fluid Sr concentrations at 25°C and a pH of around 8.85. The experiments were run under "free-drift" conditions (i.e. where solute composition and pH are allowed to vary through time) for a duration of approximately 1 week. These experiments are logistically novel in that they are the first to address solution instability issues common during free drift calcite precipitation as a result of slow CO_2 degassing and pH drift. Further, these calcite precipitations experiments are the first to measure all three carbonate tracers, $\delta^{44/40}Ca$, $\delta^{88/86}Sr$, and Sr/Ca within the same system under conditions that are not chemostatic (as is the most widely applied method in the experimental carbonate literature, e.g. Tang et al., 2008 and AlKhatib and Eisenhauer, 2018). This study also introduces a novel tracer fractionation model framework that can describe major (Ca) and minor (Sr) element behavior as well as their respective stable isotope ratios ($\delta^{44/40}Ca$, $\delta^{88/86}Sr$) and through time during a chemical reaction. This system of equations was first developed by Dr. Marie Kußner (Kußner, 2018) at the Institut de Physique du Globe de Paris. I subsequently modified these coupled equations and benchmarked them against the established CrunchTope geochemical software using separate models for each carbonate

tracer, respectively. This project involved collaboration with several of my colleagues at IPGP, namely Dr. Julien Bouchez, Dr. Marie Kußner, Dr. Elsa Amsellem, and Dr. Michael Antonelli. The results from this study are currently in preparation to be submitted for publication.

CHAPTER 2

Silicon isotopic re-equilibration during amorphous silica precipitation and implications for isotopic signatures in geochemical proxies [1]

2.1 INTRODUCTION

Secondary minerals are a critical geochemical archive of Earth's development and evolution throughout geologic time up to the modern day. Their chemical and isotopic compositions provide a snapshot of the (paleo)environmental conditions under which they formed. In modern terrestrial settings, these geochemical proxies can be used to elucidate geochemical and hydrological processes regulating global geochemical cycling of solutes that govern Earth's climate and ecosystems. Rapid analytical advancements over the past several decades have allowed for stable isotopes of many elements found as either major (Si, Mg, Ca, Fe) or minor (Li, Sr, B) constituents of minerals to be measured with high precision. These mass-dependent tracers have become powerful tools for extracting the wealth of information preserved within secondary minerals. The high sensitivity of non-traditional stable isotopes to water-mineral interactions and characteristic fractionations associated with the precipitation of individual secondary phases (quantified through a fractionation factor, α) has made them exceptionally useful. One important application of these stable isotopes is in the quantification of weathering rates where primary mineral solubilization and secondary mineral formation pathways

[1] Fernandez, N.M ; Zhang, X. ; Druhan, J.L. (**2019**) Silicon isotopic re-equilibration during amorphous silica precipitation and implications for isotopic signatures in geochemical proxies, *Geochim. Cosmochim. Acta*, **262**, 104-127. https://doi.org/10.1016/j.gca.2019.07.029

are highly coupled (Maher et al., 2006; Maher et al., 2009; Zhu and Lu, 2009) and, thus, hard to tease apart solely through dissolved solute concentrations. As a consequence, stable isotopes are frequently used to characterize precipitation weathering reactions ranging from secondary carbonate (Tipper et al., 2006; Lemarchand and Gaillardet, 2006; Tipper et al., 2008; Jacobson et al., 2015, and others) to silicate phases (Georg et al., 2006; Georg et al., 2007; Pogge von Strandmann et al., 2008; Pokrovsky et al., 2013; Geilert et al., 2015; Steinhoefel et al., 2017, and others).

Despite substantial progress, quantitative analysis of secondary mineral formation and their associated stable isotope signatures are still limited by a fundamental knowledge gap in both the establishment of a growing mineral's isotopic composition and how it evolves through time and space. This ambiguity in the processes contributing to observed isotope ratios have led to questions regarding the fidelity of geochemical proxies and the preservation of isotopic signatures imparted during mineral growth over long periods of time (Fantle and DePaolo, 2007; Fantle, 2010; Fantle, 2015; Huber et al., 2017; Gorski and Fantle, 2017). Several studies suggest that alterations to stable isotope records can occur rapidly even in low temperature environments and systems that operate close to equilibrium (Handler et al., 2009; Curti et al., 2010, and others). Evidence for such "isotopic re-equilibration" is largely found in the carbonate literature, but this behavior has also been observed in other secondary phases such as Fe oxides (Frierdich et al., 2014; Handler et al., 2014; Frierdich et al., 2015; Joshi et al., 2017) and silicates (Geilert et al., 2014; Oelze et al., 2014; Roerdink et al., 2015). Studies focusing on a variety of crystalline carbonates have shown isotopic re-equilibration to occur rapidly, on the order of weeks (Mavromatis et al., 2012; Pearce et al., 2012; Mavromatis et al., 2015; Mavromatis et al., 2016; Mavromatis et al., 2017; Oelkers et al., 2018). Notably, recent

observations for $\delta^{30}Si$ fractionation during amorphous silica precipitation in both the field (Frings et al., 2016) and laboratory (Geilert et al., 2014; Roerdink et al., 2015; Oelze et al., 2015) suggest comparable timescales of isotopic re-equilibration can occur during silicate mineral formation in low temperature environments. Isotopic re-equilibration in secondary phases such as amorphous silica, which represents an important ^{30}Si-depleted terrestrial reservoir (Basile-Doelsch et al., 2005) and an increasingly employed geochemical proxy for modern weathering environments (Georg et al., 2007; Georg et al., 2009; Oelze et al., 2014; Tatzel et al., 2015; Alfredsson et al., 2015; Steinhoefel et al., 2017, and others), implies that even isotopic signatures of slow forming secondary minerals can be significantly altered on relatively short timescales (< 1 Ma). As secondary minerals include a wide variety of crystal structures with different metal contents, solubilities and stabilities, identifying the mechanisms underlying stable isotope fractionation during the complete lifespan of formation and residence in the environment is critical and serves as the principle motivation for this study.

How then does isotopic "re-equilibration" occur and what controls its timing and extent? Isotopic re-equilibration takes place after the kinetically dominant portion of a reversible reaction has ceased and overall rates have slowed down in the approach to a dynamic equilibrium (i.e. when the forward, precipitation rate and backward, dissolution rate equal one another). As this dynamic equilibrium is initially established, the distribution of isotope ratios between phases can remain at far-from-equilibrium conditions and, thus, continue to exchange between the mineral surface and the surrounding fluid. As a result, kinetic signatures generated during precipitation begin to be "erased" through increasing contributions from equilibrium fractionation until isotopic equilibrium is established. Consequences of this dynamic interplay between

kinetic and equilibrium isotope effects imply that application of traditional kinetic (Rayleigh, 1902; Hofmann et al., 2012) or equilibrium (Méheut et al., 2007; Schauble et al., 2009; Méheut and Schauble, 2014; Dupuis et al., 2015; He et al., 2015) isotope fractionation models characterized by fixed fractionation factors (α_{kin} and α_{eq}), while viable in certain situations, would fail to fully capture the variable isotopic behavior readily observed in the α of many natural environments (Bouchez et al., 2013).

To address this limitation in conventional stable isotope fractionation frameworks, DePaolo (2011) developed a steady-state model based on dynamic equilibrium and surface exchange reactions to better describe observed variability in isotope partitioning. In the surface reaction kinetic model, isotopic re-equilibration is manifested in a variable observed fractionation factor (α_{obs}) that is influence by the relative contributions of both kinetic (α_{kin}) and equilibrium (α_{eq}) isotope fractionation and varies as a function of precipitation rate. Recent application of the surface reaction kinetic model to quantify observed $\delta^{30}Si$ fractionation between aqueous and amorphous silica in the Geilert et al.(2014) flow through and Roerdink et al.(2015) batch precipitation experiments supports the conceptual framework put forth by DePaolo (2011) to characterize isotopic re-equilibration in low temperature settings. However, assumptions that form the basis of the original DePaolo (2011) model limit its direct application to natural systems. Specifically, the underlying assumption of chemostatic conditions (where solute compositions and saturations are fixed) results in a condition where the growing mineral surface in contact with the fluid maintains a steady state isotope composition. While this steady state approach is reasonable under highly controlled precipitation experiments, it may be insufficient to predict observed fractionation factors in transient settings where saturation states are highly variable. Thus, we suggest an expanded treatment of

observed stable isotope fractionation behavior may be gained by modifying this mixed kinetic and equilibrium partitioning to incorporate a transient framework for fluid-mineral interactions during secondary mineral formation.

A transient numerical framework for combined kinetic and equilibrium isotope effects in open systems was developed by Druhan et al. (2013) using a solid solution capable of producing the same behavior as the DePaolo (2011) derivation for a coupled, co-evolving fluid and solid mineral. In this approach, the isotopic evolution between the fluid and growing mineral is dependent on the evolving isotope ratio of the mineral in communication with the fluid phase. An important parameter that arises in this transient schematic is the amount of overall mineral available for re-equilibration with the fluid. Thus, the approach offers a framework to couple observable fluid isotopic exchange to the subcomponent of the mineral mass that is in communication with the surrounding fluid, i.e. the depth into the mineral surface that the fluid can interact with. A key prediction that arises from this transient-based model is that *the rate and extent of isotopic re-equilibration during fluid-mineral interactions must be dependent on the mineral surface area* (Druhan et al., 2013; Druhan and Brown, 2015). The influence of surface area on reaction rates in water-rock interactions has been well established in the literature (Aagaard and Helgeson, 1982; Helgeson et al., 1984; Holdren and Speyer, 1985; Murphy et al., 1989), but, to date, the role that the surface area plays on (paleo)environmental isotopic signatures has yet to be explored in such a forward modeling framework. Here, we address the extent to which variations in surface area influence the observed fractionation factor between co-evolving fluid and newly formed solids through a series of amorphous silica precipitation experiments conducted under conditions resembling natural, open systems. We then compare these results with a series of transient numerical CrunchTope models using a variety of approximations for the fluid-mineral surface interaction depth.

This study is highly relevant to natural weathering environments in which amorphous silica is a common secondary product, and more generally addresses the extent to which stable isotope fractionation (1) exhibits a surface area dependence and (2) persists through time.

2.2 METHODS

2.2.1 Experimental Methods

Amorphous silica precipitation was conducted in stirred batch reactors using known weights of $SiO_{2(am)}$ seed crystals over a range of initial surface areas and solid:fluid mass ratios. The experiments were subjected to conditions where the saturation state is variable (i.e. allowed to change throughout the course of the experiment) for a timespan of approximately thirty days (Nancollas and Reddy, 1971; Wiechers et al., 1975; Inskeep and Bloom, 1985; Zhang and Dawe, 1998). Starting conditions are succinctly summarized in **Table 1**. Silica seed crystals of three distinct grain sizes and BET (Brunauer-Emett-Teller) defined specific surface areas (SSA, m^2/g) were utilized for the experiments. The silica seeds used in the high SA ("surface area") batch were a hydrophilic fumed high-purity silica powder with a BET constrained surface area of 50 m^2/g (AEROSIL® OX50). The medium and low SA batches consisted of high purity silica flours with BET constrained surface areas analyzed by AGSCO® company of 0.127 m^2/g (AGSCO® SILICA FLOUR 325) and 0.072 m^2/g (AGSCO® SILICA FLOUR 200). The batch experiments followed procedures adapted from Roerdink et al. (2015) and Geilert et al. (2014). Amorphous silica precipitation occurred heterogeneously (i.e. fumed silica or silica flour was initially present in the reactor) and solid to fluid mass ratios for the experiments using the high surface area and the medium/low surface area grains were 32 $gSiO_{2(s)}$:$gSiO_{2(aq)}$ and 50 $gSiO_{2(s)}$:$gSiO_{2(aq)}$, respectively. An initially supersaturated

solution with respect to amorphous silica was prepared by first dissolving 10 g L^{-1} of the AEROSIL® OX50 fumed silica particles in ultra-pure water (18.2mΩ) in a fluorinated ethylene propylene (FEP) bottle at a temperature of 90℃ for ~ 7-10 days, allowing the solution to attain a solubility concentration in the range of 320-330 ppm SiO_2 (Gunnarsson and Anórsson, 2000). These concentrations are higher than average dissolved SiO_2 in natural waters (~9.61 ppm, Dürr et al., 2011), but traditionally amorphous silica precipitation experiments are run at elevated values to speed up an otherwise infamously slow reaction (Iler, 1979; Fleming, 1986). To initiate precipitation, the 90℃ starting silica solution were divided into multiple HDPE batch reactors. For the high SA (50 $m^2 g^{-1}$) experiment, the 50 mL batch reactor was cooled down for ~ 30 min in a water bath to the targeted temperature of 20℃ with the remaining undissolved fumed silica crystals serving as the nucleation seeds. For the medium (0.127 $m^2 g^{-1}$) and low (0.072 $m^2 g^{-1}$) SA experiments, vacuum filtration was performed using a Merck Millipore 0.20 μm filter and then distributed into 250 mL HDPE reactor vessels that were cooled down to 20℃. Once at the targeted temperature, the initially low pH (~4.3) solutions were brought up to near neutral pH (~7.3) through the addition of 10mM NaOH solution. Precipitation in the high SA experiment was initiated immediately following the alkalization procedure. Medium and low SA experiments were initialized following the combination of alkalization and immediate addition of 4.0 g of the respective silica flours. The solutions were continuously agitated throughout the duration of the experiments on a shaker plate to ensure homogeneity and to avoid transport (diffusive) boundary layer effects between the bulk fluid and amorphous silica surfaces. Fluid samples were taken from each batch reactor at the beginning of the precipitation experiments (t = 0) and at regular time intervals in aliquots of 2.5 mL using a disposable syringe. Samples were filtered through

0.22 μm nylon membrane syringe filters and solid amorphous silica precipitates were collected at the end of the experiment via vacuum filtration using Merck Millipore 0.22 μm filters and dried at room temperature.

Table 2.1 Initial experimental conditions for amorphous silica precipitation batch runs

Physical parameters*	**High SA**	**Med SA**	**Low SA**
SiO_2 [mM]	5.3 ± 0.7	5.3 ± 0.4	5.3 ± 0.5
Ω [log Q/K]	0.48 ± 0.06	0.48 ± 0.04	0.48 ± 0.05
$SiO_{2(aq)}$ [g]	0.016 ± 0.002	0.080 ± 0.007	0.080 ± 0.008
$SiO_{2(s)}$ [g]	0.50 ± 0.01	4.00 ± 0.01	4.00 ± 0.01
$SiO_{2(s)}$: $SiO_{2(aq)}$ [g/g]†	31 ± 4	50 ± 5	50 ± 5
S [m^2]	25 ± 8	0.54 ± 0.02	0.31 ± 0.02

***Error calculations are described in **Table 2.2.**

† solid to fluid mass ratios calculated as the total amount of SiO_2 present in both solid and fluid phase at given time. Error calculated based on standard error propagation.

2.2.2 Analytical methods

Silica concentrations were quantified using 0.5 mL aliquots of the filtered samples diluted to 10 mL with ultrapure water and acidified with 2% HNO_3. The fluid phase silicon concentrations were then analyzed using an Agilent 7900 Inductively Coupled Plasma Mass Spectrometer at the Ínstitut de Physique du Globe de Paris (IPGP) in Paris, France. Instrumental precision using a multi-element standard for Si (based on the abundant isotope Si-28) and an internal standard using Sc for correction due to matrix effects was ±0.06 mM (1RSD). Although only the total dissolved silicon concentrations were determined in this study, we based our procedure on prior work demonstrating that only minor polymerization occurred during precipitation and the difference between total dissolved silica and monomeric SiO_2 falls below 10% (Geilert et al., 2014; Roerdink et al., 2015). Fluid stable isotope sample preparation began by diluting 2 mL of each filtered aliquot to a targeted volume of 10 mL with ultrapure water. Precipitated amorphous silica samples were collected via vacuum filtration through a Merck Millipore

0.22 μm filter and prepared for isotopic analysis following digestion by an adapted Alkali fusion technique (Georg et al., 2006) where 20 mg of solid sample was combined with 200 mg of analytical grade NaOH and fluxed in Ag crucibles heated to 720℃ for 12 min in a muffle furnace. The resulting product was then allowed to dissolve in PTFE vials containing 15 mL of ultrapure water for 24 hours followed by acidification with twice-distilled concentrated HNO_3 to a target 2% HNO_3 concentration.

Following these preparation procedures both fluid and solid phase samples were subjected to the same column chemistry modified from Van Den Boorn et al. (2006), Georg et al. (2006b), and Pringle et al. (2014) using a BioRad AG50W-X12 cation-exchange resin for sample purification. Silicon purification involved adding 20 μg Si as an acidified fluid sample to pre-cleaned 1.8mL resin bed in BioRad columns and eluted via addition of 5 mL MQ-e water. Silicon yields were approximately 70% for the first elution step (2 mL MQ-e) and the remaining 30% was recovered in the final elution step (3 mL MQ-e). Procedural blanks run through this column chemistry had ^{28}Si signals indistinguishable from the ^{28}Si blank on the mass spectrometer (~ 20 mV corresponding to less than 1% of the ^{28}Si sample signal). Silicon isotopic analyses were performed on a ThermoFinnigan Neptune Plus MC-ICP-MS at the Institut de Physique du Globe de Paris. Running conditions on the machine closely follow the method established by Georg et al. (2006). Samples were introduced as a wet plasma using a classic stable introduction system (SIS: double Scott/cyclonic spray chamber) and a 100 μL min^{-1} Teflon® nebulizer. To separate polyatomic interferences on the Si isotope signals the machine was run in "medium" resolution mode with a resolving power M/ΔM ~3300. Silicon concentrations introduced into the machine were 2 ppm with average signal intensities on the ^{28}Si ~ 10V. Isotopic compositions are reported in standard per mil notation ($\delta^{30}Si$) based on blank-corrected

isotope ratios calculated by a standard bracketing method using the NBS-28 (RM8546) silica sand internal standard (**eq. 2.1**):

$$\delta^{30}Si = \left[\frac{\left({}^{30}Si/{}_{28}Si\right)_{sample}}{AVG\left[\left({}^{30}Si/{}_{28}Si\right)_{std\text{-}I}, \left({}^{30}Si/{}_{28}Si\right)_{std\text{-}II}\right]} - 1 \right] \times 1000 \qquad (2.1)$$

where Std-I and Std-II refer to the NBS-28 standard measured directly before and after the sample. Repeated evaluation (n= 21) of the international terrestrial basalt standard BHVO-2 yielded an average value -0.35‰ with a long-term precision for $\delta^{30}Si$ of ± 0.11‰ (2σ), consistent with results of Savage et al. (2013), -0.28 ± 0.09‰ (2σ), for $\delta^{30}Si$ isotopic measurements conducted in the same facilities at IPGP. Mass dependent fractionation for our samples were verified through a three-isotope plot where $\delta^{29}Si = \delta^{30}Si \times 0.5019$, $R^2 = 0.97$ (**Appendix A**).

2.2.3 Transient model design

Our transient model has the novel capability to calculate the depth into the mineral that the fluid is able to interact and exchange with as a function of the mineral surface area. The model is set up so that we can explicitly simulate stable isotope ratios of aqueous and amorphous silica phases using a set of coupled TST (Transition State Theory; Aagaard and Helgeson, 1982; Helgeson et al., 1984) rate laws for the rare and abundant ^{30}Si and ^{28}Si isotopes (Druhan et al., 2013; **eq. 2.2a** and **eq. 2.2b**). The coupled equations are solved numerically for a time-evolving approach to equilibrium, such that both the fluid and solid isotopic composition are tracked during reaction progress.

$${}^{28}R_p = {}^{28}X\,{}^{28}kA\left(\frac{{}^{28}SiO_{2(aq)}}{{}^{28}X\,{}^{28}K_{eq}} - 1\right)^m \qquad (2.2a)$$

$${}^{30}R_p = {}^{30}X\,{}^{30}kA\left(\frac{{}^{30}SiO_{2(aq)}}{{}^{30}X\,{}^{28}K_{eq}} - 1\right)^m \qquad (2.2b)$$

$$R_p = kA\left(\frac{Q}{K_{eq}} - 1\right)^m \qquad (2.2c)$$

Here the activity of each stable silicon isotope in the fluid phase is denoted as $SiO_{2(aq)}$, *A* refers to the reactive surface area (m^2), *k* is the forward rate constant (moles m^{-2} s^{-1}), K_{eq} is the equilibrium constant appropriate to the temperature of the experiments, and the reaction quotient, Q, quantifies the departure from equilibrium. A high order affinity dependence can be designated using the exponent *m*. Previous experimental studies of amorphous silica formation conducted in similar conditions (Iler, 1979; Fleming, 1986; Tobler et al., 2009) used an affinity term of 3.5 and we adopt this value for consistency. All stable isotopes of silicon other than ^{30}Si are implicitly treated in **eq. 2.2a**, representing approximately 97% of the total concentration, such that the sum of the net rates ($^{30}R_p$ and $^{28}R_p$) reasonably reproduces the total bulk silica precipitation rate (R_p, **eq. 2.2c**) even with the higher order dependence. The ^iX terms are defined as the mole fractions of the two stable isotopes of silicon in the appropriate phase (discussed below) and thus couple their individual rates, ^{30}Rp and ^{28}Rp (Druhan et al., 2013; Steefel et al., 2014; Druhan et al., 2015).

The extent of isotopic re-equilibration in this transient approach is dependent on the definition of the mole fraction ^iX (where *i* represents the isotope of interest, in this case either ^{28}Si or ^{30}Si) and the sum of ^{28}X and ^{30}X is equal to 1.0. How the mole fraction is defined dictates the extent to which the solid and fluid phases are allowed to re-equilibrate with one another (Druhan et al., 2013). In the case where the fluid does not interact with the solid phase (i.e. no back reaction), the mole fraction is represented by the aqueous composition. In the case where the fluid and solid phases could re-equilibrate with one another (partially or completely), the mole fraction is represented by the solid phase, which may be defined in one of two ways. The simplest approach is to represent the solid isotope composition using the mineral volumes of the rare and

common isotopologue such that ^{i}X is set to the isotope ratio of the "bulk" or total amorphous silica present (**eq. 2.3**).

$$^{i}X_{bulk}(t) = \frac{^{i}N_{SiO_2,\ init\ bulk}(t=0) + {}^{i}N_{SiO_2,cum.ppt}(t)}{\sum_i {}^{i}N_{SiO_2,\ total}(t)} \quad (2.3)$$

Here the mole fraction of each isotope of the bulk solid ($^{i}X_{bulk}$) at a given simulation time (t) is monitored through the addition of new mineral mass ($^{i}N_{SiO2\ cum.ppt}$) from the start of the simulation (t = 0) to the present time. This value is added to the initial mass of solid present in the system ($^{i}N_{SiO2,init\ bulk}$) throughout the duration of the precipitation reaction and divided by the total mass of solid for all isotopes present at that time $\left(\sum_i {}^{i}N_{SiO_2,\ total} = {}^{i}N_{SiO_2,\ init\ bulk}(t=0) + {}^{i}N_{SiO_2,cum.ppt}(t)\right)$, assuming an ideal solid solution. This approach is thus distinct from more traditional homogeneous type models where re-equilibration with the bulk is assumed to be instantaneous (Curti et al., 2005; Curti et al., 2010; Handler et al., 2014; Joshi et al., 2017; Gorski and Fantle, 2017). Under this "bulk" approximation, the system effectively allows the isotopes of the fluid and the entire solid phase to re-equilibrate through time, as though the solid phase has an infinite surface area (i.e. unable to isotopically zone), such that the fluid interacts with the isotopic composition of the bulk solid. The second approach is to approximate the unique isotope ratio of the most recently formed mineral surface (i.e. distinct from the interior or bulk) and allow this to communicate with the surrounding fluid. In continuum scale models (such as the one used in this study), this value cannot be explicitly tracked through a discretized volume-averaged solid phase. Therefore, we approximate the mineral surface isotopic composition using a running average of the isotope ratio of the silicon that just precipitated out of solution over a given time interval (t - T) that the user can choose (**eq. 2.4**).

$$^{i}X_{surface}(t) = \frac{^{i}M_{SiO_{2,aq}}(t-T) - ^{i}M_{SiO_{2,aq}}(t)}{\sum_{i}\left(^{i}M_{SiO_{2,aq}}(t-T) - ^{i}M_{SiO_{2,aq}}(t)\right)} \qquad (2.4)$$

Where t is again the current time reached in the simulation, T is the lower bound of this time interval (T < t) to perform the running average of the concentration of $^{30}SiO_{2,aq}$ and $^{28}SiO_{2,aq}$ most recently removed from solution ($^{i}M_{SiO_{2,aq}}$), and the mole fraction ($^{i}X_{surface}$) is calculated as $^{i}M_{SiO_{2,aq}}$ divided by the total for both isotopes ($\sum_i {}^{i}M_{SiO_{2,aq}}(t-T) - {}^{i}M_{SiO_{2,aq}}(t)$). The lower bound of the time interval is defined by two distinct parameters: (1) the numerical model timestep, Δt, which is a fixed parameter dictated by the numerical model stability criteria, and (2) the number of timesteps to average over, A, which is a user specified parameter that we can adjust to constrain the time interval appropriate for each experimental data set (T = Δt x A).

It is important to note that the variable A is not an arbitrarily created free parameter but has physical meaning within our experimental design. Each experimental dataset reported in the present study features a unique surface area, meaning that the same mass of newly formed mineral is distributed over distinct total solid phase areas and thus the depth of this newest layer differs. The fluid-interaction depth then dictates the amplitude of kinetic fractionation and the apparent rate of isotopic re-equilibration observed between the fluid and bulk solid (discussed further in **Section 4.4**). By adjusting A between experiments, we are thus able to impose unique time intervals to average over, which then provide a proxy for the fluid-mineral interaction depth over a known surface area. This correlation between the amount of solid phase precipitated on a given surface area over a given time interval and the depth into the surface that the fluid can isotopically exchange with is a key feature of the modeling framework. Use of this

running average time interval in our transient model thus provides a novel approach to estimating the fluid-mineral surface interaction depth during crystal growth.

Finally, we note that the use of a higher order affinity term as implemented here (**eq. 2.2**) for amorphous silica formation does not strictly allow the fluid and solid (or solid surface) defined by the mole fraction to attain the imposed equilibrium fractionation factor at the limit where isotopic re-equilibration should be complete (as it would using a linear rate expression). For the vast majority of experimental data reported herein, this behavior exerts negligible influence on the corresponding model results. Where isotopic re-equilibration is suggested to have occurred extensively, the effect of this limitation is discussed in detail below.

Table 2.2 Results of amorphous silica precipitation batch experiments

time days	$M_{SiO2(aq)}$[a] mM	$N_{SiO2(ppt)}$[b] mmoles	f[c]	Ω[d] log (Q/K)	S[e] m^2	$logR_{bulk}$ mol s^{-1}	$logR_p$ mol $m^{-2}s^{-1}$	$\delta^{30}Si_{fluid}$ ‰ ± (2σ) n=3	$\delta^{30}Si_{ppt}$[f] ‰ ± (σ)	α_{obs}[g]
Higher surface area batch, SA = 50 m^2/g, solid:fluid = 31 g $SiO_{2(s)}$ /g $SiO_{2(aq)}$, pH = 7.35, T = 20 ℃										
0.00	5.3±0.7	-	-	0.48±0.06	25±8	-	-	-2.03±0.04	-	-
0.02	5.1±0.5	0.02±0.04	0.002±0.001	0.47±0.04	24±9	-8.09	-9.48	-1.68±0.07	-5.4±1.4	0.9963
0.11	4.6±0.6	0.05±0.04	0.006±0.001	0.42±0.06	24±9	-8.44	-9.82	-1.51±0.05	-4.0±1.0	0.9977
0.19	4.3±0.7	0.07±0.04	0.008±0.001	0.39±0.06	23±9	-8.52	-9.90	-1.34±0.05	-3.7±0.6	0.9979
0.93	3.4±0.9	0.12±0.05	0.01±0.01	0.29±0.08	23±9	-9.15	-10.51	-1.03±0.04	-3.2±0.5	0.9980
1.00	3.3±0.1	0.13±0.04	0.01±0.01	0.28±0.01	22±9	-8.98	-10.33	-1.05±0.04	-3.1±0.5	0.9982
2.00	2.9±0.6	0.15±0.03	0.02±0.01	0.22±0.05	22±9	-9.57	-10.92	-1.19±0.04	-2.6±0.4	0.9987
8.87	2.3±0.2	0.18±0.03	0.02±0.01	0.12±0.01	21±9	-10.32	-11.65	-1.63±0.05	-2.2±0.4	0.9994
13.88	2.2±0.5	0.18±0.02	0.02±0.01	0.10±0.02	21±9	-10.88	-12.20	-2.01±0.05	-2.0±0.3	1.0000
18.95	2.2±0.4	0.19±0.03	0.02±0.01	0.10±0.02	20±9	-11.17	-12.49	-2.25±0.04	-1.9±0.3	1.0003
31.08	2.1±0.4	0.19±0.04	0.02±0.01	0.07±0.02	20±8	-11.17	-12.47	-2.19±0.05	-1.9±0.3	1.0002
Medium surface area batch, SA = 0.127 m^2/g, solid:fluid = 50 g $SiO_{2(s)}$ /g $SiO_{2(aq)}$, pH = 7.31, T = 20 ℃										
0.00	5.3±0.4	-		0.48±0.04	0.54±0.02	-	-	-2.08±0.07	-	-
1.83	4.6±0.4	0.21±0.11	0.003±0.001	0.42±0.04	0.54±0.06	-8.88	-8.62	-1.44±0.12	-5.5±1.7	0.9959
2.90	4.1±0.4	0.32±0.16	0.004±0.001	0.38±0.04	0.53±0.06	-8.90	-8.63	-1.25±0.10	-4.7±1.0	0.9966
4.23	3.7±0.8	0.44±0.15	0.01±0.01	0.33±0.08	0.52±0.06	-8.98	-8.70	-1.11±0.24	-4.5±0.9	0.9963
4.95	3.6±0.5	0.47±0.23	0.01±0.01	0.32±0.04	0.52±0.06	-9.32	-9.04	-0.86±0.09	-3.9±0.7	0.9966
9.00	3.2±0.4	0.58±0.23	0.01±0.01	0.27±0.03	0.51±0.06	-9.52	-9.23	-0.79±0.07	-3.8±0.5	0.9970
14.79	3.1±0.7	0.62±0.15	0.01±0.01	0.25±0.06	0.51±0.06	-10.10	-9.80	-0.75±0.04	-3.6±0.5	0.9971
27.95	2.9±0.6	0.66±0.18	0.01±0.01	0.23±0.05	0.50±0.06	-10.43	-10.13	-0.75±0.11	-3.4±0.5	0.9973
30.00	3.0±0.5	0.66±0.21	0.01±0.01	0.23±0.04	0.49±0.06	-10.40	-10.09	-0.71±0.14	-3.4±0.5	0.9973
Low surface area batch, SA = 0.072 m^2/g, solid: fluid = 50 g $SiO_{2(s)}$ /g $SiO_{2(aq)}$, pH = 7.30, T = 20 ℃										
0.00	5.3±0.5	-		0.48±0.05	0.31±0.02	-	-	-2.14±0.07	-	-
1.83	4.7±0.5	0.17±0.13	0.002±0.001	0.43±0.04	0.31±0.04	-8.98	-8.47	-1.59±0.06	-6.0±1.9	0.9956
2.90	4.4±0.4	0.26±0.17	0.004±0.001	0.41±0.04	0.31±0.04	-9.05	-8.54	-1.44±0.06	-5.2±1.3	0.9962
4.23	4.2±0.6	0.32±0.15	0.004±0.001	0.38±0.06	0.30±0.04	-9.28	-8.76	-1.38±0.06	-4.6±1.1	0.9967
4.95	4.1±0.3	0.35±0.18	0.005±0.001	0.37±0.03	0.30±0.04	-9.22	-8.70	-1.37±0.04	-4.3±0.8	0.9970
9.00	3.9±0.3	0.41±0.17	0.01±0.01	0.35±0.03	0.30±0.04	-9.81	-9.28	-1.24±0.27	-4.2±0.9	0.9970
14.79	3.8±0.4	0.44±0.10	0.01±0.01	0.34±0.04	0.29±0.04	-10.26	-9.72	-1.25±0.08	-4.0±0.7	0.9972
27.95	3.6±0.5	0.49±0.12	0.01±0.01	0.32±0.05	0.29±0.04	-10.30	-9.77	-1.14±0.04	-3.9±0.6	0.9973
30.00	3.6±0.7	0.50±0.16	0.01±0.01	0.32±0.06	0.29±0.04	-10.24	-9.70	-1.18±0.05	-3.8±0.6	0.9974
Am. Silica initial (avg, n=3)									-1.77±0.05	
Am. Silica final (avg, n=3)									-1.81±0.03	

a. measured values with standards errors of 10% for concentrations (1SD).

b. mass precipitated calculated by subtracting dissolved $SiO_{2(aq)}$ concentrations between time intervals. Error was propagated according to sum of squares: $\sigma N_{SiO_{2(ppt)}} = \sqrt{\sigma N^2_{SiO_{2(ppt)}\text{-I}} + \sigma N^2_{SiO_{2(ppt)}\text{-II}}}$.

c. The fraction of Si in the new precipitate relative to the amorphous silica seed mass (error on weighed seeds ($\sigma_{N_{SiO_2,seed}}$) ± 0.001 g). Error was propagated according to sum of squares: $\sigma_f = \sqrt{\left(\frac{\sigma_{N_{SiO_{2(ppt)}}}}{N_{SiO_{2(ppt)}}}\right)^2 + \left(\frac{\sigma_{N_{SiO_2,seed}}}{N_{SiO_2,seed}}\right)^2} \times f$.

d. calculated saturation states (log Q/K_{sp}) with standard errors determined through standard error propagation $\sigma_\Omega = \sqrt{\left(\frac{\sigma_{M_{SiO_{2aq}}}}{M_{SiO_{2,aq}}}\right)^2} \times \Omega$.

e. volume-corrected surface area using initial BET measured or calculated surface areas, the initial total mass of am.silica present in reactor, and the reactor fluid volume at a given time *t* (**Section 4.1**).
f. silicon isotope composition of mass precipitated calculated using isotope mass balance (**eq. 6**). Associated error calculated based on error propagation (see **Section 3.3**).
g. calculated observed fractionation factors based on ratio of precipitated and fluid phase silicon isotope ratios ($\delta^{30}Si_{ppt}$ + 1000)/ ($\delta^{30}Si_{fluid}$ + 1000, **eq.7**).

2.3 RESULTS

2.3.1 Aqueous chemistry

Results from the three amorphous silica precipitation experiments conducted at similar pH (~7), saturation states (initial log Q/K_{sp} = 0.48 oversaturated with respect to amorphous silica), for a range of different mineral surface areas (50 $m^2 g^{-1}$ to 0.072 $m^2 g^{-1}$) are presented in **Table 2.** Aqueous silica and corresponding $\delta^{30}Si$ isotope ratios for the duration of the three experiments are shown in **Fig. 2.1**. Dissolved silica concentrations with time show distinct trends between the high, medium, and low surface area cases (**Fig. 2.1A**). The high SA experiment exhibits an initial, rapid decrease in dissolved silica concentrations during the first 2 days, followed by a gradual approach to equilibrium over a period of ~30 days. Notably, after 30 days, the high SA experiment reached dissolved silica levels ~13% above the theoretical amorphous silica solubility concentration of 1.75 mM at 20℃ (Gunnarsson and Anórsson, 2000). In the medium and low SA experiments, silica concentrations decrease during the first 5 days and appear to stabilize at $SiO_{2(aq)}$ values of ~3 mM and ~4 mM, approximately 1.7× and 2.3× the solubility concentrations, respectively. Aqueous silica concentrations in all cases were well above the theoretical solubility concentration and at saturation states greater than 0 at the end of the experimental runs (~30 days).

2.3.2 Precipitation rates

Time-averaged precipitation rates normalized to the surface area, R_p (reported as mol $m^{-2} s^{1}$) were calculated for all three batch runs by the following expression (**eq. 2.5**):

$$R_p = \frac{N_{SiO_{2(ppt)}\, t_I} - N_{SiO_{2(ppt)}\, t_{II}}}{S \cdot \Delta t_{II-I}} \qquad (2.5)$$

where the instantaneous amount of amorphous silica precipitated out of solution ($N_{SiO2(ppt)}$), defined in units of moles, is obtained through the decrease in aqueous silica concentrations multiplied by the volume of fluid in the reactor at the time of sampling over a given time interval ($\Delta t_{II-I} = t_{II} - t_I$) in units of seconds and normalized to the reactive surface area, *S* (m^2). The reactive surface area (*S*) is calculated based a volume-correction that accounts for solid phase lost via sampling at each given time (further details are addressed below in **Section 4.1**). Initial precipitation rates for the high, medium, and low SA experiments were $10^{-9.48}$ mol m^{-2} s^{-1}, $10^{-8.62}$ mol m^{-2} s^{-1}, and $10^{-8.47}$ mol m^{-2} s^{-1} and systematically decreased throughout the course of the experiment.

2.3.3 Silicon isotopes

Like the concentration trends, fluid $\delta^{30}Si$ express high sensitivity to the range of surface areas tested (**Fig. 2.2B)**. For all three experiments, initial fluid $\delta^{30}Si$ are −2.08 ± 0.11‰ (2σ). In comparison the initial average bulk amorphous $\delta^{30}Si$ value was measured before (−1.77 ± 0.05‰ (2σ), n=3) and at the end of the experiments, and final values were not significantly different than initial values (−1.81 ± 0.03‰ (2σ) n=3, −0.04‰ difference). Early stages of precipitation were generally characterized by an increase in fluid phase $\delta^{30}Si$. The highest SA case reached a maximum fluid $\delta^{30}Si$ of −1.03 ± 0.04‰ (2σ) (1.00 ± 0.06‰ (1σ)) enrichment with respect to starting value) within ~22 hours that was then followed by a reversal back towards lower values (−2.22 ± 0.05‰ (2σ), n=3). For this high SA case, the $\delta^{30}Si$ of the fluid stabilized at values significantly more negative than the bulk solid by −0.32 ± 0.06‰ (2σ). For the medium SA experiment, fluid $\delta^{30}Si$ reached a maximum value of -0.71 ± 0.14‰ (2σ) (1.34 ± 0.11‰ (1σ) greater than the starting fluid

value). Relative to the high SA condition, this enrichment takes place over a longer period of time (~12 days) and remains at relatively elevated values for the duration of the experiment. The low SA experiment attained a maximum fluid $\delta^{30}Si$ of -1.14 ± 0.04‰ (2σ) at ~24 days, corresponding to an enrichment of 0.90 ± 0.10‰ (2σ) above the initial fluid $\delta^{30}Si$ that, like the medium SA case, stabilizes for the remainder of the experiment. For both the medium and low SA experiments, the subsequent reversal towards initial fluid $\delta^{30}Si$ values observed in the high SA case is not captured, as shown by $\delta^{30}Si$ stabilizing at elevated values after ~1 week. Critically, in all three experiments, fluid $\delta^{30}Si$ values are distinct from the bulk amorphous silica composition at the end of the experimental duration.

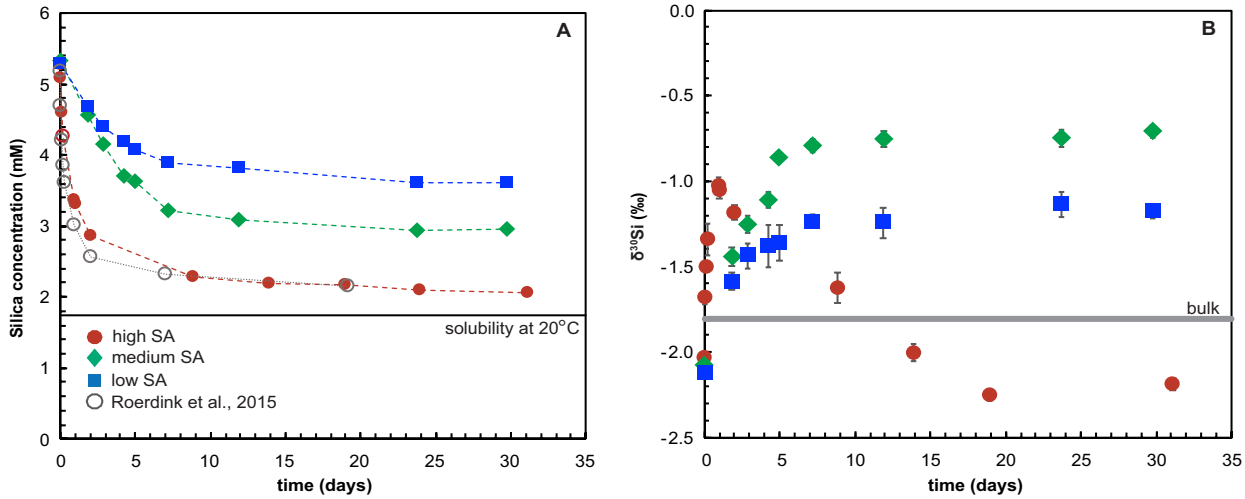

Figure 2.1 Dissolved silica concentrations and stable isotope timeseries
Timeseries of (**A**) dissolved silica concentrations and (**B**) corresponding fluid silicon isotope ratios for amorphous silica precipitation experiments conducted at 20°C and pH ~ 7.3. Error bars correspond to 2 standard deviation. High (50 m^2/g), medium (0.127 m^2/g), and low (0.072 m^2/g) surface area experiments are shown here in red circles, green diamonds, and blue squares respectively. High surface area experiments are compared against the Roerdink et al. (2015) study (grey open circles). General fluid $\delta^{30}Si$ trends start at values close to the bulk solid phase composition (grey horizontal line) followed by kinetic enrichment during precipitation and subsequent isotopic re-equilibration, the extent of which appears to be dependent on the surface area.

Assuming a closed system, the $\delta^{30}Si$ value of newly precipitated amorphous silica accumulated through time over the duration of the experiment ($\delta^{30}Si_{ppt}$) was calculated using isotopic mass balance formulations based on the initial moles of dissolved silica ($N_{SiO_{2aq,i}}$), the corresponding initial silicon isotope composition ($\delta^{30}Si_{aq,i}$), the dissolved silica in solution at a given point in time ($N_{SiO_{2,aq}}$) and its corresponding $\delta^{30}Si_{aq}$ (**eq. 2.6**).

$$\delta^{30}Si_{ppt} = \frac{N_{SiO_{2aq,i}} \cdot \delta^{30}Si_{aq,i} - N_{SiO_{2,aq}} \cdot \delta^{30}Si_{aq}}{N_{SiO_{2,ppt}}} \qquad (2.6)$$

The mass of silica precipitated ($N_{SiO2,ppt}$) was determined by subtracting the dissolved silica at a given sampling time from the initial amount (**Table 2.2**). Error presented in **Table 2.2** was calculated to 1σ using standard error propagation using three formulas: $\sigma_{a,b} = \sqrt{\left(\frac{\sigma_{N_{SiO_{2,aq}}}}{N_{SiO_{2,aq}}}\right)^2 + \left(\frac{2\sigma_{\delta^{30}Si_{aq}}}{\delta^{30}Si_{aq}}\right)^2} \times (N_{SiO_{2,aq}} \cdot \delta^{30}Si_{aq})$, sum of squares: $\sigma_c = \sqrt{(\sigma_a)^2 + (\sigma_b)^2}$, and $\sigma_{\delta^{30}Si_{ppt}} = \sqrt{\left(\frac{\sigma_c}{N_{SiO_{2aq,i}} \cdot \delta^{30}Si_{aq,i} - N_{SiO_{2,aq}} \cdot \delta^{30}Si_{aq}}\right)^2 + \left(\frac{\sigma_{N_{SiO_{2,ppt}}}}{N_{SiO_{2,ppt}}}\right)^2} \times \delta^{30}Si_{ppt}$.

Observed fractionation factors (α_{obs}) are calculated as the difference between $\delta^{30}Si$ values of dissolved silica ($\delta^{30}Si_{aq}$) and the corresponding precipitated amorphous silica ($\delta^{30}Si_{ppt}$) at each sampling time (**eq. 2.7**).

$$\alpha_{obs} = \frac{\left(\delta^{30}Si_{ppt} + 1000\right)}{\left(\delta^{30}Si_{aq} + 1000\right)} \qquad (2.7)$$

$\delta^{30}Si_{ppt}$ values were calculated according to the same isotopic mass balance formulations used in **eq. 2.6** (**Table 2.2**). Notably this definition follows the calculations used in Roerdink et al. (2015) and thus allows direct comparison. Observed fractionation factors and precipitation rates appear to be inversely correlated, where α_{obs} is generally seen to

increase as R_p (eq. 5) decreases in the approach to near equilibrium conditions. The high SA experiment expresses the largest range in α_{obs} values from 0.9963 ($\Delta^{30}Si_{ppt\text{-}fluid} = -3.73 \pm 0.20‰$) at an initial R_p of $10^{-9.48}$ mol m^{-2} s^{-1} to 1.0002 ($\Delta^{30}Si_{ppt\text{-}fluid} = +0.24 \pm 0.15‰$) at an R_p of $10^{-12.49}$ mol m^{-2} s^{-1} near the end of the experiment when concentrations and isotope ratios reach steady state values. The medium and low SA experiments produced α_{obs} values of 0.9959 ($\Delta^{30}Si_{ppt\text{-}fluid} = -4.12 \pm 0.20‰$) and 0.9956 ($\Delta^{30}Si_{ppt\text{-}fluid} = -4.42 \pm 0.22‰$) respectively. Comparison between the three experiments, together representing a broad surface area range from 50 – 0.072 m^2/g, show clear differences in both the magnitude and evolution in the observed fractionation factor as a function of reaction progress.

2.4 DISCUSSION

2.4.1 Tracking surface area during precipitation

Changes in the surface area of seed crystals during precipitation can potentially become significant enough to influence the reaction rate. Assuming homogeneous growth onto pre-existing spherical grains, the mass removed from solution in our experiments relative to the mass of the starting seed crystals would correspond to an increase in total surface area on the order of <0.01% (Steefel and Lasaga, 1994; Steefel and Lichtner, 1998; Gunter et al., 2000). These assumptions are reasonable, given that precipitation onto existing mineral surfaces in this temperature range is far more energetically favorable than overcoming a nucleation barrier (Iler, 1979). However, as in the similar experimental design used by Roerdink et al. (2015), the process of sampling inherently removes some of the suspended solid phase. As a result, the total surface area of the solid available for precipitation in fact decreases over the duration of the experiment. This somewhat counterintuitive behavior exerts a much stronger influence

on the overall surface area, as for example the 37% decrease reported by Roerdink et al. (2015). In the present study we constrain this loss of total surface area due to sampling by reporting a volume-corrected surface area (S) calculated by multiplying the initial total surface area of amorphous silica present in the reactor (in units of $m^2\ L^{-1}$) by the reactor volume at a given time, t. The initial total surface areas per unit volume for the high, medium, and low SA experiments were 495 $m^2\ L^{-1}$, 2.17 $m^2\ L^{-1}$, and 1.25 $m^2\ L^{-1}$ respectively. In our experiments the loss in total surface area was lower than that reported by Roerdink et al. (2015) due to the smaller volume of each sample, resulting in overall decreases of 19.8%, 9.6% and 7.9% for the high, medium and low surface areas, respectively (m^2, **Table 2.2**).

2.4.2 Influence of surface area on amorphous silica solubility

Observations of dissolved silica concentrations stabilizing to distinct values at the end of the three experiments (**Fig. 2.1A**) suggest that surface area could exert a direct control on amorphous silica solubility (Parks,1984; Williams et al.,1985). Standard calculation of thermodynamic equilibrium constants does not include a surface area dependence. Thus, to account for this possibility, a correction was performed on the amorphous silica equilibrium concentration determined at 20°C (Gunnarsson and Anórsson, 2000) using the Freundlich-Ostwald equation (Enüstün and Turkevich, 1960). No significant differences in solubility concentrations were found between the three amorphous silica precipitation cases (**Appendix B**). Therefore, we conclude that direct surface area control on amorphous silica solubility is unlikely over the range of surface areas used in this study.

Having verified that the equilibrium state is the same for all experiments, we may now determine the extent to which thermodynamic equilibrium was established for each

surface area case. Despite reactions having slowed to rates indistinguishable from zero and dissolved silica concentrations having stabilized at constant values, calculated saturation states (**Table 2.2**) indicate that only a metastable equilibrium was reached. Thus, from this point forward, we refer to a period of "metastable equilibrium" corresponding to the time interval over which a steady state concentration is observed and discernable net precipitation has ceased. Notably, this observation is consistent with two prior amorphous silica precipitation studies, one involving a closed batch reactor (Roerdink et al., 2015) and the other using flow-through experiments (Geilert et al., 2014), both of which both demonstrated what they termed equilibrium fractionation endmember behavior under these meta-stable conditions.

This emerging observation of "metastable equilibrium" in both previous publications and the present study points to a complexity in the establishment of true thermodynamic equilibrium for amorphous silica phases. If thermodynamic equilibrium is difficult to achieve in these highly controlled laboratory environments, then similar complexities may influence open and transient flow environments. If we consider that these natural environments commonly host longer fluid residence times and sustain slower water-rock interactions than can be reasonably constrained in the lab, then we may anticipate that these systems are better able to establish true thermodynamic equilibrium with such silica phases. However, natural environments are also commonly subject to variable boundary conditions and other forms of periodic or transient behavior, which may promote similar metastable equilibria. In this case, the application of traditional methods using simple K_{eq} calculations to characterize the thermodynamics of secondary amorphous silica reactions occurring in low temperature weathering systems would be insufficient. Though beyond the scope of the current study, which focuses on the

recording and exchange of isotopic signatures across the fluid – mineral boundary, we suggest these observations warrant further investigation.

2.4.3 The distinct effects of surface area on precipitation rates

As expected, surface area exerts a principle control on precipitation rates. This effect can be clearly discerned in the present experiments through comparison between overall bulk precipitation rates (R_{bulk}, **Table 2.2**) and precipitation rates normalized to the total available surface area (R_p, **Table 2.2**). Assuming homogeneous precipitation, higher surface area seeds yielded overall faster precipitation rates as a direct consequence of more mineral surface available (25 m^2) for the reaction to occur. The total amount of surface available for the medium and low SA cases was 2 orders of magnitude less than the high SA batch (0.54 m^2 and 0.31 m^2 respectively) and bulk precipitation rates were proportionally lower given comparable starting values of oversaturation. However, when these rates are normalized to the surface area (following the same reporting as both Geilert et al., 2014 and Roerdink et al., 2015) we obtain much closer values between the three conditions that all agree with previously reported amorphous silica precipitation rates: $R_p = 10^{-9.67}$ mol m^{-2} s^{-1} (Rimstidt and Barnes, 1980), $10^{-9.57}$ mol m^{-2} s^{-1} (Geilert et al., 2014), and $10^{-9.00}$ mol m^{-2} s^{-1} (Roerdink et al., 2015).

The amount and thickness of amorphous silica precipitated out of an initially oversaturated solution and onto the surfaces of pre-existing seeds is somewhat more complex, in that there is a dependence on both the total masses of silicon present as a solid and in solution (solid:fluid mass ratio) and the surface area of the seed crystals (assuming that amorphous silica is precipitated homogeneously onto the entire surface of each individual grain). These two distinct physical characteristics of the system, the solid:fluid mass ratio and the surface area, regulate the thickness of the newly-formed

mineral surface that can be formed. As a result, individual constraint of either the solid:fluid mass ratio or the surface area of the seed crystals would be insufficient to estimate the thickness of new precipitate accumulated during mineral formation. The present study demonstrates the relative effects of these two parameters. The medium and low SA experiment solid:fluid mass ratios (50 $SiO_{2(s)}$:$SiO_{2(aq)}$ (g/g)) are greater than the high SA value (~31 $SiO_{2(s)}$:$SiO_{2(aq)}$ (g/g)). This difference resulted from the use of both a larger fluid volume and more seed crystals in the medium and low SA design (**Table 2.1**) and would inherently suggest that the high SA experiment should form a thicker layer of new precipitate. However, following this simple calculation the corresponding accumulated depth values were 35 nm and 45 nm for the medium and low SA experiments, respectively, in comparison to only 0.22 nm for the high SA experiment (in agreement with numerical simulation results discussed in **Section 2.4.5.1**). Thus, even though the medium and low SA systems had higher solid:fluid mass ratios, their lower surface areas contributed to a much thicker depth of newly accumulated material onto the mineral surfaces.

2.4.4 Models for silicon stable isotope fractionation

Stable isotope fractionation for reversible secondary mineral formation reactions such as amorphous silica precipitation can be characterized by the balance of the forward precipitation rate, R_f, and the backward dissolution rate, R_b, between a mineral and its surrounding fluid (**Fig. 2.2**). The net rate (R_p) reflects a condition in which $R_f > R_b$ such that the mineral is actively forming, and fluid solute concentrations are decreasing with time (**Fig. 2.2A**). In this scenario, most stable isotope systems undergo kinetic fractionation where the "light" isotope is preferentially incorporated into the solid phase, leaving the remaining solution enriched in the "heavy" isotope (DePaolo, 2004). For a

system starting at equivalent fluid and solid stable isotope ratios, kinetic fractionation associated with precipitation ($\alpha_{kin} \neq 1.0$) of a secondary precipitate results in a characteristically large shift in the fluid isotope ratio towards stable isotope values distinct from the bulk composition (i.e. "kinetic enrichment"). A unique feature of reversible secondary mineral precipitation is the establishment of a dynamic equilibrium (**Fig. 2.2B**), where the net rate slows down as the backward and forward rates become equal to one another ($R_f = R_b$) and ultimately ceases ($R_p = 0$). In this state of dynamic chemical equilibrium, continued isotope exchange between the fluid and solid phase as a result of equilibrium fractionation ultimately returns the system towards equilibrium

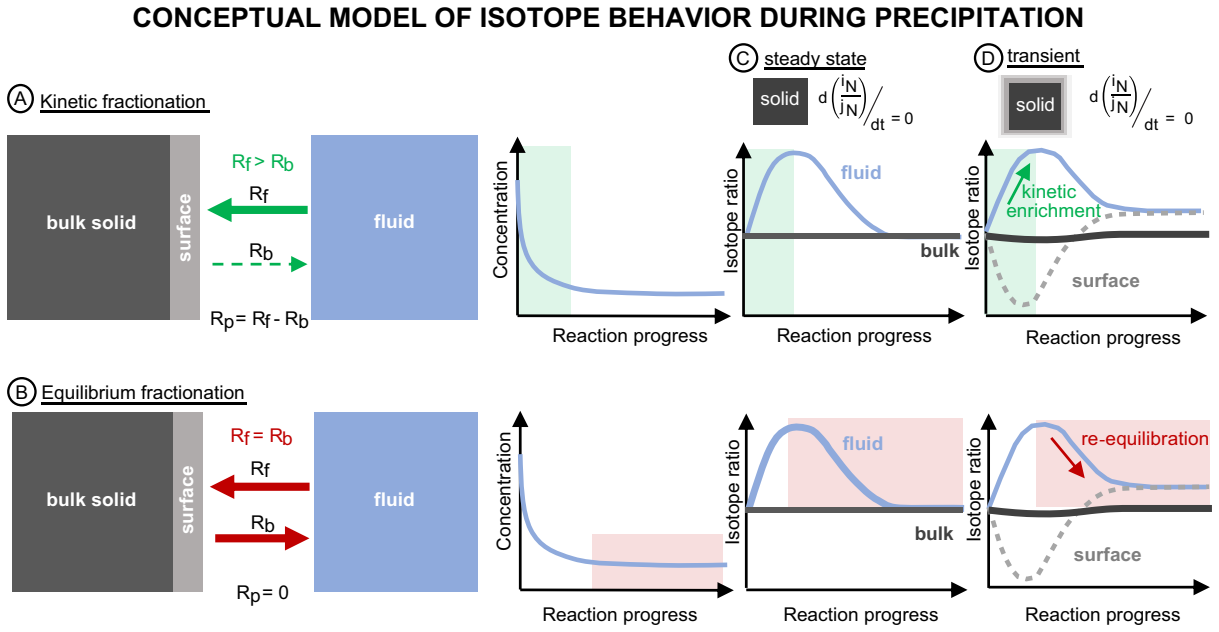

Figure 2.2 Conceptual model of isotope behavior during precipitation
Conceptual model of transient, isotopic exchange between a mineral and surrounding fluid that is governed by the balance between the forward, precipitation ($\mathbf{R_f}$) and backward, dissolution ($\mathbf{R_b}$) rates. Any imbalance between the forward and backward reaction rates where $\mathbf{R_f} > \mathbf{R_b}$ results in precipitation and kinetic fractionation (**A**). When these two rates become equal to one another (i.e. at dynamic equilibrium) than isotopic fractionation is increasingly influenced by equilibrium behavior as a result of reversible isotopic exchange (**B**). The evolution of the fluid and solid phase isotope ratios are shown under the scenarios of isotopic re-equilibration with (**C**) the bulk solid (volume averaged approach), assuming a steady state surface isotopic composition (DePaolo, 2011) and (**D**) with a growing mineral surface coupled to an isotopically co-evolving fluid phase, resulting in an isotopically zoned solid phase.

delta values (i.e. "isotopic re-equilibration"). A major consequence of this unique isotopic re-equilibration timescale is that the observed fractionation will vary with reaction progress (R_p) as the initially kinetic isotopic signature generated from precipitation transitions to values reflecting the establishment of chemical equilibrium. For a system in which $\alpha_{eq} = 1.0$, this process would return the fluid isotope ratio to a value equivalent to the solid phase (Druhan et al., 2013; Steefel et al., 2014).

Therefore, the isotope ratio chosen to represent the solid phase is a critically important parameter for determining the extent of isotopic re-equilibration in the fluid-mineral system. Traditionally, many "batch" or "steady state" models commonly employed in predicting isotope fractionation from catchment to mineral scales (Bouchez et al., 2013) choose to represent the solid phase as the composition of the entire "bulk" mineral. Underlying this assumption is the notion that the solid phase has a homogenous composition that remains at "steady state" ($d({}^{i}N/{}^{j}N)/dt = 0$, where N = element and *i,j* = given stable isotope) throughout mineral growth and interacts entirely with the surrounding fluid. Under such conditions, the isotope ratio of the fluid phase is heavily influenced by the mass of the bulk solid and rapidly shifts back to the bulk isotope value for $\alpha_{eq} = 1.0$ following kinetic perturbation (**Fig. 2.2C**). While this approach is reasonable for some systems, such as the extremely high surface areas associated with carbonate foraminifera (Keir, 1980; Halbach and Puteanus, 1984; Walter and Morse, 1985; Morse et al., 2007, and others), for the majority of terrestrial weathering environments characterized by highly variable fluid chemistry and a wide range of mineral surface areas and grain sizes (Peters, 2009; Landrot et al., 2012), it is unlikely that the solid isotope composition could be reasonably represented by the bulk mineral value (Johnson et al., 2002; Wiederhold et al., 2006; Kiczka et al., 2010).

For natural, open systems a more reasonable representation of the solid isotope composition would be the isotope ratio of the mineral surface co-evolving with the surrounding fluid ($d(^{i}N/^{j}N)/dt \neq 0$, **Fig. 2.2D**). Following a kinetic perturbation, precipitation would first kinetically fractionate the fluid, enriching it in the "heavy" isotope, while, through mass balance, the resulting precipitate would form a new mineral surface layer this is isotopically "light" in comparison. As this growth phase slows down and approaches equilibrium, the mineral becomes isotopically zoned and increasingly enriched in the light isotope. Evidence for the formation of such isotopically zoned minerals during crystal growth has been extensively reported (e.g. Skulan et al., 2002; Wiederhold et al., 2006; Kiczka et al., 2010). Ultimately, the net precipitation rate becomes negligible and at these near-equilibrium conditions, isotopic re-equilibration beings to occur. In the approach to dynamic equilibrium, the mineral surface mirrors the fluid isotopic behavior, losing its kinetic signature as isotopic exchange shifts the system towards delta values reflective of equilibrium fractionation between the fluid and the amount of newly formed mineral surface that is actively exchanging. In this approach, the extent and timing of fluid and solid phases isotopically re-equilibrating with one another should be dependent on the depth into the mineral surface that the fluid can access, which is dictated by the mineral surface area.

Therefore, the mineral surface area is predicted to exert a first order control on the extent of fluid-mineral chemical and isotopic exchange during secondary mineral formation. To test this hypothesis, we apply three different isotope fractionation models to our experimental results: (1) A Rayleigh distillation model where the fluid is assumed to be isolated from any exchange with the solid phase, (2) A steady state surface reaction kinetic model where the fluid only interacts with a constant solid surface composition,

and (3) A modified-transient model developed in this study (section 2.3) that allows for the fluid and solid to interact and isotopically co-evolve.

2.4.4.1 The Rayleigh model: A kinetic perspective

Rayleigh distillation models have been successfully used to interpret silicon isotope fractionation in multiple prior studies (De La Rocha et al., 1998; R B Georg et al., 2007; Opfergelt and Delmelle, 2012; Reynolds, 2012; Pogge von Strandmann et al., 2012; Hughes et al., 2013). Under the assumption of a well-mixed, closed, and kinetically controlled system, in which a mineral is irreversibly precipitated from solution as a

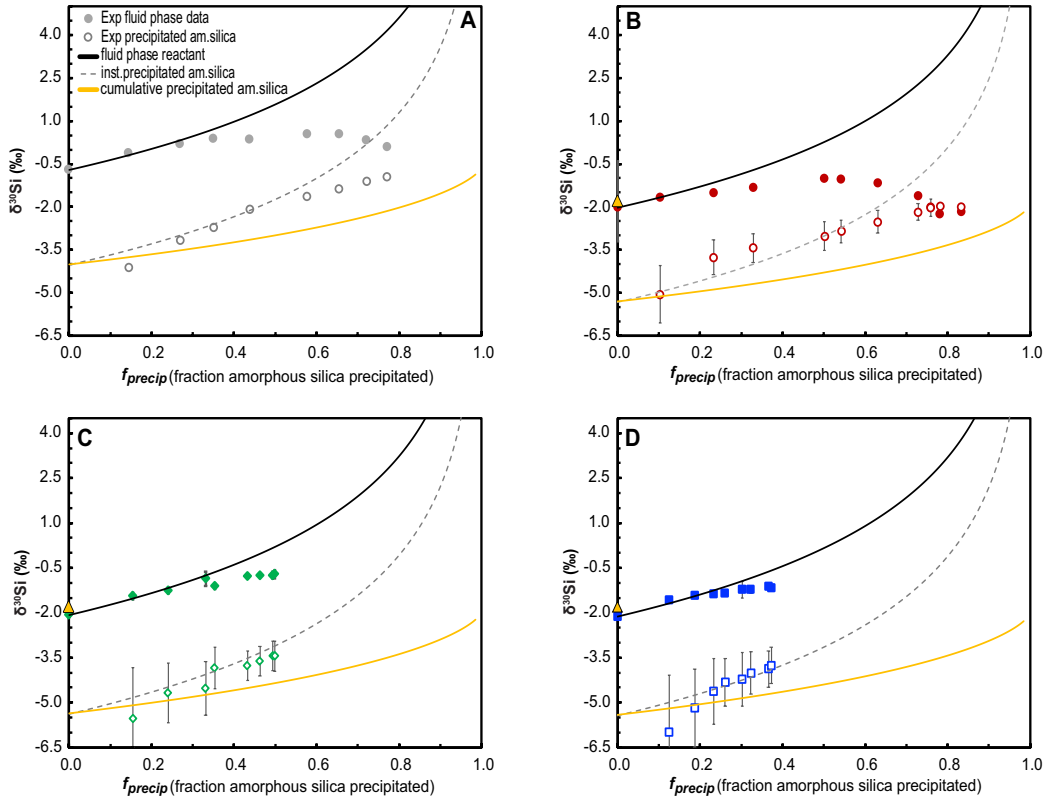

Figure 2.3 Rayleigh model predictions

Rayleigh model predictions for both fluid (solid black line), instantaneously precipitated amorphous silica (dashed line), and cumulative precipitated amorphous silica (solid yellow line) $\delta^{30}Si$ as a function of the fraction of amorphous silica precipitated (f_{precip}). Experimental results of both measured fluid (filled circles) and calculated cumulative precipitated amorphous silica (open circles) are shown for (A) the Roerdink et al. (2015) study, and the present study (**B**) high, (**C**) medium, and (**D**) low surface area experiments. Cumulatively precipitated $\delta^{30}Si$ were determined through closed system, isotope mass balance calculations. A fixed α_{kin} of 0.9967 was implemented for all Rayleigh predictions. Error bars for fluid $\delta^{30}Si$ and precipitated $\delta^{30}Si$ correspond to 2 standard deviation and 1 standard deviation respectively.

reaction product subject to a single fixed fractionation factor, the isotopic distillation of the residual reactant can be described as $R = R_0 \cdot f^{(\alpha_{kin} - 1)}$ (Rayleigh, 1902). In this expression, the instantaneous isotope ratio of the reactant pool (R) is equal to its initial isotope ratio (R_0) multiplied by the fraction of reactant remaining in solution with respect to its starting concentration (f), which is raised to the power ($\alpha_{kin} - 1$) where the fractionation factor (α_{kin}) is constant.

Given the success with which Rayleigh approaches have been used in prior Si studies, we begin our analysis of the present amorphous silica precipitation experiments using this framework. However, it is immediately apparent that a Rayleigh model using a fixed fractionation factor of 0.9967 (Roerdink et al., 2015) fails to capture the variability in both measured fluid $\delta^{30}Si$ and $\delta^{30}Si$ of the cumulative precipitated amorphous silica calculated according to closed system, mass balance (**Section 2.3.3, eq. 2.6**) as a function of reaction progress (**Fig. 2.3**). In all three batch datasets, the Rayleigh model reasonably reproduces the trend in fluid isotope enrichment early in the experiment (when precipitation rates are high), but systematically over-estimates the evolution of fluid $\delta^{30}Si$ as precipitation rates slow down in the approach to metastable equilibrium. As a consequence, experimental $\delta^{30}Si$ values appear to "fall off" the Rayleigh line. This general observation is also supported by data generated in similar amorphous silica batch experiments using identical high surface area grains (50 m^2/g) reported by Roerdink et al. (2015) (**Fig. 2.3A)**. Notably, the extent to which the experimental data deviate from Rayleigh fractionation appears to differ between the unique values of surface area. Additionally, calculated $\delta^{30}Si$ of the cumulative precipitated amorphous silica are more elevated than the Rayleigh

predictions and appear to follow a general trend that roughly coincides with the prediction of the instantaneous precipitate.

There are several possible explanations for the observed misfit between our experimental data and the Rayleigh model. The quality of reagents used to prepare the solutions and starting amorphous silica grains minimize the potential for any significant sorption processes involving impurities like iron oxides (Delstanche et al., 2009) or aluminum hydroxides (Oelze et al., 2014) that could influence fluid $\delta^{30}Si$. Additionally, the effects of partially open system behavior or incomplete separation of one phase relative to the other are negated by the experimental and sampling design. Another possibility is that additional fractionation factors may be influencing the system due to precipitation of multiple silica polymorphs such as cristobalite and quartz during the course of the reaction. However, this effect is unlikely given that the saturation states attained in these experiments coupled with the purity of the initial amorphous silica seeds makes the formation of these alternative polymorphs energetically unfavorable.

Thus, a more likely cause for variability in the fractionation factor is due to non-negligible back-reaction from the solid phase to the fluid as a result of the approach to equilibrium. Such mixed contributions from both kinetic and equilibrium isotope effects lead to an overall fractionation factor that is not constant through time and thus violates the assumptions inherent in Rayleigh distillation. Evidence for this behavior is best shown in the high SA experiment (**Fig. 2.3B**) where fluid $\delta^{30}Si$ deviate quickly from Rayleigh predictions due to fast reaction kinetics pushing the system rapidly towards equilibrium and ultimately converging to values equivalent to the precipitated amorphous silica $\delta^{30}Si$ at the end of the experiment. In order to reach these nearly equivalent values of fluid and precipitated amorphous silica phases at near-equilibrium

conditions, isotopic exchange must have occurred. Departure of the medium (**Fig. 2.3C**) and low (**Fig. 2.3D**) surface area fluid $\delta^{30}Si$ from the Rayleigh trend is comparatively smaller than what was observed for the high surface area data, as these systems featured slower kinetics. But, the fluid values of both eventually start to converge back towards the amorphous silica precipitate $\delta^{30}Si$ near the end of the experiments. In all examples, the effect of the approach to equilibrium is to diminish the magnitude of the kinetic fractionation factor, leading to overall or effective values closer to 1.0. As a result, the cumulative precipitate becomes increasingly less fractionated relative to the fluid, which gives the appearance of matching the instantaneous product Rayleigh prediction rather than the cumulative value if the fractionation factor had remained constant.

Ultimately, the Rayleigh fractionation model assumes that the product pool is instantaneously isolated such that no reversal or back-reaction can occur. The present data do not satisfy this requirement, as contributions from the back reaction are apparent. Application of a constant, kinetic fractionation factor to represent the overall effective fractionation factor of this reversible amorphous silica precipitation reaction leads to predictions of $\delta^{30}Si$ fractionation that, in this case, highly over-estimate our observations. Thus, we proceed by considering a model framework that allows for variability in the observed fractionation factor as a result of combined kinetic and equilibrium effects.

2.4.4.2 A steady state model for mixed kinetic and equilibrium behavior

A stable isotope framework that can predict the observed fractionation factor (α_{obs}) at steady state resulting from a balance between kinetic and equilibrium effects is provided by the surface reaction kinetic model (DePaolo, 2011). This approach has been successfully applied to quantify the fractionation observed for two prior amorphous silica precipitation studies (Geilert et al. 2014; Roerdink et al. 2015) and has since begun

to be discussed in the interpretation of $\delta^{30}Si$ signatures in weathering environments (Frings et al. 2016). This steady state model takes the form of an analytical solution where α_{obs} is predicted based on mixed contributions from both kinetic (α_{kin}) and equilibrium (α_{eq}) isotopic fractionation end members, which vary as a function of the balance between forward precipitation (R_p) and backward dissolution (R_b) rates (eq. 10 in DePaolo, 2011).

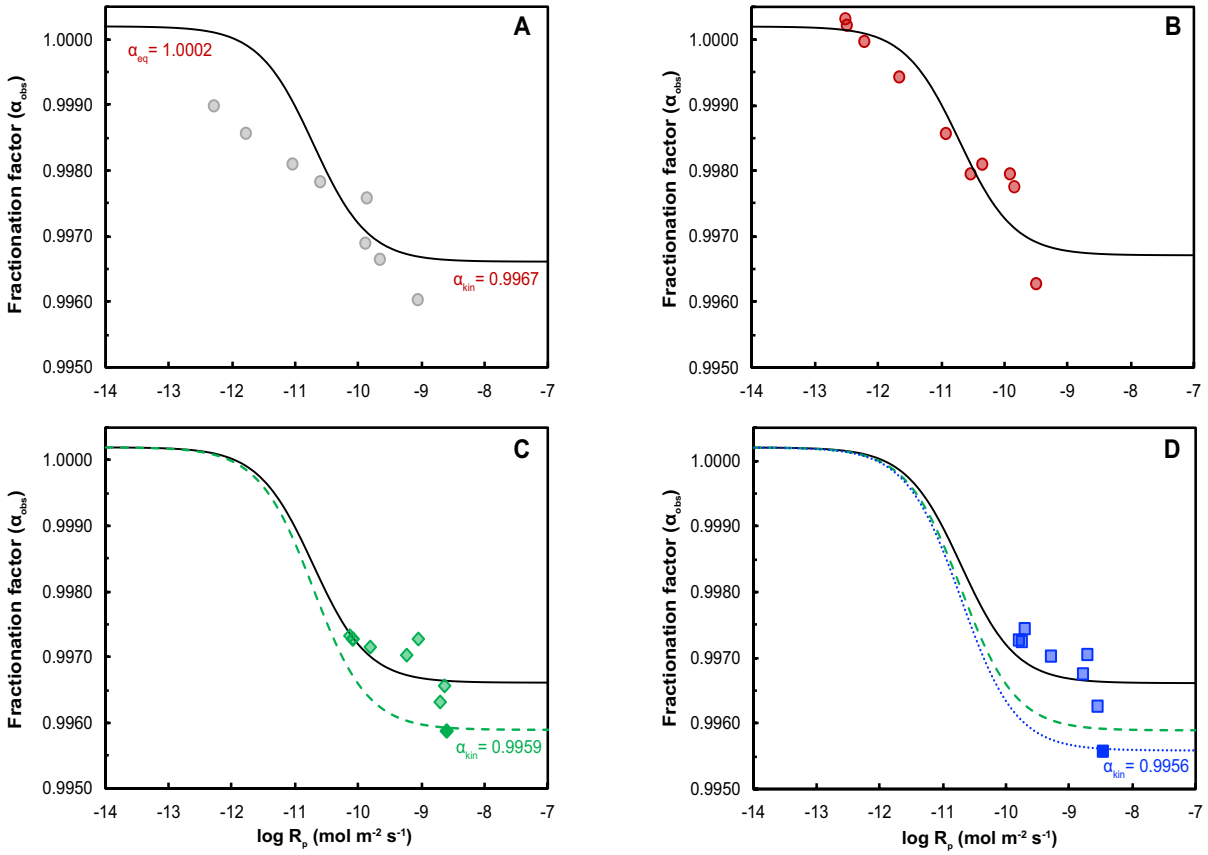

Figure 2.4 Apparent fractionation factors as a function of precipitation rate
Calculated fractionation factors for amorphous silica precipitation as a function of precipitation rate (**A**) as reported by the Roerdink et al., (2015), (**B**) from our high, (**C**) medium, and (**D**) low surface area experiments. The DePaolo (2011) surface reaction kinetic model is represented as a black line and is based on the relative contributions of α_{kin} (0.9967) and α_{eq} (1.0002) and a dissolution rate, $R_b = 1.95 \times 10^{-11}$ mol m^{-2} s^{-1} (Loucaides et al., 2008). At relatively fast precipitation rates, $\delta^{30}Si$ fractionation is kinetically controlled whereas at slow precipitation rates equilibrium fractionation exerts a stronger influence. In the high surface area case, the considerable variability in the apparent fractionation factor as a function of log R_p reflects mixtures of both α_{kin} and α_{eq}. A narrower range of fractionation is expressed in the medium and low surface area cases. Surface kinetic model results are shown for different α_{kin} values of (**C**) 0.9959 (green dashed line) and (**D**) 0.9956 (blue dashed line), respectively, but these models do not reproduce the remainder of the datasets.

Application of the steady state model to our experimental results show that α varies systematically with experimentally constrained values of R_p (**Section 2.3.2; Table 2.2**), lying principally within the transitional zone between the kinetic (lower plateau) and equilibrium (upper plateau) endmembers (**Fig. 2.4**). Steady state model predictions for an α_{kin}= 0.9967 and α_{eq} = 1.0002 agree with the earlier Roerdink et al. (2015) results (**Fig. 2.4A)** and our high surface area α_{obs} values (**Fig. 2.4B)**. The large variability observed in these high surface area cases as a function of reaction progress suggests significant effects of the equilibrium end member and thus isotopic re-equilibration. Arguments for dismissing other potential processes that can cause variability in the fractionation factor such as neo-formation of polymorphs or the precipitation of additional secondary phases have been discussed in detail in **Section 2.4.4.2**. Medium (**Fig. 2.4C)** and low (**Fig. 2.4D**) surface area α_{obs} values plot preferentially closer to the kinetic endmember as a function of precipitation rate and reflect relatively less isotopic re-equilibration.

The equilibrium fractionation factor between $SiO_{2(aq)} \leftrightarrow SiO_{2(am)}$ has yet to be constrained experimentally, and thus α_{eq} = 1.0002 was estimated by taking the reciprocal of eqn. 10 (DePaolo, 2011), and applying a linear regression analysis on $\frac{1}{\alpha_p}$ vs. $\frac{R_p}{R_p+R_b}$ for the high SA experiment where near-equilibrium conditions were obtained. The unidirectional dissolution rate, R_b (1.95×10^{-11} mol m^{-2} s^{-1} at pH = 7.5) is set to a fixed value based on dissolution experiments using the same high surface area amorphous silica crystals (Loucaides et al., 2008). Although R_b is treated as a constant in the present study, DePaolo (2011) suggested a second approach in which R_b scales as a function of R_p. We have elected to use the version of the surface kinetic model which assumes a constant R_b for two principle reasons. First, at present, there are no reliable constraints on the

functional form of the relationship between R_b and R_p for amorphous silica precipitation. Second, this approach is in agreement with two prior studies utilizing the same fixed R_b model framework for Si precipitation, thus allowing us to draw direct comparison to their results. As a final check we attempted to fit our present dataset using the $R_b = R_p^{1/2}$ functional form proposed for calcite (DePaolo, 2011), but failed to reproduce observed α variability with this approach. Thus, further work is necessary before we can defensibly suggest any variability in R_b for amorphous silica precipitation and associated implications for observed fractionation factors.

The initial observed fractionation for the high SA experiment (ε_{obs} = -3.73‰) is smaller than those observed at the start of the medium (ε_{obs} = -4.12‰) and low (ε_{obs} = -4.42‰) SA experiments. The corresponding α_{kin} (0.9967) value which reasonably captures both the Roerdink et al. (2015) dataset and our high SA experiment (**Fig. 2.4, solid black line**) similarly fails to capture the evolution of the initially high α_{obs} values for the low (0.9954) and medium (0.9959) surface area conditions. These higher initial α_{obs} may imply either larger kinetic fractionation in the medium and low SA experiments or the presence of transient effects influencing the silicon isotope behavior. However, implementing unique α_{kin}values of 0.9959 (**Fig. 2.4C, dashed line**) and 0.9956 (**Fig. 2.4D, dotted line**) to account for differences in the α_{kin} endmember of the medium and low SA cases is unable to capture the subsequent evolution of α_{obs} as a function of R_p. Thus, differences in the largest observed fractionation factors between the three surface area experiments imply an influence of transient isotope behavior arising from the progressive growth of amorphous silica from an isotopically evolving fluid. This behavior is inconsistent with the assumptions of DePaolo (2011) model, which is based on a steady

state mineral surface composition. Thus, we now seek to provide a novel framework based on the influence of the physical characteristics of the system (i.e. surface area and solid:fluid mass ratios) on kinetic behavior through a transient model capable of characterizing the isotopic co-evolution of the fluid and growing mineral surface.

2.4.4.3 A transient model for mixed kinetic and equilibrium behavior

To explore the effects of surface area and solid to fluid ratios in a fully transient framework, we developed a numerical model (described in **Section 2.2.3**) using CrunchTope, an isotope-enabled, multi-component reactive transport software (Steefel et al., 2015). The input parameters used for our numerical simulations corresponded to the experimental conditions for each of the three datasets with distinct surface area values (**Table 2.3**). Across all simulations we used one common set of reaction rate constants, initial aqueous silica concentrations, and kinetic and equilibrium fractionation factors for all three experiments. The only parameters that vary between the three cases are the surface area and the solid to fluid ratios. Before applying our transient model to the $\delta^{30}Si$ batch data, we first verified that the simulation reproduced our experimental $SiO_{2(aq)}$ concentrations and found good agreement (**Fig. 2.5A**) using a TST (Transition State Theory) rate expression (**eq. 2.2**) of order m = 3.5 (justification is provided in **Section 2.2.3**).

Experimentally determined $\delta^{30}Si$ data were then simulated using three separate isotopic fractionation models: (1) a "no back-reaction" model (**Fig. 2.5B**), (2) a steady state ("bulk") model (**Fig. 2.5C**), and (3) a transient ("mineral surface") model (**Fig. 2.5D**). In the "no back-reaction" simulation, isotope fractionation is strictly kinetic, $\alpha_{obs} = \alpha_{kin}$ (0.9967), analogous to models utilized previously for simplified fractionation during mineral precipitation (e.g. Curti et al., 2005; Curti et al., 2010; Druhan et al. 2014; Joshi et

al., 2017; Gorski and Fantle, 2017). Limited by a strictly kinetic approach (i.e. no isotopic re-equilibration), the "no back-reaction" model fails to reproduce measured fluid $\delta^{30}Si$ variability with time. In the "bulk" simulation, the fluid is allowed to isotopically re-equilibrate with the entirety of the bulk mineral composition, ${}^{i}X_{bulk}$ (**eqn. 2.3**), that is tracked through time in the model. In this approach, the bulk $\delta^{30}Si$ remains unchanged

Table 2.3 Transient model input parameter values

Input parameters	High SA	Medium SA	Low SA
Duration (days)	35	35	35
Δt (days)	5.0×10^{-5}	5.0×10^{-5}	5.0×10^{-5}
A (timestep average)	20,000	800,000	600,000
log k^a (moles m^{-2} s^{-1})	-9.67	-9.67	-9.67
$SiO_{2(aq)}$ (mM)	5.30	5.30	5.30
pH_{init}	7.35	7.31	7.30
Temperature (°C)	20	20	20
solid:fluid ($m^3_{am.silica}/m^3_{fluid}$)	0.0050	0.0086	0.0087
surface area (m^2/g)	50.0	0.127	0.072
$\delta^{30}Si_{fluid,init}$ (‰)	-2.03	-2.08	-2.14
$\delta^{30}Si_{am.silica}$ (‰)	-1.80	-1.80	-1.80
α_{kin}[b]	0.9967	0.9967	0.9967
α_{eq}	1.0000	1.0000	1.0000

a. Precipitation rate constant value reported by Rimstidt & Barnes (1980) for 20°C.
b. Kinetic fractionation factor reported by Roerdink et al. (2015).

throughout the reaction because the addition of precipitate is small relative to the initial mass present in the system. Application of this "bulk" model under-estimates the kinetic fractionation observed in the fluid $\delta^{30}Si$ of all three experiments as a result of a large influence from the bulk $\delta^{30}Si$ value due to its comparatively large mass. Notably, the high SA case is predicted to have both a smaller extent of silicon isotopic re-equilibration and continued disequilibrium between the fluid and amorphous silica phases at the end of the experiment. A lack of agreement between the "bulk" model and the experimental $\delta^{30}Si$ data implies that fluid interaction with the entirety of the bulk amorphous silica is unlikely under this given range of surface areas.

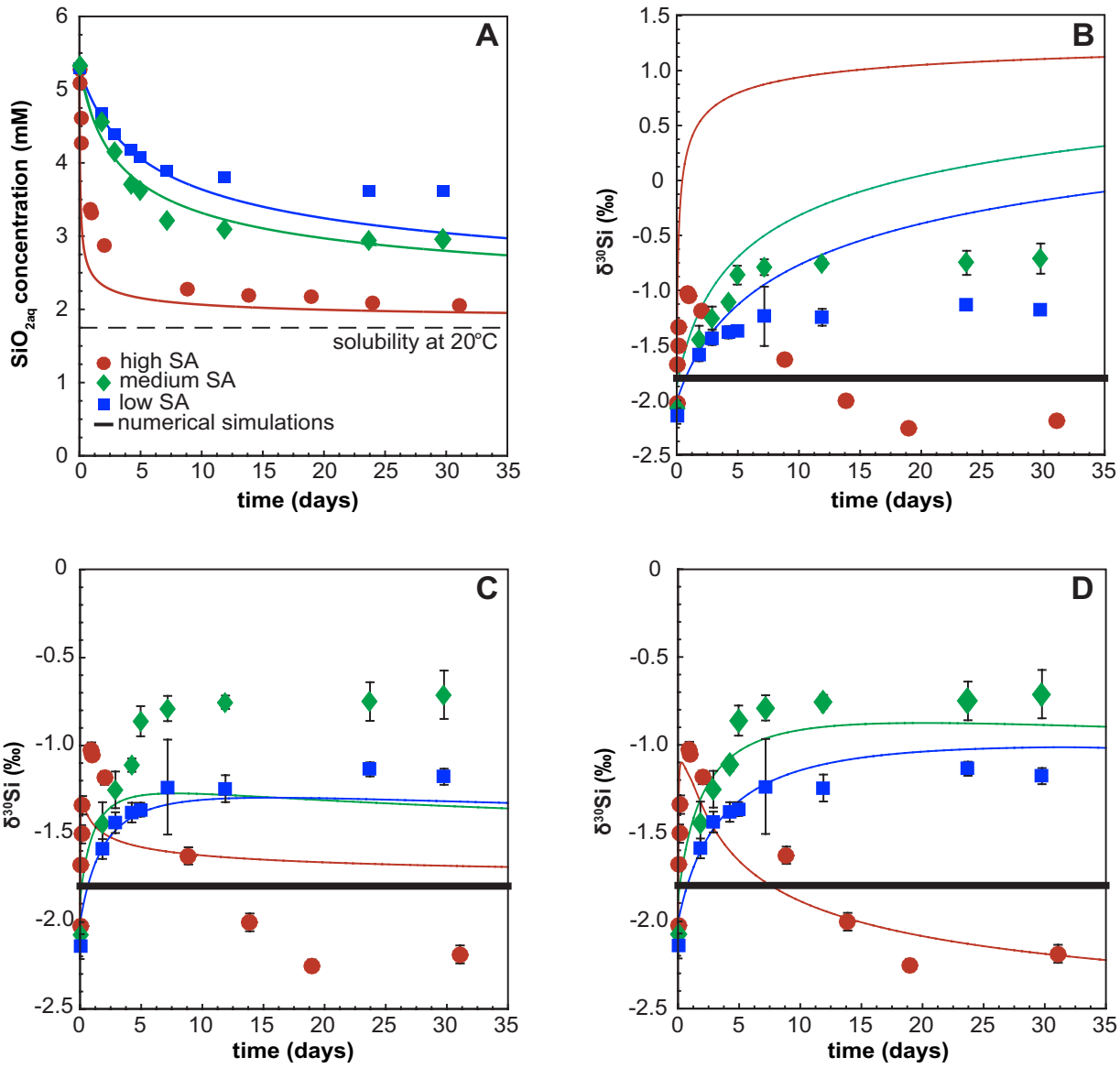

Figure 2.5 Transient model simulations

Transient model results for (**A**) aqueous silica concentrations with time during amorphous silica precipitation for the high (red line), medium (green line), and low (blue line) surface area simulations compared against experimental data (filled circles). Corresponding simulations of fluid $\delta^{30}Si$ were run under three different isotopic exchange scenarios between the growing amorphous silica and the surrounding fluid: (**B**) no back reaction allowed (i.e. no isotopic re-equilibration) and $\alpha_{obs} = \alpha_{kin}$ (0.9967); (**C**) fluid isotopic re-equilibration with the bulk solid isotopic composition ($^{i}X_{bulk}$); (**D**) fluid isotopic re-equilibration with a co-evolving mineral surface composition ($^{i}X_{surface}$). Experimental data are shown with error bars represent 2 standard deviation.

In our final "mineral surface" simulation (**Fig.2.5D**), the fluid is allowed to isotopically re-equilibrate with a co-evolving mineral surface during mineral growth, ${}^{i}X_{surface}$ (**eq. 2.4**). As described earlier (**Section 2.2.3**), the amount of the mineral surface that the fluid is allowed to interact with is estimated in this model by a unique time interval over which a running average of the isotopic composition of the amorphous silica precipitating out of solution is calculated (t - T, where $T = \Delta t \times A$). The time intervals are individually constrained in the model for each experiment, resulting in values of ~1 day in the high SA case and ~30 days (nearly the entire length of the experimental run) for the medium and low SA cases (**Table 2.3**).

"Mineral surface" model simulations based on these unique time intervals and a single set of α_{kin} (0.9967) and α_{eq} (1.0000) successfully reproduced fluid $\delta^{30}Si$ trends in all three surface area experiments. Notably, the "mineral surface" transient model captured the full extent of isotopic re-equilibration observed in the high SA experiment including final fluid $\delta^{30}Si$ values significantly more negative than the average bulk composition. This result provides key evidence for the mineral fluid phase isotopically re-equilibrating with the mineral surface rather than the bulk. The values of this isotopically depleted, newly formed mineral surface are explored in further detail below (**Section 2.4.5**). A major prediction from this transient model is that fluid $\delta^{30}Si$ can re-equilibrate to values distinct from the bulk amorphous silica composition at metastable equilibrium, is validated by this comparison.

In the medium and low SA experiments, the apparent kinetic fractionations that were underestimated by the "bulk" model (**Fig. 2.5C**), are successfully predicted in the transient model. Elevated fluid $\delta^{30}Si$ values observed throughout the duration of these lower surface area experiments are also reproduced and result from slower precipitation

kinetics maintaining the systems at far-from equilibrium conditions. Thus, strong consensus between transient "mineral surface" model predictions and our three experiments indicate that reactive surface area (i.e. fluid-mineral interaction depth) and corresponding transient isotope behavior (deriving from the isotopic co-evolution of the fluid and growing amorphous silica surface) has a first order control on $\delta^{30}Si$ fractionation during amorphous silica precipitation.

A key component of our transient model is the time interval and its dependence on the reactive surface area. As further detailed in **Section 2.2.3**, the mass of dissolved silica removed from solution over the given time interval is used as an approximation for the depth into the mineral surface in contact with the surrounding fluid. In our transient framework, fluid $\delta^{30}Si$ re-equilibration is dependent on the amount of mineral surface that the fluid can isotopically interact with (which is dictated by the surface area). Thus, the time interval serves as a proxy for the fluid-mineral interaction depth.

To further explore this relationship, a sensitivity analysis was conducted on the high SA case where, all other parameters remaining constant, transient simulations were run for three different time intervals: 2.4 hrs, 1 hr, and 10 days (**Fig. 2.6**). Overall, changing T has no impact on dissolved silica concentrations (**Fig. 2.6A**). However, fluid $\delta^{30}Si$ does change considerably with varying T (**Fig. 2.6B**). In the case where T = 2.4 hrs (i.e. the running average is performed on the mass precipitated over the past 2.4 hrs) the fluid interacts and re-equilibrates with a thin portion of the recently formed mineral surface that is largely depleted in ^{30}Si due to the initial period of kinetic fractionation. As a result, fluid $\delta^{30}Si$ after initial kinetic fractionation re-equilibrated to significantly more negative values (-3.32‰ at 35 days). On the other hand, when T is set to 10 days the running

average is performed over a greater portion of the mineral surface and thus fluid $\delta^{30}Si$ re-equilibrates towards values considerably closer to the bulk. As is shown in **Fig. 2.6B**, time intervals of 2.4 hours and 10 days both fail to capture the measured fluid $\delta^{30}Si$ timeseries trend for our high SA case whereas we find good agreement when setting T to 1 day. This sensitivity analysis supports the dependence of the time interval on surface area and its role as a proxy for the fluid-mineral interaction depth, which controls the extent to which the fluid and growing mineral surface can isotopically co-evolve and re-equilibrate.

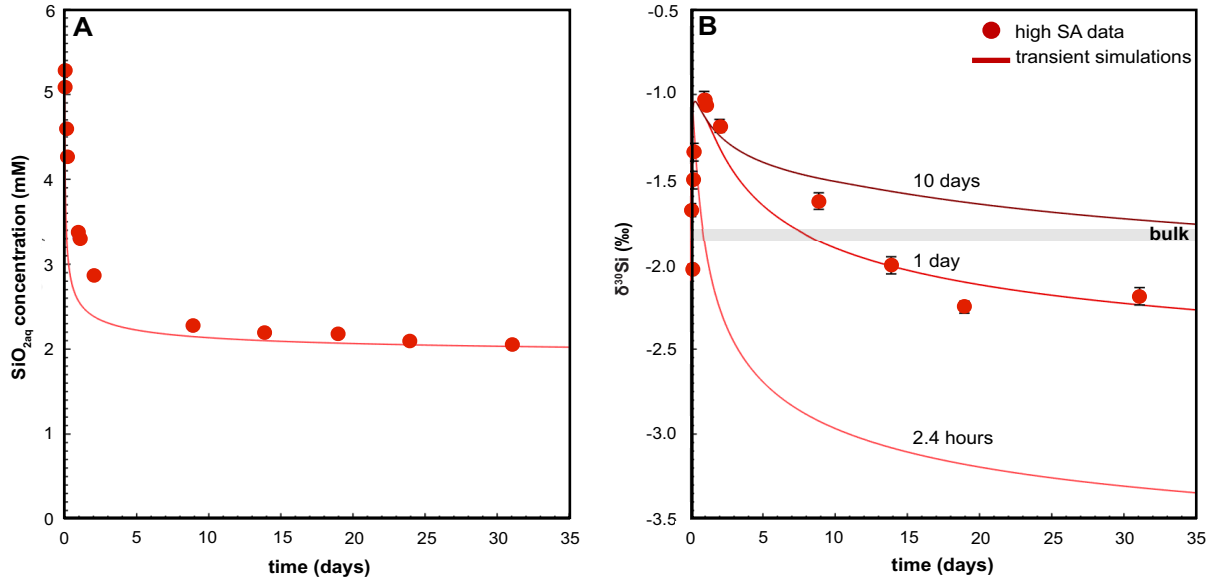

Figure 2.6 Sensitivity analyses of time interval, T, for high SA case

Sensitivity analysis of the time interval, T, for the high surface area case. Concentration (**A**) and fluid $\delta^{30}Si$ (**B**) timeseries for both the experimental data (solid red circle, error bars correspond to 2 standard deviation) and transient simulations (solid lines) are shown. Three time interval scenarios are presented that reflect the running average of the isotopic composition of silica mass precipitated over the past (1) 2.4 hrs (light red line), (2) 1 day (red line), and (3) 10 days (dark red line). These three simulations are indistinguishable in the silicon concentrations.

2.4.5 Estimating the solid-fluid interaction depth and extent of re-equilibration

2.4.5.1 Numerical approach

A major implication that arises from our transient "mineral surface" model is that the mass of new mineral that the fluid can interact with is now being tracked within the model framework. Thus, we are now poised to explore how the depth into the mineral surface that the fluid exchanges with is dictated by surface area. As a first approximation, we start by calculating the growth rate of accumulating amorphous silica precipitating out of solution using the following expression (**eq. 2.8;** Rimstidt and Barnes, 1980; Geilert et al., 2014):

$$R_G = \left[\frac{N_{SiO_{2(ppt),\,t+1}} - N_{SiO_{2(ppt),\,t}}}{S \cdot \Delta t}\right] * M_v \qquad (2.8)$$

where the instantaneous growth rate (R_G) in units of nm/s is determined by the precipitation rate (**eq. 2.5**) and the molar volume, M_v, of 30 cm^3 mol^{-1}. Through R_G, the amount of new amorphous silica accumulated onto the seeds, referred to as the "surface growth", can be plotted as a function of time both experimentally and numerically (**Fig. 2.7**). In general, the accumulated surface thicknesses calculated using the numerical model results increase with time and stabilize as the growth rate decreases in the approach to metastable equilibrium, The results are in close agreement with the experimentally constrained surface thickness accumulation as a function of surface area and the amount of surface-normal growth reported earlier (**Section 2.4.3**). This observation is also in agreement with the Geilert et al. (2014) amorphous silica precipitation study. Growth of the amorphous silica surface is dependent on the reactive surface area available. For a lower available surface area, the same mass of new mineral

formed must achieve a thicker depth at an equivalent point in time. This is reflected in the medium (total accumulated depth = 36.5 nm) and low (total accumulated depth = 58.0 nm) surface area numerical model results, which show significantly more overall surface growth as compared to the high SA case (total accumulated depth = 0.193 nm) despite starting at higher solid:fluid mass ratios. Similarly, the lower available surface area simulation achieves a given depth at an earlier time relative to the medium and high SA cases.

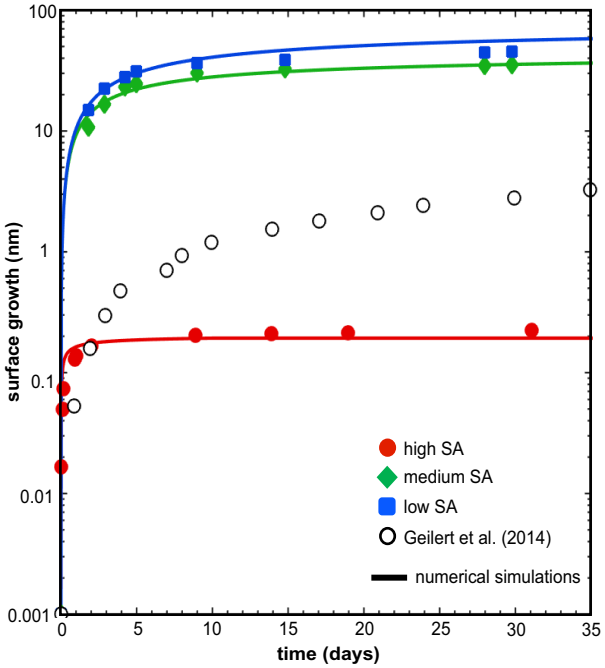

Figure 2.7 Amorphous silica surface thickness accumulation through time
Amorphous silica surface thickness accumulation through time. Surface growth was calculated both experimentally for the high SA (red circle), medium SA (green diamond), and low SA (blue square) cases, and numerically (solid lines) from our transient model simulations shown as solid lines. Results are compared against Geilert et al. (2014) reported values (open circles).

Having confirmed this estimate of total surface growth both experimentally and numerically, we may now track the $\delta^{30}Si$ of both the bulk phase and the net accumulated surface throughout the course of our transient simulations for the three surface area cases (**Fig. 2.8**). Accurate behavior of the model is verified by checking mass balance. The model tracks the isotope ratio of the entire bulk mass of $SiO_{2(am)}$, including the seed crystals through time, as well as the mass lost from the fluid that was incorporated into the new amorphous silica surface for both isotopes. Using these values, we show that the initial $SiO_{2(am)}$ subtracted from the bulk $SiO_{2(am)}$ at any given timestep perfectly recovers the mass

of $SiO_{2(aq)}$ lost from the fluid and the corresponding mass-weighted difference in $\delta^{30}Si$ (**Table 2.2**), thereby verifying that mass balance is fully adhered to in the model both for concentration and isotope ratio. As a final check, we verify that the mass and isotope ratio of $SiO_{2(aq)}$ and net accumulated $SiO_{2(am)}$ sum to the initial isotope ratio of the fluid at the beginning of the experiment.

In these simple, closed system batch reactors, our numerical simulations show good agreement with the experimentally calculated ($\delta^{30}Si_{ppt}$) and measured (bulk $\delta^{30}Si_{(am)}$) values (**Table 2.2**). However, in a more complex open system, this numerical approach would be our only recourse to estimate such values. Thus, a significant advantage that arises from our transient model is that the net accumulated surface $\delta^{30}Si$ can be estimated numerically by tracking the ^{28}Si and ^{30}Si cumulatively precipitated out of solution over

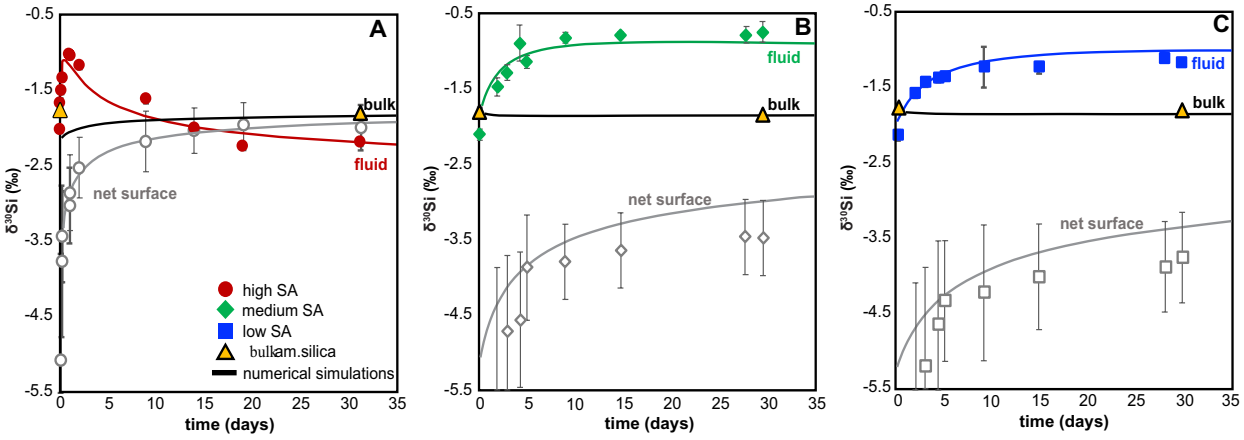

Figure 2.8 Transient model results of solid phase Si stable isotope composition
Transient model results of the bulk and cumulative newly precipitated amorphous silica $\delta^{30}Si$ tracked throughout the simulations for the (**A**) high, (**B**) medium, and (**C**) low surface area cases. Experimentally measured $\delta^{30}Si$ (filled circles) and numerically calculated $\delta^{30}Si$ (colored, solid lines) for the fluid phase are presented. Good agreement is found between $\delta^{30}Si_{ppt}$ (shown as grey, open points) calculated from isotope mass balance (error bars correspond to 1 standard deviation, **Table 2**), and numerically estimated accumulated $\delta^{30}Si$ (grey solid lines). Measured bulk $\delta^{30}Si$ (yellow triangles) are presented alongside transient bulk $\delta^{30}Si$ predictions (black solid lines). In the high SA case, $\delta^{30}Si_{ppt}$ mirrors the evolution of fluid $\delta^{30}Si$ with time and ultimately reach near-equivalent values towards the end of the experiment. This observation is in contrast to the medium and low SA cases where both experimental data and numerical simulations retain far from equilibrium isotopic signatures.

the length of the simulation, representing a component of the overall bulk solid measured directly at the end of the experiment.

As a result of the large mass of silica initially contained in the bulk phase seed crystals relative to the fluid, bulk $\delta^{30}Si$ is not appreciably sensitive to precipitation over the duration of the experiment. This is demonstrated both by direct measurement and within the numerical model. In contrast, $\delta^{30}Si$ of the growing mineral surface shifts significantly through time, reflecting both the preferential incorporation of ^{28}Si during the kinetically dominated portion of the experiment and subsequent re-equilibration with the surrounding fluid at later times. In the high SA case (**Fig. 2.8A**), the reaction is sufficiently rapid to allow the net accumulated $SiO_{2(am)}$ $\delta^{30}Si$ to approach the fluid $\delta^{30}Si$ at metastable equilibrium whereas in the medium (**Fig. 2.8B**) and low (**Fig. 2.8C**) surface area cases the net surface remains far from both bulk and fluid values at the end of the experiments.

Notably, the numerical model prediction of net accumulated $\delta^{30}Si$ at the end of the high SA experiment predicts a slight turnover where the newly accumulated precipitate values become more elevated than the fluid despite an equilibrium fractionation factor of 1.0. We reassert that this behavior does not violate mass balance (**Table 2.2**) and can be attributed to the higher-order rate law (**eq. 2.2**), which impedes complete isotopic equilibration. As discussed earlier, the isotopic solid solution derivation used here (Druhan et al., 2013) is only strictly valid under a linear TST expression in the limit as isotopic equilibrium is acheived. Interestingly, our experimentally calculated net surface $\delta^{30}Si$ based on simple mass balance (**eq. 2.6**) also show the net surface approaching and then becoming greater than the fluid $\delta^{30}Si$ values. Though beyond the scope of the present study, this independent observation agrees with the numerical model and suggests

implications for the behavior of isotope exchange at higher order rates near equilibrium. In addition, this strong agreement between our numerical and experimental $\delta^{30}Si_{ppt}$ values indicate that the solid phase became isotopically zoned normal to the mineral surface, particularly in the high SA case. These results build upon and expand previous transient-based models (Druhan et al., 2013; Steefel et al., 2014; Druhan et al., 2015) suggesting that the formation of isotopic heterogeneity (i.e. zoning) within a growing mineral phase imparts a significant influence on observed fluid isotopic values.

Having now constrained $\delta^{30}Si$ of the net accumulated surface throughout the course of our transient simulations, we turn to the component of this newly formed mineral that the fluid interacts with through time. For the medium and low SA cases, the depth into the mineral surface that defines the mole fractions (**eq. 2.4**) is defined by the user-specified time interval (T) and the depth of the accumulated surface thickness tracked through time (calculated above, **eq. 2.8** and **Fig. 2.7**). The mineral-fluid interaction depth is then calculated based on the cumulative amount of $SiO_{2(am)}$ precipitated over the given time interval. For these two surface areas, the time interval necessary to accurately recover our observations in the numerical simulations was long (~30 days). This means that the majority of the net accumulated precipitate was included in the solid solution model (**eq. 2.2**). As a result, these values (**Table 2.4**) for the medium and low SA cases were 14.3 nm and 27.9 nm, respectively, at the end of the simulation. These values represent 39% and 48% of the total depth of freshly accumulated $SiO_{2(am)}$ precipitated out of the solution over the 35-day simulation for the medium and low SA cases, respectively. This calculation suggests that early in the reaction, when precipitation rates are highest, the fluid interacts with effectively the entire growing amorphous silica surface. Thus, for these medium and low SA cases, slower precipitation kinetics maintained far from

isotopic equilibrium conditions throughout the course of the experiment, offsetting the contribution from the backward reaction (i.e. delaying the onset of isotopic re-equilibration) while also allowing the fluid to interact with a large portion of the newly-formed mineral surface.

Table 2.4 Fluid interaction depths into amorphous silica

Depth calc. methods	**High SA**	**Medium SA**	**Low SA**
Transient (this study)	0.095 nm	14.3 nm	27.9 nm
Mavromatis et al. (2017)	0.110 nm	22.4 nm	34.1 nm

For the high SA case, the time interval T necessary to recover our observations was much shorter (1 day). Following the same calculations used above at early time when precipitation rates were rapid, the fluid initially interacts with approximately 1 monomolecular surface layer (depth = 0.095 nm). However, as time proceeds and reaction rates slow down, this short time interval means that the fluid-mineral surface interaction depth becomes very thin as a result of less precipitation onto the newly formed mineral surface. At this late stage of the experiment, the combination of slow precipitation rate (where contributions from isotopic re-equilibration become more substantial), and a small solid phase component defining the mole fractions (**eq. 2.2**) allows the fluid to shift to substantially lower values. This behavior is complicated by the high order reaction rate, resulting in an inability to perfectly resolve the fluid-mineral interaction depth at near-equilibrium conditions using the selected time interval as a proxy.

To circumvent this limitation, we offer a simple scaling calculation for the high SA case where the original starting solid:fluid mass ratio is increased to the starting solid:fluid mass ratio for the medium and low SA cases. Normalizing to the same

solid:fluid mass ratios allows us to directly compare the mass precipitated out of solution over the duration of the three experiments. The result is that the net accumulated mass of $SiO_{2(am)}$ for the normalized high SA case (0.793 mmoles) was 18% and 27% more than the mass accumulated over the same duration in the medium (0.647 mmoles) and low (0.582 mmoles) SA experiments, respectively. However, the depth of this new mineral growth calculated for the high SA case using this scaling approach (0.108 nm) is smaller than the medium and low SA interaction depths as a result of the correspondingly scaled high surface area (SSA_{init} = 216 m^2). These results suggest that the original seed crystal isotopic ratio is much less isolated from the surrounding fluid in the high SA case, and that only a very small veneer of new precipitate with correspondingly negative values is available to include in the mole fraction calculation (**eq. 2.4**). This difference is consistent with the observation of rapid turnover in the fluid $\delta^{30}Si$ towards values, which approach, and ultimately become more negative, than the bulk.

A significant implication arising from these simulations is that isotopic re-equilibration can exert a large influence on the overall $\delta^{30}Si$ value of a newly formed amorphous silica surface (**Fig. 2.8A**). Our model is constructed such that over a given time interval, a higher precipitation rate will result in a larger mass included in the definition of the mole fractions used to calculate the corresponding evolution of the fluid isotope ratio (**eq. 2.2, 2.4**). This means that at rapid mineral growth rates, a larger component of the new mineral phase is interacting with the fluid. As the growth rate slows, this fraction of the total new precipitate diminishes, suggesting that in the approach to equilibrium the ability of the fluid to alter the solid isotope ratio also diminishes. Though this behavior is imposed through our model framework, we have demonstrated that the approach accurately recovers the behavior of the co-evolving fluid

and solid surfaces across a variety of growth rates and surface areas. Thus, according to our transient model simulations, the rate at which stable isotopic re-equilibration can occur during secondary amorphous silica formation is a balance between the amount of newly formed solid available to interact with the fluid and the proximity to equilibrium. What re-equilibration is able to occur can be accomplished relatively quickly (~1 month) and can involve a large portion of the newly formed solid. This finding is in contrast to stable mineral recrystallization results of foraminiferal tests, which observe only ~5% recrystallization over 100 days (Chanda et al., 2019), though our results are unique to the (paleo)environmental $\delta^{30}Si$ signatures within secondary amorphous silica solids.

2.4.5.2 Isotope mass balance approach

The extent to which these isotopic signatures of mineral growth are reset is fundamental to the fidelity of geochemical and paleoclimatology/paleoceanography proxies used to infer modern and ancient environments. Several recrystallization models have been proposed in the literature to quantify the magnitudes and rates of stable mineral recrystallization, including the frequently employed "fractional approach" model based on mole fractions of the solid and fluid phases (summarized by Gorski and Fantle, 2017) or simple isotope mass balance models like those developed by Mavromatis et al.(2016, 2017) that generally take the form of (**eq. 2.9**):

$$\delta_{fluid,eq} = \delta_{fluid}\left(1 - f_{solid}\right) + \delta_{solid} \times f_{solid} \qquad (2.9)$$

where the fraction of the fluid phase concentration that derives from exchange with the solid phase (f_{solid}) is dependent on the isotopic ratio of the fluid at equilibrium ($\delta_{fluid,eq}$), the isotopic composition of the fluid at the end of the precipitation event (δ_{fluid}), and the isotopic composition of the solid phase (δ_{solid}). This approach requires information

regarding the crystal structure, specifically the geometry of the unit cell and how the particles are arranged within a given unit cell, in order to estimate the concentration of the given element of interest in the outer surface layer (necessary for quantifying exchange between the solid and fluid phases).

As an independent constraint, we applied these calculations for our amorphous silica precipitation data (**see Appendix C**). Fluid interaction depth values obtained using the Mavromatis et al. (2016, 2017) model were similar to our transient-based estimations, but systematically returned slightly higher values. For the medium and low SA cases their approach suggests that as much as 60% of the total new precipitate is still interacting with the fluid in comparison to our prior estimates of 39% and 48%, respectively (**Table 2.4**). Given the differences in the two approaches, this level of agreement suggests our approach is robust. Two sources of discrepancy may contribute to the differences in these methods for calculating the fluid-solid interaction depth. The first resides in the unit cell geometry approximation, which in this case was not available for amorphous silica explicitly and so had to be approximated by a rhombohedral unit cell used for quartz (V = 113 Å, edge length 5.405 Å**)** where there are ~ 3atoms Si/ unit cell (**Fig. C.1)**. The second limitation arises from fluid interaction depth calculations using simplified closed-system isotopic mass balance equations (e.g., **eq. 2.9**) where steady state assumptions have to be made. As shown earlier in this study, such assumptions are incorrect based on our transient model results and thus yield inaccurate interpretations. These limitations highlight potential advantages in using the transient model approach to constrain the fluid-solid interaction and re-equilibration depth: (1) there is no need to use crystal structure geometries and other parameters to approximate outer surface layer elemental concentrations; (2) the isotopic composition of the component of the surface directly

interacting with the fluid can be directly tracked. This tracking is particularly effective for cases where rates adhere to linear TST rate laws and/or express slower overall kinetics.

2.4.6 Implications for silicate weathering proxies

Our experiments and transient models indicate that the observed fractionation factors during secondary amorphous silica formation are surface area dependent, and that this dependence is more nuanced than simply a scaling of the reaction rate. This relationship could have important implications for other commonly formed secondary minerals. Average observed fractionation factors produced in this study ($\varepsilon_{am.silica-SiO2(aq)}$ = -2.5‰) are generally higher than what is observed for clays (ε = -1.5‰, Frings et al., 2016) or for amorphous silica precipitation in flow throw experiments (ε = -2.10‰, Geilert et al., 2014), but are consistent with ε observed for previous batch amorphous silica precipitation studies: ε = -3.4‰ (am.silica batch experiments, Roerdink et al.,2015) and ε = -3.9‰ (biogenic opal precipitation, Ziegler et al., 2005). Despite conducting our amorphous silica precipitation experiments at dissolved SiO_2 concentrations higher than what is traditionally observed in natural weathering environments (Dürr et al., 2011; Opfergelt and Delmelle, 2012; Patrick J Frings et al., 2016; Poitrasson, 2017), the results from this study can be extendable to secondary silica proxies in natural weathering environments where the rate of mineral formation and, thus, the timing and extent of isotope re-equilibration could potentially exhibit a similar dependence on surface area.

For example, findings from our study could help explain the paradox of uniformly low $\delta^{30}Si$ signatures in secondary clays within weathering environments (ranging between -2.95 to -0.16‰ (Poitrasson, 2017)) and correspondingly high $\delta^{30}Si$ in soil waters (Ziegler

et al., 2005; Opfergelt et al., 2010; Opfergelt and Delmelle, 2012), despite estimated equilibrium fractionation greater than 1.0 for secondary clays (Méheut et al., 2007). Secondary clays in low temperature environments typically form through conversion of high surface area aluminum oxide precursors, like allophane and gibbsite, towards more stable crystalline, lower surface area clays like kaolinite (i.e. low temperature silica diagenesis). Oelze et al.(2014) showed that Si adsorption onto gibbsite yields a significant kinetic fractionation and proposed that these large kinetic signatures are preserved due to their quick conversion to secondary clays. This explanation is supported by our transient framework in that lower surface area grains minimize the extent of isotopic exchange and thus preserve kinetic signatures in both fluid and secondary mineral phases for significantly long periods of time.

The results of this study can also be extended to iron oxide formation, another commonly formed secondary phase in natural environments, where, for instance, the extent of stable isotope exchange between dissolved Fe(II) and Fe(III) in hematite was found be greater in grains of smaller particle size, or higher reactive surface area (Frierdich et al., 2015). Ultimately, to better interpret isotope fractionation during secondary mineral formation in weathering environments, a transient approach that considers the physical characteristics of the solid phase is required. Our transient model, then, represents a new generation of isotope fractionation models that can be applied to many different systems to better predict observed fractionation factors in natural settings and quantify the extent to which these signatures are preserved in the surrounding porous media.

2.5 SUMMARY AND CONCLUSIONS

This study reports, **(1)** δ^{30}Si isotopic fractionation during amorphous silica precipitation "free-drift" experiments conducted over a range of surface areas at ambient temperatures (20°C) and near-neutral pH (~7.3) ; (**2**) the development and application of a transient-based numerical model for simulating isotopic fractionation between interacting minerals and fluids in dynamic, open systems characterizing weathering environments; and (**3**) a novel approach for tracking isotopic zoning in minerals using a time interval to perform a running average of the newly precipitated mineral surface isotopic composition in contact with the surrounding fluid. Our main findings can be summarized as follows:

(1) Surface area exerts a first order control on δ^{30}Si re-equilibration during secondary amorphous silica precipitation. Fluids interacting with mineral grains of high surface area will isotopically re-equilibrate over short timescales (days to weeks) whereas interaction with grains of reasonably lower surface areas will preserve the kinetic isotopic signature over longer periods of time. This study provides further evidence that fluid – mineral interactions do have the capacity to alter isotope archives recorded in geochemical proxies under specific conditions.

(2) The extent to which isotopic re-equilibration significantly alters the overall kinetic isotopic signature of newly formed secondary minerals is dependent on the fluid-surface interaction depth, which is in turn a function of the mass precipitated and the surface area. In the case of amorphous silica formation, isotopic re-equilibration is a balance between the portion of the total accumulated mineral surface interacting with the fluid and the extent to which growth rates are sufficiently slow to impede the

influence of the back reaction. In this sense, low surface areas seem to protect or preserve secondary solid phase isotopic signatures.

(3) Finally, in application to modern weathering environments, our results show that variability in observed fractionation factors generated in open, transient systems could have a dependence on both surface area and solid:fluid mass ratios. Thus, at the continuum scale, metrics for the isotopic composition of the evolving mineral surface are required for accurate interpretations of observed isotopic signatures used for characterizing environmental conditions of mineral formation. In this regard, a transient approach is necessary to characterize mineral isotopic heterogeneity.

CHAPTER 3

A first look at Ge/Si partitioning during amorphous silica precipitation and implications for Ge/Si as a tracer for silicate weathering[2]

3.1 INTRODUCTION

Secondary mineral formation plays a key role in silicate weathering rates, scavenging solutes generated through otherwise congruent dissolution of primary minerals within the parent bedrock. This retention of elements liberated through chemical weathering in the form of secondary mineral phases such as clays is a vital process in soil and regolith formation and the development of the diverse heterogeneous landscapes that characterize the Earth's surface. However, the presence of these secondary mineral precipitation processes complicates our ability to accurately assess the extent of solute generation taking place within a given weathering environment (Maher et al., 2009). Moreover, neglecting the effects of these secondary phases creates over-estimates of predicted global silicate weathering rates (Hiley and Porder, 2008). To address this problem, application of metal stable isotopes and trace element ratios are now increasingly utilized as a more precise metric of secondary mineral formation and the role of these pathways in overall silicate weathering fluxes. In particular, silicon stable isotopes and trace element substitutions of silicon in common minerals (e.g. germanium) have been demonstrated as powerful and complementary tracers of silicate weathering

[2] Fernandez, N.M ; Perez-Fodich, A. ; Derry, L. A.; Druhan, J.L. *in prep.*

processes (Kurtz et al., 2002; Opfergelt et al., 2010; Delvigne et al., 2016; Baronas et al., 2018).

In the weathering environment, $\delta^{30}Si$ and Ge/Si are both sensitive to secondary weathering processes, notably secondary mineral precipitation, biological uptake, and adsorption onto Fe-oxides. Ge behaves like a pseudo-isotope of Si in these systems due to several key similarities. They are both group IV elements and have identical electron structures. They both have similar bond lengths, Si-O and Ge-O are 1.75 and 1.64 Å, respectively, and are of similar sizes with Ge being slightly larger (atomic radius = 1.25 Å) compared to Si, (atomic radius = 1.11 Å). These common physical structures facilitate the incorporation of Ge into secondary silicate phases as a substitute for Si in the same manner commonly observed for other pseudo-isotope trace replacements, such as Sr for Ca in carbonates, following Goldschmidt's principle (Goldschmidt, 1958). These two tracers $\delta^{30}Si$ and Ge/Si have important distinctions in both underlying fractionation mechanisms and terminology. While $\delta^{30}Si$ fractionation can be described by fractionation factors (α or $\Delta_{solid\text{-}diss}$), Ge/Si partitioning is generally characterized by a partition coefficient (K_d) between a solid and a fluid phase.

In natural environments, congruent primary dissolution is not associated with substantial or systematic $\delta^{30}Si$ and Ge/Si fractionation. Thus, we can assume that corresponding fluid values represent the dissolving mineral stoichiometry (~1.5 μmol mol^{-1}, Murnane & Stallard 1990; Froelich et al., 1992, Kurtz et al., 2002). On the other hand, secondary mineral formation exerts a first-order control on both dissolved $\delta^{30}Si$ (Ziegler et al., 2005; Georg et al., 2006, 2007, 2009; Opfergelt et al., 2011; Pogge von Strandmann et al., 2012;Hughes et al., 2013; Riotte et al., 2019l; and others) and Ge/Si signatures (Kurtz

et al., 2002; Scribner et al., 2006; Derry et al., 2006; Lugolobi et al., 2010; and others). This pair of silicate weathering tracers are known to co-evolve under such conditions (Lugolobi et al., 2010; Opfergelt et al., 2010; Delvigne et al., 2016; Baronas et al., 2018) and for the most part the manner in which they fractionate is comparable. The $\delta^{30}Si$ and Ge/Si fractionation signatures of secondary clays are typically inversely correlated in that the "light" Si-28 is preferentially incorporated into the newly-formed clay due to kinetic isotope effects and Ge is similarly preferentially partitioned into the solid phase as a result of Ge being compatible with secondary clays at equilibrium (K_d ~10.7 on average for secondary clays; Kurtz et al., 2002). The result is a secondary clay that is low in $\delta^{30}Si$, -2.95 to –0.16‰ (Ziegler et al., 2005; Georg et al., 2006; Cornelis et al., 2010; Opfergelt et al., 2012; Hughes et al., 2013; Frings et al., 2016; Riotte et al., 2018; and others) and more elevated in Ge with Ge/Si values greater than 5 μmol mol^{-1} (Lugolobi et al., 2010; and others). As a result, the fluid from which these phases form must become isotopically "heavier" (higher $\delta^{30}Si$ values) and lower in Ge/Si values with respect to the bedrock). This correlation between $\delta^{30}Si$ and Ge/Si partitioning observed for secondary mineral formation is not the same for all secondary weathering processes. For instance, phytolith formation generally results in a solid phase with low Ge/Si values (Derry et al., 2005; Blecker et al., 2007; Opfergelt et al., 2010). Low Ge/Si phytoliths have generally been hypothesized to be a result of Ge toxicity to plants at certain concentrations (Sankhla and Sankhla, 1967; Halperin, 1995), but this has been disputed (Blecket et al., 2007). Unlike for abiotic secondary mineral formation, both physiological and chemical processes can dictate Ge incorporation or exclusion in growing phytoliths (Loomis and Durst, 1992; Cakmak et al., 1995; Epstein, 2001; Blecker et al., 2007), rendering these biological

mechanisms quite distinct and less well understood compared to its abiotic counterpart. Despite certain conditions where Ge/Si behaves differently from δ^{30}Si during secondary processes we anticipate that the underlying fractionation mechanisms of silicon isotopes and Ge/Si are inherently analogous in that both systems undergo kinetic and equilibrium fractionation processes (similar to that proposed for Ca stable isotopes and Sr/Ca ratios). However, the coevolution of δ^{30}Si and Ge/Si throughout the course of a secondary silicate precipitation process has not been directly demonstrated (Cornelis et al., 2010).

As a point of comparison, evolution of both δ^{44}Ca and Sr/Ca fractionation during carbonate formation and recrystallization have been extensively studied under laboratory conditions (Lorens et al., 1981; Parkman et al., 1998; Huang et al., 2001; Gabitov and Watson, 2006; Tang et al., 2008; Gabitov et al., 2014; Harouaka et al., 2014; Alkhatib and Eisenhauer, 2017) and across a variety of natural environments (Fantle and Tipper, 2014). Like δ^{30}Si and Ge/Si, δ^{44}Ca and Sr/Ca have been shown to behave similarly during secondary mineral precipitation where the "light" Ca-40 is preferentially enriched in the growing solid relative to the surrounding fluid. On the other hand, Sr is sequestered into the mineral surface despite being incompatible with the bulk solid phase due to fast precipitation kinetics relative to slow diffusivity rates of Sr in the crystal lattice (otherwise called "entrapment"). The origin of this non-equilibrium or kinetically driven fractionation derives from dehydration kinetics at the fluid-mineral surface interface (Hofmann et al., 2012). The extent of kinetic fractionation – "enrichment" in the case of δ^{44}Ca or "entrapment" in the case of Sr/Ca – has been shown to be dependent on temperature, precipitation rate, and solute chemistry. Notably, the rate of Sr uptake into actively growing calcite was observed to increase with both increasing precipitation rates

(Parkman et al., 1998; Gabitov and Watson, 2006; Tang et al., 2008; Alkhatib and Eisenhauer, 2017) and initial Sr concentrations in solution (Gabitov and Watson, 2006). As precipitation rates slowdown in the approach to equilibrium, initial, kinetically dominated observed signatures begin to reflect increasing contributions from equilibrium fractionation. In these near-equilibrium conditions, thermodynamics begins to takeover where Sr and the isotopically light Ca-40 are re-introduced into solution, driving fluid δ^{44}Ca and Sr/Ca values to higher and lower values, respectively. Furthermore, given the rapid formation rates of carbonates, direct observations of both δ^{44}Ca and Sr/Ca partitioning during active mineral growth show significant deviations from thermodynamically predicted equilibrium values based on solid solution models (Kolitov, 2010). At (near) equilibrium conditions, solid solution thermodynamics is the driving force for observed partitioning where Sr and the isotopically light Ca-40 are preferentially re-introduced into solution, driving fluid δ^{44}Ca and Sr/Ca values to higher and lower values, respectively. It has been observed throughout the course of carbonate formation that observed fractionation factors and partition coefficients can reflect a mixture of both kinetic and equilibrium behavior as a function of the proximity of the system to equilibrum (Tang et al., 2008; DePaolo, 2011; Alkhatib and Eisenhauer, 2017). Thus, several models have been put forth to attempt to characterize the δ^{44}Ca and Sr/Ca fractionation mechanisms based on their shared similarities: Surface Entrapment Model (SEM, Watson, 2004), Surface reaction kinetic model (SRKM, DePaolo, 2011), Ion-by-ion growth model, (Nielsen et al., 2012), and the Unified Uptake Kinetic Model (UUKM, Thien et al., 2013).

Notably, the SRKM model (DePaolo, 2011) successfully described experimentally observed $\delta^{44}Ca$ and Sr/Ca based on mixed kinetic and equilibrium effects deriving from the competition between the forward, precipitation (R_f) and backward, dissolution (R_b) rates in the approach to equilibrium during mineral growth. At the early stages of mineral growth, when overall rates (R_p) are fast, $\delta^{44}Ca$ and Sr/Ca fractionation is dictated by the forward, precipitation rate ($R_f >> R_b$), which drives the kinetically driven mass transfer of the lighter, Ca-40, and increases Sr sequestration from the fluid to the growing mineral (i.e. kinetic fractionation). As mineral growth rates slowdown in the approach to equilibrium, there is increasingly more contributions from the backward, dissolution rate leading to bi-directional mass transfer of Ca isotopologues and Sr that is driven by equilibrium fractionation. Thus, the initially Ca-40 enriched and Sr concentrated recently formed mineral will over time lose this kinetic signature in favor of higher $\delta^{44}Ca$ and lower Sr/Ca equilibrium values. Findings from application of the SRKM model to the calcite precipitation experimental studies, showed that for the range of experimentally determined calcite growth rates, both $\delta^{44}Ca$ and Sr/Ca reflected contributions from both kinetic and equilibrium effects. These results only applied for mineral growth under "chemostatic" conditions characteristic of marine environments. But, if extended further, these combined kinetic and equilibrium effects in "free-drifting" conditions (i.e. where saturation states and solute compositions are allowed to change with reaction progress), more representative of terrestrial settings, should lead to significant zoning at the mineral surface that reflects the reaction extent (Druhan et al., 2013). Thus, despite complex feedbacks between trace element impurities and precipitation rates, $\delta^{44}Ca$ and Sr/Ca fractionation during calcium carbonate formation is relatively documented and modeled.

Such behavior is inherently harder to document over the longer timescales of trace element and stable isotope partitioning due to silicate weathering, but the point of comparison provides a framework in which to test hypotheses of analogous $\delta^{30}Si$ and Ge/Si fractionation pathways.

To explore the extent to which $\delta^{30}Si$ and Ge/Si fractionation are similarly influenced by both kinetic and equilibrium effects, we analyzed samples from a series of highly constrained amorphous silica precipitation experiments recently reported by Fernandez et al. (2019). This approach leveraged the relatively rapid kinetics of opal formation (Geilert et al., 2014, Roerdink et al., 2015, and others) to document $\delta^{30}Si$ fractionation behavior under variable or "free-drifting" conditions across various surface areas and solid to fluid ratios. The study showed clear evidence for kinetic isotope fractionation followed by rapid isotopic re-equilibration, the extent to which is dependent on the overall precipitation rate and, thus, by extension the surface area of the seed crystals used in the experiments. In this context, the mechanisms of $\delta^{30}Si$ fractionation during amorphous silica precipitation were comparable to that of $\delta^{44}Ca$ during carbonate formation (Tang et al., 2008), but were shown to depend on both chemical (oversaturation state, solute compositions) and physical (surface area, solid to fluid ratios) characteristics of the system. Thus, the utility of the silicon isotopic tracer incorporates a variety of physiochemical effects and parsing this signature in natural weathering environments would pose a poorly constrained problem. In this regard, the analogous behavior of Ge/Si ratios offer a promising tool to complement $\delta^{30}Si$ if the factors affecting this signature can be similarly constrained. A prior study (Opfergelt et al., 2010) has postulated that Ge incorporation into secondary silicate phases may be inhibited or

subjected to slow rates during formation, implying that Ge/Si is not sensitive to kinetic processes in the same manner as $\delta^{30}Si$. In this study, we directly measure the extent of Ge incorporation and Ge/Si fractionation during active amorphous silica precipitation under highly constrained laboratory conditions. This experiment is the first, to our knowledge, to directly parse the effects of kinetically limited mineral growth on Ge/Si relative to $\delta^{30}Si$ signatures.

3.2 METHODS

3.2.1 Batch experiments

The samples analyzed in this study were generated from amorphous silica precipitation batch experiments conducted by Fernandez et al. (2019). We refer the reader to this prior publication for complete descriptions of the experimental design and initial conditions. To summarize, amorphous silica precipitation experiments were conducted in closed batch reactors using several sets of $SiO_{2(s)}$ seed crystal surface areas (50 to 0.072 m^2/g) and solid:fluid silicon mass ratios (50 to 31 $SiO_{2(s)}$ [g]:$SiO_{2(aq)}$[g]) at an ambient temperature of 20°C. All experiments started at a comparable dissolved $SiO_{2(aq)}$ concentration (5.3 mM) and pH (7.3) and were run for approximately 30 days, resulting in an initial oversaturation of 0.48 ± 0.06 (log Q/K) with respect to $SiO_{2(s)}$. Each batch reactor contained one of three seed crystal grain sizes, with specific surface areas that will from now on be referred to as high (SSA = 50 $m^2\ g^{-1}$), medium (SSA = 0.127 $m^2\ g^{-1}$), and low (SSA = 0.0127 $m^2\ g^{-1}$) experiments. Starting oversaturated solutions were prepared by dissolving 10 g of high surface area fumed silica grains in 1L of MQ-e water at 90°C for ~1 week until starting $SiO_{2(aq)}$ concentration were reached. Then, the solution was either cooled directly to the targeted starting temperature (20°C) in the case of the high

surface area batch or subjected to vacuum filtration to separate the solution from the undissolved high surface area grains and then quickly cooled to 20°C (as was the case for the medium and low surface area batches). These solutions, initially at a pH ~ 4.5, were then titrated with 10 mM NaOH to near neutral pH to initial precipitation. In the medium and low surface area batches, amorphous silica grains of the respective specific surface area were added to oversaturated solution to initiate precipitation. In all batches, precipitation occurred onto pre-existing grains homogeneously distributed in solution with starting masses of approximately 4 g for the medium and low surface area batches and 0.5 g for the high surface area batch.

3.2.2 Germanium analyses

Germanium concentrations were analyzed using hydride-generation ICP mass-spectrometry (HG-ICP-MS) (Heumann, 1988; Mortlock & Froelich, 1996; Aguirre 2019) at Cornell University using a custom HG sample introduction system and an Element 2 ICP-MS by Thermo-Finnigan. Aqueous samples are prepared by adding an enriched ^{70}Ge spike solution and allowed to equilibrate for at least 48 hours at room temperature. The spike solution is added to target an $^{70}Ge/^{74}Ge$ ratio of 10, inferred from the Si concentrations. To measure Ge concentrations, the prepared samples are introduced into the hydride generation system with a 4% $NaBH_4$ solution to reduce aqueous $Ge(OH)_4$ to volatile GeH_4, passing through an air-separation filter along with Ar as carrier gas into the ICP-MS. Germanium is quantified by standard curve method and isotope dilution using the $^{70}Ge/^{74}Ge$ ratio. Mass bias and signal drift were corrected using standard sample bracketing. We measured Ge standards at 5, 20, 50, 100 and 200 ng L^{-1}. To cross-check the isotope dilution calculations, standard response curves were generated at m/z

=74 for each Ge concentration. The $^{70}Ge/^{74}Ge$ in the spike equal to 162, thus the contribution from m/z = 74 is insignificant. The contribution of the spike addition to the uncertainty of Ge measurements is negligible (Heumann 1988).

3.2.3 Trace element model design and assumptions

Ge partitioning during amorphous silica precipitation was simulated using the geochemical, multi-component reactive transport software, CrunchTope (Steefel et al., 2015). The fractionation model framework within CrunchTope uses a two-endmember solid solution to create a simple, binary mechanical mixture between two substituting elements in a solid phase such as rare and major isotopes of a major element(ex. $^{28}Si_{1-x}$ $^{30}Si_x0_{2(am)}$) or trace and major elements (ex. $Ge_{1-x}Si_xO_{2(am)}$), where x represents the mole fraction of either the rare isotope or trace element. For the purposes of this current study, an ideal solid solution between amorphous GeO_2 and SiO_2 takes the following form (**eqn. 3.1**):

$$(1-x)Si(OH)_{4(aq)} + xGe(OH)_{4(aq)} \rightleftharpoons (Si_{(1-x)}Ge_x)O_{2(s)} + 2H_2O \quad (3.1)$$

where Ge in the form of $Ge(OH)_{4(aq)}$ species in solution is shown substituting for Si in amorphous silica, $SiO_{2(s)}$ in this solid solution stoichiometry and x represents the mole fraction of $GeO_{2(am)}$. An ideal solid solution means that each element (in the case of isotopes, each individual isotope), can substitute for one another in the same site within the crystal structure without changing the thermodynamic (i.e. enthalpy of mixing) and physical (i.e. molar volume) aspects of a growing mineral phase. In other words, the mineral phase with either of the stable isotopes substituted into its crystal structure would appear to be completely indistinguishable from one another (Gresens, 1981; Anderson and Crerar, 1993). Thus, in an ideal solid solution the sum of the activity

coefficients must equal 1. Under this ideal solid solution assumption, the mole fraction, x, can then be treated as a variable, which allows for traditional net TST (transition state theory rate laws) to be recast such that each endmember component can be treated individually as shown below (**eqn. 3.2**):

$$^{Ge}R_p = {}^{Ge}X\,{}^{Ge}k_f A\left(\frac{Ge(OH)_{4,aq}}{{}^{Ge}X\,{}^{Ge}K_{sp}} - 1\right)^m \qquad (3.2a)$$

$$^{Si}R_p = {}^{Si}X\,{}^{Si}k_f A\left(\frac{Si(OH)_{4,aq}}{{}^{Si}X\,{}^{Si}K_{sp}} - 1\right)^m \qquad (3.2b)$$

$$^{i}X = \frac{n_{Si,Ge}}{n_{Si} + n_{Ge}} \qquad (3.2c)$$

where the individual TST rate laws for displayed for Ge (**$^{Ge}R_p$, eqn. 3.2a**) and Si (**$^{Si}R_p$, eqn. 3.2b**) are coupled by the mole fractions for $GeO_{2(am)}$ and $SiO_{2(am)}$, ^{i}X (i = Si, Ge) defined by the moles of either Ge or Si ($n_{Ge,Si}$) over the total moles amorphous silica present assuming ideal solid solution (**eqn. 3.2c**). These rate equations are dependent on the total surface area of the amorphous silica grains (A, [m^2]), the rate constants ($^{i}k_f$, [moles m^{-2} s^{-1}]) , the relative activities of the major ($Si(OH)_4$) and trace element ($Ge(OH)_4$) in solution and their respective equilibrium constants ($^{i}K_{sp}$). The rate order, m, is set to 3.5 in this model to stay consistent with the silicon stable isotope fractionation model that was developed in Fernandez et al. (2019) and observations in the literature for amorphous silica precipitation kinetics (Iler, 1979; Fleming, 1986; Tobler et al., 2009). The kinetic and equilibrium fractionation factors for trace elements in this model are provided through

the partition coefficients K_d^{kin} and K_d^{eq}, which link the precipitation rate $\left(\frac{Ge_{k_f}}{Si_{k_f}}\right)$ and equilibrium $\left(\frac{Ge_{K_{sp}}}{Si_{K_{sp}}}\right)$ constants, respectively.

This setup follows the same fractionation framework initially developed for stable isotopes (Druhan et al., 2013) and recently applied to Si stable isotope fractionation during identical amorphous silica growth experiments (Fernandez et al., 2019). Importantly, the application of this model to Ge trace element partitioning during secondary amorphous silica growth assumes that Ge partitioning behavior is analogous to silicon stable isotopes, a notion that will be directly tested for the first time in this study. In the event of secondary mineral formation, this partition model theory notably allows both fluid and solid phase trace element ratio (Ge/Si) compositions to be monitored through time via coupled net precipitation rates and mole fractions (**eqn. 3.2**) within an ideal solid solution framework. For stable isotopes, the underlying assumption of ideal solid solution is valid because isotopic substitution into the crystal structure of a growing solid phase is one of the closest approximations to a true ideal solid solution (Anderson and Crerar, 1993). However, if we are going to apply this same partition model to Ge, we need to spend some time validating whether an ideal solid solution assumption is reasonable for trace element partitioning during secondary silicate mineral growth.

The validity of an ideal Ge–Si solid solution for amorphous silica is essentially unknown due to the lack of thermodynamic information available in the literature. Thus, this particular issue of Ge–Si mixing behavior represents a critical knowledge gap in the Ge literature that this paper strives to fill in and advance our current understanding of the mechanisms driving Ge partitioning. Shared chemical properties (valence state and inorganic aqueous speciation) between Ge and Si as a result of their close proximity in

the periodic table (both metalloids) and the trace concentrations in which Ge is present in aqueous phases relative to Si (6 order of magnitude difference) implies that Ge substitutes ideally for Si during secondary silicate formation (Capobianco and Watson, 1981; Martlocka nd Froelich, 1987; Foelich et al., 1992). A major feature that distinguishes Ge from other trace elements impurities substituting into a growing mineral phase is that Ge and Si speciation in the aqueous phase are very similar and are present in the same form at near neutral pH, namely as neutral hydroxides $Si(OH)_4$ and $Ge(OH)_4$ respectively (Pokrovski and Schott, 1998). This shared aqueous speciation behavior implies that Ge follows similar incorporation mechanics to that of Si and, thus, can be readily substituted in a growing secondary silicate. Further, what limited thermodynamic data are available from the laboratory studies that do exist for characterizing Ge substitution behavior during silicate formation (notably for sodium feldspar and forsterite) provide evidence in support of a Ge–Si binary solid solution following ideal mixing behavior (Capobianco and Watson, 1981; Capobianco and Navrotsky, 1982).

In relevance to the current study (amorphous SiO_2–GeO_2 solid solution) two observations are particularly relevant. First, colorimetric data from the Capobianco and Watson (1981) experimental study of Ge partitioning in sodium feldspars indicate that amorphous glasses tend to conform better to ideal solid solution than their crystalline counterparts. Second, Evans and Derry (2002) showed that to some extent quartz and its Ge-crystalline counterpart (argutite) also follow ideality. In total, six order of magnitude differences in Ge and Si concentrations in solution, intuition based on their shared properties, and observations from what limited data do exist suggest that an ideal solid solution is a reasonable assumption for Ge–Si binary mixing during amorphous silica growth.

In this treatment of the trace elements, Ge is treated in the same manner as the rare or less abundant isotopologue in a stable isotope system. However, there are distinct differences between the stable isotope and trace element derivations that are important to note. For instance, in the treatment of stable isotopes in this framework the activities of the individual isotopes (^{28}Si and ^{30}Si) must sum up to overall activity of Si in solution. But for trace elements, the activities of Ge and Si are considered independent. What this ultimately entails are that the kinetics and thermodynamic parameters of both amorphous SiO_2 and GeO_2 must be acquired individually. For amorphous silica precipitation, its kinetics and thermodynamics are well established in the literature. Precipitation rate and equilibrium constants at 20°C are $10^{-9.67}$ moles m^{-2} s^{-1} (Rimstdt and Barnes, 1980) and $10^{-2.7135}$ (Gunnarsson and Anórsson, 2000) respectively. This makes parameterization of **eqn. 3.2a** straightforward since we have the numbers needed to put into the Si rate law. However, parameterizing **eqn. 3.2b** is more complicated. Experimentally determined thermodynamic data for germanates are scarce and only exist for a few minerals including argutite ($GeO_{2(hex)}$) (Arnorsson 1988; Pokrovski and Schott, 1998) and some chain-silicates and phyllosilicates (Pokrovskii & Schott, 1998; Shtenberg et al., 2017). Up to now, we are not aware of any kinetic data that exists for the formation of $GeO_{2(am)}$. Since there is essentially no existing thermodynamic or kinetic data available in the literature for Ge partitioning during amorphous silica precipitation, we have to rely on estimates for both parameters.

For the amorphous germanium oxide (GeO_2) solubility constant, we could assume that its value is approximately the same as that for amorphous silica due to the similarities in the chemical properties between Si and Ge. Yet, under the assumption of ideal solid-solution behavior between Ge and Si, $GeO_{2(am)}$ and $SiO_{2(am)}$ are implied to have distinct

equilibrium constants according to the equilibrium model by Evans and Derry (2002) (see **eqn. 3.3** below).

$$GeO_{2(am)} + 2H_2O \rightleftharpoons GeOH_{4(aq)} \quad (3.3a)$$

$$SiO_{2(am)} + 2H_2O \rightleftharpoons SiOH_{4(aq)} \quad (3.3b)$$

$${}^{Ge}K_{sp} = \frac{a_{Ge(OH)_{4(aq)}}}{a_{Si(OH)_{4(aq)}}} \times \frac{{}^{Si}X}{{}^{Ge}X} \times {}^{Si}K_{sp} = \frac{(Ge/Si)_{fluid}}{(Ge/Si)_{solid}} \times {}^{Si}K_{sp} \quad (3.3c)$$

where, $a_{Ge(OH)4}$ and $a_{Si(OH)4}$ are the activities of germanic and silicic acid respectively, and ${}^{Si}K_{sp}$ is the solubility constant for amorphous silica ($10^{-2.7135}$ M). This model derives from an ideal binary mixture between amorphous SiO_2 and GeO_2 solid phase endmembers, $Ge_xSi_{1-x}O_2$, where through the combination of **eqn. (3.3a**) and **eqn. (3.3b**) the equilibrium constant for amorphous GeO_2 can be determined (**eqn. 3.3c**). Similarly, we assume that ideal solid solution behavior between $GeO_{2(am)}$–$SiO_{2(am)}$ is appropriate for this system. Since the equilibrium ratio for aqueous $Ge(OH)_4/Si(OH)_4$ is unknown for amorphous silica, we resort to estimating this value using the known equilibrium ratio ($Ge/Si_{eq} = 10^{-1.2838}$; Evans and Derry, 2002) for quartz and argutite (crystalline GeO_2), the closest known solid solution to that for amorphous SiO_2 and GeO_2, under the assumption that partitioning for amorphous phases is similar to crystalline ones. Based on this assumption and using the known solubility constant for amorphous silica (${}^{Si}K_{sp}$), we estimated the equilibrium constant for amorphous GeO_2 to be $10^{-3.9973}$. We consider this estimation to be a lower limit considering the fact that amorphous silica phases should be able to incorporate more Ge into its crystal structure compared to quartz.

We estimate Ge kinetics during amorphous silica formation via a best-fit approximation to the experimental data (**see section 3.4.2.1 below**). Ge batch model simulations for amorphous silica precipitation were performed for different timescales

(35 to 500 days), surface areas (0.072 to 50 m^2 g^{-1}), and Ge precipitation scenarios using identical starting fluid and solid phase Ge/Si ratios, temperature, and pH. The results from these simulations and their comparison with the experimental Ge/Si data will be discussed in further detail below in **Section 3.4.1**.

3.3 RESULTS

3.3.1 Time evolution of Ge/Si

Measured fluid Ge/Si ratios (**Table 3.1**) monitored as a function of experimental duration, 30 days, (**Fig. 3.1**) are presented alongside measured dissolved SiO_2 concentrations and their corresponding $\delta^{30}Si$ values for the high, medium, and low surface area batches reported by Fernandez et al. (2019). Dissolved silica concentrations as a function of time (**Fig. 3.1A**) for all experiments decrease with time until a metastable equilibrium (high SA batches) or steady state (medium and low SA batches) is attained with respect to the amorphous silica solubility concentration at 20ºC (Gunnarsson and Anórsson, 2000). Average, initial Ge/Si fluid ratios (8.45 ± 0.30 μmol/mol, (1SD, n=3)) are higher with respect to the average bulk amorphous silica (0.49 ± 0.19 μmol/mol, (1SD, n=3)). The source contributing to these relatively high initial fluid Ge/Si values comes directly from the leaching of Ge during the preparation of the initial solutions for the experiments where high surface area seeds were dissolved at 90°C in order to reach oversaturation with respect to amorphous silica when the solution was subsequently cooled down to 20°C (see **Section 2.1**).

Evolution of the bulk amorphous silica Ge/Si ratios (**Fig. 3.1B**) were calculated based on the accumulation of mass SiO_2 ($N_{SiO_{2(ppt)}}$, Fernandez et al., 2019) and GeO_2 ($N_{GeO_{2(ppt)}}$, **Table 3.1**) precipitated out of solution cumulatively onto the pre-existing seed

mass initially present in the batch reactor. Bulk amorphous silica Ge/Si calculated in this manner for all the surface area experiments is observed to slightly increase throughout the experiment compared to the measured Ge/Si ratios. Although this overall increase in the bulk composition is quite minimal (within standard error), the high surface area batch shows the largest shifts in the growing amorphous silica Ge/Si (0.28 – 0.34 μmol/mol) compared to the lower surface area batches (+0.02 μmol/mol increase with respect to initial value).

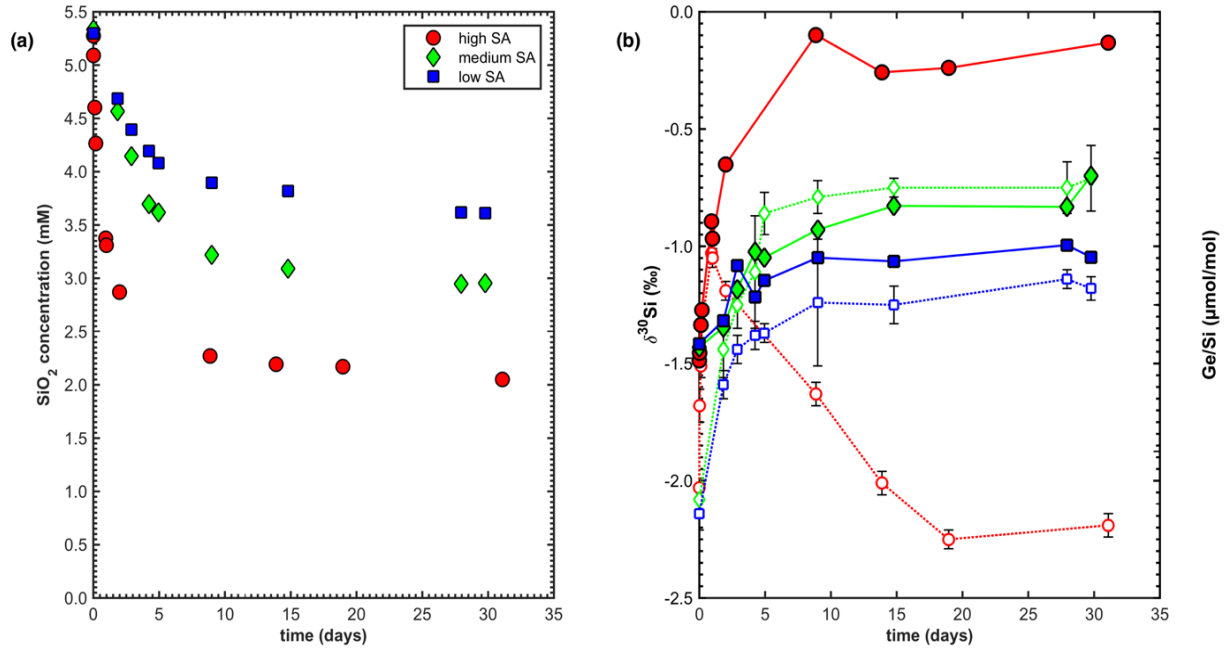

Figure 3.1 Dissolved SiO_2, Ge/Si, and δ^{30}Si timeseries
Dissolved SiO_2 concentration timeseries for the high (red circles), medium (green diamonds), and low (blue squares) surface area batch experiments (**A**) from Fernandez et al. (2019) and (**B**) corresponding measured fluid $\boldsymbol{\delta}^{30}$Si (open markers, Fernandez et al., 2019) and Ge/Si ratios (solid markers, this study) behavior as a function of the experimental duration, ~30 days. Error bars correspond to 2 standard deviations for the Si stable isotope measurements. Initial Ge/Si composition of the bulk phase is represented by the grey bar and red, green, and blue lines correspond to the evolving Ge/Si amorphous silica composition with time (see **Table 3.2**).

Table 3.1. Germanium data for amorphous silica precipitation experiments[a]

No.	time	M_{Ge}[b]	$n_{GeO_{2,ppt}}$[c]	Ge/Si_{fluid}	$Ge/Si_{am.silica}$[d]	$K_{D,obs}$[e]
	days	pM	pmoles	µmol/mol	µmol/mol	
High surface area batch (50 m^2 g^{-1})						
1	0.00	42776	-	8.11	0.28	0.03
2	0.02	42599	52	8.37	0.30	0.04
3	0.11	42855	80	9.32	0.26	0.03
4	0.19	41908	169	9.82	0.38	0.04
5	0.93	43382	143	12.85	0.20	0.02
6	1.00	40579	314	12.25	0.53	0.04
7	2.00	42451	271	14.79	0.31	0.02
8	8.87	43638	262	19.21	0.17	0.01
9	13.88	39336	488	17.93	0.67	0.04
10	18.95	39278	530	18.08	0.68	0.04
11	31.08	38855	586	18.95	0.73	0.04
Seed			**2291**		**0.28**	
Medium surface area batch (0.127 m^2 g^{-1})						
1	0.00	45631	-	8.56	0.56	0.07
2	1.83	42161	994	9.24	0.61	0.07
3	2.90	43658	755	10.53	0.59	0.07
4	4.23	43641	890	11.81	0.58	0.06
5	4.95	42024	1406	11.62	0.61	0.05
6	9.00	40454	1901	12.57	0.63	0.05
7	14.79	41350	1815	13.38	0.62	0.05
8	27.95	39346	2397	13.35	0.64	0.05
9	30.00	42548	1792	14.40	0.60	0.04
Seed			**39982**		**0.56**	
Low surface area batch (0.072 m^2 g^{-1})						
1	0.00	45957	-	8.67	0.64	0.07
2	1.83	44345	514	9.46	0.67	0.07
3	2.90	49849	-724	11.35	0.59	0.07
4	4.23	43084	1042	10.27	0.68	0.05
5	4.95	44194	883	10.83	0.67	0.07
6	9.00	45226	748	11.61	0.65	0.06
7	14.79	43839	1187	11.49	0.67	0.06
8	27.95	43555	1363	12.04	0.67	0.06
9	30.00	41984	1833	11.63	0.70	0.06
Seed			**46054**		**0.64**	

a. Additional details on dissolved silica concentrations, saturation states, precipitation rates, evolving surface area, and Si stable isotope ratios can be found in Fernandez et al. (2019).
b. Measured fluid Ge concentrations with associated errors of XX.
c. Cumulative mass of amorphous GeO_2 precipitated out of solution. Values determined by subtracting the picomoles Ge in solution at time, t, from initial amount in solution, at t=0.
d. Amorphous silica Ge/Si ratios were estimated by tracking the total amount of GeO_2 and SiO_2 accumulating in the growing bulk ($n_{Ge,SiO2,\ bulk(t=0)} + n_{Ge,SiO2,cumulative(t)}$).
e. The partition coefficient calculated as $\frac{(Ge/Si)_{am.silica}}{(Ge/Si)_{fluid}}$, monitored throughout the course of the reaction for an evolving bulk solid phase.

Measured fluid Ge/Si ratios are presented along with recently published fluid $\delta^{30}Si$ for these amorphous silica precipitation experiments as a function of time (**Fig. 3.1B**).

Measured Ge/Si for all experiments are shown to increase with time and subsequently stabilize at these elevated values near the end of the experiment. The Ge/Si ratios at which the experiments ultimately stabilize, increase as a function of the starting seed surface area. For instance, the high surface area batch near the end of the experiment attains Ge/Si ratios ~18.95 μmol/mol, roughly 4.5 μmol/mol and 6.9 μmol/mol greater than the medium (Ge/Si_{max} = 14.40 μmol/mol) and low (Ge/Si_{max} = 12.04 μmol/mol) surface area batches, respectively. Fluid Ge/Si ratios for all batches remain elevated with respect to the bulk amorphous silica composition at the end of the experimental duration. The Ge/Si fluid ratios for lower surface area batches correlate strongly with their corresponding fluid δ^{30}Si, effectively displaying the same evolving behavior with time. On the other hand, measured fluid Ge/Si and δ^{30}Si for the high surface area case quickly diverge as fluid δ^{30}Si begins to isotopically re-equilibrate to lower δ^{30}Si after roughly 1 day.

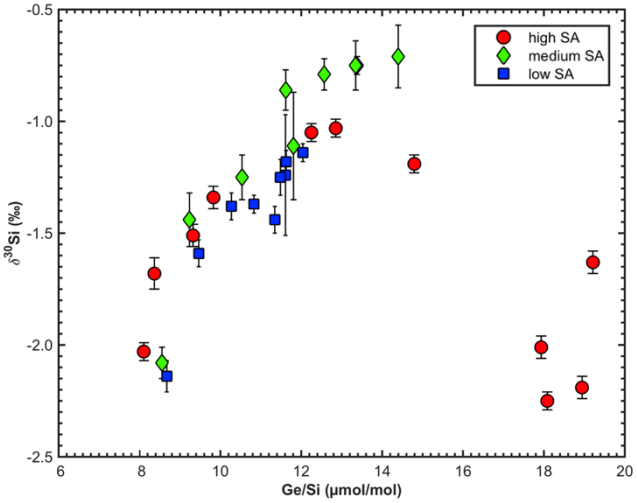

Figure 3.2 Fluid δ^{30}Si vs Ge/Si
Fluid δ^{30}Si as a function of Ge/Si ratio for the high (red circles), medium (green diamonds), and low (blue squares) surface area batches. Starting values are the points on the far left of the graph. A"boomerang"- like relationship characterizes the δ^{30}Si and Ge/Si variability in the high surface area batch, which represents fast δ^{30}Si re-equilibration relative to the rates Ge/Si equilibrium partitioning (that are negligible over this experimental timespan). Error bars represent 2 standard deviation for the Si stable isotope data.

3.3.2 δ^{30}Si vs. Ge/Si

Measured fluid δ^{30}Si are shown as a function of measured fluid Ge/Si (**Fig. 3.2**) for all amorphous silica precipitation experiments. Starting at initial δ^{30}Si and Ge/Si values around –2‰ and 8.49 μmol/mol respectively, fluid δ^{30}Si and Ge/Si are both observed to increase as a function of reaction progress. For the medium and low surface area batches, δ^{30}Si and Ge/Si are linearly correlated (**R^2 = 0.86** and **R^2 = 0.84**, respectively) throughout the course of the reaction. However, just as observed in the timeseries (**Fig. 3.1B**), a switch is observed in the high surface area batch at ~1 day where fluid δ^{30}Si starts to decrease with time as fluid Ge/Si ratios continue to increase. The result of this increased disparity as precipitation rates decrease in the approach to equilibrium is the appearance of a "boomerang" relationship between fluid δ^{30}Si and Ge/Si.

3.4 DISCUSSION

3.4.1 Defining the instantaneous partition coefficient, K_d^{inst}

For these "free-drifting" amorphous silica precipitation experiments, the instantaneous partition coefficient (K_d^{inst}) for Ge can be influenced by heterogeneity in the growing mineral surface as a result of the co-evolution of the fluid and solid as a function of time. Even under "chemostatic" conditions where mineral growth occurs under fixed saturation states and solute compositions, heterogeneity in the growing mineral surface has been observed for Sr/Ca during calcite precipitation (Tang et al., 2008). In the calcite literature, the effect of mineral zoning on the instantaneous partition coefficient was accounted for by recasting the traditional method of calculating the partition coefficient (**eqn. 3.4a**) in terms of a Rayleigh distillation type evolution in the bulk as shown below (**eqn. 3.4b**):

$$K_d^{inst} = \frac{\left(Ge/Si\right)_{bulk\ am.silica}}{\left(Ge/Si\right)_{aq}} \quad (3.4a)$$

$$\left(\frac{Ge}{Si}\right)_{bulk,am.silica} = \left(\frac{Ge}{Si}\right)_{aq,0} \times \frac{1-\left(\frac{Si}{Si_0}\right)_{aq}^{K_d^{inst}}}{1-\left(\frac{Si}{Si_0}\right)_{aq}} \quad (3.4b)$$

These two approaches to calculating K_d^{inst} are derived from Tang et al.(2008) and we apply it to Ge/Si for amorphous silica precipitation. In **eqn. 3.4b**, the $\left(\frac{Ge}{Si}\right)_{aq,0}$ represents the initial fluid Ge/Si ratio, $\left(\frac{Si}{Si_0}\right)_{aq}$ represents the fraction of Si remaining in solution (Si = concentration of $SiO_{2(aq)}$ at time, t whereas $Si_{0,aq}$ = initial $SiO_{2(aq)}$ concentration), and $\left(\frac{Ge}{Si}\right)_{bulk,am.silica}$ represents the Ge/Si ratio of the bulk amorphous silica. With these values known at each sampling time interval, the K_d^{inst} can then be solved for through simple algebraic rearrangement (**Appendix D**). Thus, the bulk solid composition is an important parameter in this calculation. As is in the case with the chemostatic calcite precipitation experiments, the bulk trace element ratio can be set to one fixed value like the initial or final bulk solid trace element ratio. If the bulk solid trace element ratio can be tracked throughout the course of the experiment through the mass of Si and Ge precipitated out of solution as a function of time (as was done in Fernandez et al., 2019 for Si and in this study for Ge, **Table 3.1**), then the bulk solid composition can be treated as a variable. We apply these two approaches to the bulk amorphous silica Ge/Si ratio and calculated the $K_{d,inst}$ using these assumptions using both **eqn.3.4a** and **eqn. 3.4b** for all surface area batches (**Fig. 3.3**).

Applying these four different approaches to calculating the instantaneous partition coefficient yields values that all lie within the same order of magnitude for all surface area experiments. In all cases, the differences between the variously calculated partition coefficients increase with decreasing precipitation rates. These results suggest that the instantaneous partition coefficient for this particular series of experiments does not seem to be significantly influenced by the evolution of the bulk Ge/Si ratio. Further, the observation of calculated partition coefficients << 1 confirms that Ge is incompatible with respect to amorphous silica. The largest range between the calculated partition coefficients is observed for the high surface area experiment, 0.01 (**eqn.3.4b** with evolving bulk am.silica Ge/Si) to 0.02 (**eqn.3.4a** with evolving bulk am.silica Ge/Si) at $10^{-12.49}$ mol m^{-2} s^{-1} (**Fig 3.3A**). The medium surface area batch expresses the largest range in partition

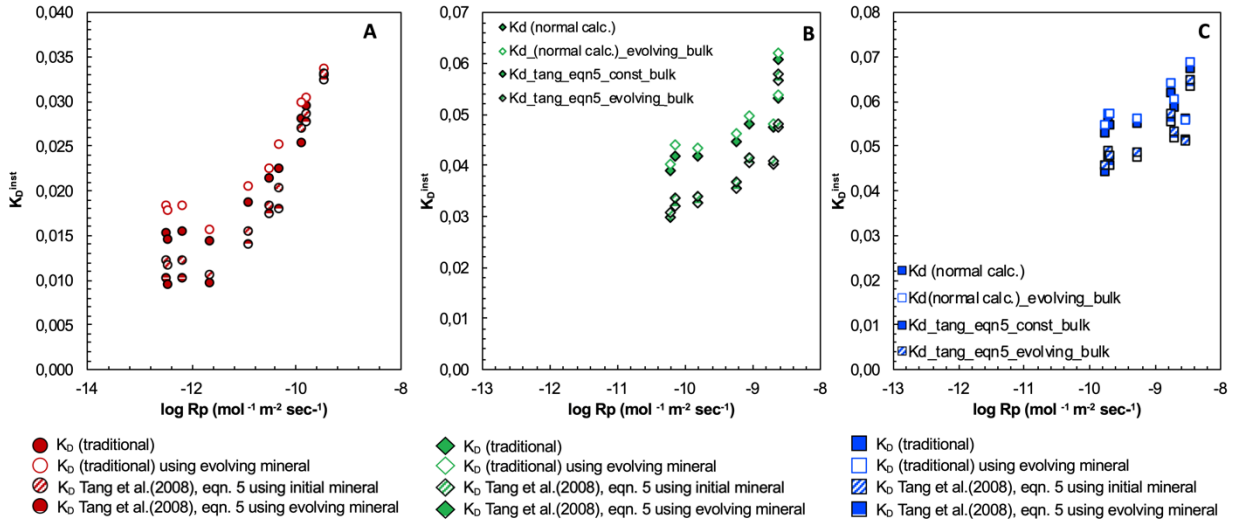

Figure 3.3 K_D^{inst} vs. log R_p for Ge/Si partitioning during am.silica formation
Instantaneous partition coefficient, $K_{d,inst}$, as a function of experimentally determined silica precipitation rates (presented here in log units; Fernandez et al., 2019) for the high (**A**), medium (**B**), and low (**C**) surface area amorphous silica precipitation batch experiments. The different K_d trends represent different methods of calculating the partition coefficient. To account for both evolving bulk amorphous silica composition with time in these "free-drifting" experiments, the $K_{d,inst}$ be can be calculated either through the traditional method (**eqn.3.3a**) or through modified Rayleigh distillation approach (**eqn.3.3b**, Tang et al., 2008).

coefficients from ~0.06 at $10^{-8.62}$ mol m^{-2} s^{-1} to ~0.03 at $10^{-10.15}$ mol m^{-2} s^{-1} (**Fig 3.3B**). A major finding that can be extracted from this exercise is that the K_d^{inst}. in all surface area cases appears to be rate dependent with K_d^{inst} decreasing with decreasing precipitation rates in the approach to a metastable equilibrium.

3.4.2 Trace model

To begin to interpret the fluid Ge/Si behavior observed in all amorphous silica precipitation experiments as a function of time, we ran a series of numerical simulations using the trace element batch model recently developed in the multi-component, geochemical software, CrunchTope (Perez-Fodich and Derry, *submitted*). Since this is the first study of its kind investigating Ge partitioning under experimental conditions, we have no information to guide us in regard to the mechanisms behind Ge fractionation during amorphous silica precipitation. Thus, we ran the trace element model under two broad scenarios: (1) where Ge is treated conservatively and (2) where Ge is allowed to precipitate over long timescales. Each scenario was run across the range of amorphous silica starting surface areas tested in the experiments and across different timescales ranging from the 35 days (the approximate experimental timescale) to 500 days (an annual timescale). For the Ge trace model, it is important to note that no re-equilibration is allowed to occur between the amorphous silica and its surrounding fluid. This assumption is properly justified by the observation that instantaneous partition coefficients are relatively well constrained between all experiments (**section 3.4.1**) Thus, the mole fraction in the model is automatically set to the aqueous $Si(OH)_4$ and $Ge(OH)_4$ compositions in the coupled TST rate expressions (**eqn. 3.2a and 3.2b**). This "no back-reaction" constraint is appropriate for the Ge trace element system based on the lack of evidence for re-equilibration observed in the literature for other water – secondary silicate

mineral interactions (Evans and Derry, 2002; Aguirre, 2019). Thus, observed Ge/Si variability in the models only reflect differences in the precipitation and equilibrium rate constants assuming a steady state mineral surface composition. Initial conditions for these scenarios and further details on the trace model set up can be found in **Table 3.2** and **Section 3.2.3**, respectively. Results from these trace element batch simulations are shown in **Fig.3.4.**

Table 3.2 Initial conditions for the Ge trace element batch model

Parameters	units	conservative	Ge incorporation
reaction order		3.5	3.5
duration	days	35	35
		500	500
		5000	5000
timestep	hours	20	20
T	ºC	25	25
pH		7.33	7.33
Specific surface area	$m^2\ g^{-1}$	50	50
		0.127	0.127
		0.072	0.072
$Si(OH)_{4(aq)}$[a]	mM	5.277	5.277
$Ge(OH)_{4(aq)}$[b]	mM	4.2776×10^{-5}	4.2776×10^{-5}
log $k_{f(SiO2)}$[c]		-9.67	-9.67
log $k_{f(GeO2)}$[d]		-	(-18.5 – -11.3)
log $K_{eq(SiO2)}$[e]		-2.7135	-2.7135
log $K_{eq(GeO2)}$[f]		-3.9973	(-5.021 – -2.7135)
Ge/Si $_{fluid}$	µmol/mol	8.11	8.11
Ge/Si $_{am.silica}$	µmol/mol	0.28	0.28
$K_{D,eq}$[g]		0.052	(0.005 – 1.00)
$K_{D,kin}$[h]		-	(1.5×10^{-9} – 0.02)

f. Measured starting dissolved silica concentrations from Fernandez et al. (2019).
g. Measured starting dissolved germanium concentrations from this study.
h. Rimstidt and Barnes (1980).
i. Determined through taking a best-fit of the experimental Ge/Si fluid data.
j. Gunnarsson and Anórsson (2000)
k. Estimated using Evans and Derry (2002) equilibrium model for germanium bearing quartz (**Section 2.3, eqn.2**).
l. Equilibrium partition coefficient calculated as the ratio between $GeO_{2(am)}$ and $SiO_{2(am)}$ equilibrium constants: $\frac{K_{eq,GeO_2}}{K_{eq,SiO_2}}$.

m. Kinetic partition coefficient calculated as the ratio between $GeO_{2(am)}$ and $SiO_{2(am)}$ precipitation rate constants: $\frac{k_{f,GeO_2}}{k_{f,SiO_2}}$.

3.4.2.1 Conservative treatment of Germanium

For the conservative Ge scenario, the trace model was set up so that Ge was not allowed to be incorporated into the growing amorphous silica phase. Thus, only changes in the dissolved silica concentration as it is being removed from solution and incorporated into the newly formed mineral surface would drive fluid Ge/Si ratios to higher values. Throughout the simulation, Ge remains fixed at the initial dissolved $Ge(OH)_4$ concentration specified in the initial conditions (4.2776×10^{-5} mM). Treating Ge as a conservative element in the simulation does not impact the predicted dissolved SiO_2 concentrations, which agree nicely with the experimentally determined data (**Fig. 3.4A**). Correspondingly, predicted fluid Ge/Si ratios can match our experimental results and replicate the observed shift in the ratios towards more elevated ratios relative to each surface area batch experiment (**Fig. 3.4B**). Thus, from this first set of simulations under a conservative Ge scenario the rate of dissolve silica precipitating out of solution during amorphous silica growth exerts a first order control on observed fluid Ge/Si ratios over the course of the experiment. Different rates of dissolved silica removal are reflected in the seed crystal surface area such that silica precipitation onto higher surface area seeds corresponds to fast precipitation rates and vice versa for seeds of lower surface area. Consequently, the high surface area batch shows both a quicker increase in the fluid Ge/Si ratios and stabilization to more overall elevated values with respect to the medium and low surface area batches.

Notably, in this conservative scenario shifts in fluid Ge/Si correspond solely to changes in the silica precipitation rate. However, based on previous literature on Ge partitioning during quartz formation (Evans & Derry, 2002) and secondary clay formation (Murnane & Stallard 1990; Kurtz et al., 2002; Lugolobi et al., 2010; Opfergelt et al., 2010; Baronas et al., 2018), it is unlikely that Ge behaves conservatively during amorphous silica precipitation. Therefore, the results from these simulations suggest that the rate of Ge incorporation is much slower than silica precipitation and, consequently, the experimental duration of ~ 1 month may be too short to observe significant Ge partitioning. To test whether these findings are indeed plausible, we proceed to the next suite of simulations where we will allow for Ge to be incorporated into the growing amorphous silica precipitate over a range of different kinetic and equilibrium partition coefficients. The following numerical experiments are targeted to determine a range of

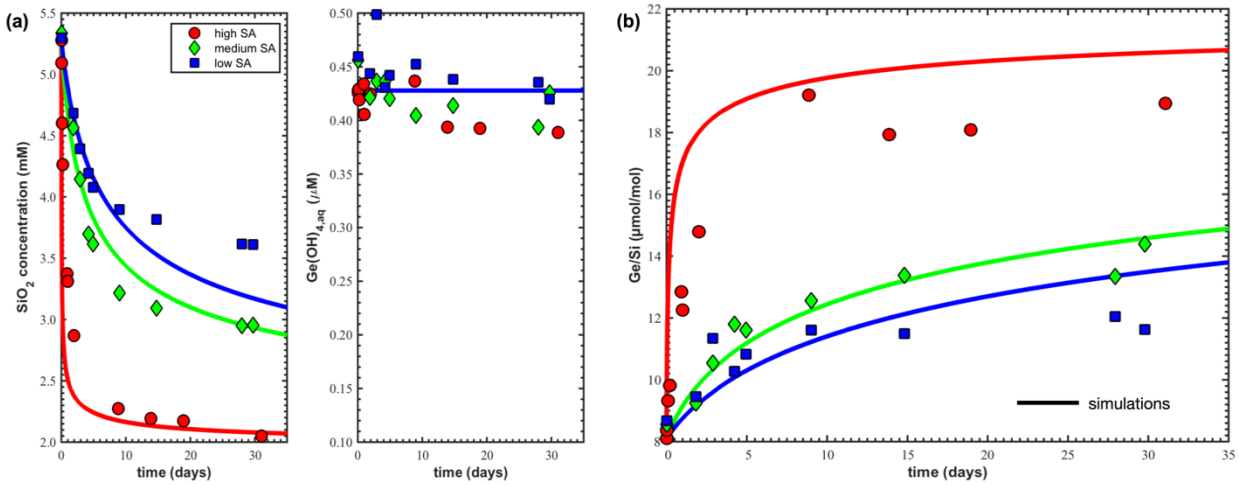

Figure 3.4 Trace model Ge/Si simulations under a conservative Ge scenario

Trace model simulations for the high (red line), medium (green line), and low (blue line) surface area conditions run under a conservative Ge scenario (i.e. where fluid Ge concentrations remain constant). Simulations of dissolved silica and $Ge(OH)_4$ concentrations as a function of time are shown (**A**), showing that the model is behaving correctly. Model predictions on the evolution of fluid Ge/Si over the course of the experiment (**B**) replicate nicely the observed experimental behavior (filled in markers), which occurs as a result of the overall faster silica precipitation kinetics with respect to Ge, which drives the fluid Ge/Si to these elevated values.

plausible kinetic ($K_d^{kin} = k_f^{Ge} / k_f^{Si}$) and thermodynamic ($K_d^{eq} = K_{eq}^{Ge} / K_{eq}^{Si}$) partition coefficients for amorphous silica formation.

3.4.2.2 Ge incorporation into amorphous silica

The goal of this next series of simulations is to determine a range of realistic kinetic (K_d^{kin}) and thermodynamic (K_d^{eq}) partition coefficients for amorphous silica formation. Ge in these trace models is incorporated into am.silica based on the solid–solution model (**eqn.3.1**, **section 3.2.3**). Since there is currently no kinetic or thermodynamic data available in the literature for Ge partitioning during amorphous silica precipitation, simulations were run using a wide range of GeO_2 kinetic rate constants (-18.5 to -11.3) and equilibrium constants (-5.021 to -2.7135) over the experimental duration (**Fig. 3.5; Table 3.2**). Specific combinations of Ge kinetic and equilibrium parameters used in the trace models were determine by a

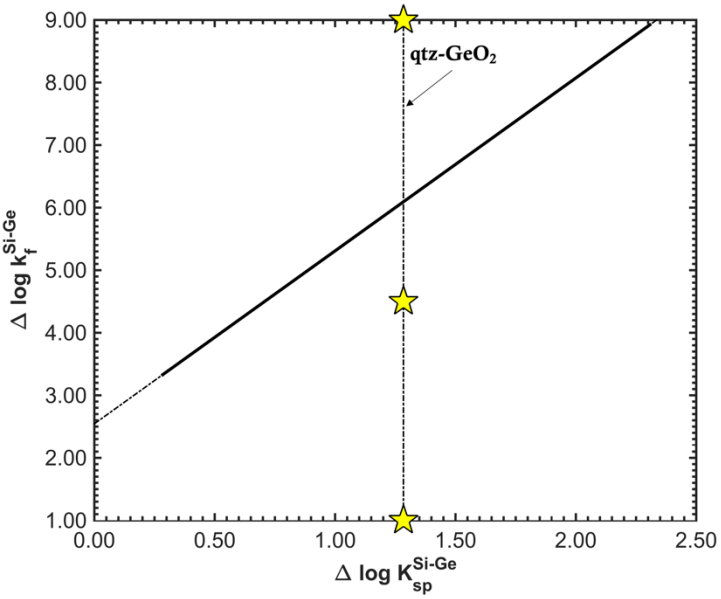

Figure 3.5 k_f^{Ge} vs. K_{sp}^{Ge} parameter space for trace model benchmarking

Kinetic and thermodynamic parameter space for the trace model simulations represented as the log difference between the kinetic rate ($\Delta\log k_f^{Si\text{-}Ge} = \log k_f^{Si} - \log k_f^{Ge}$) and equilibrium ($\Delta\log K_{sp}^{Si\text{-}Ge} = \log K_{sp}^{Si} - \log K_{sp}^{Ge}$) constants of silica and germanium. Representing the parameter pairs in this fashion allows the magnitude differences between Ge and Si to be better visualized. Kinetic rate constants were determined based on a "best-fit" approach to the experimental data at a given equilibrium constant for all surface areas (i.e. the same kinetic rate and equilibrium constants were used for all surface area cases). The yellow star– line represents the Ge equilibrium constant ($^{Ge}K_{sp} = 10^{-3.9973}$) calculated based on an equilibrium thermodynamic model assuming ideal solid–state solution (**eqn. 2**) between quartz (SiO_2) and argutite (GeO_2). Kinetic rate and equilibrium constants are linearly correlated with slower GeO_2 precipitation kinetic rates corresponding to lower Ge equilibrium constants.

single "best-fit" approximation to all the experimental data, i.e. all surface area experiments. Silica kinetic and thermodynamic parameters for these simulations were kept constant with log kinetic rate and equilibrium constant of -9.67 (Rimstidt & Barnes, 1980) and -2.7135 (Gunnarsson and Anórsson, 2000), respectively (**Table 3.2**). We

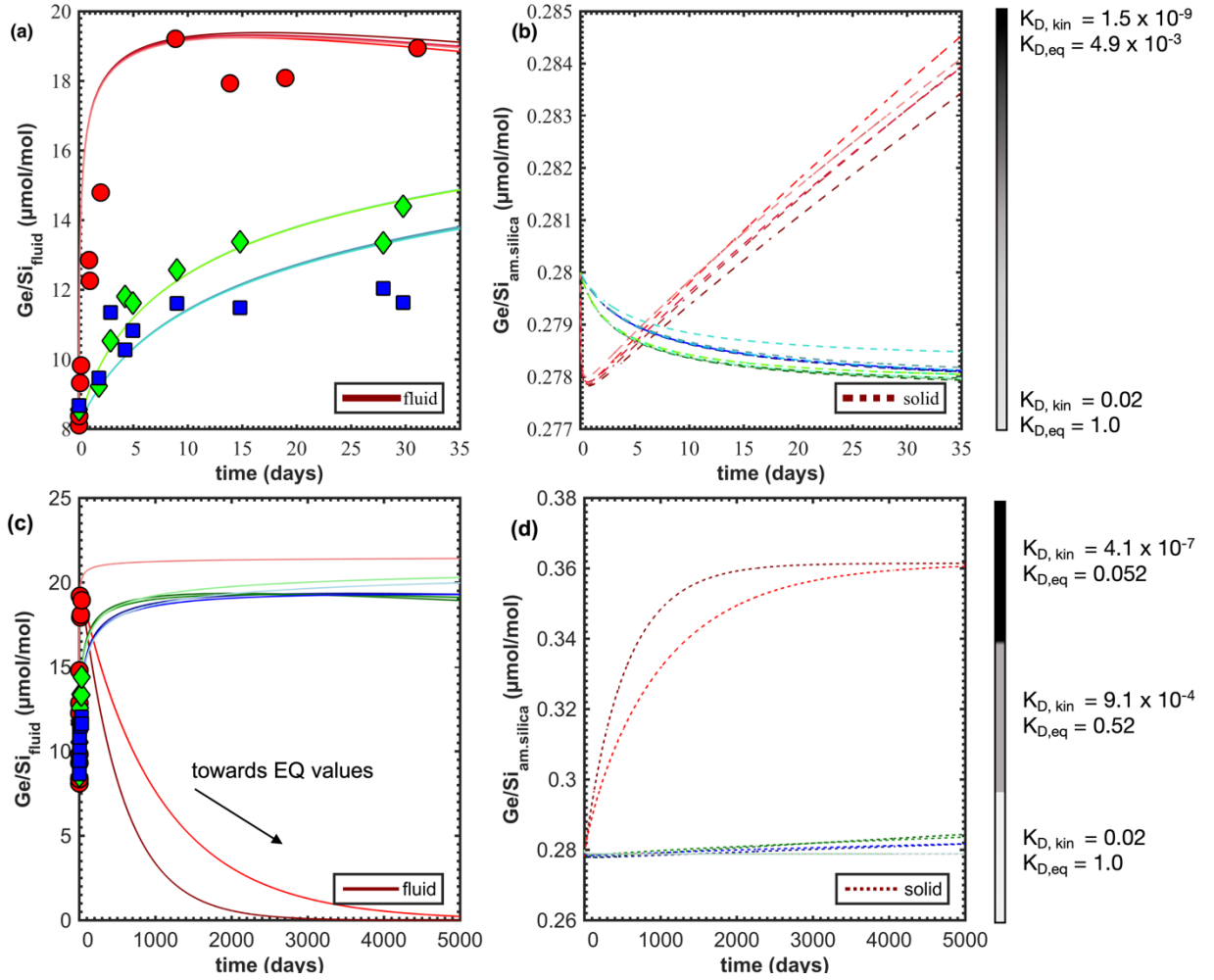

Figure 3.6 Trace model Ge/Si simulations for a Ge incorporation scenario

Trace model simulations of both fluid and solid Ge/Si over time where Ge is allowed to precipitate and get incorporated into the growing amorphous silica. Experimental, short- (35 days, **A and B**) and long- (5000 days or ~14years, **C and D**) term simulations are shown. Short-term simulations were run over a wide range of kinetic and equilibrium partition coefficients, resulting in very little differences between simulations over these timescales. Long-term simulations were run over a distinct range of kinetic and equilibrium partition coefficients based on individually constrained kinetic and thermodynamic parameters that provide an lower limit ($K_{d,\,kin}$ = 4.1 x 10-7, $K_{d,eq}$ = 0.052, dark shading), upper limit ($K_{d,\,kin}$ = 0.02, $K_{d,eq}$ = 1.0, light shading), and an intermediate set of parameters ($K_{d,\,kin}$ = 9.1 x 10^{-4}, $K_{d,eq}$ = 0.52). The upper limit simulation over these long timescales predicts no equilibrium partitioning. The lower limit simulation predicts large and fast equilibrium partitioning driving fluid Ge/Si down to lower values.

compare the range of "best-fit" determined Ge kinetic rate and equilibrium constants against those of silica (presented as $\Delta\log k_f^{Si-Ge}$ and $\Delta\log K_{sp}^{Si-Ge}$, respectively), which resulted in a clear linear trendline where the thermodynamically calculated K_{sp}^{Si-Ge} for the silica – GeO_2 solid solution (10-3.9973; *see eqn. 2, Section 2.3*) is shown as a reference (**Fig. 3.5**).

Surprisingly, results from these "best fit" Ge incorporation model simulations show results improved to that of the conservative Ge scenario for the fluid Ge/Si evolution over time (**Fig. 3.6A**). Little variability is observed between runs despite kinetic ($K_{d,kin}$) and equilibrium ($K_{d,eq}$) partition coefficients spanning 9 and 2.5 orders of magnitude, respectively. Predicted fluid Ge/Si ratios match the experimentally observed evolution with time (**Fig. 3.4D**). The high surface area batch simulation accurately predicts a rapid attainment of highly elevated fluid Ge/Si ratios near the end of the experiment followed by gradual increases throughout the experimental duration for the lower surface area batches, respectively. A similar observation is shown for the solid phase evolution with time (**Fig. 3.6B**). All simulations are tightly bound with solid Ge/Si initially decreasing due to the large amount of silica precipitated. In the high surface area case, solid Ge/Si starts to increase with reaction progress as silica precipitation rates start to slow down in the approach to near equilibrium conditions when more Ge is incorporated into the newly formed amorphous silica.

These findings confirm our postulations based on the conservative Ge approach model results that (1) Ge incorporation is kinetically very slow, ranging anywhere between 9–2.5 order of magnitude slower than silica precipitation kinetics, and (2) the duration of the experiments (30 days) was not long enough to capture the full fluid and solid Ge/Si evolution as a function of reaction progress. The high surface area

experiments, with the fastest overall precipitation rates, exhibited the largest range in behavior and, thus represented the most promising case for distinguishing between kinetic rate and equilibrium constant parameter pairs. Yet, unfortunately, these experiments were just not run over sufficient time to provide any meaningful sensitivity.

However, there are several independent constraints we can capitalize on to give us a more reasonable kinetic–thermodynamic parameter space. First, there is the thermodynamic equilibrium constant for Ge that was calculated based on the assumption of a solid-state solution between quartz (SiO_2) –argutite (GeO_2) (**eqn. 3.3**). As already state above (**Section 3.2.3**), this value, $10^{-3.9973}$ ($K_d^{eq} = 10^{-1.28}$), should represent the lower limit for the amorphous GeO_2 equilibrium constant given that it corresponds to a maximum kinetic rate constant (k_f^{Ge}) of 10^{-16} moles m^{-2} s^{-1} (6 orders of magnitude slower than the silica rate constant, $\Delta \log k_f^{Si\text{-}Ge}$; **Fig. 3.5**) and a $K_d^{kin} << 1$ based on "best fit" trace model runs to the experimental data. The upper bound for the thermodynamic and kinetic parameter pairs is assumed to be when the equilibrium partition coefficient, K_d^{eq}, is equal to 1, which implies that there is no equilibrium fractionation. This corresponds, respectively, with a Ge equilibrium constant equal to that of silica ($^{Ge}K_{sp} = {}^{Si}K_{sp} = 10^{-2.7135}$) and a kinetic rate constant (k_f^{Ge}) equal to $10^{-11.3}$ moles m^{-2} s^{-1}. To summarize, we estimate the thermodynamic and kinetic parameters for Ge precipitation during amorphous silica formation to be between $10^{-3.9973}$ and $10^{-2.7135}$ and 10^{-16} to $10^{-11.3}$ moles m^{-2} s^{-1} for K_{sp}^{Ge} and k_f^{Ge}, respectively.

3.4.3 Ge/Si the "equilibrium tracer"

Trace models using these individually constrained thermodynamic and kinetic parameters were run out to longer timescales (5000 days or ~14 years) to further explore the Ge/Si evolution of fluid and solid with reaction progress (**Fig. 3.6C,D**). We find that

the predicted evolution of fluid and solid Ge/Si vary considerably between simulations for the high surface area case where overall rates are fastest whereas model predictions remain tightly constrained for the lower surface area cases as a result of slower overall kinetics. High surface area trace model run at the parameter pair defining the lower bound of our imposed constraints (log K_{sp}^{Ge} = -3.9973, log k_f^{Ge} = -16.0) predicts a larger and overall faster decrease in the fluid Ge/Si over time, reaching values of 0.003 μmol mol^{-1} at 5000 days. These predictions are in distinct contrast with the high surface area simulations based on the thermodynamic and kinetic parameter pair upper limit constraints (log K_{sp}^{Ge} = -2.7135, log k_f^{Ge} = -11.3) where fluid Ge/Si remains at elevated values around ~21 μmol mol^{-1} as a result of no equilibrium partitioning ($K_{d,eq}$ = 1). A third simulation serving as an intermediate between the lower and upper bounds of the parameter pairs (log K_{sp}^{Ge} = -2.9973, log k_f^{Ge} = -12.7) show similar fluid Ge/Si behavior to that of the lower limit predictions with equilibrium partitioning driving down fluid Ge/Si to lower values over time, reaching 0.23 μmol mol^{-1} at 5000 days.

While all these scenarios are possible for amorphous silica precipitation, based on the available data from natural systems we assume that equilibrium partitioning in amorphous silica precipitation most likely occurs and, thus, the upper limit model predictions ought to be unrealistic in application to weathering environments. Except in the case of hydrothermal vents, fluid Ge/Si ratios in natural waters are generally low, 0.6 μmol/mol average (Mortlock and and Froelich, 1987; Froelich et al., 1992; Kurtz et al., 2002; Lugolobi et al., 2010) reflecting Ge incorporation into secondary silicates. Observations of low Ge/Si ratios in natural waters supports the long-term predictions from batch models run under a Ge precipitation scenario where fluid Ge/Si is ultimately expected to arrive at low values in the approach to equilibrium. Thus, we predict that the

fluid Ge/Si for amorphous silica formation will probably behave according to the lower-limit and intermediate simulations as long as log ΔK_{sp}^{Si-Ge} remains greater than 0. This prediction is further supported by experimentally calculated, instantaneous partition coefficients (K_d^{inst}; **Table 3.1**) increasing slightly during the course of the experiment, implying Ge incorporation into the newly formed amorphous silica is most likely due to equilibrium partitioning.

Based on these findings, we are now poised to provide a mechanism for Ge/Si fractionation during amorphous silica and, by extension, other secondary silicate phases. At the beginning of secondary mineral formation, order of magnitude faster silica precipitation rates with respect to germanium cause initially high fluid Ge/Si ratios. On these timescales, Ge ultimately acts essentially as a conservative element preferentially excluded from the growing mineral phase as silica removal dominates the initial shifts to high fluid Ge/Si values. In this regard, observed fluid Ge/Si behavior on the short, experimental timescales is analogous to biogenic phytolith formation known to preferentially exclude Ge exclusion, resulting in lower Ge/Si ratios in biologically formed opal (0.03 – 0.50 μmol/mol) and elevated fluid Ge/Si (Derry et al., 2005; Blecker et al., 2005; Delvigne et al.,2009; Lugolobi et al., 2010). After a period of a month the time it takes for silica precipitation rates to slow down in the approach to equilibrium, high fluid Ge/Si ratios start to shift towards values representative of equilibrium. In these simulations, only the high surface area condition shows this behavior while fluid Ge/Si in the medium and low surface area batch runs are still increasing with time. Evolution of fluid Ge/Si ratios predicted over long, decadal timescales imply that Ge precipitation is extremely slow for the amorphous silica system, which supports the initial hypothesis

put forth by Opfergelt et al. (2010) who suggested that high observed Ge/Si ratios in soil solutions might reflect inhibited or slow secondary mineral formation.

Importantly, results from these trace model simulations highlight the importance of Ge equilibrium partitioning, which ultimately dominates the long-term evolution of fluid Ge/Si signatures. Additionally, there is substantial evidence based from these results suggesting that amorphous silica precipitation onto lower surface area seeds heavily lags the extent of reaction progress. We predict that a shift in fluid Ge/Si to lower values as typically observed in natural waters will be seen over a period of a couple years (in the high surface area case) to several decades (in the lower surface area cases). In this regard, Ge/Si partitioning is quite distinct from δ^{30}Si fractionation during amorphous silica formation, which is controlled by both kinetic and equilibrium effects. Therefore, Ge is dominated principally by equilibrium fractionation making Ge/Si a unique tracer of equilibrium chemical processes.

3.4.4 Looking towards the future: Ge/Si and δ^{30}Si multi-tracer approach

Evidence from the experimental data and numerical batch model simulations now supports the idea of Ge/Si as a strictly equilibrium tracer. Based on this new finding, we are now poised to interpret the observed δ^{30}Si vs Ge/Si "boomerang" relationship observed in the amorphous silica precipitation experiments (**Fig. 3.7A**). High precipitation rates at the beginning of the reaction result in a strong, positive correlation between δ^{30}Si and Ge/Si until maximum isotope kinetic enrichment is obtained. Interestingly, phytolith formation and biological uptake are the only processes where Ge/Si and δ^{30}Si are positively correlated in that both fluid Ge/Si and δ^{30}Si shift towards higher values (Ziegler et al., 2005). Afterwards, shown uniquely in the high surface area

batch, as precipitation rates begin to slow down considerably, $\delta^{30}Si$ and Ge/Si display a negative correlation where increasing contributions from equilibrium fractionation return fluid $\delta^{30}Si$ back to starting values (otherwise called isotopic re-equilibration). Notably, the timescales for $\delta^{30}Si$ and Ge/Si fractionation are drastically different from one another, with $\delta^{30}Si$ kinetically fractionating and then subsequently re-equilibrating before Ge equilibrium partitioning is even initiated. Thus, these $\delta^{30}Si$ vs Ge/Si relationships provide important information on the progress of the secondary mineral reaction where high $\delta^{30}Si$ and Ge/Si ratios reflect early stages of secondary mineral formation and low $\delta^{30}Si$ and Ge/Si ratios reflect extensive equilibration.

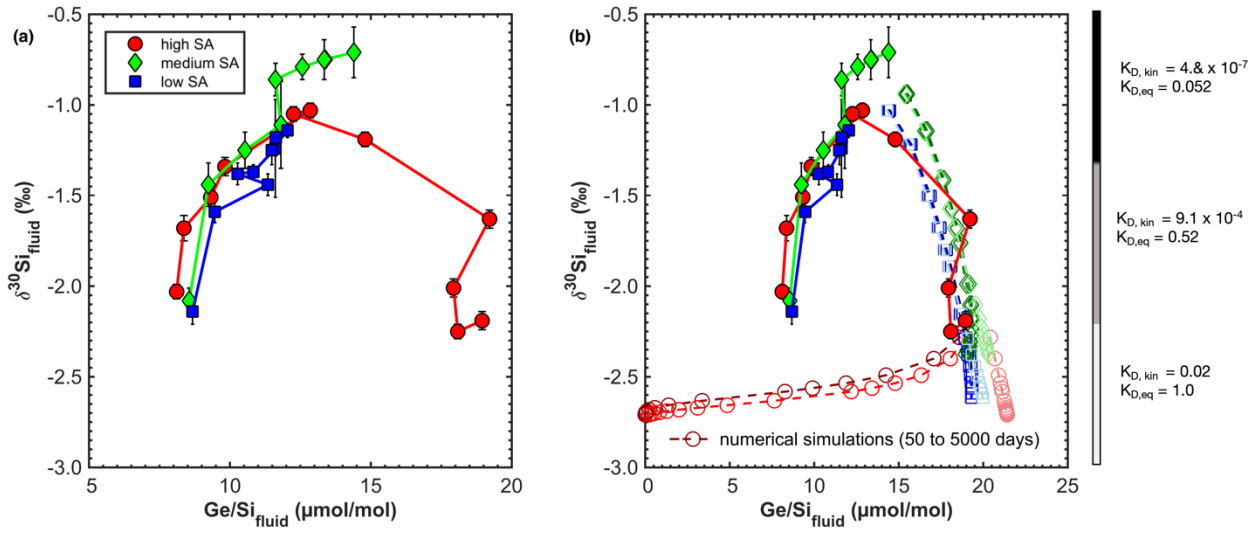

Figure 3.7 Fluid $\delta^{30}Si$ vs. Ge/Si relationships extended out to longer timescales
Measured fluid **δ**30Si as a function of Ge/Si (**A**) for the surface area batch experiments presented alongside trace model fluid **δ**30Si and Ge/Si predictions for the respective surface area conditions over longer timescales, from 50 to 500 days (**B**), using the non-conservative Ge scenario (open markers, dashed lines) for kinetic and thermodynamic parameters representing the (KD, kin = 4.1 x 10-7, KD,eq = 0.052, dark shading), upper limit (KD, kin = 0.02, KD,eq = 1.0, light shading), and an intermediate set of parameters (KD, kin = 9.1 x 10-4 , KD,eq = 0.52). Trace model estimations suggest that Ge/Si equilibrium fractionation may exhibit some surface area dependence.

To extend out to the timescales common in natural weathering environments, trace element batch model fluid Ge/Si ratios under the slow Ge precipitation scenario and transient batch model fluid $\delta^{30}Si$ (Fernandez et al., 2019) were run out to 5000 days for all surface area cases using the upper, intermediate, and lower limit kinetic and thermodynamic constants. The results are presented along with the experimental data in **Fig. 3.7B**. Notably, Ge/Si and $\delta^{30}Si$ models predict Ge/Si equilibrium partitioning as a function of surface area. Precipitation onto higher surface area seeds results in a quasi-hysteresis loop that reflects the interplay between rapid $\delta^{30}Si$ kinetic fractionation and subsequent re-equilibration and slower, continued Ge/Si approach to equilibrium over much longer timescales. Whereas the lower surface area amorphous silica seeds significantly slow down precipitation rates and, as a consequence, Ge/Si and $\delta^{30}Si$ fractionation. As a result, precipitation onto lower surface area seeds retains relatively high values Ge/Si and $\delta^{30}Si$ and, thus, kinetic $\delta^{30}Si$ signatures over much longer timescales. Thus, depending on the average surface area of the porous media, fluid Ge/Si and $\delta^{30}Si$ can provide enormous insight into the fluid residence times within the weathering zone based on the extent of Ge/Si and $\delta^{30}Si$ partitioning relative to one another.

Finally, based on these notable findings, $\delta^{30}Si$ vs Ge/Si relationships can give constraints on the weathering intensity of a weathering system and the overall fluid residence times of the system where young, lower weathering intensity environments should have high $\delta^{30}Si$ and Ge/Si signatures and vice versa for older, more intensely weathered systems. Therefore, Ge/Si serves as a nice complement to $\delta^{30}Si$, which has been

demonstrated in the recent literature to be a tracer of kinetic processes (Geilert et al., 2014; Roerdink et al., 2015; Oelze et al., 2015). The application of these two tracers in tandem can serve a powerful tool to constrain silicate weathering processes on both short ($\delta^{30}Si$) and long (Ge/Si) timescales. The combining of complementary trace element and stable isotope systems represents the way forward in the weathering field, with its potential only now starting to be realized in the literature (Cardinal et al., 2010; Cornelis et al., 2010; Opfergelt et al., 2010; Delvigne et al., 2016; Baronas et al., 2018).

3.5 CONCLUSIONS

This study reports for the first time Ge/Si fractionation during amorphous silica precipitation across a range of surface areas under highly controlled, laboratory settings. Our findings show that Ge incorporation kinetics are very slow (~ 2.5 to 6 orders of magnitude slower than silica precipitation rates) and, as a result, gives the appearance of conservative behavior over short timescales (~ 30 days). These results support the hypothesis put forth by Opfergelt et al. (2010) with regards to secondary clay formation in field settings. Thus, Ge/Si fractionation is controlled strictly by equilibrium processes, making it a unique equilibrium tracer. Over long timescales, Ge/Si equilibrium partitioning appears to exhibit some dependence on the surface area with fluid Ge/Si returning to equilibrium values faster during precipitation onto higher surface area seeds relative to lower surface area seeds. $\delta^{30}Si$ and Ge/Si multi-tracer approach have the potential to provide important constrains on weathering intensity, fluid residence times and the amount of secondary silicate formation taking place in the weathering zone. Finally, successful application of the trace element batch model to the experimental dataset over a range of surface areas suggests that the framework developed in the

CrunchTope software under the assumption that trace elements behave analogously to stable isotopes is valid for germanium. Thus, CrunchTope can now be considered as both isotope- and trace element–enabled.

CHAPTER 4

Silicon isotope – discharge relationships in small catchments spanning different climates and lithologies [3]

4.1 INTRODUCTION

Chemical weathering of silicate rocks sustains long term solute cycling through water-rock interactions in the terrestrial subsurface. The slow transformation of bedrock into the diverse landscapes that characterize Earth's surface occurs in part due to the infiltration of weakly acidic precipitation, which promotes dissolution at the surfaces of primary minerals and releases solutes into solution. This generation and accruement of alkalinity and cation concentrations are subsequently drained to rivers and ultimately transferred from the continents to the oceans. Silicate weathering thus serves important roles in the supply of essential nutrients to ecosystems, the transfer of mass from the terrestrial landscape, and the regulation of Earth's climate over geologic timescales via the drawdown of atmospheric CO_2. As a result, a principle objective of modern Critical Zone (CZ) science is to better understand how solutes are produced and transported from "weathering zones" on land to long-term oceanic reservoirs.

At present, accurately quantifying terrestrial silicate weathering rates poses a significant challenge in the Earth science community. This is largely due to the complexity of silicate weathering reactions and the "weathering zone" in which these reactions takes place (Ameli et al., 2017; Aguirre et al., 2017; Chorover et al., 2017). Silicate

[3] Fernandez, N.M ; Bouchez, J.; Derry, L.A; Chorover, J. ; Gaillardet, J.; Druhan, J.L. *in prep.*

weathering ultimately represents a balance between multiple processes (i.e. dissolution and precipitation, reactivity and transport) and timescales (short versus long fluid residence times, fast vs. slow reactions) (Bao et al., 2017; Li et al., 2017; Bhavna et al., 2019; Maher and Navarre-Stichler, 2019). Water infiltrating into the subsurface interacts with and dissolves primary minerals such as feldspar, muscovite and quartz, as well as carbonates, and recycled clays, which supply solutes that subsequently drive the precipitation of secondary phases (i.e., secondary clays and amorphous(hydr)oxides). Further, biological activity can significantly influence the extent of solute export as many lithologically derived elements are either taken up or excluded by vegetation roots and attendant microorganisms (Derry et al., 2005; Cornelis et al., 2016; and others). Consequently, solutes generated by the chemical weathering of bedrock are rarely preserved conservatively in the dissolved load, but are more often partially scavenged by secondary mineral formation and biological uptake processes to be stored and cycled within the near surface in the form of regolith, soils and cellular structures.

This highly coupled nature of primary mineral dissolution and secondary cycling (Zhu et al., 2004; Maher et al., 2006; Maher et al., 2009) is further complicated by the balance between reactivity and transport. In the absence of transport processes (e.g. in a closed vessel) the approach to *chemical equilibrium* is quantified through a timescale associated with reaction progress towards a thermodynamically based state of equivalent forward and reverse reaction rates. In open hydrologic systems characterizing the "weathering zone", time and distance are coupled in that the proximity of a *steady state* to chemical equilibrium is defined in terms of two characteristic timescales, one describing the collective chemical weathering rate(s) of the system, and the other describing the rate solutes are transported due to the combined effects of advection,

diffusion, and dispersion (Lichtner, 1985; Lichtner, 1988; Johnson and DePaolo, 1994; Steefel and Maher, 2009; Maher and Chamberlain, 2014). As a result, the extent to which an observed steady state within a weathering system reflects true chemical equilibrium depends on this balance between transport and reactivity, which includes contributions from secondary mineral formation (Noack et al., 1993; Stéfansso and Gíslason, 2001; Maher et al., 2009; Maher, 2010, 2011 and others). This coupling creates a critical limitation in that the observed steady state becomes an underdetermined problem where infinite combinations of reactivity and transport pathways can generate the same result (Velbel and Price, 2007). If our ultimate goal is quantitative constraint of the individual chemical and transport pathways that contribute to weathering, we therefore must attempt to reduce the number of possibilities that can generate an observed steady state in a given system.

In the present study, we consider two methods by which these complexities have been parsed. First, to some extent, the broad range of fluid travel times and flow field heterogeneities characteristic of the weathering zone may be circumvented, or at least summarized, in the diagnostic relationship between concentration (C) and discharge (Q) of streams and rivers draining landscapes. In essence, these relationships are the culmination of all reactivity and transport leading to a mass flux of chemical weathering from the "weathering zone". Thus, they are frequently used as a diagnostic tool to assess the interaction between solute generation and hydrological processes, which allow the watershed to function as a chemical reactor (Anderson et al., 1997; Horneberger et al., 2001; Godsey et al., 2005, 2009; Chorover et al., 2017; Hunsaker et al., 2017; Kim et al., 2017; McIntosh et al., 2017; Winnick et al., 2017, and many others). Second, non-traditional stable isotopes (Li, Mg, Ca, B, Si, Fe, Cu, Zn), which are highly sensitive to a specific

subset of chemical weathering processes, can provide further insight into overall catchment dynamics. For example, the stable isotopes of silicon, the 2nd most abundant element in Earth's crust (designated $\delta^{30/28}$Si) have been frequently used to infer and quantify solute fluxes associated with silicate weathering (Georg et al., 2006; Georg et al., 2007; Georg et al., 2009; Cardinal et al., 2010; Hughes et al., 2011; Hughes et al., 2012; Opfergelt and Delmelle, 2011; Pokrovsky et al., 2013; Frings et al., 2016; Riotte et al., 2018, and others). Silicon stable isotopes can be fractionated by biological uptake and secondary mineral precipitation processes and, thus, used to tease apart the contributions of these secondary processes to overall mineral weathering rates, providing critical constraint on the fate and transport of chemically generated solutes within the critical zone.

Though these two techniques have been broadly applied individually, to date, there are only a few studies combining C-Q relationships with associated isotope ratio – discharge (hereafter referred to as R-Q) datasets (Georg et al., 2006; Cenki-Tok et al., 2009: Lemarchand et al., 2010; and others). Here, we suggest that such a combination may be broadly synergistic. For example, the application of C-Q as a diagnostic weathering signature is inherently limited by chemostatic behavior (i.e. when solute concentrations remain constant with respect to discharge). This lack of apparent sensitivity is unfortunately common in many C-Q relationships, including Si (Godsey et al., 2009; Godsey et al., 2019). However, the specific signatures of stable isotope indicative of a subset of chemical reactions contributing to the overall concentration may provide additional sensitivity. For example, associated shifts in stable isotope ratios of silicon ($\square^{30}$Si) result from secondary mineral precipitation. Thus, isotope ratios may provide a window into the transient effects associated with frequent changes in discharge, even

when bulk concentrations are invariant. Further, there is strong evidence suggesting that frequently observed chemostasis is an artifact of low frequency datasets (i.e. monthly, seasonally, and yearly) that essentially masks important short-term hydrochemical responses that are typically driven by major hydrological, "storm" or "flooding", events (Neal et al., 2012; Floury et al., 2017). As a consequence, capturing hydrochemical dynamics at these storm event scales (i.e. hourly to daily) provides first-order insight into the drivers of solute export and associated large isotopic shifts at the catchment scale. Flood events, thus, are a vital component in solute generation and transport dynamics but has yet to be fully exploited by high frequency chemical and isotopic datasets.

In the present study, we developed a novel, riverine chemical (Si concentrations) and stable isotope ($\delta^{30/28}$Si) high frequency dataset for multiple storm events, which gives us a first look into hydrochemical catchment dynamics over these short timescales analogous to a "snapshot" in time. We leverage the characteristically large variations in of solute export flux associated with hydrograph response to substantial precipitation events, characterized by large variations in discharge over a short time (hours to weeks). We suggest that this coupled response in C and Q (Benettin et al., 2017; Li et al., 2017) serves as a basis to begin to constrain associated R-Q relationships, ultimately offering a new quantitative metric for chemical weathering reactions occurring within the critical zone. Towards this purpose, we constrain, for the first time, characteristic stable silicon isotope --- discharge (Si R-Q) relationships for storm events across seven catchments spanning different climates, lithologies, and biomes as part of a cross-CZO project (SAVI, *Science Across Virtual Institutes*) between French (OZCAR; Gaillardet et al., 2018), Canadian (Hakai Institute) and American Critical Zone networks (U.S National Research Council Committee on Basic Research Opportunities in the Earth Sciences, 2001). The

purpose of this study is to constrain the behavior of stream $\delta^{30}Si$ signatures with discharge over short timescale precipitation events (hours to months) to gain insight into (1) the characteristic response of stream $\delta^{30/28}Si$ signatures as a function of runoff and (2) to provide an isotopic complement to C—Q relationships as an improved constraint of the pathways contributing to cumulative solute discharge fluxes.

4.2 SITE DESCRIPTIONS

We present datasets spanning the northern hemisphere across two continents (North America and Europe) and two Caribbean islands. The sites are all small catchments (0.08 to 17 km^2) with 1st to 3rd order drainage networks spanning a range of diverse climates (tropical to semi-arid), lithologies (volcanic, granitic, and shale), and ecological biomes (Caribbean tropical forests to "Bog" forests and woody wetlands to traditional mixed conifer forests). Notably, this large-scale dataset is unique in that it is based on storm events that take place over short timescales (i.e. days to weeks) and, thus, is distinct from traditional riverine stable isotope hydrogeochemical datasets collected over monthly and seasonal timescales (Georg et al., 2006; Geoerg et al., 2007; Hughes et al., 2013; Fantle and Tipper, 2014; Pokrovsky et al., 2013; Frings et al., 2016; Riotte et al., 2019). A summary of catchment characteristics is presented in **Table 4.1** and further individual site details are discussed in the following sub-sections. Hydrological characterization of each storm event is provided in greater detail in **Section 4.4.**

4.2.1 Sapine (44°37'N; 3°82'W)

Sapine is a small granitic catchment in the Mont-Lozère watershed in the National Park of Cevennes in Southern France. Located approximately 80 km from the Mediterranean Sea at an elevation between 1150 – 1350 m (Cognard-Plancq et al., 2003),

the Sapine catchment (basin area = 0.54 km^2) has been continuously monitored since the 1980s by the *Observatoirs Hydrométérologique Mediterranéen Cévennes-Vivarais* (OHMV) established originally to determine the environmental impact of anthropogenic activities on semi-natural ecosystems (Lelong et al. 1990), where Sapine was considered a pristine control site. The catchment is now part of the French Critical Zone research network, OZCAR (*Observatoires de la Zone Critique: Applications et Recherche; Gaillardet et al., 2018*).

The Mont-Lozère region is presently characterized by a Mediterranean climate with average temperatures ranging from –5°C in January to 17°C in July and a mean annual rainfall of 2000 mm. The autumn and spring are characterized by periods of intense rain called "cévenols" or flash flood events. The predominant lithology consists of porphyritic granodiorite and monzogranite (part of the Pont-de-Montvert-Borne complex) where large (10 cm) orthoclase megacrysts and fine-grained andesine, potassium feldspar, biotite, and quartz make up the overall primary mineral assemblage (Kußner, 2018). A thin, high permeability, soil layer (~0.6m; Cognard-Plancq et al.2001; Marc et al., 2001) with a vegetation cover of principally Beech (Fagus sylvatica) forest overlies a relatively deep regolith layer (10 m thick). Sapine is a perennial, first order stream hydrologically characterized by quick responses in discharge and stage height to rainfall (Martin et al., 2003).

The sampled storm event was the first of significance following the dry season, occurring over a one-week period from Oct.11 – 18 in 2016 (see **Section 4.4.1**). Mean annual runoff for the 2015-2016 year was 3.07 mm day^{-1} (Kußner, 2018; **Table 4.1**). Notably, no development of overland flow from infiltration excess is observed during storm events at this site (Martin et al., 2003). The highly heterogeneous nature of the subsurface coupled with observation of very low weathering rate (480 mol/ha/yr)

suggests a "weathering-limited or 'kinetically-limited" environment where the physical transport of soil material is faster than the chemical alteration of the underlying bedrock (Kußner, 2018).

4.2.2 La Jara (35°50'N-36°00'N; 106°24'W–106°37'W)

The La Jara Creek Catchment (basin area = 3.3 km^2) event reported in this study was a spring snow-melt spanning early March to Late May in 2017 where peak discharge (0.15 m^3/s) was approximately 3x higher than the last major peak discharge observed during the snowmelt event in 2007 of the last large snowmelt event in 2007 (0.06 m^3/s; McIntosh et al., 2017; see *Section 4.1*). Located in the Valles Caldera National Preserve (VCNP) in the Jemez Mountains of northern New Mexico, U.S., La Jara Creek catchment is part of the Jemez Critical Zone Observatory (National Research Councel, 2010; White et al., 2015). The creek drains a 21km wide caldera formed ~1.25 Ma with elevations of 2664 – 32934 m (Zapata-Rios et al., 2015; McIntosh et al., 2017). Situated within a resurgent dome, the lithology that La Jara Creek drains is the most complex of all catchments investigated in this study. In general, the lithology is largely dominated by Pleistocene aged Bandelier Tuff and fine grained rhyodacite with primary mineral assemblages consisting of Ca-clinophilite, alkali feldspar, cristobalite, albite, and quartz and some minor accessory minerals such as apatite, hematite, zircon, titanite, ilmenite, and faujasite (Zapata-Rios et al., 2015). A deep regolith (42–27m from ridge to base; Olyphan et al.,2016) and a relatively uniform (~1m thick) soil layer overlies the the rhyolitic bedrock. The vegetation is characterized as a mixed conifer forest containing Spruce-fir (*Picea pungens*), ponderosa pine (*Pinus ponderosa*), aspen (*Populas tremuloides*), and gambel oak (*Quercus gambelii*) at higher elevations and forest meadows and grasslands in the valley (Muldavin et al., 2006; Coop and Givnish, 2007). The climate is characterized as semi-arid with a bimodal annual

precipitation pattern totaling 710 mm, where snowfall accounts for ~44% of the total precipitation (McIntosh et al., 2017). The hydrology is typical for snowmelt-driven systems, with peak stream discharge occurring in late March – Early April.

La Jara Creek is a perennial stream with contributions to overall streamflow predominantly deriving principally from shallow and deep groundwater flow paths and no significant contributions from overland flow (Bales et al., 2006; Henderson and Shuman 2010; Zapatas-Rios et al., 2015; McIntosh et al., 2017). The mean annual runoff for the 2017 year was 1.25 mm day^{-1} (Troch et al., 2018; **Table 4.1**).

4.2.3 Elder Creek (39°43′44 ′′ N, 123°38′39′′W)

The event reported for Elder Creek watershed (basin area = 17 km^2) was an extremely intense storm spanning a 10-day period from January 5 – 13, 2017, in the middle of the wet season (**Section 4.4.1**). Elder Creek (elevation of 400 –700m) is a perennial 2nd order stream that flows for 16 km within the Angelo Coast Range Reserve in Northern Mendocino County, CA, USA. Samples were taken at the headwaters of Elder Creek next to the highly monitored Rivendell site (Salve et al., 2012; Rempe and Dietrich, 2014), a thin soil mantled hillslope (average slope angle 30°), part of the the Eel River Critical Zone Observatory (ER-CZO; National Research Councel, 2010; White et al., 2015).

The lithology consists of a tectonically folded mudstone dominated by turbidite sequences and interbedded with lenses of sandstones and conglomerates and is part of the Coastal Belt of the Franciscan Formation. This setting reflects a complex formation history associated with close proximity to the Mendocino triple junction (Blake Jr et al., 1985). The primary mineral assemblage of the bedrock is similar to that of clay-rich sales, i.e. a composition of quartz, plagioclase, Fe-rich chlorite, illite, montmorillonite, smectite, and kaolinite (Kim et al., 2014). Between the shallow soil layer (0.5–0.75m) and coherent

bedrock there is a thick section of fractured, partially weathered regolith (25-5m from ridge to base). The deepest section of this weathered rock is fluid saturated, hosting a water table that fluctuates by several meters in height through the year. Above this periodically saturated section a substantial portion of the regolith is partially saturated and hosts the deep roots of a densely vegetated coniferous forest composed predominantly of Douglas-fir (*Pseudotsuga menziesii*) and Pacific madrone (*Arbutus menziesii*) (Hahm et al., 2017). The Elder Creek catchment resides in a Mediterranean climate consisting of warm, dry summers and cold, wet winters where average temperatures range from -8 to 32°C and the mean annual precipitation is 1900 mm with rainfall concentrated in the months of October – April (Salve et al., 2012).

Elder Creek is supplied principally from subsurface pathways with no consistent observations of overland flow (Salve et al., 2012; Kim et al.,2014). The mean annual runoff for the 2016-2017 year was 4.78 mm day^{-1} based on streamflow data provided by the Berkeley Sensor Database (Ogla et al., 2010).

4.2.4 Quiock Creek (16°17′ N, 61°70′W)

The event reported for the Quiock Creek catchment (basin area = 0.08 km^2) took place from 6th – 26th October 2015, during the wet season. The 2015 wet season was defined by a major tropical storm Erika in late August where extensive flooding and mudslides caused major road damage on the Basse-Terre Island, followed by a category 1 hurricane Kate in early November. Located on Basse Terre Island as part of the Guadeloupe archipelago in the French West Indies, Quiock Creek is a small tributary (first order, perennial stream) of the Bras-David River. The site is part of the French INSU-CNRS CZO network (Lloret et al., 2011, 2013; Dessert et al., 2015) and OZCAR (Gaillardet et al., 2018). The elevation ranges from 200 – 350 m and is characterized by a wet tropical climate that

is generally composed of a dry season from January to June and a wet, cyclonic season from July to December. Mean annual air temperature and rainfall are 25°C and 3500 mm respectively.

The predominant lithology is Pleistocene andesitic pyroclastic deposits (Boudon et al., 1988; Clergue et al., 2015). The overlying soil is thick (>15m; Colmet-Daage and Bernard, 1979) and strongly depleted with secondary minerals constituting roughly 95 wt. % of the bulk soil (Buss et al., 2010). The vegetation is characterized by a dense, humid tropical forest consisting of a variety of tree and plant species such as Gommier (*Dacyrodes excelsa*), Ironwood (*Sloanea spp.*), *Cordia reticulata*, *Amanoa caribaea*, *Tapura latiforlia*, and sedges (*cyperaceae*) lined with sharp amorphous silica edges (Imbert et al., 1998). The principle hydrologic characteristics are high evapotranspiration (63%) as is typical for tropical rainforests with significant contributions from tropical storms and hurricanes, which can (like in the case of hurricane Rafael, October 2012) account for ~5% of the total annual rainfall (Zahibo et al., 2007).

Mean annual runoff for Quock creek is 1.56 mm day^{-1} (Fries et al., 2019; **Table 4.1**). A unique feature of the Quiock creek catchment is the significant input of volcanic ash, deriving from the active Montserrat Volcano (located~ 65km from Guadeloupe), as well as Saharan dust, both representing large sources of quartz and clays to the soil (Clergue et al., 2015; Dessert et al., 2020).

4.2.5 Hakai (51°39′12.9672′′N, 128°7′48.4032′′W)

Two storm events are reported from Watershed 708 in Calvert Island, British Columbia, CAN that took place between at the beginning of the wet season from Sept.16 – 19, 2017 and Oct.14 – 21, 2017 respectively. This is a third order, perennial stream draining watershed 708 (basin area. = 7.8 km^2), one of four watersheds comprising the

Hakai Critical Zone Observatory integrated into the Critcal Zone Exploration Network, CZEN, (Sullivan et al., 2017) in the northern section of Calvert Island located off the central coast of British Columbia, Canada (Oliver et al.,2017). The elevation ranges from 160 m (near the coast) to 426 m (inland). Calvert Island is part of British Columbia's coastal perhumid rainforests located in the hypermaritime region of the Coastal Western Hemlock zone (Wang et al., 2012). The climate generally consists of cool summers (annual maximum temperature = 17.9°C) and mild winters (annual. minimum temperature = 0.9°C) with average annual precipitation around 3356 mm y^{-1} (Wang et al., 2012). Wet and dry seasons at this site are less pronounced than some of the other catchments, but generally span from October to April and May to August, respectively. Notably, both Calvert and Hectate Islands (another site included in the Hakai CZO) represent a global "hotspot" for dissolved organic carbon with average DOC annual yields of 24.1 (22.2 – 26.0) Mg C km^{-2} (Oliver et al., 2017).

Granodiorite (tonalite) is the principal lithology, overlain by relatively thin (< 1m), organic-rich soils (Green et al., 2014; Thompson et al., 2016). Bog forests and wetlands characterize the vegetation consisting principally of shore pine (*pinus contorta*), yellow cedars (*chamaecyparis nootkatensis*), western red cedar (*thuja plicata*), and shrubs (*sphqgnum spp.*) and grasses (Thompson et al., 2016; Oliver et al., 2017; Levy-Booth et al., 2018). Mean annual runoff for Watershed 708 for the 2017 year was 5.71 mm day^{-1} based on stream data provided by the Hakai Metadata Catalogue (Korover et al., 2019; **Table 4.1**).

4.2.6 Providence Creek (37°65'2''N, 119°20'55''W)

The storm event analyzed from Providence Creek, located near Fresno, California, USA in the Southern Sierra Nevada, took place during the winter wet season of 2018 over the course of two days (Jan.8 – 9, 2018). This second order, perennial stream drains

catchment P303 (basin area = 7.8 km^2) as part of the Kings River Experimental Watersheds (Hunsaker, 2013) in the Southern Sierra CZO network (National Research Councel, 2010; White et al., 2015). The range in elevation for this catchment is 1731-2025 m, placing it within the rain-snow transition zone where snow constitutes roughly 35-60% of the annual precipitation (Bales et al., 2018). The climate is Mediterranean with over 90% of the mean annual precipitation (1015 mm; O'Green et al. 2018) taking place between October and April (Hunsaker et al., 2017). The lithology is granitic (granodiorite) with a relatively thick partially weathered regolith (35m for catchment P303; Holbrook et al., 2014) and thin soils (1.0 to 1.5 m). Vegetation is predominantly a mixed conifer forest (Hunsaker et al., 2012) composed predominantly of white fir (*Abies concolor*) and ponderosa pine (*Pinus ponderosa*) (Bales et al., 2011). Mean annual runoff is approximately 0.77 mm day^{-1} (Hunsaker et al., 2017; **Table 4.1**). Streamflow in Providence Creek is largely supplied by deep (50–75%) and shallow (~32%) subsurface flow with rainstorm runoff, mainly in the form of snowmelt, only slightly contributing to the observed annual streamflow (3%) (Bales et al.,2011).

4.2.7 Rio Icacos (18°17'N, 65°47'W)

The storm event reported for the Rio Icacos watershed (basin area = 3.26 km^2) in the Carribean, volcanic island of Puerto Rico, USA, occurred in over a one-day period (May 25, 2012). Rio Icacos is a well characterized second order, perennial stream that is part of the Luquillo CZO network (National Research Council, 2010; White et al., 2015). The Rio Icacos drainage area (3.26 km^2) is located at an elevation of 600 – 800 m and characterized by a Caribbean, wet, tropical climate with a mean annual temperature of 22°C and mean annual precipitation of 4200 mm (White et al., 1998; McDowell and Asbury,1994; Ferrier et al., 2010). Like the other Caribbean catchment in this study, Quiock Creek, strong

precipitation events are mainly driven by hurricanes and tropical storms. Hydrologically, Rio Icacos is characterized by comparatively high discharge conditions relative to the other sites included in this study, with a mean annual runoff of 579 mm day^{-1} based on streamflow data provided by the USGS (station I.D. 50075000).

The watershed is composed of a granitic (tonalite) lithology overlain by a thick saprolite layer (2 – 8 m) and capped by a 0.5 – 1m deep soil (White et al., 1998). Just as with the Quiock Creek catchment, the Rio Icacos watershed also received contributions from Saharan Dust as is common for Caribbean islands (21 ± 7 t km^{-2} yr^{-1} Pette-Ridge et al., 2009). Vegetation is characterized as a mature Colorado forest composed principally of palo coloraodo (*Cyrilla racemiflora*), caimitillo (*Micropholis garciniaefolia, M. chrysophylloides*), and laurel sabino (*Magnolia splendens*) tree species (Foster et al., 1999; Murphy et al., 2012). Contributions to the Rio Icacos streamflow derive mostly from overland and shallow subsurface flow, particularly during storm events (Ziegler et al., 2005; Kurtz et al., 2011).

Table 4.1 Catchment characteristics

Site	Location	CZO Network	Basin area	Elevation	Climate	Lithology	Biome	MAT †	MAP†	MAR†	Denudation rate[h]	CWR[i]	Stream order
			km²	m				°C	mm	mm day⁻¹	μg m⁻² yr⁻¹ (10⁶)		
Sapine[a]	Mont-Lozère, FR	OZCAR	0.54	1350-1150	mediterranean	Granodiorite	Coniferous forest	7 (-5 to 17)	2000	3.07	8.26	66.1	1
La Jara creek[b]	New Mexico, USA	Catalina-Jemez	3.3	2664-2934	Semi-arid	Rhyolite	Mixed conifer forest	5.1	670	1.25	1.22	0.951	1
Elder creek[c]	California, USA	Eel River	17.0	400-700	mediterranean	Argillite, sandstone	Coniferous forest	11 (-8 to 32)	1900	4.78	38.6	27.6	2
Quiock creek[d]	Basse-Terre, GDLP, FR	OZCAR	0.08	200-350	Wet tropical	andesite	Caribbean tropical forest	25	3500	1.56	363	9.07	1
Hakai[e] (Watershed 708)	Calvert Island, BC, CAN	Hakai	7.8	160-426	Perhumid, coastal temperate rainforest	Granite (tonalite)	"Bog" forests, woody wetlands, evergreen forests	8 (0.9 to 17.9)	3356	5.71	-	-	3
Providence creek (P303) [f]	Fresno, California, USA	Southern Sierra	1.32	1731-2025	mediterranean	Granodiorite	Mixed conifer forest	8 (3 to 19)	1015	0.77	200	102	2
Rio Icacos[g]	Puerto-Rico, USA	Luquillo	3.26	600-800	Wet tropical	Granite (tonalite)	Mature Colorado forest	22	4200	579	192	15.2	2

† Mean annual temperature (MAT), mean annual precipitation(MAP), mean annual runoff (MAR).

a. *Durand et al.(1992) ;Cognard-Plancq et al.(2003); Martin et al.(2003) ; Kußner, 2018*

b. *Vázquez-Ortega et al.(2015) ; Zapata-Rios et al.(2015) ; Orem et al.(2016) ; McIntosh et al.(2017) ; Troch et al. (2018)*

c. *Salve et al.(2012) ; Kim et al.(2014) ;Rempe et al.(2014) ; Kim et al .(2017)*

d. *Gaillardet et al.(2011) ; Clergue et al.(2015) ; Dessert et al.(2015) ; Fries et al.(2019)*

e. *Thompson et al.(2016) ; Oliver et al.(2017)*

f. *Dixon et al.(2009); Safeeq and Hunsaker (2016);Hunsaker and Johnson (2017); Bales et al.(2018)*

g. *White and Blum (1995); Stonestrom et al.(1998) ; White et al.(1998); White et al.(2001) ; Derry et al.(2006) ; Ferrier et al. (2010); Kurtz et al.(2011); Scholl and Murphy (2014); Porder et al.(2015); Dialynas et al.(2016)*

h. Annual estimates of the denudation rates for each site. *Sapine : Allée and Boumédiène (2004)* ; La Jara : *Orem and Pelletier (2016)* ; Elder Creek : *Brown and Chanson (2012)*; Quiock Creek : *Rad et al.(2006,2013);* Providence Creek : *Dixon et al.(2009)* ; Rio Icacos : *Riebe et al.(2013)*.

i. Annual chemical weathering rates for each site: Sapine *: Martin et al. (2003)* ; La Jara : *McIntosh et al. (2017)* ; Elder Creek : *Kim et al. (2017)*; Quiock Creek : *Gaillardet et al.(2015) ;* Providence Creek : *Dixon et al.(2009)* ; Rio Icacos : *Millot et al.(2002)* .

4.3 METHODS

4.3.1 Hydrometeorological data

Annual and storm event rainfall intensity (mm h^{-1}) and stream discharge timeseries were collected from a range of meta-databases available through the countries maintaining the respective CZO networks of each site. The French OZCAR network manages the Guadeloupe (Quiock) and Mont-Lozère (Sapine) sites, affording high frequency hydro-meteorological data (5 minute and 30 minute measurements, respectively) collected and distributed by the Observatoire de l'Eau et de l'Érosion (ObsERA; https://webobsera.ipgp.fr) and by the Observatoire Hydrométérologique Méditerranéan Cévennes-Vivarais (OHMCV; https://ohmcv.osug.fr). The Hakai Institute provides 5 min stream discharge data through their Metadata Catalogue (https://hectate.hakai.org/geonetworks/srv/fre/catalog.search#/home). For the U.S critical zone networks, high frequency 15 min stream discharge and rainfall intensity data were obtained through the USGS National Water Information System (NWIS; https://waterdata.usgs.gov/nwis), CUAHSI Hydrologic Information System (HIS; https://data.cuahsi.org), and the respective CZO data repositories such as the Berkeley Sensor Database for the Eel River CZO (https://sensor.berkeley.edu) and the Climate and Hydrology Database Projects (CLIMDB/HYDROB; https://climhy.Iternet.edu) sponsored through the NSF-LTER (Long Term Ecological Research) network, USGS, and US Forest Service. Further information regarding data collection and methodology for the respective sites can be found through the references provided.

4.3.2 Elemental analyses

Non-acidified, filtered (0.22μm) stream water samples were analyzed by two laboratories for silica (^{28}Si), major and minor cations (^{23}Na,^{24}Mg, ^{39}K, ^{44}Ca, ^{27}Al, ^{88}Sr), and anion (Cl-, SO_4^2) concentrations for all catchments. Major, minor, and Si analyses for La Jara Creek, Hakai, Providence Creek, and Rio Icacos were performed by the Arizona Laboratory for Emerging Contaminants (ALEC) using an Agilent 7700 inductively coupled plasma mass spectrometer (ICP-MS) at the University of Arizona, Tuscon, AZ, USA. For Sapine, Elder Creek, and Quiock Creek, these analyses were performed at the Institut de Physique du Globe de Paris (IPGP) on an Agilent 7900 ICP-MS. Instrumental precision (± 5%) was determined using the certified river water reference standard SLRS-6. Anion concentrations were determined through ion chromatography analyses at both ALEC and IPGP.

4.3.3 Rainwater corrections to elemental concentrations

During storm events, direct contributions from rainwater to the overall stream chemistry can be significant, particularly in catchments located in proximity to a sea or ocean (i.e. the three islands - Rio Icacos, Quiock Creek, Hakai, as well as Sapine and Elder Creek). To remove this rainwater dilution effect from the observed stream solute concentrations, we employ a common correction technique following Gaillardet et al., (1999) as follows (**eqn. 4.1)**:

$$[\mathrm{X}]^{*} = [\mathrm{X}]_{\mathrm{meas}} - \left(\frac{\mathrm{X}}{\mathrm{Cl}}\right)_{\mathrm{rain}} \times [\mathrm{Cl}^{-}]_{\mathrm{meas}} \quad (4.1)$$

Where, for a given element X (Na, Mg, K, Ca), the measured stream water concentration ($[X]_{meas}$) is subtracted from the sea salt aerosol input determined from the measured chloride concentrations in the stream ($[Cl^{-}]_{meas}$) and the appropriate seawater elemental

ratio $\left(\frac{X}{Cl}\right)_{rain}$. For the major elements, the following seawater ratios are used: 0.859 (Na/Cl), 0.019 (K/Cl), 0.097 (Mg/Cl), and 0.019 (Ca/Cl) (Riley and Tongudai, 1967; Stallard 1980; Gaillardet et al., 1999). This rain-corrected elemental concentration is designated as X^* and is used throughout the present study. A key assumption made when using this calculation is that all the dissolved Cl^- in the stream water derives strictly from the atmosphere and not from other sources, particularly evaporites. There is no evidence for evaporites in any of these catchments, which are mostly either mono-lithological or volcanic. The only catchment where evaporites could potentially be present is in the semi-arid La Jara, which is situated directly within a hydrothermally active (< 300°C; Fraser and Gardner, 1994) resurgent caldera system (Smith and Bailey, 1968). Thus, there is a possibility that hydrothermally produced secondary halite could be present in the system. Prior findings from fluid inclusion studies showed the presence of trace amounts of secondary halite within quartz phenocrysts at 363m depth (Sasada and Goff, 1995). Yet, prior geochemical and mineralogical characterizations of the site found no evidence of evaporites like secondary halite nor the presence of geothermal waters impacting the overall solute chemistry of La Jara (Lieu et al., 2008). Results from these rainwater corrections are discuused in greater detail in **Section 4.4.2**. Notably, the principle emphasis of the current study is on silica, which is generally not impacted by atmospheric aerosols with $Si/Cl \sim 1.8 \times 10^{-4}$ (De La Rocha et al.2000; Millero et al., 2008) and, thus, does not require this rainwater dilution correction.

4.3.4 Silicon isotope analyses

Stream water samples were prepared for Si stable isotope analyses using a column chemistry modified from Van Den Boorn et al. (2006), Georg et al., (2006), and Pringle et al. (2014). Si purification was conducted by loading 10-20µg dissolved Si onto a pre-cleaned 1.8 mL BioRad AG50W-X12 cation-exchange resin bed in BioRad columns. Si was eluted by addition of 5mL MQ-e water for a target concentration of 1-2ppm (~ 9-18V). Approximately 70% of silicon is recuperated in the first elution step (2mL MQ-e) with the remaining 30% recovered in the final elution step (3 mL MQ-e). All silicon isotopic analyses were performed on a Thermo Finnigan Neptune Plus MC-ICP-MS at the Institut de Physique du Globe de Paris. Sample introduction was in the form of a wet plasma using a SIS (Standard Introduction System), double Scott/cyclonic spray chamber and a 100 µL min^{-1} Teflon® nebulizer. Measurements were run at medium resolution mode with a resolving power $M/\Delta M \sim 3300$ to reduce polyatomic interferences (notably the NO^+ interference on the ^{30}Si signal). To correct for instrument drift, a high-resolution peak centering was performed every hour to maintain a stable signal. Isotopic compositions are reported in standard per mil notation ($\delta^{30}Si$, $\delta^{29}Si$) based on blank-corrected ratios calculated through a standard bracketing method (**eqn. 4.2**) using the silica sand internal standard (NBS-28, RM 8546):

$$\delta^{30}Si = \left[\frac{\left({}^{30}Si/{}^{28}Si \right)_{sample}}{\left({}^{30}Si/{}^{28}Si \right)_{std\text{-}I}, \left({}^{30}Si/{}^{28}Si \right)_{std\text{-}II}} - 1 \right] \times 1000 \quad (4.2a)$$

$$\delta^{29}Si = \left[\frac{\left({}^{29}Si/{}^{28}Si \right)_{sample}}{\left({}^{29}Si/{}^{28}Si \right)_{std\text{-}I}, \left({}^{29}Si/{}^{28}Si \right)_{std\text{-}II}} - 1 \right] \times 1000 \quad (4.2b)$$

Where std-I and std-II correspond to the NBS-28 standard measured directly before and after the sample measurement. Repeated evaluation (n = 400) of the certified basalt standard BHVO-2 resulted in an appropriate value with long term precision of -0.31 ± 0.12 ‰. These results are consistent with previous measurements conducted at the IPGP facilities (-0.28 ± 0.09‰, 2σ). Mass dependent fractionation for all samples analyzed was verified using a three-isotope plot where $\delta^{29}Si = \delta^{30}Si \times 0.5088$**, $R^2 = 0.98$**.

Table 4.2 Storm event hydrological characteristics

Site	Duration	Seasonal context	Q_{max}	Q_{min}	Q_{avg}	$Q_{0.95}$[a]	$Q_{0.50}$[b]	$Q_{0.05}$[c]	q_{avg}[d]	q_{max}[e]	q^{*}[f]
	DD/MM/YY hh:mm		$m^3 s^{-1}$						mm day^{-1}		
Sapine	5 days (10/12-10/17, 16)	Dry → wet transition	0.054	4.26×10^{-4}	0.020	5.0×10^{-8}	1×10^{-5}	5×10^{-5}	3.23	8.35	2.72
La Jara creek	3 months (03/13-05/18, 17)	Snowmelt event	0.125	0.026	0.077	0.03	2.23	21.44	2.03	3.26	2.62
Elder creek	7 days (01/05-01/12, 17)	Wet season	33.70	1.34	6.31	0.51	11.44	45.75	37.2	163	34.0
Quiock creek	20 days (10/06-10/26, 17)	"wet", tropical storm season	0.030	1.50×10^{-4}	0.0028	3.04×10^{-6}	1.20×10^{-3}	0.01	2.08	26.6	17.1
Hakai (Watershed 708)	2 days (1) (09/16-09/19, 17) 7 days (2) (10/14-10/21, 17)	Dry → wet transition	0.61 (1) 5.34 (2)	0.18 (1) 0.15 (2)	0.33 (1) 1.47 (2)	3.0×10^{-3}	0.28	1.74	3.68 (1) 16.2 (2)	6.76 (1) 59.2 (2)	1.18 (1) 10.4 (2)
Providence creek (P303)	19 hrs (01/08 12:24-01/09 07:24, 18)	Wet season	0.35	0.0023	0.0071	1.8×10^{-4}	3.89×10^{-3}	0.052	1.34	2.22	2.88
Rio Icacos	6 hrs (05/28 11:00-05/28 17:24, 12)	"drier" season	2.52	0.43	0.90	1.28	19.35	43.3	39.0	64.5	0.11

a. low flow conditions for given year where flood event took place; $Q_{0.95}$ = low flow discharge exceeded 95% of the time.
b. median flow conditions for given year where flood event took place; $Q_{0.50}$ = median flow discharge exceeded 50% of the time.
c. high flow conditions for given year where flood event took place $Q_{0.05}$ = high flow discharge exceeded 5% of the time.
d. Average runoff for the given storm event calculated by normalizing the average discharge to the respective basin area (see **Table 4.1**).
e. Maximum runoff of the storm event determined by normalizing maximum discharge to the basin area (see **Table 4.1**).
f. Maximum runoff of the respective storm event (q_{max}) normalized to the mean annual runoff (see **Table 4.1**).

4.4 RESULTS/DISCUSSION

4.4.1 Flood events

Hydrographs (**Fig. 4.1A-G)** showing both rainfall and stream discharge through time for each storm event within the respective sites are presented and their hydrological characteristics are summarized in **Table 4.2**. Most of these storm events occurred within and at the start of the wet seasons for these catchments with the exceptions of La Jara (a snowmelt event) and Rio Icacos (within the drier period of the Caribbean year). Annual flow duration curves are provided as a comparison for the range in discharges observed in the given storm events (**Fig. 4.2**). For four of these flood events (La Jara, Elder Creek, Quiock, Creek, and Rio Icacos), the maximum event discharge value was higher than the annual high flow discharge at 5% exceedance, i.e. flow that is equaled or exceeded only 5% of the time ($\mathbf{Q_{0.05}}$, **Table 4.2**). As anticipated for significant precipitation events, mean runoff for each of our storms was generally higher than the mean annual runoff for these sites (**Table 4.1**). The most notable example is the Elder Creek storm event, which achieved a mean runoff 7.8x greater and a maximum runoff roughly 34x greater than the mean annual value (**Table 4.2**). The most muted example is the first of the two Hakai storm events in September 2016, when the mean runoff during the storm barely exceeded the mean annual value, and maximum runoff was only 1.2x greater.

The cumulative volume of water discharged in these storm events represents on average 3% of the total annual volume of water discharged by the respective streams. The Quiock Creek storm event comprised the largest fraction of total volume (11%), while the Rio Icacos event represents the smallest (~0.0003%). A cross-comparison of events shows that the cumulative volume discharged from the Elder Creek storm event is ~ 60x higher

than the average volume discharged from the events recorded in the other six sites. Though this metric is strongly biased by the duration of each storm event (e.g. the Rio Icacos storm was only approximately 6 hours long), the combination of cumulative volume fraction and magnitude of mean runoff indicate the relative intensity of each storm event within and across the catchments. In this regard, based on all the datasets included in this study, the Elder Creek storm event was the most extreme despite the fact that it was not the event which produced the largest cumulative volume fraction of runoff (9.5% of the annual cumulative discharge volume compared to 11% for Quiock Creek).

Concentration— and $\delta^{30}Si$—discharge relationships presented in the subsequent sections are reported using the storm event runoff (q in mm day^{-1}) normalized to the annual runoff (q_{annual}, **Table 4.1**) as shown below (**eqn. 4.3**):

$$q^* = \frac{q_{(t)}}{q_{annual}} \qquad (4.3)$$

where $q_{(t)}$ represents the runoff at time, t, during the storm event and q^* is the storm runoff normalized to the annual value. Presenting the runoff in this manner allows us to properly compare across catchments with respect to their relative storm intensities. Such accounting is necessary given that storm events represent extreme hydrologic episodes that greatly impact overall hydrochemical dynamics in a given catchment. Thus, having a standard method in which to characterize the relative intensity of the storm provides important context in which to interpret geochemical and isotopic data within and across sites.

All of the discharge timeseries hydrographs (**Fig. 4.1**) exhibit two peaks, where the first, generally lower magnitude peak is followed by a relatively larger and longer duration peak. This is a result of the fact that many of these hydrographs correspond with

several pulses of precipitation throughout the course of the timeseries. In other cases, such as La Jara where the hydrograph corresponds to a snow melt event, the double peaks in discharge arises despite little to no rainfall. The timing between the first and second discharge peaks can be fast, essentially overlapping, (as is the case for the Sapine flood event, **Fig. 4.1A**, spanning a timescale of 10 hrs) or slow, taking several days for the second peak to be observed (as is the case for Providence Creek, **Fig. 4.1F**, spanning a timescale of 2.5 days). The duration of some events, such as La Jara, took place over a couple of months (**Fig. 4.1B**) while others, such as Rio Icacos, only span a few hours (**Fig. 4.1G**). These differences are an inherent result of the unique characteristics of each location, for example the type of storm event (e.g. snowmelt vs. rainfall driven events), contributions from different sources of runoff (e.g. base flow vs. shallow subsurface flow), and the physical, critical zone structure of the respective catchment (deep vs. shallow regoliths, permeability and preferential flow paths, hillslope angles, and others).

From these observations, we find a wide variety of timing and forms in the hydrographs of these different storm events reflecting the variability and complexity of individual storm events and the unique drainage patterns of the individual catchments. Essentially, differences in fluid residence times and the input of multiple pulses of water (or melting events) to the system drive complex discharge responses. We now proceed in documenting how both water chemistry and $\delta^{30}Si$ vary over the course of these transient conditions and what relationships we can observe both within a given storm event time series and across these broad range of environments.

4.4.2 Atmospheric contributions to stream chemistry

Rainwater corrections (**eqn. 4.1**, **Section 4.3.3**) provide a means of distinction between water sources (rainwater vs. subsurface flow) and their relative impacts on the overall stream solute chemistry during a storm event. Based on these calculations we observe that that Na^+ is the most impacted by rainwater sources relative to the other major cations (K, Mg, Ca) across all sites (**Fig. E1**). Storm events for catchments within volcanic islands (Quiock Creek, Rio Icacos, Hakai) tend to have the largest contributions from rainwater, constituting an average 96% of the Na concentration in streams during the storm events. Quiock Creek's stream chemistry was generally the most impacted from rainwater where atmospheric input constituted effectively 100% of the dissolved Na^+ and Mg^{2+} values

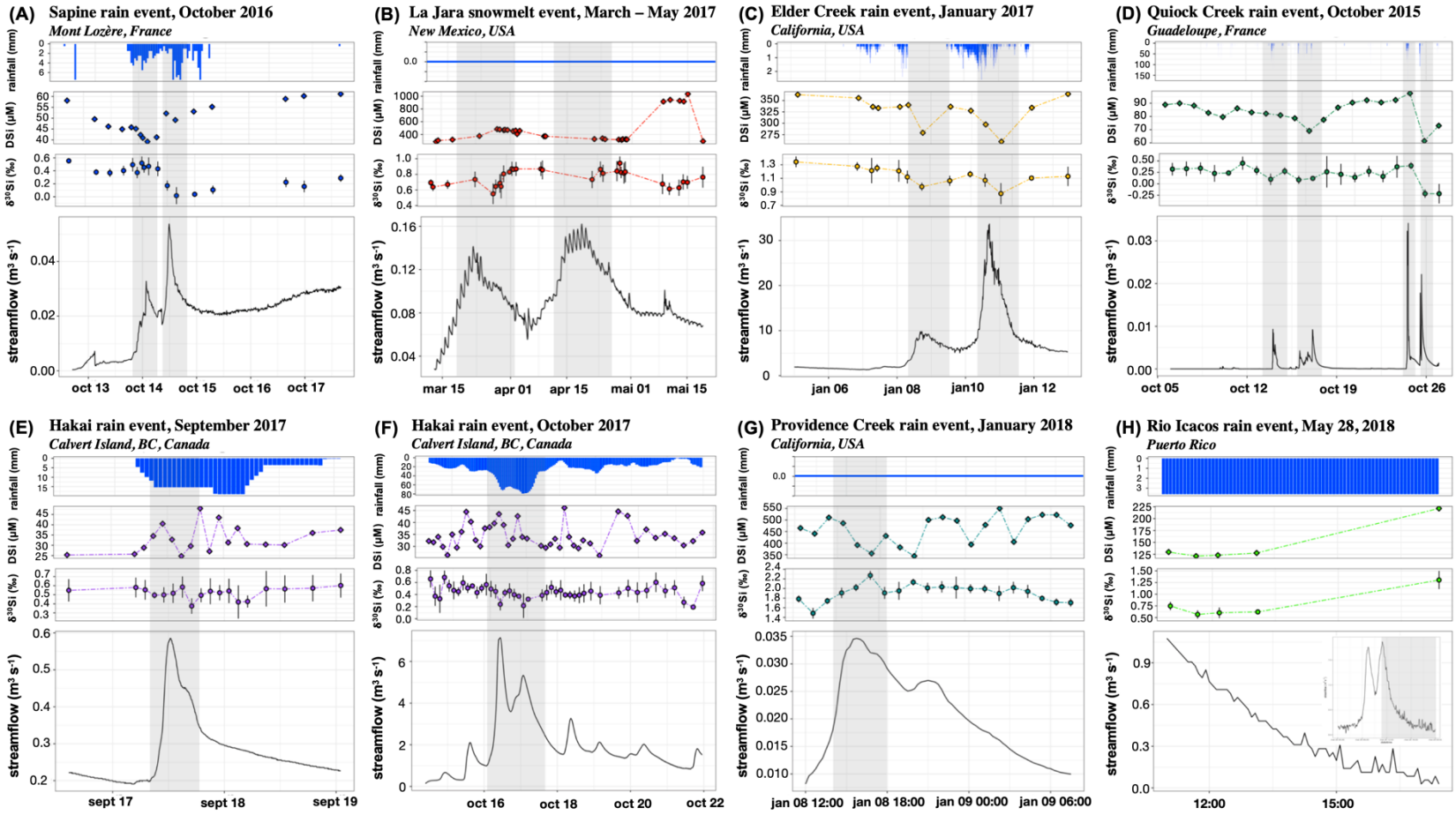

Figure 4.1 Storm event hydrographs

Storm event hydrographs for each catchment showing both discharge (streamflow) and rainfall intensity through time. From A to G, the sites are shown in the following order: (**A**) Sapine, (**B**) La Jara Creek, (**C**) Elder Creek, (**D**) Quiock Creek, (**E & F**) Haka watershed 708, (**G**), Providence Creek, and (**H**) Rio Icacos. Measured dissolved silicon (diamonds) and silicon stable isotope ratios (colored circles) are also provided as a function of time in the hydrographs. Grey shading represents major peaks in the hydrograph. Error bars correspond to 2 standard deviations. At the timescale an individual storm event, these dissolved silica concentrations and silicon isotope ratios are highly variable as a function of discharge.

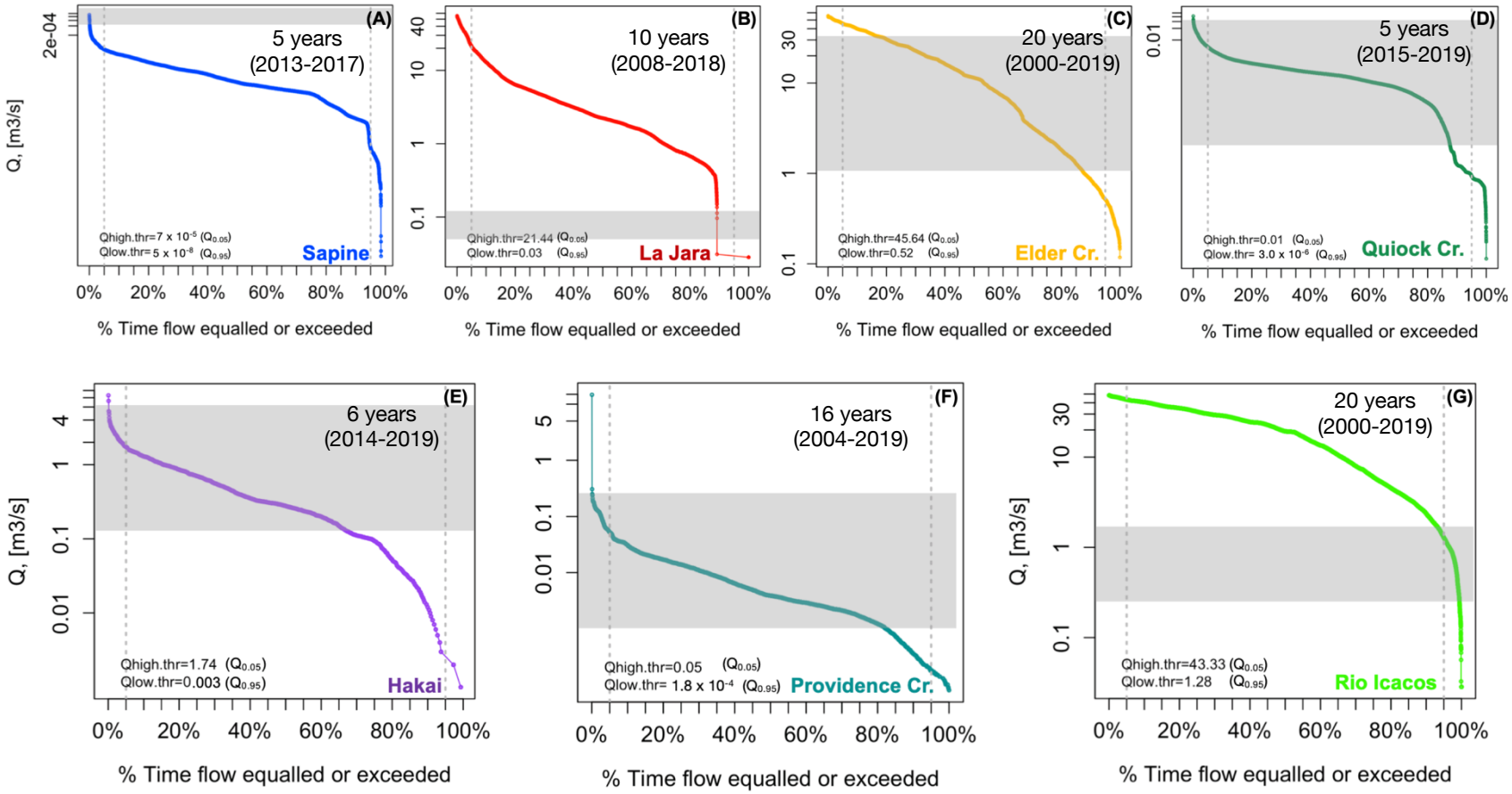

Figure 4.2 Flow duration curves

Flow duration curves calculated from a longer term (multi-annual), daily discharge timeseries that represents the flow conditions observed during the given year that the storm events took place. The length of the long term datasets used for each site is displayed on the respective plots (for instance, 20 years for collected daily discharge data for Rio Icacos; **G**).Grey dashed lined represent high and low discharge values that are exceeded 5% of the time ($Q_{0.05}$) and 95% of the time ($Q_{0.95}$) respectively for each site. Shaded grey areas reflect the range in discharge for the respective storm or snowmelt events.

(with an exception at peak discharge where rain accounted for only 96% and 99% of these ions, respectively), 95% of dissolved K^+, and 43% of dissolved Ca^{2+} (**Table E1**). The sites showing the least impact from direct precipitation input (only 2% of dissolved Na^+) where those situated farther inland and away from the influence of sea salt aerosols, notably the semi-arid La Jara catchment located approximately 800 km from the Gulf of California (the furthest inland respective to the other sites). From this analysis it is evident that proximity of the catchment to an ocean or sea will dictate the relative atmospheric contributions to the stream chemistry. Although outside the scope of this study, these results further emphasize the importance of atmospheric contributions to heavily depleted weathering zones common of most volcanic islands with large weathering fluxes (Gialson et al., 1996; Louvat and Allègre,1997; Dessert et al., 2003; Rad et al., 2006; Clergue et al., 2015).

Although dissolved silicon shows negligible sensitivity to atmospheric aerosols or rainwater dilution, we cannot rule out the possibility that contributions from aeolian dust transported via the atmosphere could be significant (Frings et al., 2016). This is particularly true for mid-latitude sites located within the westward trajectory of the Saharan dust plume (e.g. Quiock Creek and Rio Icacos) where total dust fluxes can span 170×10^6 (Pospero 1996a,b) to 760×10^6 tonnes yr^{-1} (Callot et al.(2000), respectively. In Guadeloupe and Rio Icacos alone, these fluxes are approximately 100 kg ha^{-1} yr^{-1} (Clergue et al., 2015) and 210 $\pm$ 70 kg ha^{-1} yr^{-1} (Pette-Ridge et al., 2009), respectively. The composition of Saharan dust (< 20μm) is composed principally of clays in the form of mica/illite (60% by weight) and to a small extent kaolinite (5%) with quartz comprising roughly 10% of the average mineralogy (Prospero et al., 1981). Based on dust dissolution batch experiments, the amount of dust that could dissolve and thus contribute to the

stream chemistry can range between 1–10% over relatively short timescales (hours to days) depending on the particle size, solution pH and attendant saturation state (Guerzoni et al., 1999; Frings et al., 2016). Thus, the potential for dust contributions to some solutes may be non-negligible to stream water chemistry in our Caribbean sites. Further, a recent study on the Quiock catchment based on Sr and Nd isotope results show that cation solute sources originate predominantly from atmospheric contributions as a result of a deep, depleted underlying regolith that has "lost contact" with the original bedrock (Dessert et al., 2020). These findings highlight the central role of atmospheric dust contributions to overall nutrient cycling in these highly weathered environments typical of the Caribbean islands. However, silicon dust fluxes have been notoriously difficult to constrain with only rough estimates of global mass balance (~0.5×10^{12} mol Si yr^{-1}) determined based on unconstrained dust deposition and dissolution rates (Tréguer et al., 1995; Laurelle et al., 2009; De La Rocha, 2013). Hence, we acknowledge that dust contributions may constitute a potential source to our stream solute chemistry, particularly for heavily depleted weathering systems such as Quiock Creek and Rio Icacos, but with little to no information available to support atmospheric dust corrections on stream dissolved Si concentrations, we proceed under the assumption that this pathways exerts a minor effect on our Si data.

4.4.3 Dissolved Si concentrations and isotope ratios event characteristics

Dissolved Si (referred to here as "DSi" following current notation, Frings et al., 2016) concentrations for all seven catchments (n = 168, **Table 4.3**) are highly variable, with an average value of 196 ± 192 (1SD) μmol L^{-1}. The overall range spans roughly two orders of magnitude from 25 (Hakai) to 1035 μmol L^{-1} (La Jara; **Fig. 4.3C, D**), which agrees with

the prior reported range of 20 to 1000 µmol L^{-1} observed on a global scale for both large and small rivers (Frings et al. 2016). Rain events with the tightest constrained range in dissolved Si concentrations were Hakai and Sapine, with differences between minimum and maximum values reflecting a change in DSi of ~23 μM and ~22μM, respectively. La Jara and Providence Creek events, which both involved large contributions from snowmelt, show the largest variability in dissolved Si concentrations, ~747 μM and ~206 μM respectively.

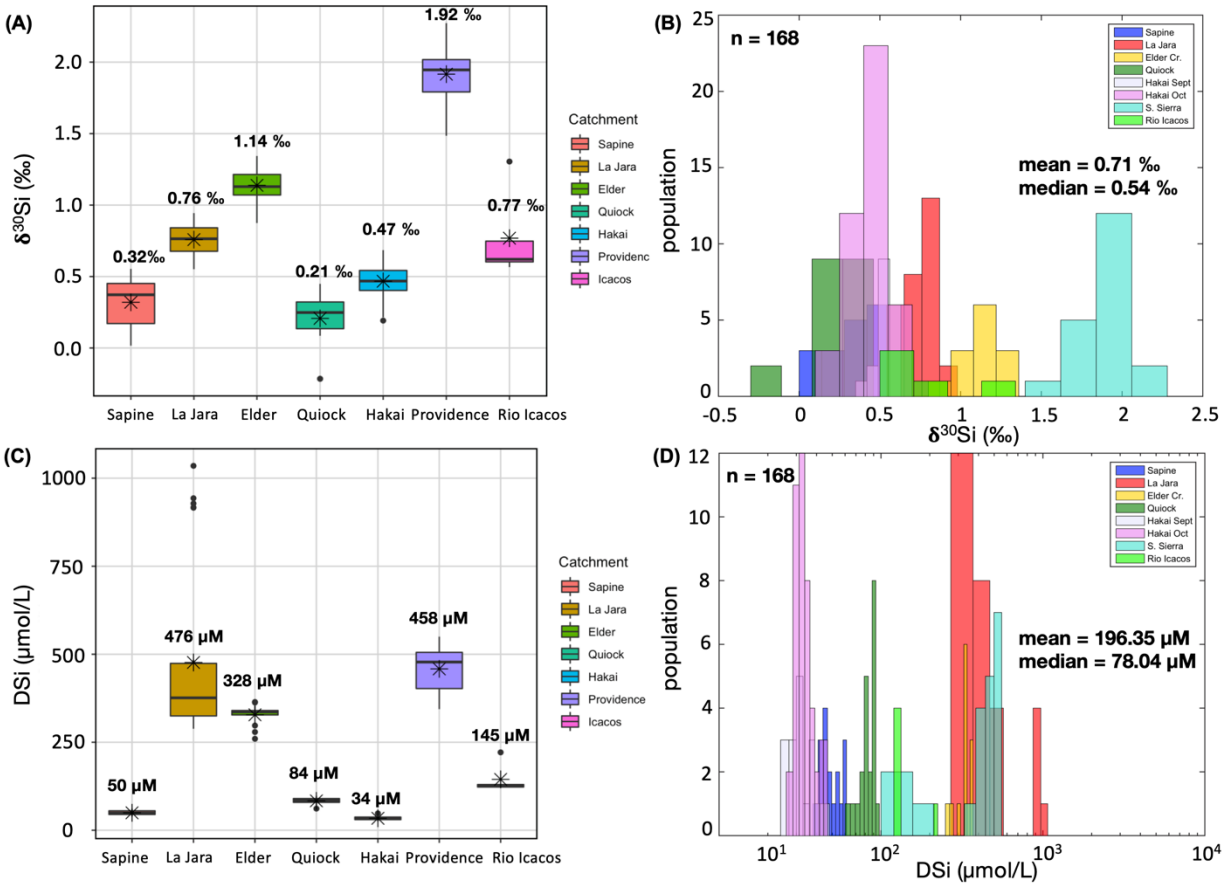

Figure 4.3 Box-and-Whisker plots and histograms of dissolved Si concentrations and δ^{30}Si
Box-and-whisker plots of dissolved Si concentrations and δ^{30}Si are provided for each given site and storm event (**A, C**) where numbers above each box represent the average value (which is equally marked with a star). Box lengths represent the variability in DSi and δ^{30}Si and black points represent outliers in the respective datasets for each site. Histograms are also provided for all sites and storm events, which are shown together with individual colors representing the respective sites (**B**, **D**). The mean and median values presented reflect the total dataset (all 168 samples analyzed). Silicon chemistry data is summarized in **Table 4.3**.

The dissolved $\delta^{30}Si$ for all catchments (n = 168, **Fig. 4.3A, B**) reflects a mean value of +0.71 ± 0.54 ‰ with the lowest measured value found in a Quiock Creek sample (-0.22 ± 0.12 ‰) and largest measured value found in a Providence Creek sample (+2.27 ± 0.09 ‰ (Providence Creek; **Table 4.3**). The dissolved load $\delta^{30}Si$ across all catchments is elevated in comparison to the reported $\delta^{30}Si$ of the average silicate bedrock value (-0.28 ± 0.15 ‰, Savage et al., 2013). The magnitude and variability observed across all catchments tends to generally fall within the reported global riverine $\delta^{30}Si$ range from -0.23 to +4.6 ‰ (Frings et al., 2016) though values do not reach as high as this upper limit. This is expected as the highest global riverine $\delta^{30}Si$ values recorded derive from large rivers (i.e. Yellow River in China or White Nile River in East Africa) draining lowland and highly irrigated regions (Ding et al., 2011; Cockerton et al., 2013). These large river basins drain areas on the order of several million square kilometers that include a multitude of watersheds and low order streams with generally diverse lithologies. At this scale, mixing of waters generated from various and widespread sources (from highland to lowland areas) and the residence time of the water as its transported over these vast distances is generally what dictates the signal of these large rivers. Thus, a major take-a-way point is that low order streams investigated in this study are overall less $\delta^{30}Si$ enriched relative to large rivers, which is what we expect in these smaller headwater catchments representing the inception of chemical weathering compared to the more chemically evolved large river basins.

The largest variability in dissolved $\delta^{30}Si$ over a given flood event was observed at Providence Creek (+1.48 ± 0.11 ‰ to 2.27 ± 0.09 ‰), while the smallest variation was

associated with La Jara Creek (+0.55 ± 0.13 ‰ to +0.94 ± 0.09 ‰). The average variability observed within each flood event (+0.61‰) falls within the overall annual global seasonal variability observed for a given location spanning low order streams to large rivers (~ +0.5 to 1.0 ‰, Frings et al., 2016). Thus, despite a narrower range in $\delta^{30}Si$, these headwater streams express similar seasonal variability to those observed in large rivers at a global scale.

Table 4.3 Storm event silicon chemistry characteristics

Statistics	Sapine (n = 17)	La Jara (n = 29)	Elder (n = 13)	Quiock (n = 20)	Hakai (n = 82)	Providence (n = 20)	Rio Icacos (n = 5)	All sites (n =168)
Dissolved silica (μmol/L)								
minimum	39.24	288.2	259.8	61.45	24.74	343.9	121.2	24.7
maximum	61.13	1035.0	364.4	97.53	47.94	549.9	221.3	1035
mean	49.61	476.5	327.9	83.57	34.00	458.4	144.6	196.35
median	49.16	376.1	336.1	84.60	32.97	477.8	127.7	78.04
1st quartile[a]	44.94	324.8	327.5	79.36	30.30	402.4	123.0	35.39
3rd quartile[b]	55.22	473.9	340.1	90.07	37.35	505.2	129.7	338.81
@ peak Q[c]	52.18	288.2	259.8	61.45	32.78 (1) 38.95 (2)	486.07	129.72	259.78
@ min Q[d]	58.10	328.3	362.9	89.94	25.71 (1) 32.23 (2)	464.96	221.28	83.08
$\delta^{30}Si$ (‰)								
minimum	0.02	0.55	0.87	-0.22	0.19	1.48	0.57	-0.22
maximum	0.55	0.94	1.34	0.45	0.68	2.27	1.30	2.27
mean	0.32	0.76	1.14	0.21	0.47	1.92	0.77	0.71
median	0.37	0.76	1.13	0.25	0.47	1.94	0.62	0.54
1st quartile[a]	0.17	0.68	1.07	0.14	0.40	1.79	0.60	0.39
3rd quartile[b]	0.55	0.84	1.21	0.32	0.54	2.02	0.75	0.84
@ peak Q[c]	0.17	0.73	0.87	-0.21	0.52 (1) 0.43 (2)	1.91	0.75	0.87
@ min Q[d]	0.55	0.69	1.34	0.33	0.58 (1) 0.66 (2)	1.78	1.30	0.29

a. 1st quartile indicates 25% of the observations lie below this value.
b. 3rd quartile indicates that 75% of the of the observations lie below this value.
c. Value of DSi (μM) or $\delta^{30}Si$ (‰) at **maximum** discharge during either the storm event at the respective catchment or across all sites (noted here as **All sites**).
d. Value of DSi (μM) or $\delta^{30}Si$ (‰) at minimum discharge during either the storm event at the respective catchment or across all sites (noted here as **All sites**).

4.4.4 Dissolved Si concentrations and isotope ratios within storm events

4.4.4.1 Observations

Dissolved Si and δ^{30}Si timeseries within each individual storm are distinct and reflect the diversity of hydrological and geological characteristics that define each catchment investigated in this study (**Fig. 4.1, Fig. 4.4**). The richness of these complex storm event datasets provides a rare opportunity to probe into the hydrogeochemical processes taking place within a catchment and how these processes evolve with time (i.e. during a wet vs dry season or at a transition between the two, snowmelt vs. rain).

Several trends can be observed when comparing across site-specific hydrographs (**Fig. 4.1**). For instance, both DSi and δ^{30}Si of the dissolved load tend to decrease along the ascending limb at peak discharge. This decrease in both DSi and δ^{30}Si can occur either simultaneously with peaks in discharge (as is observed for Sapine, Elder Creek, Quiock Creek, and Rio Icacos, (**Fig. 4.1A,C,D,H**) or offset (as is seen for La Jara and Providence Creek; **Fig. 4.1B,G)**. In storm events, the variability within the Si geochemical and isotopic datasets appear to reflect the complexity in the hydrograph structures, such as that observed for the Hakai October 2017 storm event where there are a multitude of peaks in discharge over a rather short period of time (**Fig. 4.1F**). However, even in simple hydrographs, like the Hakai September 2017 storm event (**Fig. 4.1E**), there can be quite a lot of complexity within the dissolved Si geochemical data. In most of these storm events characterized by two or more peaks in discharge, the general trend of decreasing DSi and δ^{30}Si as a function of increasing discharge is for the most part maintained between the peaks in discharge (as is shown clearly in the Elder Creek storm event, **Fig. 4.1C**).

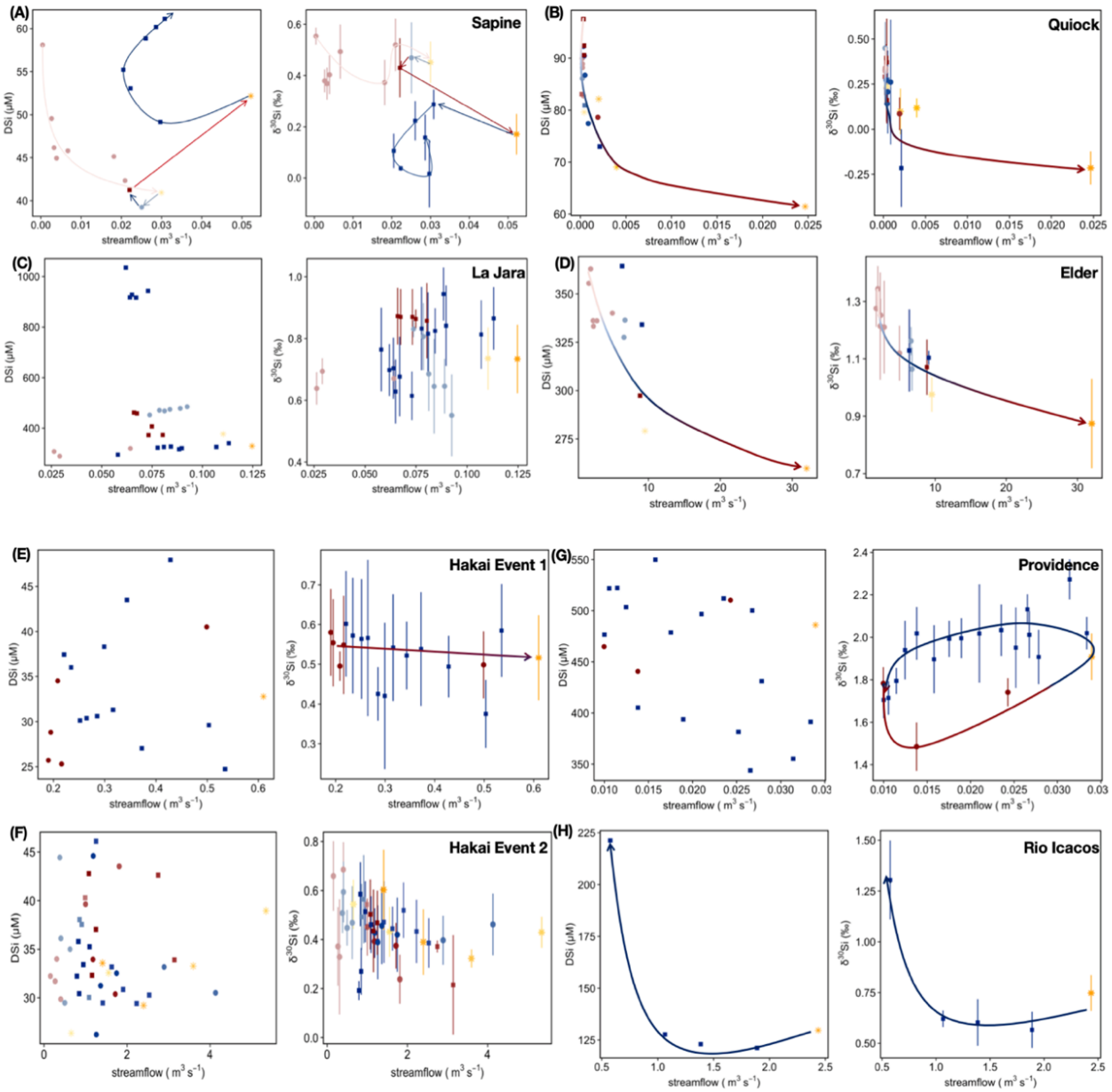

Figure 4.4 DSi (C) and δ^{30}Si(R) –discharge (Q) relationships within catchments

Dissolved silicon and δ^{30}Si vs. discharge (shown here as stream flow in units of $m^3\ s^{-1}$) relationships for each individual storm event. Filled red circles represent data from the ascending limbs of the hydrographs whereas blue filled squares represent that from the descending limbs of the hydrographs, respectively. Yellow stars represent the respective peaks in discharge throughout the course of the storm event. Gradients from light to darker colors represent peaks in the hydrograph from early in the timeseries to later periods in the timeseries, respectively. Arrows with gradients from red to blue (generally representing ascending to descending limb) reflect the overall path of the Si geochemical and isotopic data as a function of discharge throughout the duration of the storm event. Error bars correspond to 2 standard deviations. In general, silicon exhibits complex behavior with respect to discharge that does not correspond to the traditional hysteresis relationships observed in traditional monthly and seasonal datasets (Winnick et al. 2017).

The most notable case in which this general trend is not observed across peaks in the hydrograph is in the second discharge peak for Sapine where DSi increases while $\delta^{30}Si$ decreases along the descending limb (**Fig. 4.1A**). Additionally, storm event DSi and $\delta^{30}Si$ across these different catchments generally don't return to the baseline, antecedent conditions observed prior to the storm event. To better understand the complexity of these stream Si geochemical and stable isotope datasets and identify the sources behind these trends in DSi and $\delta^{30}Si$ within storm events, we need to look specifically at how silicon varies as a function of discharge through classic concentration(C)–discharge(Q) relationships and complementary stable isotope (R)–discharge relationships.

The classic view of Si – Q across sites (**Section 4.4**) masks an underlying relationship within each site which reminds us that this is a set of storm events and not monthly or seasonal signatures (as are more frequently encountered in the literature (Georg et al., 2006, 2007; Tipper et al., 2012; Hughes et al., 2013; Pokrovsky et al., 2013; Dellinger et al., 2015; Steinhoefel et al., 2017;Baronas et al., 2018; Riotte et al., 2019 and others). Prior studies have illustrated clear hysteresis in DSi on a seasonal scale (Winnick et al., 2015), but at the individual storm event scale (on the order of hours to weeks) such patterns are not systematically observed (**Fig. 4.4**). Instead, each site exhibits unique variability and relationships between C and Q that, in tandem with Si stable isotope environmental tracers, can provide crucial insight into the specific chemical and transport processes occurring within a watershed over such short event-response timescales (Floury et al., 2017).

4.4.4.2 Conceptual model

To better understand C–Q and R–Q trends observed within individual storm events (**Fig. 4.4**), we return to laboratory observations (such as those shown in **Chapter 2**) to derive expected correlations between DSi and δ^{30}Si. We begin with a perennial stream that hasn't seen a storm event for a long period of time. Before the storm event, the silicon chemistry and stable isotopes of the stream would represent the baseflow or groundwater that is consistently fed into the stream at a relatively constant rate throughout the course of the year. During these baseflow conditions, the groundwater discharge into the stream represents a longer fluid residence time sufficient to allow for the water to react with the surrounding porous media. Thus, the stream water is anticipated to have a more chemically evolved signature characterized by relatively elevated dissolved Si and δ^{30}Si that reflects a steady state between primary silicate dissolution and the formation of secondary silicates (i.e. clays, hydr(oxides), and amorphous silica). From these elevated dissolved Si and δ^{30}Si chemistry signatures defining the baseflow, there are three distinct scenarios under

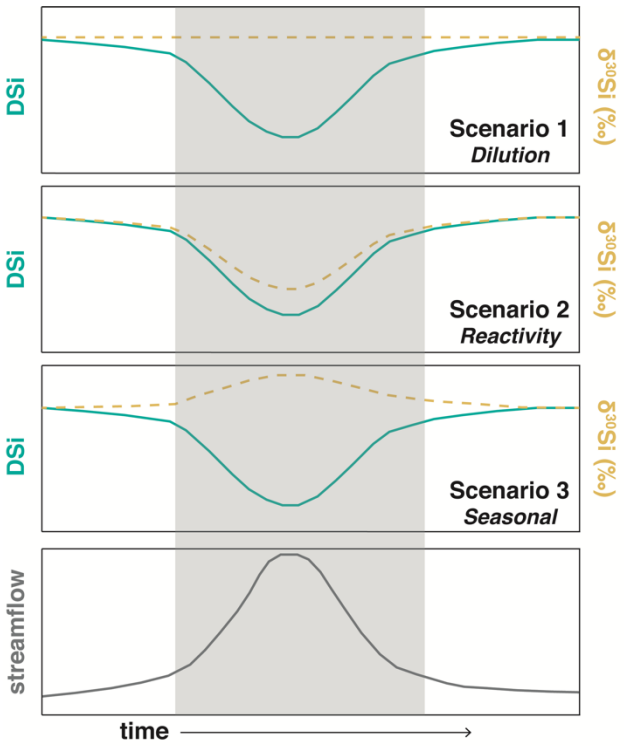

Figure 4.5 Conceptual diagram of DSi and δ^{30}Si variability as a function of discharge

An idealized hydrograph is presented outlining three scenarios for anticipated DSi (green solid line) and δ^{30}Si (yellow dashed line) behavior as a function of discharge. Further details on each of the Scenarios are discussed in **Section 4.4.4.2**.

which DSi and $\delta^{30}Si$ can evolve as a function of changes in discharge during a storm event (**Fig. 4.5)**.

In the first scenario, consider an observation in which DSi concentrations decrease as discharge increases through time while $\delta^{30}Si$ roughly remains unchanged. This scenario would occur under conditions in which only dilution taking place between fresh, unreacted event water mixing with the baseflow, groundwater. This type of behavior would be typically found in a catchment with weak infiltration (poor plumbing) where overland flow is the predominant contributor to the stream discharge during a storm event. In this case, fluid residence times are extremely fast to the point where the event water has no time to react. As a result, this unreacted runoff water dilutes the stream baseflow chemistry, yielding a decrease in DSi concentrations, but effectively unchanged baseflow $\delta^{30}Si$ signature. As stream discharge rebounds to pre-storm values at the end of the storm event, DSi concentrations will eventually recover to baseflow conditions and, thus, increase along the descending limb of the hydrograph.

In a second scenario, consider an observation in which an increase in discharge along the ascending limb of a hydrograph results in a drop in both DSi and $\delta^{30}Si$ that then slowly recovers back to baseflow values after peak discharge along the descending limb. This type of behavior is would be anticipated in catchments where infiltration rates are fast during a storm event and shallow subsurface water is perched in the soil and shallow regolith layers and rapidly released into the stream. Generally, this shallow subsurface "event" water has very quick fluid residence times and, thus, interacts with the porous media as it flushes through the system without reaching saturation and precipitation of secondary phases. This behavior produces a fluid of distinctly low DSi and $\delta^{30}Si$

signatures relative to baseflow. This "new", weakly reacted shallow groundwater mixes with the deep "older" baseflow as its discharged into the stream, driving stream Si concentrations and δ^{30}Si to lower values as a consequence. This is distinct to the dilution process described above which involves mixing of fresh, dilute event water without impacting Si stable isotopes. Thus, the drop in δ^{30}Si values anticipated in this scenario arises from a light δ^{30}Si source (like secondary clays or primary silicates) in the shallow subsurface that the "new", weakly acidic event water is able to quickly react with along its fluid pathway before ultimately being released into the stream. This would require relatively fast reaction rates (on the order of hours or days), which are generally supported by laboratory experiments for both primary silicate dissolution (Kennedy, 1971; Wels et al., 1991). After this drop in stream DSi and δ^{30}Si following a peak in discharge during a storm event, the Si chemistry is expected to slowly recover to baseline conditions, thus increasing with time as streamflow decreases back to pre-storm rates. The extent and timing of this rebound to pre-storm, baseflow conditions depends on how long this "new" shallow groundwater source is active and how much of this event water was mixed into the deep groundwater, baseflow source (Evans and Davies, 1998).

In a final scenario, let us consider any situation that involves an increase in δ^{30}Si as a function of discharge. This scenario requires specific climatic conditions in which seasonal precipitation follows a distinct alternating pattern between long periods of relatively dry and rainy conditions (over a timespan of several months). A Mediterranean climate is a perfect example of this type of seasonal variability, which several of the catchments investigated in this study reside within (Sapine, Eel River, and Providence Creek). Catchments residing in semi-arid climates that are driven by snowmelt driven

events (as is observed in La Jara) are another example. The storm event would need to take place at the transition between the dry and rainy periods where water left over from the previous rainy season or snowmelt event has had several months to become saturated with respect to secondary minerals and react within the system. The formation of secondary minerals would drive the chemical and isotopic signatures of these saturated, residual porewaters, making them more depleted in DSi and elevated in $\delta^{30}Si$ over the course of the dry season. The first storm event coming out of the dry season would then effectively flush this old, reacted porewater out of the system driving the stream $\delta^{30}Si$ up to higher values as a result. The extent to which the stream $\delta^{30}Si$ would increase as a function of discharge depends on the draining efficiency of the catchment or, in other words, how efficient the catchment is in flushing recently infiltrated event water into the stream. For instance, if the catchment has a poor draining efficiency, a greater portion of event water from the previous rainy season remains within the interstitial pores of the shallow subsurface and, thus, the stream receives a greater quantity of elevated $\delta^{30}Si$ porewater during the first storm event. Thus, in this final scenario, any increase in $\delta^{30}Si$ increase as a function of discharge reflects a combination of seasonal variability and plumbing characteristics of a given catchment.

From these scenarios we can now better interpret the behaviors observed in the storm events investigated in this study. For instance, situations in which both DSi and $\delta^{30}Si$ are observed to clearly decrease with increasing discharge are displayed in the Elder Creek (**Fig. 4.1C, Fig. 4.4B**) and Quiock Creek (**Fig. 4.1D, Fig. 4.4C**) events (**Scenario 2, Fig. 4.5**). In these particular storm events, the time for the "new" event fluid to move through the system is very rapid compared to the timescale of dissolution reactions and

certainly precipitation of secondary phases (**Chapter 2**). Thus, these systems can be considered to be "dissolution-limited" or, in other words, concentrations are limited by the rate at which primary minerals can dissolve (Hornberger et al., 2001). For Elder Creek, which was a particularly exceptional storm event (called an "atmospheric river") $\delta^{30}Si$ dropped by ~38μM and ~0.20‰, respectively, over the course of ~9 hours implying very fast fluid residence times (minutes to a couple of hours) compared to the timescales of a given reaction. On the other hand, the Quiock Creek storm event displayed a similar drop in DSi to that observed for Elder Creek (~36 μM) and a more significant decrease in $\delta^{30}Si$ (~0.61 ‰) over a period of ~ 1 day. Thus, the chemical signature of the "new" event water flushing into the stream is predominantly kinetic, reflecting early stages of the reaction where dissolution rates are rapid and secondary minerals have not reached saturation yet (see **Chapter 2**).

A storm event that suggests a dilution scenario can be suggested by Sapine (**Fig. 4.1A, Fig. 4.4A**) where in the first peak in discharge, DSi concentrations are observed to decrease at the same time that changes in $\delta^{30}Si$ remain relatively minor. This indicates that in the first portion of the storm event, "new" event water contributing to Sapine has very fast fluid residence times and only minimal weathering reactions took place (**Scenario 1**). Further, since this storm event was the first coming out of the dry season, small changes in the $\delta^{30}Si$ along the ascending limb of the first hydrograph could reflect the "flushing" out of residual "old" porewater within the shallow subsurface left over from the previous rainy season and continued to react throughout the course of the dry season (**Scenario 3, Fig. 4.5**). However, in the second peak in the hydrograph, DSi and $\delta^{30}Si$ completely change behavior, with DSi increasing and $\delta^{30}Si$ decreasing as a function

of discharge. This inverse relationship between DSi and δ^{30}Si could represent the replenishment of groundwater with younger precipitation, causing the baseflow source to reflect an increase in contribution from primary silicate dissolution.

Snowmelt driven events like that shown clearly for La Jara (**Fig. 4.1B, Fig. 4.4C**) reflect DSi and δ^{30}Si behavior representative of the final, third scenario (**Fig. 4.5, Scenario 3**) discussed above where fluid residence times are long and event fluid draining into the stream is chemically evolved. Unlike the other storm events investigated, the La Jara snowmelt event takes place over a couple of months (from March to May), with peaks in discharge taking place over a period of a couple of weeks, rather than a couple of hours (as is the case for Elder Creek). Overall, DSi is generally observed to slightly decrease as a function of discharge whereas δ^{30}Si generally increases with increasing discharge. This relationship between DSi and δ^{30}Si could reflect this interplay between fast secondary silicate formation kinetics relative to primary silicate dissolution, which dominates the La Jara stream chemical signature for most of the event. Interestingly, near the end of the snowmelt event a drastic increase in DSi and a minor decrease in δ^{30}Si is observed, though this falls outside of any of our identified hydrograph events.

Only a few of the storm events analyzed are highlighted in this section. The remaining storm events exhibit very complex DSi and δ^{30}Si behavior as a function of discharge that makes it challenging to interpret. These storm events remind us that there are still a variety of hydrogeochemical processes and the interplay between fluid residence times and weathering reactions that we still don't yet fully understand. However, despite these limitations, there is strong evidence to suggest that using C–Q

and R–Q relationships in tandem can provide important information on solute generation and transport in a given catchment during storm events.

4.4.5 Dissolved Si concentrations and isotope ratios as a function of discharge across sites

Large variability is observed in both DSi and associated Si stable isotope ratios between locations, but also at some sites within a given flood event, as for example in the La Jara timeseries (**Fig. 4.1B**). Weighted averages are reported for both DSi ($\overline{\mathbf{DSi}}$) and δ^{30}Si ($\overline{\boldsymbol{\delta^{30}\mathbf{Si}}}$) reflecting a flux weighted average concentration, thus adjusting raw average values closer to the measurements observed at peak discharge (**eq. 4.4**)

$$\overline{[E]} = \frac{\sum q_{(t)} \times [E]_{meas,t}}{\sum q_{(t)}} \qquad (4.4)$$

where q_t is the measured stream runoff as a function of time (t) through the course of the event, $[E]_{meas,t}$ represents the elemental concentration or dissolved Si stable isotope ratio

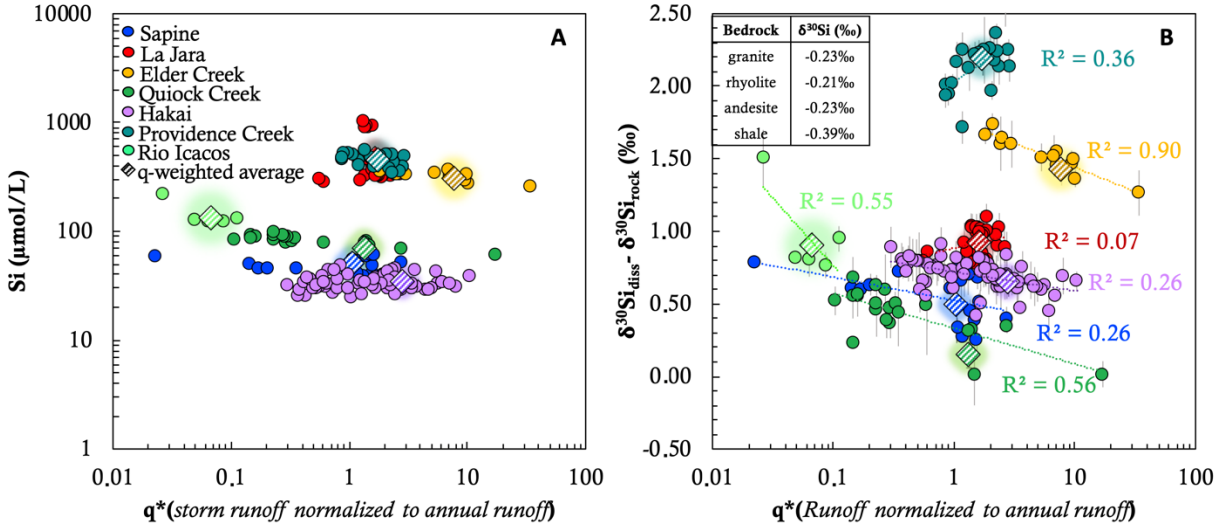

Figure 4.6 Stream DSi vs. δ^{30}Si as a function of discharge across sites
Dissolved Si and stream $\boldsymbol{\delta^{30}}$Si corrected for the bedrock as a function of event runoff normalized to the annual discharge (**see eqn. 4**). The bedrock values used in the correction are shown in **B** that, other than the shale value in which the Elder Creek shale bedrock was directly measured, come from the following references: Granite (Savage et al., 2012; Ziegler et al., 2005), rhyolite (Savage et al., 2011), and andesite (Opfergelt et al., 2012). Error bars repesent two standard deviation (95th percentile).

measured at the given sampling time (t), and $\overline{[E]}$ represents the discharge weighted mean. This approach was adopted as a way to compare the relative intensities in the solute fluxes between storm events. The discharge weighted average DSi concentration for all catchments (187 ± 178 μmol L^{-1}, 1SD) is slightly higher than the global riverine DSi average of approx. 160 μmol L^{-1} (Dürr et al., 2011). Between catchments, La Jara Creek shows the highest weighted mean DSi (464 ± 229 μmol L^{-1}, 1SD) and largest variability (288 to 1035 μmol L^{-1}), whereas the Hakai flood event shows the least variability and lowest weighted mean DSi concentrations (33.8 ± 0.63 μmol L^{-1}, 1SD). The overall discharge weighted mean the stream $\delta^{30}Si$ across all catchments was 0.70 ± 0.61 ‰.

Across all catchments, there is no single systematic relationship observed between DSi and the corresponding Si stable isotope ratios with discharge. Silicon concentration with respect to discharge normalized to the basin area (mm day^{-1}) follow power—law slopes between +/- 0.20 (**Table 4.4**) indicating chemostatic behavior (Godsey et al., 2009; Herndon et al., 2015; Li et al., 2017) despite 3 order of magnitude changes in discharge (**Fig. 4.6A**). One exception is Rio Icacos where some dilution is observed. When discharge is normalized to the annual runoff (**eqn. 4.3**, **Table E.2)** to account for the intensity of these storm events, stream $\delta^{30}Si$ vs. discharge relationships between catchments appear to be scattered with no clear trend established across the weighted average values of the given storm events (**Fig. 4.6B**). Stream $\delta^{30}Si$ in this case is corrected for the respective lithology of the given catchment which range from granite to shale. Literature values were used to describe the $\delta^{30}Si$ of the local bedrock (**Table E.2, Fig. 4.6B**), with the shale bedrock value being the only exception (Elder Creek shale bedrock was measured

directly). This approach in the use of literature values for the catchments draining a volcanic lithology is, in this case, reasonable considering the tight range in granitoids and upper continental crust (UCC) $\delta^{30}Si$ values (Savage et al., 2012, 2013). Within a given catchment and storm event, a generally negative correlation is observed with the highest stream $\delta^{30}Si$ at low discharge and vice versa at high discharge. The only exceptions where this negative correlation is not well established is for La Jara and Providence Creek. The relationship between $\delta^{30}Si$ vs. discharge is less clear in these sites due to larger variability in the data, but generally follow a trend inverse to the rest of the catchments where at low discharge, stream $\delta^{30}Si$ are low and vice versa at high discharge. Notably, these two catchments have important similarities that might be a reason for these observed differences. Particularly, La Jara and Providence Creek are catchments in which snowmelt plays an active role in the hydrology of their systems. Further, both catchments have the lowest mean annual precipitation (670 mm and 1015 mm respectively, **Table 4.1**) out of the seven catchments investigated. These commonalities suggest that La Jara and Providence Creek might possibly share comparable subsurface hydrological mechanisms and sources of water to their stream outlets that are distinct from the other sites, despite the fact that Providence Creek exhibits very high values of measured stream $\delta^{30}Si$.

Table 4.4 Power – law relationships between DSi and discharge ($C = aQ^b$)

Site	a values	b values
Sapine	183092	-0.021
La Jara creek	526.64	-0.043
Elder creek	380.38	-0.093
Quiock creek	47.504	-0.076
Hakai (Watershed 708)	36.242 (1)	+ 0.135 (1)
	34.057 (2)	-0.121 (2)
Providence creek (P303)	259.65	-0.141
Rio Icacos	155,5	-0.374

4.4.6 Stream δ^{30}Si and dissolved Si concentrations relationships <u>across sites</u>

A significant finding arising out of these storm events is the existence of a positive correlation is observed in dissolved δ^{30}Si vs. log DSi (**Fig. 4.7A**) across all 7 sites (R^2 = 0.82). Within this positive relationship three distinct clusters of data that can be defined based on statistical cluster analyses (**Fig. 4.7B, C**). Based on the results from the cluster analysis, the clusters identified represent regions of low, medium, and high DSi and δ^{30}Si (**Fig. 7B**).

These three distinct clusters can be interpreted as potentially reflecting the relative weathering intensity of the given catchments. In this weathering intensity context, catchments lying principally in the low DSi, low δ^{30}Si cluster (Hakai and Sapine) represent low chemical weathering intensity environments where the dissolved silicon chemistry reflects greater contributions from primary mineral dissolution as compared to secondary mineral formation and fluid residence times in the subsurface are relatively fast. Catchments residing in the high DSi, high δ^{30}Si cluster (Providence Creek, Elder Creek, and La Jara), reflect a potentially intermediate intensity chemical weathering style characterized by significant contributions from secondary mineral formation (i.e. high incongruent weathering) and longer fluid residence times sufficient for primary mineral

dissolution to reach a relative steady state that favors the formation of secondary silicates. Finally, catchments within the intermediate DSi and low to intermediate $\delta^{30}Si$ cluster (Rio Icacos and Quiock Creek) could represent more extensive weathering or a high intensity chemical weathering style defined by an interplay between secondary mineral

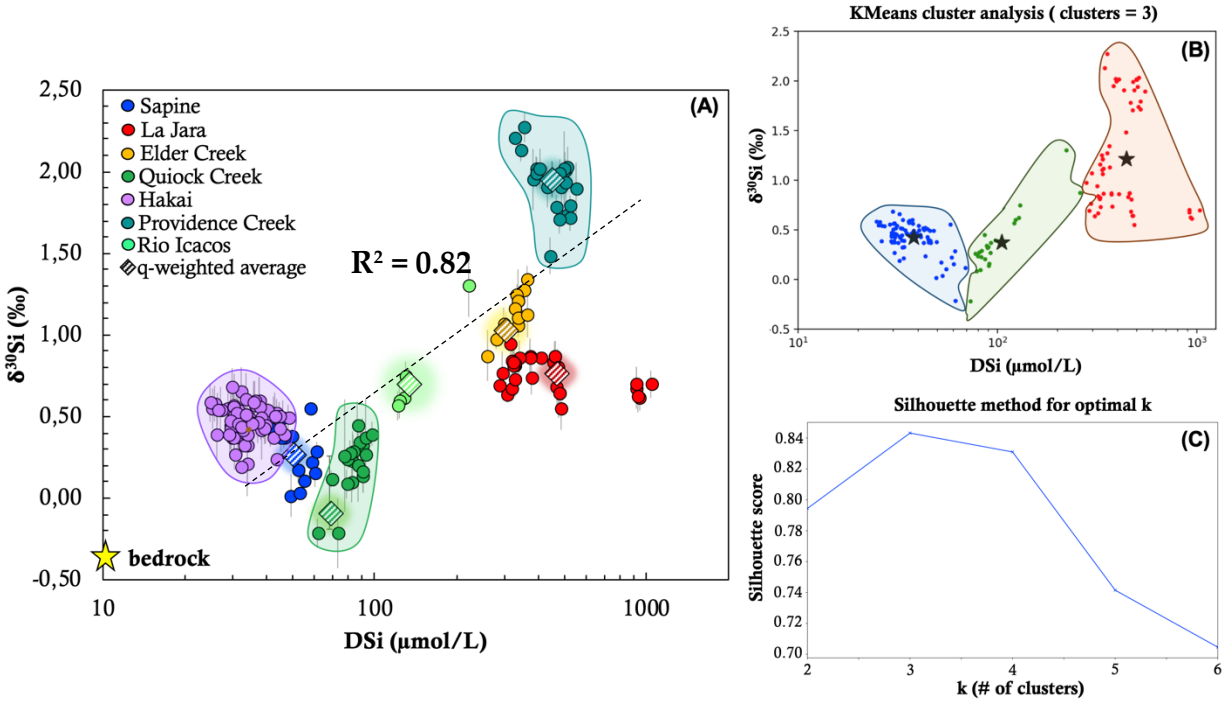

Figure 4.7 Stream $\delta^{30}Si$ vs. DSi across sites

Stream "^{30}Si plotted against dissolved Si (DSi) concentrations across catchments. (**A**)A positive relationship is observed between "^{30}Si and DSi (R^2 = 0.46) where Hakai and Quiock Creek represent the low DSi, low "^{30}Si endmember and Providence Creek represents the high DSi, high "^{30}Si endmember. Three endmembers are proposed: (1) Hakai, which we hypothesize to represent a congruent weathering endmember, (2) Providence Creek which we propose represents an incongruent endmember, and (3) Quiock, which could be representative of a biological or vegetation-controlled endmember. This grouping between low, medium, and high congruent weathering endmembers is further supported by a statistical cluster analysis of the data using a K-means cluster approach where three general groupings of the data were identified (**B**). The KMeans method involves identifying a specific number of clusters (k) and then assigning each datapoint to the nearest cluster based on its "Euclidian distance" (i.e. the straight-line distance between two points). The optimal number of clusters (k) to properly describe this dataset was determined to be 3 based on the silhouette score (**C**), which ranges from -1 (data assigned to wrong cluster) to +1 (data assigned to correct cluster). Thus, the higher the silhouette score the better the given number of clusters are in grouping the data (further details can be found in **Appendix E, Fig. E.2**).

dissolution and formation as a result of thick overlying soils and regolith layers limiting access to fresh primary mineral sources.

Further, based on geographic and a-priori knowledge of the distinct catchments (**Section 4.2**), we can probe deeper into the statistically identified clusters in the DSi vs $\delta^{30}Si$ dataset and identify catchments that represent distinct weathering intensity endmembers. In the high DSi and $\delta^{30}Si$ cluster, Providence Creek is identified as an intermediate intensity endmember where the stream chemistry is driven mostly by deep, long residence time, groundwater input (Aguirre, 2018) resulting in substantial secondary mineral formation and significantly more elevated dissolved $\delta^{30}Si$ values. Within the low DSi and low $\delta^{30}Si$ values, Hakai, with almost ubiquitously uniform DSi concentrations and $\delta^{30}Si$ close to the bedrock, is the closest approximation to a congruent, low chemical weathering intensity endmember. Finally, within the intermediate cluster with intermediate to low $\delta^{30}Si$ values that is defined principally by catchments residing in tropical, Caribbean climates (Rio Icacos in Puerto Rico and Quiock Creek in Guadeloupe) defined by deep, heavily depleted soils, Quiock Creek represents the high weathering intensity endmember. Characterized by greater than 15m thick (Clergue et al., 2015) and secondary mineral enriched (constituting ~95% of bulk soil, Buss et al., 2010), Quiock Creek catchment is a notably silicon depleted and intensively weathered system. The notably sharp decrease in both DSi and $\delta^{30}Si$ at peak discharge observed in the Quiock storm event (**Fig 4.1D**), is representative of substantial secondary mineral re-dissolution (as has been suggested for the Basse-Terre and Quiock Creek by Clergue et al., 2015 and Dessert et al., 2020) or associated phytolith dissolution (Ziegler et al., 2005; Cardinal et al., 2010; Hughes et al., 2013).

Thus, to summarize the positive relationship observed between DSi and δ^{30}Si is significant in that it is universally consistent across all 7 catchments, even based on data reflecting response to individual storm events, and is broadly consistent with the three end-member weathering regimes suggested by the background (e.g. non-event) isotopic patterns of weathering signatures in rivers (Opfergelt et al., 2012; Delinger et al., 2015; Frings et al., 2016). To further unravel the factors contributing to the linear relationship between DSi and δ^{30}Si and the statistically and geographically identified clusters in the data we will now begin to look at various potential controls on dissolved silicon chemistry and stable isotopes.

4.4.7 Characterizing observed event δ^{30}Si through Rayleigh Distillation

As a first order test of the underlying factors contributing to this observed relationship, we apply a simple Rayleigh distillation batch model $\left(\delta^{30}Si_{diss} = \delta^{30}Si_0 + \Delta_{sec-diss} \times ln\left(f_{diss}^{Si}\right)\right)$ to our dataset to determine whether fractionating processes such as mineral precipitation, plant uptake, or adsorption can be described by a constant collective fractionation factor which adequately reproduces the variability observed within and between the given sites (**Fig. 4.8**). The fractionation of dissolved Si remaining in solution (f_{diss}^{Si}) was calculated by normalizing the measured Si/Na* ratio of the stream water to the bedrock Si/Na ratios (granitoids: 15.47, Brichau et al., 2008 ; shale: 11.0, Stallard 1980). Assuming that Na is conservative in the dissolved phase, a f_{diss}^{Si} is greater than 1 this indicates an excess of dissolved silicon relative to the amount derived from dissolution of the bedrock. This scenario would imply that another source outside primary mineral dissolution and atmospheric/rainwater input is contributing to the dissolved Si load, which is not observed for any of the catchments. On

the other hand, a f_{diss}^{Si} value less than 1 indicates that silicon is being scavenged from secondary weathering processes (Delinger et al., 2015) and this is what is ubiquitously observed for our sites. The initial dissolved silicon isotopic composition ($\delta^{30}Si_0$) for simplicity was set equal to the average bedrock signature assuming an initial solution that reflects only bedrock dissolution. The fractionation factor chosen in such a simple

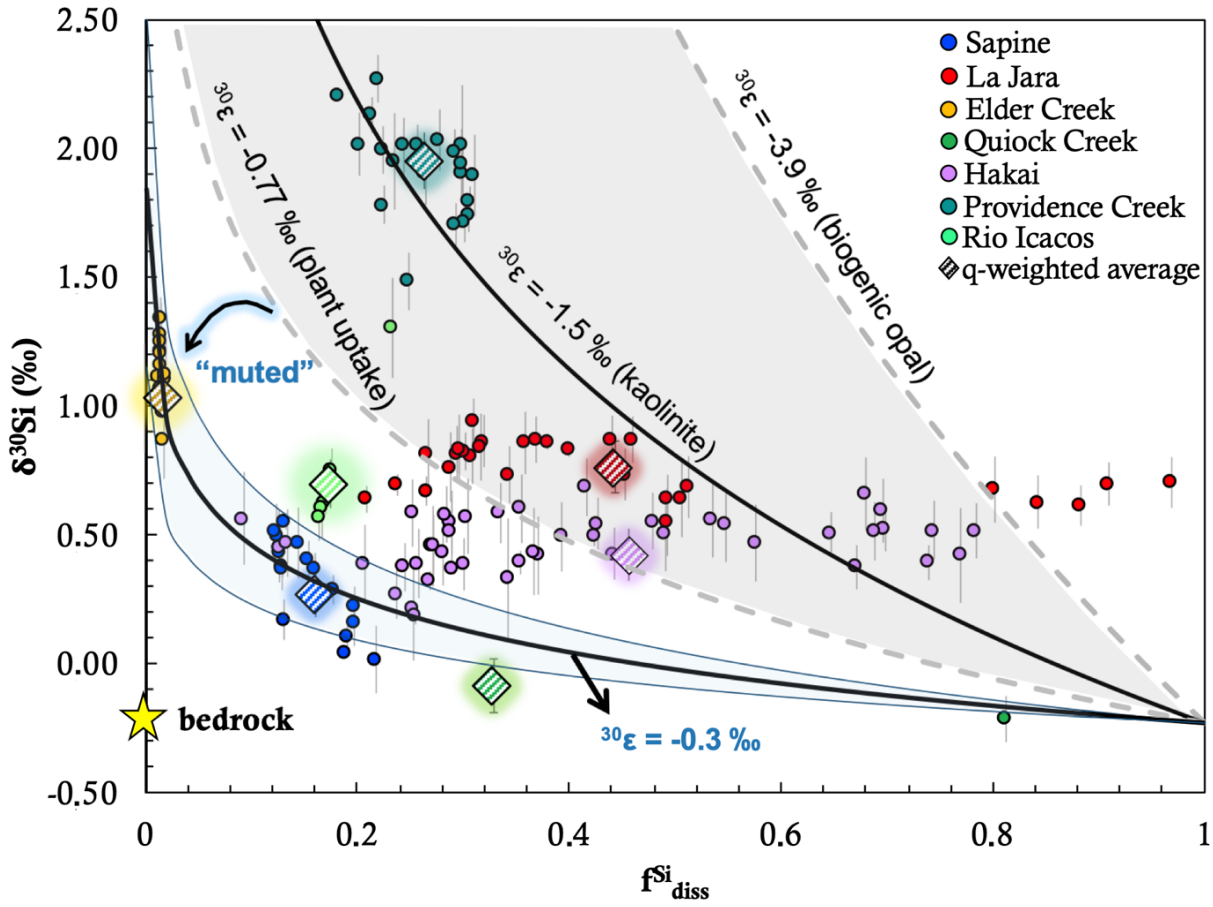

Figure 4.8 Rayleigh distillation model

Rayleigh distillation model predictions using a range of secondary mineral fractionation factors (shown here in grey)spanning $^{30}\varepsilon$ of -3.9‰ (biogenic opal; Ziegler et al., 2005) to -1.5‰ (kaolinite: Ziegler et al., 2005; George et al., 2007; Méheut et al., 2007) and -0.77‰ (biological uptake, Opfergelt et al., 2006). Rayleigh predictions for a "muted" or "diminished" fractionation factor as a result of dilution is shaded here in blue. The range in the muted fractionation factors shown here (-0.4‰ to -0.2 ‰, with an average of -0.3 ‰) was determined based on a "best-fit" approach. Notably, Providence Creek storm event is well characterized by a Rayleigh model for kaolinite formation whereas Elder Creek, Sapine, Rio Icacos, and Guadeloupe fall within the range predicted with a muted fractionation factor. The fraction of dissolved Si is calculating by the Li/Na* ratios of the stream water normalized to the bedrock ratio.

Rayleigh distillation model could span a range of secondary processes known to occur in a natural weathering environment from biogenic opal precipitation (-3.9 ‰, Ziegler et al., 2005) to abiotic amorphous silica precipitation (-2.67 ‰, average value from Geilert et al., 2014, Roerdink et al., 2015, Fernandez et al., 2019) to kaolinite formation (-1.5 ‰, Ziegler et al., 2005; Georg et al., 2007; Méheut et al., 2007) to Si adsorption onto Fe-oxides (-1.08 ‰, Delstanche et al., 2009) to plant uptake (-0.77 ‰, Opfergelt et al., 2006). Despite this broad range of possible parameter values, application of these multiple Rayleigh fractionation models generally fails to capture the variability observed in the stream waters during these storm events. The only possible exception that could be made is for the Providence Creek storm event where the corresponding stream δ^{30}Si appear to fall on the Rayleigh model curve assuming strictly kaolinite precipitation. La Jara and Hakai appear to fall across the entire range of fraction Si remaining in solution without any appreciable shift in the isotope ratios. Sapine, Quiock Creek, Elder Creek, and Rio Icacos fall well outside the predicted range of values but do appear to generally demonstrate enrichment as a function of silicon loss following a muted or dampened apparent fractionation factor of -0.2 ± 0.1‰. Diminished apparent fractionation factors are common in natural environments and are attributed to transport limitations arising from fluid mixing, which can affect observed stable isotope fractionation (Abe and Hunkeler, 2006; Green et al., 2010; Eckert et al., 2012). Fluid mixing in this case refers to perhaps older, reacted fluid mixing and being diluted with younger and less reacted fluid resulting in a diminishment in the overall fractionation factor. A major point to clarify here is that mixing itself does not fractionate stable isotopes, what it does is combine the signals derived from a multitude of other fluid pathways in the system (Druhan et al., 2017). Thus, what appears to be a deviation from the Rayleigh model predictions using

intrinsic fractionation factors established for a variety of secondary silicate weathering reactions is, in fact, just a result of older, groundwater being diluted by younger, less reacted water resulting in a muted observed fractionation factor. A considerable implication arising from this condition is that Elder Creek, Sapine, Quiock Creek, and Rio Icacos could perhaps be controlled by similar transport limitations.

In general, Rayleigh distillation does not appear to adequately describe the underlying range of process generating the observed fractionation within and across the given sites and storm events, which supports arguments that have been put forth in the literature for silicon isotope systematics (Fernandez et al., 2019). This is particularly true for La Jara and Hakai storm events that exhibit no real Rayleigh behavior. For Hakai, this further supports our hypothesis that stream $\delta^{30}Si$ are mostly generated via congruent weathering of the bedrock. Yet, within given storm events there does appear to be certain datasets that do show some tendency for isotopic enrichment along a common fractionating pathway. This tendency is evident among the Elder Creek, Sapine, Quiock Creek, and Rio Icacos storm datasets that exhibit similar fractionation behavior despite "muted" or "diminished" $\delta^{30}Si$ signals as a result of transport limitations. Providence Creek remains a significant outlier in this dataset and is the only storm event that appears to have a distinct Si stable isotope enrichment pathway that is best matched by a Rayleigh model assuming kaolinite formation. Although kaolinite formation may not be the principal fractionation mechanism for observed Providence Creek $\delta^{30}Si$, it is clear that the stream water is heavily fractionated and most likely driven by the formation of secondary silicates phases. These results also provide further evidence in support of Providence Creek being an incongruent endmember in this large-scale dataset based on stream $\delta^{30}Si$

vs. DSi relationships (**Fig. 4.7**). Based on this Rayleigh distillation model application, we can already start to extract certain important take-a-ways with the most notable being that each storm event reflects stream $\delta^{30}Si$ behavior that is distinct for each individual catchment. To continue our analysis and interpretation of the positive relationship between $\delta^{30}Si$ and DSi observed across catchments, we next explore the potential range of mechanisms that could give rise to this notable finding.

4.4.8 Lithological control on stream $\delta^{30}Si$

When the stream $\delta^{30}Si$ values are corrected for the corresponding bedrock composition ($\delta^{30}Si_{diss} - \delta^{30}Si_{bedrock}$, Bouchez et al., 2013), we see that differences between catchments and storm events as a function of normalized discharge are effectively unchanged (**Fig. 4.6B**). This implies that bedrock lithology exerts a minimal influence on the overall riverine $\delta^{30}Si$ signatures. Observed fractionation factors ($\Delta_{diss\text{-}rock}$) show wide variability across all catchments ranging from 0.02 ‰ (Quiock Creek) to 2.36 ‰ (Providence Creek) and even within each given storm event (e.g. 0.02 ‰ to 0.68 ‰ for the Quiock storm event) reflecting a balance between hydrologic and chemical controls. Thus, these data suggest that it is the critical zone structure and geochemical functioning from infiltration to discharge, rather than parent lithology, that ultimately governs the expression of the $\delta^{30}Si$ signature in small, first and second order catchments. We will explore this balance between transport and chemical processes in greater detail in the subsequent discussion.

As a final check of lithologic influences, we explore the relationship between dissolved $\delta^{30}Si$ and the proportion of carbonate to silicate weathering influencing the DSi load. This is done using several lithological proxies such as the Ca*/Si, (Mg/Na)* and (Ca/Na)* elemental ratios (**Fig. 4.9**). Stream Ca^*/Si values measured in this study fall well within the range characterizing silicate rocks (~ 0.2 – 10, Gaillardet et al., 1999) and, thus, are predominantly controlled by silicate weathering (**Fig. 4.9A**). A weak positive trend can be observed between the stream $\delta^{30}Si$ and Ca^*/Si ratios across catchments with Quiock being the Ca depleted endmember at very low stream $\delta^{30}Si$ values and Elder Creek as the more Ca enriched endmember. This covariation suggests a stream $\delta^{30}Si$ that

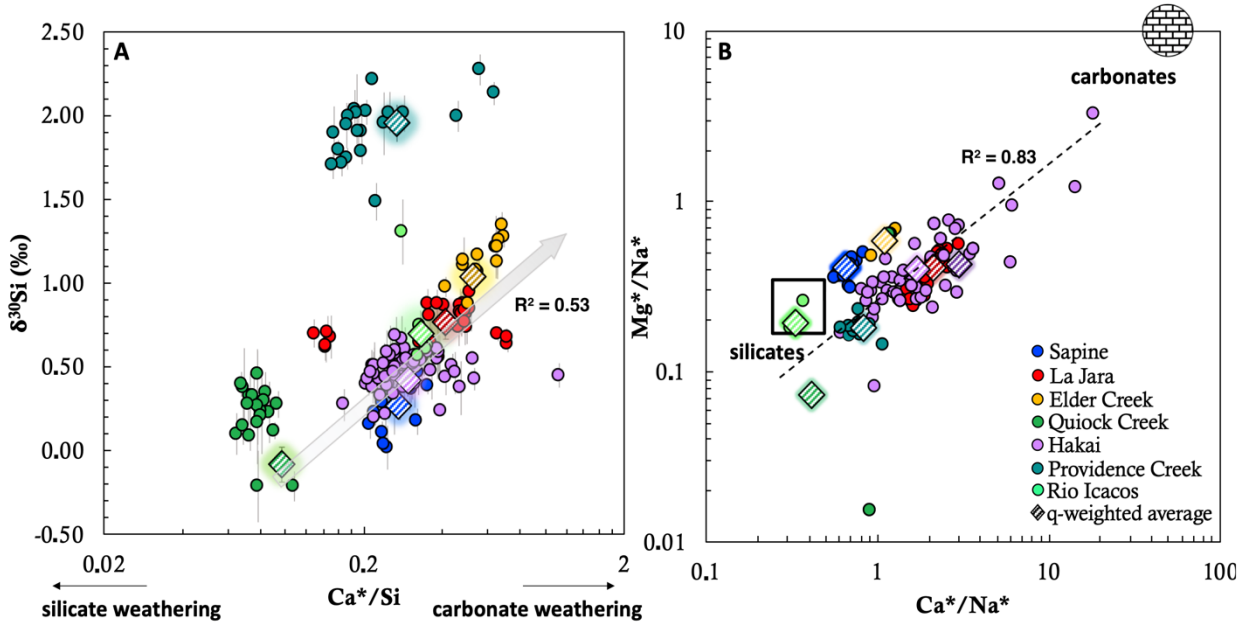

Figure 4.9 Stream $\delta^{30}Si$ vs. Ca* /Si ratios and Mg* /Na* vs. Ca*/Na* relationships
Determining lithologic control on stream $\boldsymbol{\delta^{30}Si}$ using Ca*/Si ratio (**A**) and Mg*/Na* vs. Ca*/Na* relationships, which provide information on the proportion of carbonate to silicate to the dissolved load and the weathering style. Dissolved Ca, Mg, and Na concentrations corrected for atmospheric input are designated Ca*, Mg*, and Na* respectively. Typical Ca*/Si ratios for silicates is ~ 0.2 – 10. Outside of the outlier, Providence Creek, a positive correlation ($R^2 = 0.53$) can be observed suggesting that stream $\boldsymbol{\delta^{30}Si}$ might be sensitive to the style of weathering. Error bars correspond to 2 standard deviation for the Si stable isotope data.

is potentially sensitive to the weathering style (i.e. silicate vs. carbonate weathering), which is typically a reflection of the source lithology and the overall make-up of the overlying soil and regolith. For instance, Elder Creek, the only argillite/shale catchment in this study, is known to contain at least 0.61–1.73% and 0.41–5.19% calcite in its soil and parent bedrock, respectively (Kim et al., 2014). La Jara could potentially have higher calcite content in its critical zone structure due to legacy, secondary carbonates generated during earlier episodes of hydrothermal activity in the area. Thus, it is possible in these systems that there is some carbonate dissolution occurring and that streams $\delta^{30}Si$ might be even slightly sensitive to the presence of carbonate in the system.

However, there is evidence to suggest that small contributions from carbonate weathering is not a suitable explanation for the fluid Ca*/Si ratios observed for all our sites. For example, Quiock Creek, a heavily weathered system, is depleted in all major cations with almost 48% of its dissolved Ca deriving from atmospheric contributions and the rest coming primarily through vegetation turnover and recycling (Dessert et al., 2020). Due to the deep soil and regolith profiles at Quiock, the parent bedrock is actually no longer a participant in neither Ca nor Si cycling (Dessert et al., 2020). Thus, for Quiock, our "depleted Ca endmember" in the positive covariation between stream $\delta^{30}Si$ and Ca^{*}/Si ratios is not a representative of a pure silicate endmember (as would be hypothesized at first glance), but rather a result of a very unique, site-specific, Ca cycling process that is unrelated to the its source lithology. Further, Providence Creek remains a significant outlier with respect to the other catchments due to its unusually high stream $\delta^{30}Si$ values despite residing well within the silicate weathering regime as shown both in **Fig. 4.9A** and **Fig. 4.9B**. These findings imply that stream $\delta^{30}Si$ is not very sensitive to

weathering style. Rather, the observed stream chemistry and $\delta^{30}Si$ for Providence Creek is most likely driven by a unique fractionation pathway driven through secondary physiochemical processes like secondary clay formation.

To summarize, the observed correlation between stream $\delta^{30}Si$ and Ca^{*}/Si more likely reflects a combination of the primary/secondary mineral assemblages within the respective critical zone structures of each catchment, cation sources derived outside of parent bedrock weathering, and site-specific secondary physiochemical processes such as secondary clay formation. These findings notably highlight two important points: (1) stream $\delta^{30}Si$ shows little dependence on lithology and (2) more importantly, its catchment specific processes and critical zone structures that ultimately drive observed global variability across these low order stream systems.

4.4.9 Weathering intensity control on stream $\delta^{30}Si$

The typical metric used to quantify weathering intensity is the use of the W/D ratio or the ratio of the chemical weathering rate (W) over the denudation rate (weathering (W) + erosion(E)) (Bouchez et al., 2014). Generally, low W/D (<0.01) corresponds to high elevation regions with overall high denudation rates largely resulting from physical erosion, and thus a low chemical weathering intensity "kinetically-limited" regime. In contrast high W/D (> 0.1) corresponds to low land areas, such as flood plains, with low denudation rates and high weathering intensity "supply-limited" regime (Bouchez and von Blanckenburg, 2014). A W/D between 0.01 and 0.1 reflects a transitional regime between the "kinetically-limited" highlands and the "supply-limited" lowlands where secondary mineral formation processes correspond to an intermediate weathering intensity. Weathering intensity has been shown to be parabolically correlated with

dissolved load Li stable isotope (δ^7Li) signatures in the Amazonian basin (Dellinger et al., 2015). Across this observed relationship, Dellinger et al. (2015) identified three weathering intensity regimes. Low weathering intensity corresponded to low δ^7Li and high dissolved Li fluxes, reflecting primarily congruent weathering in kinetically-limited conditions where fluid residence times are fast. An intermediate weathering intensity corresponds to enriched fluid δ^7Li signatures and intermediate Li fluxes that arise due to secondary mineral precipitation such as clay formation (i.e. incongruent weathering). A high weathering intensity regime results in low δ^7Li, similar to that observed in a low weathering intensity regime, but with lower dissolved Li fluxes that reflect a heavily depleted system where clay dissolution is the predominant source of dissolved solutes.

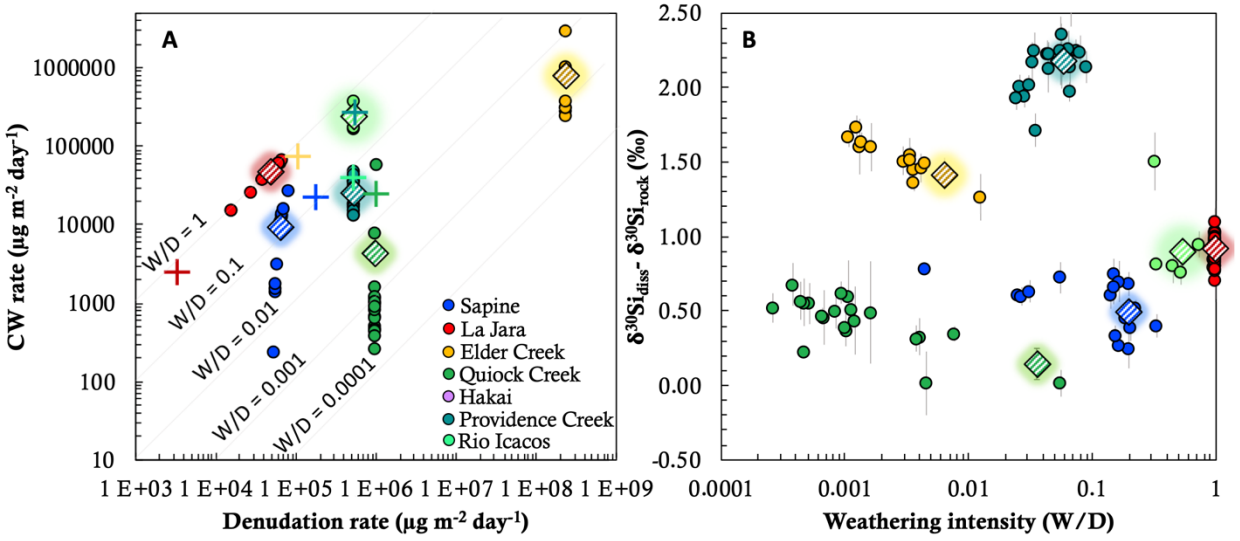

Figure 4.10 Chemical weathering vs. denudation rates and stream δ^{30}Si sensitivity to weathering intensity

Sensitivity of stream **δ^{30}Si** to weathering intensity. (**A**) Calculated chemical weathering rates (Bouchez and Gaillardet, 2014) and estimated denudation rates (**Table 1,** Allée and Boumédiène, 2004; Orem and Pelletier, 2016; Brown and Chanson, 2012; Rad et al, 2006,2013; Dixon et al., 2009; Riebe et al., 2013). (**B**) lithology corrected stream **δ^{30}Si** as a function of the estimated W/D ratios. Crosses (+) represent estimated annual W/D ratios based on annual chemical weathering rates determined in the literature (**Table 1,** Sapine: *Martin et al., 2003*; La Jara: *McIntosh et al., 2017*; Elder Creek: *Kim et al., 2017*; Quiock Creek: *Gaillardet et al., 2015*; Providence Creek: *Dixon et al., 2009*; Rio Icacos: *Millot et al., 2002*).

Thus, river δ^7Li was found to strongly correlate with weathering intensity in large river basin settings, which provides insight into the balance between chemical and fluid transport across seasonal to annual timescale resolution. We will now explore the extent to which dissolved δ^{30}Si across small, low-order catchments subject to highly transient precipitation events display similar sensitivities to weathering intensity.

Our datasets are unique to the Dellinger et al. (2015) study both in the use of silicon, which is subject to additional fractionating pathways such as biological uptake, and in the use of event response relationships rather than systematic baseflow conditions. We explore whether these unique conditions still result in a stream δ^{30}Si trend similar to δ^7Li as a function of weathering intensity by constraining W/D ratios for our catchments. This is accomplished using chemical weathering rates (W) calculated using the approach described in Bouchez and Gaillardet (2014), where the sum of the major cation concentrations (μg m^{-3}) is multiplied by the discharge (m^3 s^{-1}) normalized to the basin area (m^2) at a given time during the storm event, and through estimated physical denudation rates found in the literature for all catchments except Hakai (**Table 4.1,** Sapine- Allée and Boumédiène, 2004; La Jara- Orem and Pelletier, 2016; Elder creek- Brown and Chanson, 2012); Quiock creek- Rad et al., 2006, 2013; Providence creek- Dixon et al.,2009; Rio Icacos- Riebe et al., 2013). Our estimations for the physical denudation rate are inherently crude because no sediment flux yields were measured for these storm events and, thus, these rates represent a mean, annual rate. Thus, the calculated W/D ratios have a large uncertainty. Despite these limitations, the span in W/D ratios are significant across all the catchments and range from 0.0001(Quiock) to 1 (La Jara).

Calculated chemical weathering rates as a function of the estimated denudation rate (**Fig. 4.10A**) show little correlation between the complete set of 7 catchments, but there are some features discernible between individual groups. For example, La Jara and Rio Icacos, which have similar basin area sizes (~3 km^2), but completely different climates (semi-arid vs tropical wet) and different lithologies (rhyolitic vs. granitic) seem to reach similar W/D ratios (~1) (**Fig. 4.10B**). These observations would seem to suggest that La Jara, at least during this snow melt event, reflects a source of high intensity weathering on the order of what is generally observed for tropical environments with heavily depleted silica soils. In addition, the Elder Creek storm event appears to have both the highest denudation and chemical weathering rates, but a lower W/D ratio, implying that relatively "young" waters from "kinetically-limited" and of low- to-intermediate weathering intensity zones are being flushed out of the system. However, interpretations based on these observations must be regarded cautiously because (1) this is a large-scale dataset based on individual storm events rather than season or annual variability and (2) calculated denudation rates do not reflect the actual rates for these specific storm events, which are not constrained. This precaution is illustrated when

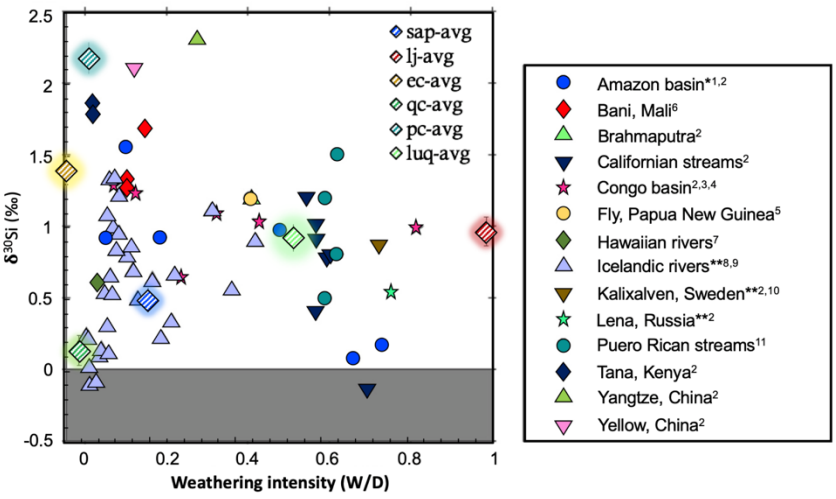

Figure 4.11 Comparison of storm event δ^{30}Si and weathering intensity with global observations

Relationship between mean discharge weighted stream **δ^{30}Si** data and calculated W/D ratios determined in this study compared with global river data synthesized by Frings et al. (2016).

storm event W/D are compared to the annual W/D ratios (crosses **Fig. 4.10A**, see **Table 4.1** for annual chemical weathering and denudation rates). Here it becomes clear that the relationships observed between the storm events of the given catchments are not preserved at an annual timescale. Specifically, the annual W/D ratios appear to collapse into the intermediate weathering intensity regime between 0.01 and 0.1. However, this observation highlights a potential advantage of constraining catchment behavior at the event resolution rather than at the annual or seasonal resolution in that, within this context, storm events could provide a unique "snapshot" of the pulses of different water sources and ages reflecting different weathering intensities and fluid residence times that are masked at lower resolution sampling.

Although not as clearly established as was the case for lithium, a "croissant" or "boomerang" relationship between dissolved $\delta^{30}Si$ and weathering intensity could be roughly discerned (**Fig. 4.10B**) where Providence Creek and Elder Creek, with W/D ratios between 0.01 and 0.1 and high dissolved $\delta^{30}Si$ values, seem to represent to some extent an intermediate weathering intensity endmember. Although, this "boomerang relationship" is notably much less robust than that observed for Li stable isotopes (R^2 = 0.13; Dellinger et al., 2015). High and low weathering intensity endmembers, however, are almost impossible to identify. The criteria for a high intensity weathering endmember are low dissolved silicon concentrations and low dissolved $\delta^{30}Si$ that reflect clay dissolution or more "incongruent" weathering. Neither La Jara nor Rio Icacos meet these criteria despite having high W/D ratios. The DSi concentration for Rio Icacos is not exceptionally low with respect to the other catchments (**Fig. 4.7**) and the dissolved $\delta^{30}Si$ remain at higher values with respect to both the bedrock and other catchments, such as

Sapine and Quiock. La Jara displays the highest dissolved Si concentrations (**Fig. 4.7**) with respect to the other catchments and, like for Rio Icacos, remains at dissolved $\delta^{30}Si$ highly elevated with respect to the parent bedrock composition and other catchments. The same complications arise for determining a "low weathering intensity" endmember, which should have high dissolved Si concentrations and low dissolved $\delta^{30}Si$ close to the dissolving primary mineral assemblage. We find that none of these catchments meet these criteria, at least based on event responses. Quiock, despite low W/D ratios and low dissolved $\delta^{30}Si$, has low DSi concentrations. It is most likely the case that such a parabolic relationship is not possible for a large-scale $\delta^{30}Si$ dataset established on storm events across low-order catchments, where inherently complex transient hydrological and chemical processes can play a key role in stream $\delta^{30}Si$ signatures. When we compare our dataset with previously published values (synthesized by Frings et al., 2016), we find that this lack of a distinct relationship between $\delta^{30}Si$ and weathering intensity is fairly universal (**Fig. 4.11**) even beyond the timescale of individual events. These complications in identifying low and high weathering intensity endmembers highlights an important characteristic in stream $\delta^{30}Si$ that is not observed in $\delta^{7}Li$, namely the behavior of a major ion relative to a trace element, the sensitivity of $\delta^{30}Si$ to secondary processes outside of secondary clay formation/dissolution such as vegetation and biological uptake, secondary mineral formation and the inherent complexities of transport and chemical processes over short, event-based, timescales.

4.4.10 Secondary clay control on stream $\delta^{30}Si$

The formation and re-dissolution of secondary clays exert a major influence on Si isotope fractionation and overall river $\delta^{30}Si$ signatures (Georg et al., 2006, 2007, 2009; Cardinal et al., 2010; Opfergelt et al., 2010, 2012; Hughes et al., 2013; Frings et al., 2016; Poitrasson, 2018, and others). To explore this effect on Si isotope fractionation signatures in our systems, we constrain three proxies for secondary clay formation across all catchments analyzed in this study: (1) Si/Al (**Fig. 4.12A**) (2) Σ+/Si (**Fig. 4.12B**), and (3) Si/(Na+K)* (**Fig. 4.12C**). Both Si/Al and Σ+/Si (where Σ+ is sum of the major cations Na,

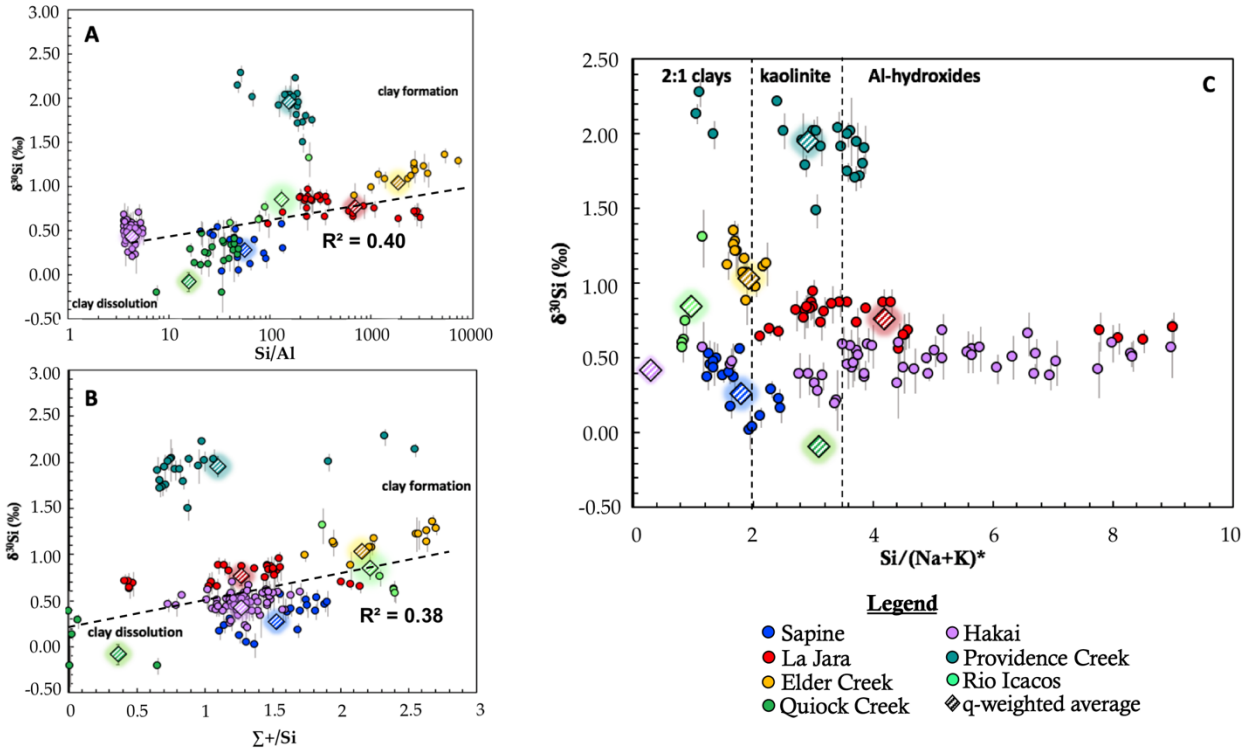

Figure 4.12 Secondary clay control on stream $\delta^{30}Si$ signatures

Secondary clay formation control on stream $\boldsymbol{\delta}^{30}Si$ signatures using three commonly used proxies: (**A**) Si/Al, (**B**) ∑+/ Si, where ∑+ equals the sum of the dissolved cations, and (**C**) Si/(Na+K*). The Si/Al and ∑+/ Si proxies both provide information on the extent of clay formation vs. clay dissolution whereas the Si/(Na+K*) provides information on the types of clays that can be formed and, thus, the extent of Si depletion in the system. Na and K concentrations were corrected for atmospheric input and are thus depicted as (Na + K)*. Error bars correspond to 2 standard deviation for Si stable isotope measurements.

K, Mg, and Ca) ratios provide constraints on clay formation and clay dissolution. Al is preferentially removed from the dissolved load relative to Si during clay formation and, thus, the Si/Al ratio increases in the fluid. A similar process occurs for the Σ+/Si clay proxy, but in this case clay formation removes Si faster relative to other major cations (due to the Goldschmidt rule, Goldschmidt, 1958) and, thus, the Σ+/Si of the fluid increases as secondary clays form. During clay formation, the "light" ^{28}Si is preferentially incorporated into the secondary clay leaving the remaining solution enriched in the "heavy" ^{30}Si. Thus, $\delta^{30}Si$ of the dissolved load increases during secondary clay formation and vice versa during clay dissolution.

When our riverine $\delta^{30}Si$ are compared to their respective Si/Al and Σ+/Si ratios, a positive correlation is observed with high Si/Al and Σ+/Si corresponding to higher $\delta^{30}Si$ values. However, this trend is not perfect and Providence Creek, once again, appears as a significant outlier. Elder Creek exhibits the highest Si/Al and Σ+/Si ratios, and one of the highest flux-average $\delta^{30}Si$ values, potentially reflecting clay formation under kinetically dominated conditions. Quiock, rather than Hakai, could potentially represent a clay or phytolith dissolution endmember with low Si/Al and dissolved $\delta^{30}Si$. Despite having the lowest Si/Al ratios, Hakai $\delta^{30}Si$ is unlikely to be controlled by clay dissolution processes (as would be erroneously interpreted by looking at this relationship). Our principle argument for rejecting this influence of clay dissolution control on the Hakai $\delta^{30}Si$ is that the average Si/Al ratios for this catchment (4.3) is in close agreement with the typical Si/Al ratio for granitoid rocks (~ 4) and the stream $\delta^{30}Si$ values (as stated above)

are close to bedrock values, thus implying that primary mineral dissolution is principally controlling the $\delta^{30}Si$ behavior in the Hakai catchment.

The final proxy for secondary mineral formation, $Si/(Na+K)^*$ can provide insight into the type of clays precipitating within these catchments (Stallard and Edmond 1987; Hughes et al. 2013). Na and K are generally less incorporated into secondary minerals relative to Si. Based on the stoichiometry of the secondary clay, a decrease in the $Si/(Na+K)^*$ indicates that Si is being incorporated into either 2:1 clays with a $Si/(Na+K)^*$ ratio < 2 (i.e bisiallitisation) or 1:1 clays such as kaolinite with $Si/(Na+K)^*$ ratios from 2.5 to 3.5 (monosiallitisation) or, in conditions where all Si has been scavenged, Al-hydroxides such as gibbsite that can be produced via the decomposition and transformation of kaolinite when DSi < $10^{-4.5}$ M with dissolved $Si/(Na+K)^*$ ratios > 3.5 (allitisation) (Alexander, 1958; Stallard and Edmond, 1987; Guyot et al., 2007; Hughes et al., 2013). We can thus employ $Si/(Na+K)^*$ ratios to define the boundaries between these three different clay formation and determine which phases are most likely to be reflected during flushing by these storm events. Such an analysis of the classes of clays potentially forming provides an indication of the extent of the desilication process and the overall weathering stage of these catchments (Hughes et al., 2013; Cornelis and Delvaux, 2016). We find that most of the catchments show preferential formation of 2:1 and 1:1 clays except for La Jara, which shows a potential shift towards formation of kaolinite during the ascending limb of the storm event and then transitions to a preference for Al-hydroxide formation along the descending limb near the end of the storm event. This implies a transition between water sources from a relatively silica enriched pool at the beginning of the storm event to a more silica depleted source at the end of the event. Hakai appears to lie along all three clay formation zones, but this might be an artifact of

the congruent dissolution signature. An interesting observation is that Quiock Creek, flushing heavily depleted soils, should be lying in the Al-hydroxides regime and, yet, based on the Si/(Na+K)* ratios of these storm events it shows contributions from waters that are more silica enriched than would be anticipated. These results hint at the role of clay and/or phytolith dissolution as the principal source of dissolved Si in Quiock, maintaining DSi concentrations at levels higher than would be expected for such a depleted system. Similar interpretations postulated for stream δ^{30}Si vs. DSi (**Fig. 4.7**) and δ^{30}Si vs. Ca/Si (**Fig. 4.9**) relationships and findings from previous studies (Clergue et al., 2015; Dessert et al., 2020) confirm that clay and/or phytolith dissolution is most likely the principal source of dissolved Si in Quiock Creek.

Finally, based on these observations as well as those from the previous section we are now well suited to provide an explanation for the Providence Creek outlier. In all stream δ^{30}Si vs. elemental ratio proxies and weathering intensity relationships, Providence Creek always presented a distinct outlier from the rest of the storm events. The only exception was presented in stream δ^{30}Si vs DSi relationship where Providence Creek represented an important high δ^{30}Si, high DSi endmember. Application of a Rayleigh distillation model (**Fig. 4.8**) showed that Providence Creek was the only storm event that could be described without a "muted" fractionation factor, lying well within the range of known secondary precipitation processes. These results suggested a unique fractionating pathway for this system that is distinct from the rest. We anticipated that this unique fractionating pathway is driven principally by substantial secondary clay formation. This hypothesis seems reasonable when applying the weathering intensity concept in which Providence Creek represents an intermediate weathering intensity

endmember. In this definition of intermediate weathering intensity, the system has long fluid residence times sufficient for the fluid to reach oversaturation with respect to secondary phases and, thus, favor the formation of secondary minerals (Dellinger et al., 2015). However, when we apply secondary clay proxies to the Providence Creek stream $\delta^{30}Si$ dataset we find Si/Al or $\sum+/Si$ ratios that are average in comparison to the other storm events. This observation is not what we would anticipate if considerable secondary clay formation was occurring. It is clear based on the Si/(Na+K)* data that kaolinite formation is certainly taking place at Providence Creek, but there appears to be another process taking place in tandem that is keeping DSi concentrations to values high enough to sustain active kaolinite formation. These conditions could only be met in long residence time waters capable of interacting with the bedrock long enough to reach oversaturation with kaolinite Thus, the high DSi and associated $\delta^{30}Si$ behavior observed at Providence Creek most likely reflects a significant groundwater source. These findings highlight the advantages of utilizing $\delta^{30}Si$ and secondary clay proxies to identify water sources contributing to the overall solute flux. Next we will explore the potential influence of vegetation on stream $\delta^{30}Si$ (**section 4.4.11**), which hints at the potential for vegetation to regulate the overall desilication process by either providing a fresh source of biologically cycled Si (Derry et al., 2005; Cornelis and Delvaux, 2016), particularly in highly depleted soils characteristic of tropical rainforests (Dessert et al., 2020), or removing dissolved Si via vegetation uptake and biogenic opal formation (Opfergelt et al., 2006).

4.4.11 Role of biological cycling on stream $\delta^{30}Si$

Silicon is an essential micronutrient and biological cycling has been shown to fractionate $\delta^{30}Si$, thus making it fundamentally distinct from $\delta^{7}Li$, which is only sensitive to secondary mineral formation processes (Ding et al., 2005, 2008; Opfergelt et al.,2006, 2008, 2010; Delvigne et al., 2009; Cornelis et al., 2010; Riotte et al., 2019; Yang et al., 2019 and others). Biological uptake fractionates Si isotopes in the same way as secondary mineral formation where the "lighter" Si-28 is preferentially incorporated into plants during the formation of phytoliths or through siliceous organisms living in suspension such as diatoms. Thus, the generally obscured relationship between stream $\delta^{30}Si$, DSi, and weathering intensity relative to that of Li stable isotope systematics (**section 4.4.8**) is likely influenced by secondary biological uptake processes. As a result, it becomes apparent that weathering intensity, in this context, cannot be defined in the same manner as lithium and must incorporate a biological cycling component.

Silicon biogeochemical cycling and uptake in terrestrial environments has been extensively studied over the past 30 years (Lucas et al., 1993; Morris, 1996; Alexandre et al., 1997, 2011; Kunilatsu et al., 2001; Clarke, 2003; Farmer, 2005; Fulweiler and Nelson, 2005; Blecker et al., 2006; Street-Perrott and Barker, 2008; Cornelis et al., 2010a,b; Meurier et al., 2010; and others). Si-accumulating-plants incorporate dissolved Si into their cellular structures and precipitate amorphous silica in their tissues in the form of opal phytoliths, thus serving as important contributors to the overall silica biogeochemical cycle and silica fluxes out of watersheds. A large (annual global phytolith opal production ~ 60–200 Tmol yr^{-1}; Conley, 2002) and long-term bioavailable silicon reservoir is present in the shallow subsurface in various weathering environments (Derry et al., 2005; Street-Perrott and

Barker, 2008; Cornelis and Delvaux, 2016). Such prevalent silica biogeochemical cycling and uptake is thus a principle of overall dissolved silica fluxes and their corresponding silicon isotope compositions which are difficult to parse from secondary mineral precipitation signatures as they both fractionate in the same direction. Other complementary analyses are necessary to distinguish biological contribution to the overall stream signature.

One such approach is the comparison of dissolved $\delta^{30}Si$ to (K/Na)* and (Mg/Na)* ratios, where K and Mg are known to be sensitive to plant uptake and thus can be considered as biological proxies (Tipper et al., 2012; Hughes et al., 2013; Chapela et al., 2014, 2017; and others). Generally, K and Mg are essential plant nutrients that are preferentially accumulated in the roots and leaves of plants (Campo et al., 2000). Thus, if dissolved K and Mg in a given system are controlled solely by plant uptake, theoretically (K,Mg)/Na fluid ratios should decrease. However, the inherent ambiguity in using these

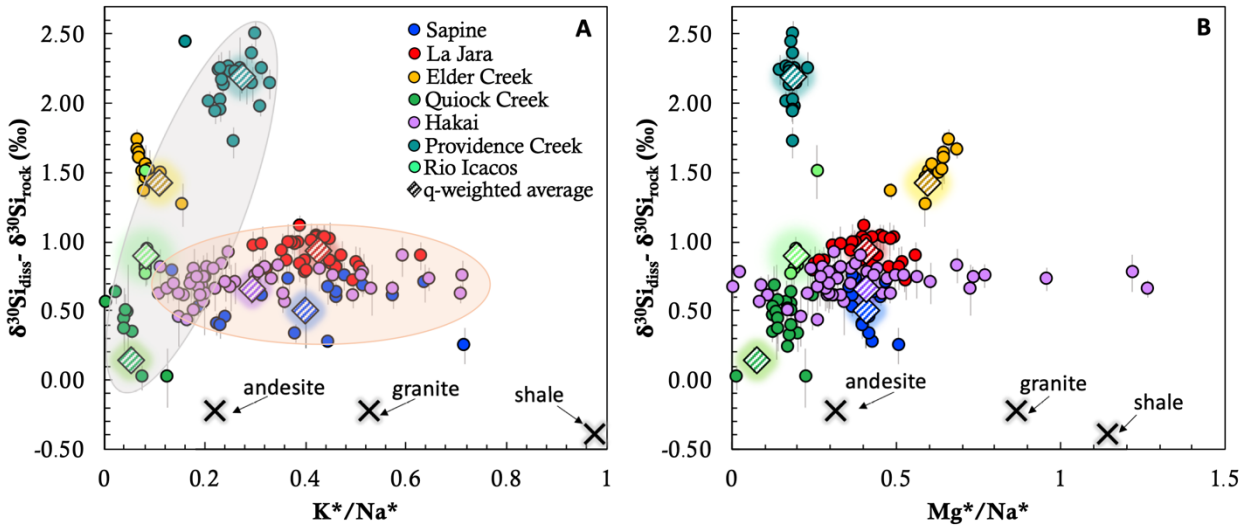

Figure 4.13 Testing possible vegetation control on stream $\delta^{30}Si$ signatures
Impact of vegetation on stream **δ**30Si signatures using (K/Na)* and (Mg/Na)* ratios, two biologically sensitive proxies. Lithologic rock ratios are provided from Stallard, 1980.

(K/Na)* and (Mg/Na)* elemental ratios is that they are also impacted by secondary mineral formation processes, which also can drive (K, Mg)/Na ratios to lower values. So, it is possible that dissolved K and Mg in certain catchments are controlled by biological cycling (Quiock Creek) whereas in others they reflect weathering reactions (like for instance Hakai that is our congruent weathering endmember) or some combination of both. In light of this limitation, (K/Na)* and (Mg/Na)* vs. stream $\delta^{30}Si$ relationships (**Fig. 4.13**) are presented to see if we can deduce any signs of contributions from vegetation that could influence observed storm event $\delta^{30}Si$ across catchments.

Comparison of (K/Na)* to $\delta^{30}Si$ (**Fig. 4.13A**) shows a rather bimodal correlation where one group of catchments (Quiock Creek, Rio Icacos, Elder Creek, and Providence Creek) appear to be linearly correlated. The linearly correlation observed in the four catchments constituting the first group appears to be bounded by low (K/Na)* around 0.05 and low $\delta^{30}Si$ endmember (Quiock Creek) and a high $\delta^{30}Si$ and relatively higher (K/Na)* values around 0.24 (Providence Creek). Another group can be parsed from this dataset (Sapine, La Jara, and Hakai) that appear to be spread across a range of (K/Na)* ratios that encapsulate the range of andesitic and granitic bedrock (0.22 and 0.53, respectively) within a tightly constrained range of stream $\delta^{30}Si$ values. This is in contrast to the four catchments in the first group whose (K/Na)* ratios are slightly lower than bedrock ratios and, thus slightly more depleted in K relative to the remaining three catchments. Based on these results, it can be perhaps suggested Quiock, Rio Icacos, Elder Creek, and Providence Creek might be subject to biological processes, principally plant uptake and/or phytolith formation. But the evidence provided by (K, Mg)/Na elemental ratios is insufficient to confirm this hypothesis and determine what contributions derive from

secondary mineral formation vs. vegetation cycling. This ambiguity is even further exacerbated in (Mg:Na)* vs stream $\delta^{30}Si$ where no clear relationships are established across the storm events (**Fig. 4.13B**). Thus, these proxies are imperfect for providing a definitive answer on contributions from vegetation to overall stream chemistry and it is clear that another approach is necessary.

Recent studies have turned to a multi-tracer approach to tease apart such competing secondary processes (Derry et al., 2006; Pett-Ridge et al., 2009; Meek et al., 2016; Baronas et al., 2018). Emphasis has centered of $\delta^{7}Li$ as a viable and promising complementary tracer to correct for the secondary mineral precipitation contribution in stable isotope systems that are impacted by vegetation, such as Ba, using a steady state isotope mass balance approach (Charbonnier, 2019). Ge/Si trace element ratios may also help constrain vegetation effects since they fractionate in the opposite direction to $\delta^{30}Si$ during plant uptake (Kurtz et al., 2002; Derry et al., 2006; Cornelis et al., 2010; Delvigne et al., 2016; Baronas et al., 2018). Such paired use of $\delta^{7}Li$ and Ge/Si ratios as complements to $\delta^{30}Si$ thus hold promise in parsing between secondary mineral precipitation and plant uptake signatures in future studies.

4.5 CONCLUSIONS

This study reports a novel, large-scale dataset of $\delta^{30}Si$—Q relationships across eight storm events from seven catchments spanning different climatological and lithological gradients. The catchments chosen for this study were notably low-order and headwater streams with a single lithology. $\delta^{30}Si$—Q relationships can serve as effective complements to traditional C–Q relationships. Variability in stream chemistry and $\delta^{30}Si$ as a function of discharge on the short, timescales of storm events show that these traditionally

considered "chemostatic" systems (Godsey et al., 2019) are actually more dynamic than previously anticipated. But these transient effects are unfortunately masked by coarse time resolution data on the order of monthly and annual timescales that is pervasive in the literature. Additional major findings from this study can be summarized as follows:

(1) A global relationship exists across catchments and storm events between dissolved Si concentrations and stream $\delta^{30}Si$. This relationship is bounded by three endmembers: (1) a low $\delta^{30}Si$ and low dissolved Si endmember reflective of low weathering intensity where Si is sourced from congruent dissolution of the parent bedrock; (2) a high $\delta^{30}Si$ and high dissolved Si, intermediate weathering intensity endmember dominated by secondary weathering processes such as secondary clay formation, biological uptake, and phytolith formation; (3) and finally a low $\delta^{30}Si$, low dissolved Si high weathering intensity endmember characterized by a system heavily depleted in major solutes where sources of Si derive from secondary clay dissolution and biological reservoirs.

(2) Overall chemostatic conditions observed at either large spatial scales (i.e. across catchments; Godsey et al., 2009) or at long timescales within a given catchment (seasonal or monthly, Winnick et al., 2015) are not observed at the individual storm event timescale in low order streams. Under these conditions, DSi and $\delta^{30}Si$ express complex variability as a function of discharge.

(3) The existence of muted or diminished fractionation factors for our dataset confirms the sensitivity of observed Si stable isotope fractionation to transport limitation processes such as fluid mixing.

(4) Site-specific catchment processes and unique characteristics of a given system drive observed global riverine $\delta^{30}Si$ behavior.

(5) Multi-tracer studies are necessary in order to parse out the effects of biological uptake and cycling on silicate weathering and stream $\delta^{30}Si$ signatures. Vegetation must be considered as a vital process that controls the overall weathering intensity observed in catchments and will, thus, play a large role in observed silicate weathering rate.

CHAPTER 5

Addressing the potential of self-consistent $\delta^{44}Ca$, $\delta^{88/86}Sr$, and Sr/Ca partitioning during calcite precipitation: An experimental and modeling study[4]

5.1 INTRODUCTION

Global biogeochemical cycling of calcium (Ca) starting from the weathering of Ca-bearing minerals on the continents and its long-term storage in ocean sediment via the precipitation of calcium carbonate is intricately linked to the global carbon cycle, serving as a critical sink in the global carbon cycle. As a consequence, the global Ca cycle has been one of the most well studied systems in the Earth sciences. Several decades of research have been dedicated to understanding past and present Ca oceanic budgets and the various pathways of calcium carbonate formation within marine environments in order to better constrain past and present climates. However, dissolved Ca fluxes from rivers, which represent the largest source of Ca to the oceans and, thus, serves as a principal control on the oceanic Ca budget, is one of the least understood systems in the global Ca cycle.

Observed river Ca fluxes are driven by the weathering of Ca-bearing rocks freshly exposed at the Earth's surface. The two primary weathering sources of dissolved Ca derive from carbonate and silicate weathering, which make up roughly 2/3 and 10 –26 % of the riverine Ca budget (Meybeck, 1987; Berner and Berner, 1996; Gaillardet et al., 1999).

[4] Fernandez, N.M ; Amsellem, E.; Antonelli, M.E.; Bouchez, J. ; Druhan, J.L. *in prep.*

Chemical weathering on the continents takes place in the near-surface environment we commonly refer to as the "Critical Zone", which extends from the top of the tree canopy to the bedrock residing deep in the sub-surface. The Critical Zone thus integrates complex interactions between air, water, vegetation, and rock that ultimately generate the surrounding landscapes and regulates ecosystems observed on the planet's surface. The chemical weathering within the Critical Zone reflects an intricate balance between the dissolution of Ca-bearing minerals (such as Ca-plagioclase, pyroxenes, calcium carbonates, gypsum, and others) and often the subsequent formation of more stable secondary carbonate phases, such as calcite. The balance between these chemical transformations and hydrological transport exert a first order control on overall solute fluxes and the supply of essential nutrients to the ecosystems composing the terrestrial biosphere. This interplay between primary mineral dissolution and secondary mineral formation is difficult to tease apart. A variety of different combinations of dissolution and precipitation reactions operating in tandem can generate the same observed weathering flux. To address this problem, the Na-silicate weathering literature have resorted to non-traditional stable isotopes, like silicon stable isotopes, and trace-elemental ratios, such Ge/Si, that have been used either separately (Kurtz et al, 2002; Frings et al., 2016) or in tandem, (Delvigne et al., 2016; Baronas et al., 2018). These weathering tracers have been largely successful in identifying and deconvolving the various pathways of secondary mineral formation and other secondary weathering reactions taking place in the Critical Zone. However, unlike Na-silicate weathering tracers that were developed principally for the purpose of tracing terrestrial biogeochemical solute cycling, carbonate tracers like Ca stable isotopes and Sr/Ca elemental ratios were developed for an entirely different

system. Only recently have they been applied within the context of Ca-silicate and carbonate weathering on land.

Ca stable isotopes and Sr/Ca trace elemental ratios have their foundations in the marine community where they were developed principally as marine proxies. Their signatures preserved within the calcium carbonate shells of marine organisms such as planktonic foraminifera and coccolithophores serve as proxies for ancient marine conditions such as paleo-sea surface temperatures (Nägler et al., 2000; Böhm et al., 2006; Hippler et al., 2006; Langer et al., 2007), carbonate equilibria (Keul et al., 2017), and oceanic Ca reconstructions (Fantle, 2010) as well as to understand diagenetic processes impacting deep marine sedimentary records (Fantle and DePaolo, 2007; Fantle, 2010; Fantle and Higgins, 2014; Fantle, 2015; Gorski and Fantle, 2017; Huber et al., 2017; Chanda et al., 2019). Additionally, Ca stable isotopes have been used to some extent to trace the recycling of ancient carbonate sediments within the mantle (Huang et al., 2011). To develop these marine proxies further, numerous laboratory experiments have been conducted to quantitatively characterize Ca stable isotope (Lemarchand et al., 2004; Gussone et al., 2005; Tang et al., 2008a; AlKhatib and Eisenhauer, 2017) and Sr/Ca (Lorens, 1981; Mucci and Morse; 1983; Tesoriero and Pankow, 1996; Parkman et al., 1998; Watson, 2004; Wasylenki et al., 2005; Gabitov and Watson, 2006; Tang et al., 2008b; Böhm et al., 2012; Gabitov et al., 2014; AlKhatib and Eisenhauer, 2017) fractionation during various carbonate precipitation reactions. From this extensive body of work, many fractionation models have been developed in order to describe and predict the behavior of these marine tracers within the slow, steady state ("chemostatic"), conditions reflective of deep-sea environments (Watson, 2004; DePaolo, 2011; Nielsen et al., 2012; Nielsen et al., 2013; Thien et al., 2013; Fantle and Gorski, 2017).

Initial attempts at characterizing the terrestrial Ca biogeochemical cycling was done through the use of Sr and its radiogenic isotope ratio ($^{87}Sr/^{86}Sr$) due to their shared chemical similarities as alkaline-earth elements with similar charge and sizes (Graustein and Armstrong, 1983; Blum et al., 2002: Kennedy et al., 2002; Bullen and Bailey, 2005; Bélanger and Holmden; 2010); Blum et al., 2012). However, findings from studies using combined tracer approaches using radiogenic Sr with trace element tracers such as Sr/Ca (Baes and Bloom, 1988; Poszwa et al., 2000; Bullen and Bailey, 2005; Drouet et al., 2005; Berger et al., 2006; Meek et al., 2012) found that Ca and radiogenic Sr behave quite distinctly from one another in terrestrial environments; notably, that whereas Sr radiogenic isotopes trace only solute sources, Ca appeared to be sensitive to both sources and biogeochemical processes taking place within the weathering zone. From these studies, it was evident that Ca and its stable isotopes could be effective tools in deconvolving important biogeochemical reactions and hydrological pathways driving Ca generation and mobility within the terrestrial biosphere. Thus, over the past 10 to 15 years there has been growing interest to develop Ca stable isotopes, along with stable isotopes of other alkaline-earth metals (Mg, Sr, and Ba), and their respective trace element ratios (i.e. Sr/Ca) as effective weathering proxies (Schmitt et al., 2003; Schmitt et al., 2012; Fantle and Tipper, 2014; Griffith et al., 2020).

However, all that we currently know about these Ca-weathering tracers and their fractionation mechanisms derive predominantly from the marine literature. Laboratory experiments conducted to quantitatively characterize Ca stable isotope (Lemarchand et al., 2004; Gussone et al., 2005; Tang et al., 2008a; AlKhatib and Eisenhauer, 2017) and Sr/Ca (Lorens, 1981; Mucci and Morse; 1983; Tesoriero and Pankow, 1996; Parkman et al., 1998; Watson, 2004; Wasylenki et al., 2005; Gabitov and Watson, 2006; Tang et al.,

2008b; Böhm et al., 2012; Gabitov et al., 2014; AlKhatib and Eisenhauer, 2017) fractionation during various carbonate precipitation reactions were designed specifically for slow, steady state, deep sea environments. Fractionation models and conceptual frameworks developed based on the observations from this exhaustive experimental literature are based on assumptions that are only valid in marine environments (Watson, 2004; DePaolo, 2011; Nielsen et al., 2012; Nielsen et al., 2013; Thien et al., 2013; Fantle and Gorski, 2017). In terrestrial settings where carbonate reaction rates are fast and solute compositions are constantly evolving in a manner intimately linked to spontaneous carbonate growth (what we refer to as "free-drift" conditions), it is unlikely that tracers within these transient conditions would behave similarly to what is well observed in marine settings. Thus, our current understanding of the behavior of Ca, Sr, and other originally "marine" proxies in terrestrial weathering zones is extremely limited.

In this regard, there has been some progress to try to describe fractionation of these tracers in a terrestrial weathering, "free-drift" contexts. For instance, a study of calcium carbonate precipitation field experiments in a Colorado watershed (Druhan et al., 2013) highlights the distinct behavior of Ca stable isotopes in terrestrial settings though the successful application of a stable isotope fractionation model modified to include transient isotope effects that are non-existent in a marine context. In the silicate literature, transient isotope effects for Si stable isotope fractionation related to fluid and solid phase mineral surface co-evolution and physical properties of the system (i.e. surface area and solid to fluid ratios) have been observed and successfully characterized through these modified, "transient" fractionation models (Fernandez et al., 2019). Further, these transient effects have been observed to influence trace element ratios (Ge/Si) in a similar way that can be described based on analogous stable isotope transient models suggesting

that stable isotopes and trace elements behave in a complementary manner (**Chapter 3**, Fernandez et al., *in prep*). We hypothesize that Ca and Sr trace-elemental ratios and stable isotopes are also self-consistent and could also serve as notable complements to each other. To date, application of Ca, Sr stable isotopes and Sr/Ca trace element ratios in tandem has rarely been investigated in the literature (Böhm et al., 2012; AlKhatib and Eisenhauer, 2017) and, based on our current knowledge, a complementary relationship between these respective tracers has not yet been demonstrated for carbonate formation under free drift conditions. In this study, we seek to improve upon our understanding of Ca-weathering tracers by quantifying the behavior of multiple stable isotope (Ca, Sr) and trace element (Sr/Ca) tracers of secondary calcium carbonate formation (commonly, formed secondary phase in weathering environments) in a self-consistent, experimental and modeling framework based on "free-drift", dynamic conditions inherent in continental weathering systems.

5.1.1 Fractionation mechanism for carbonate formation tracers

Laboratory studies conducted over the previous several decades have largely centered on calcite formation due to its stability and high abundance in Earth surface environments (Hartmann and Moosdor, 2012) and its well characterized growth mechanisms (Burton et al., 1951; Nancollas and Reddy, 1971; Zhang and Nancollas, 1998; Teng et al., 1998, 1999, 2000; Dove et al., 2008; Bracco et al., 2012). Other polymorphs including vaterite, aragonite, and amorphous calcium carbonates have also been characterized for Ca stable isotopes (Gussonne et al., 2003, 2005), Sr stable isotopes (Böhm et al., 2012; Fruchter et al.,2016), and/or Sr/Ca trace element ratios (Kulik et al.,2010;), or a combination of the three (AlKhatib and Eisenhauer, 2017a). Highly constrained laboratory experiments exploring Ca stable isotope fractionation during calcite growth

show that this partitioning follows a kinetic fractionation mechanism during precipitation where the light ^{40}Ca is preferentially incorporated into the forming carbonate mineral, leaving the fluid enriched in the heavier ^{44}Ca (Lemarchand et al., 2004; Gussone et al., 2005; Tang et al., 2008a; AlKhatib and Eisenhauer, 2017b). The origin of this kinetic behavior has been attributed to the mass dependency of ion desolvation, a crucial step necessary in the incorporation of Ca^{2+} into the crystal structure during calcite growth (Hofmann et al., 2012). Strontium stable isotopes have been observed to behave similarly to Ca stable isotopes during both calcite (Böhm et al., 2012; AlKhatib and

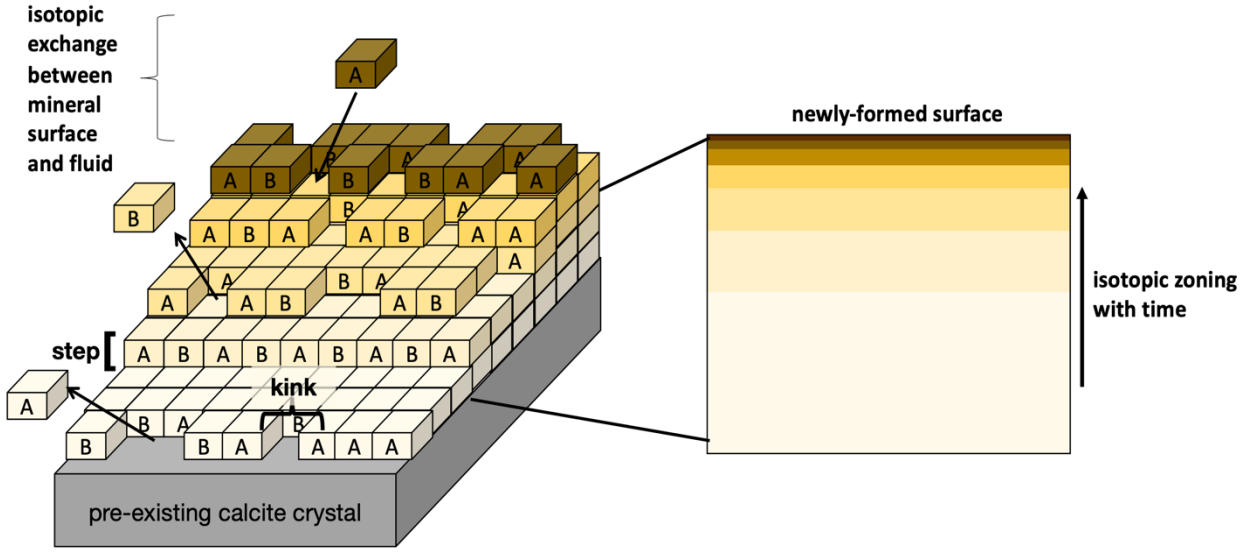

Figure 5.1 Isotopic zoning during calcite growth

Conceptual model of mineral isotopic zoning during calcite precipitation under non-steady state conditions following AB crystal growth mechanics where ion A and B attachment/detachment occurs along step edges and kink sites (modified from Nielsen et al., 2012). The evolution of the Ca isotope ratio of the newly formed calcite surface is dictated by the extent of isotopic exchange between the fluid and mineral surface. At the early stages of the reaction, when precipitation rates are fastest, kinetic fractionation ensues where the the light ^{40}Ca is preferentially incorporated into the growing mineral surface. Since most of the mass precipitated occurs in this early stage of calcite formation, the kinetic signature generated during this time represents a large component of the newly formed mineral surface. As the reaction continues to proceed, the remaining mass of calcite precipitated out of solution becomes increasingly heavier isotopically as precipitation rates begin to slow down in the approach to equilibrium and contributions from the backward, dissolution rate starts to become important. The result is the establishment of an isotopically heterogeneous calcite mineral surface that is unique from the pre-existing calcite seed composition.

Eisenhauer, 2017b) and strontianite ($SrCO_3$) growth (Mavromatis et al., 2017), preferentially incorporating the light ^{86}Sr into the crystal structure leaving the residual fluid enriched in the heavier ^{88}Sr.

Calcite precipitation may be thought of as a bi-directional mass transfer between the growing carbonate mineral and its surrounding fluid that is controlled by the balance between the forward, precipitation (R_f) and backward, dissolution (R_b) rates. Precipitation is thus a condition in which R_f outweighs R_b and thus the mass-dependent fractionation associated with R_f is primarily expressed. As a result of this two-way mass transfer, in the approach to a dynamic chemical equilibrium (i.e. when the overall reaction rate equals zero and $R_f = R_b$) isotopic exchange between the fluid and growing mineral results in increasing contributions from equilibrium isotope fractionation to the overall Ca isotope signature (**Fig. 5.1**; Tang et al., 2008; DePaolo, 2011; AlKhatib and Eisenhauer, 2017a,b; Oelker et al., 2018). This rate-dependence in the observational or apparent fractionation factor as a function of growth rate is observed for Ca stable isotopes during calcite growth where the observed fractionation factor generally increases with decreasing precipitation rates. Strontium stable isotopes also exhibit to a lesser extent a similar rate-dependence with observed fractionation factors increasing as a function of decreasing precipitation rates (Böhm et al., 2012; AlKhatib and Eisenhauer, 2017b). Although, the limited range in precipitation rates investigated in these prior $\delta Sr^{88/86}$ studies biased towards faster rates ($10^{-5.1}$ to $10^{-6.5}$ mol m^{-2} s^{-1}, AlKhatib and Eisenhauer, 2017b) makes this inverse relationship between the rate and observed fractionation factor far less straightforward as compared to Ca stable isotopes.

The role of strontium in calcite growth and the evolution of Sr/Ca trace element with reaction progress has been well-studied under laboratory conditions (Lorens et al.,

1981; Tesoriero and Pankow, 1995; Parkman et al., 1998; Huang et al., 2001; Wasylenki et al., 2005; Gabitov and Watson, 2006; Tang et al., 2008b; Harouaka et al., 2014; Gabitov et al., 2014; AlKhatib and Eisenhauer, 2017b; and others). Trace amounts of strontium in solution during calcite precipitation are typically incorporated into the growing mineral, the extent to which is dependent on temperature, growth rates, and solute chemistry. The aqueous strontium ion (Sr^{2+}_{aq}), like other impurities (such as Mg^{2+}, Ba^{2+}, Cd^{2+}), generally tends to impede calcite growth rates in a manner that is proportional to its initial amount in solution (i.e. initially high concentrations of Sr^{2+}_{aq} lead to a decrease in $R_{p,calcite}$, Meyer 1984). However, it has also been observed that, in certain situations, small amounts of Sr^{2+}_{aq} present in solution actually accelerates calcite growth rates (Wasylenki et al., 2005). This general observation of slower calcite growth rates as a function of increased presence of Sr^{2+}_{aq} have been attributed to increased Sr uptake into the calcite crystal structure blocking available kink sites for Ca to attach onto (Wasylenki et al., 2015) and/or increased calcite solubility as a result of the solid solution between calcite–strontianite (Davis et al., 2000; Nielsen et al., 2013). Like Ca and Sr stable isotopes, Sr/Ca trace element partitioning is also observed to deviate from predictions based on thermodynamically driven equilibrium fractionation (Kolitov, 2010). How Sr content will ultimately influence Ca, Sr stable isotope and Sr/Ca partitioning in free-drift conditions has yet to be investigated. Thus, we seek in this study to explore these relationships by running calcite precipitation experiments across a range of Sr/Ca ratios that reflect the overall variability observed in terrestrial environments (**Fig. 5.2**).

Observed similarities between Ca,Sr stable isotopes and Ca/Sr trace element partitioning have inspired the development of several fractionation models such as the

Surface Entrapment Model (SEM, Watson, 2004), Surface reaction kinetic model (SRKM, DePaolo 2011), Ion-by-ion growth model (Nielsen et al., 2012), the Unified uptake kinetic model (UUKM, Thien et al., 2013). The SRKM, DePaolo (2011) in particular was the first to predict variability in the observed fractionation factors as a result of mixed kinetic and equilibrium effects, which are controlled by the balance between forward, precipitation and backward, dissolution rates. This assumption of rate-dependence in the observed fractionation factor was fully integrated into the SRKM, DePaolo (2011) model in the form of analytical equations that were ultimately successful in describing observed $\delta^{44}Ca$ and Sr/Ca fractionation for highly controlled calcite precipitation experiments conducted under "steady state" or chemostatic conditions. In this sense, the SRKM model is limited to cases where calcite formation takes place under steady state solute compositions. The reason lies within the derivation of the underlying equations in the model, which requires conditions in which the growing calcite surface composition remains fixed throughout the course of the reaction in order to take on an analytical form. As we will see in the next section, this assumption of a steady state calcite surface composition breaks down in free-drifting, transient conditions where solute

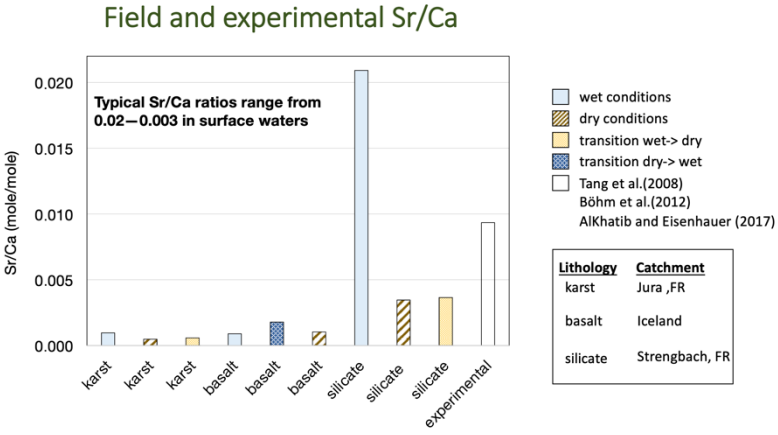

Figure 5.2 Field and experimental Sr/Ca ratios
Average Sr/Ca values for a variety of different catchments consisting of predominantly karst (Julien and Damien's Jura data), basaltic (Jacobson et al., 2015; Hindshaw et al., 2013), and silicate (Cenki-Tok et al., 2009) lithologies respectively as well as experimental Ca/Sr values during calcite precipitation experiments conducted by Tang et al., 2008. For these different catchments, the data is parsed out in terms of seasonal variability (i.e. Ca/Sr ratios during "wet" , "dry", and "transitional" (spring/autumn) seasons).

compositions vary throughout the course of calcite growth. Although the SRKM model, along with the other various fractionation models mentioned above, were developed originally for chemostatic calcite precipitation, they serve important purposes in lying the groundwork for tracer partitioning during mineral growth that we will attempt in this study to build upon to address $\delta^{44}Ca$, $\delta^{88/86}Sr$ and Sr/Ca during transient calcite growth.

5.1.2 Carbonate formation and tracer fractionation under free-drift conditions

To date, few experimental studies have addressed calcium stable isotopes during carbonate formation under such variable, "free-drifting" conditions (Reddy and Nancollas, 1971; Nancollas and Reddy, 1971; Zhang and Dawe, 1998). This is in large part a result of the inherent characteristics of the "free-drift" method, notably the varying nature of these type of experiments. Transient changes in solute composition and overall kinetics introduces a suite of complexities (i.e. slow pH drift, rapid precipitation rates, and unstable near-equilibrium conditions) that makes it challenging to properly constrain the underlying mechanisms driving carbonate formation and associated calcium stable isotope fractionation. Thus, this free-drift approach is considered antiquated and has mostly been abandoned in the carbonate community (Nielsen, 2012). Chemostatic or steady state methods for calcite growth have been very successful in establishing the wealth of knowledge that currently exists on the kinetics, thermodynamics, growth mechanisms and dependencies on trace impurities and other physiochemical characteristics of the system. Hence, our current understanding of carbonate (particularly calcite) formation, which is by far the most well studied system in regard to mineral growth, can be largely attributed to the fruits of these chemostatic

experimental studies. Thus, we believe that the robust foundation laid out by these prior studies makes us poised to revisit the complexities of the free-drift method in pursuit of characterizing calcite formation in these dynamic weathering or Critical Zone systems. Properly addressing carbonate formation under free drift conditions offers an exciting and novel step forward in the carbonate community in tackling the largely unknown terrestrial component of the global Ca cycle.

In the free-drift studies that do exist, only ^{45}Ca radiotracer exchange was explored as a tracer of interaction between the fluid and growing calcite, which found that calcite formation under free drift conditions abides by higher order (2^{nd} order) kinetics and results in an isotopically heterogeneous newly formed calcite mineral surface (Reddy and Nancollas, 1971). Although the findings from Reddy and Nancollas (1971) are notable, no free-drift studies afterwards have contributed further on transient crystal growth and its effects on tracer partitioning. Further, none of these "free-drift" studies have specifically addressed Ca or Sr stable isotope or trace element fractionation, though there have been attempts to address the controls on Ca isotope behavior in dynamic environments based on field observations (Schmitt et al., 2003; Tipper et al., 2006, 2008; Cenki-Tok et al., 2009; Hindshaw et al., 2011; Druhan et al., 2013; Jacobson et al., 2015; Griffith et al., 2020) and numerical reactive transport modeling (Druhan et al., 2013).

Fortunately, a wealth of information exists for other mid-mass stable isotope systems that can provide insight into stable isotope and trace element fractionation during calcite precipitation under dynamic conditions. For example, several studies of the stable isotope ratios of Mg, Sr, and Ba in carbonates (Pearce et al., 2012; Mavromatis et al., 2012, 2016, 2017; Oelkers et al., 2018) and Si in secondary silicates have recently been published exploring mineral growth under free-drift conditions (Oelze et al., 2014; Geilert et al.,

2015; Roerdink et al., 2015; Fernandez et al., 2019). Application of the DePaolo (2011) surface reaction kinetic model in the recent silicate studies (Oelze et al., 2014; Geilert et al., 2015; Roerdink et al., 2015; Fernandez et al., 2019; Fernandez et al., *in prep*) suggest that the concept of dynamic equilibrium and surface isotopic exchange reactions offer an appropriate conceptual framework for both stable isotope and trace element (principally, Ge) behavior in non-steady state systems. However, recent findings showing that physical characteristics of the growing mineral such as surface area and solid:fluid ratios exert a significant influence on observed Si isotope fractionation and lead to the formation of isotopically zoned mineral surfaces (Fernandez et al., 2019) imply that there are more complex interactions taking place in free-drift conditions that cannot be accounted for in the steady state SRKM fractionation model. Thus, mineral growth in free-drift settings requires a new generation of isotope fractionation models which specifically omit the steady state assumption imposed in the SRK model, thereby allowing the fluid and solid phase isotope ratios to be coupled to one another, co-evolving with time based on the extent of fluid-mineral surface interaction (Druhan et al., 2013). These "transient" models (Fernandez et al., 2019) have so far been successful in predicting Si isotope fractionation during highly constrained amorphous silica precipitation experiments. We hypothesize that these new, "transient", models can be used effectively to describe Ca, Sr stable isotope along with Sr/Ca trace element behavior during calcite precipitation under free-drift conditions as has been done recently for these other mid-mass and trace element systems.

5.1.3 New generation multi-tracer models

Multi-tracer studies over the last decade are starting to be more frequently employed in the literature as an effective tool to better resolve the weathering and biological processes that ultimately control observed solute fluxes (Pett-Ridge, et al., 2009; Schmitt et al., 2012; Meek et al., 2016). A major advantage of using such a multi-tracer approach in the field is that information on hydro- and bio-geochemical reaction pathways and sources that would be otherwise overlooked by using only one stable isotope or trace element tracer can be filled in by the application of a second or third complementary tracer. For example, a large majority of stable isotope and trace element tracers (including $\delta^{44}Ca$, $\delta^{26}Mg$, $\delta^{11}B$, Sr/Ca) are sensitive to both secondary mineral formation and biological processes (Schmidt et al., 2012). However, some tracers (such as Li and B stable isotopes) are predominately controlled by the secondary mineral present in a system and the processes controlling their formation (Lemarchand et al., 2010; Lemarchand et al., 2012). Whereas other tracers such as $\delta^{44}Ca$ and $\delta^{26}Mg$, are more sensitive to biological processes such as biogenic mineral formation and plant uptake along with a whole suite of other water–plant interactions (Schmitt et al., 2003, 2013, 2018; Tipper et al., 2010, 2012). There are also trace element tracers (Sr/Ca, Ge/Si) which, in addition to secondary mineral and biological reaction pathways, can also provide unique insight into the lithologic controls and the primary mineral sources contributing to the observed solute chemistry (Derry et al., 2006; Pett-Ridge, et al., 2009; Meek et al., 2016). Further, some tracers, particularly radiogenic Sr isotopes ($^{87}Sr/^{86}Sr$) that are not fractionated by chemical weathering reactions and serve as fingerprints of strictly solute sources such as lithology, subsurface water, or atmospheric deposition (Hogan and Blum, 2003; Oliva et al., 2004; Rad et al., 2006; and others) as well as groundwater flow path (Johnson and DePaolo,

1997a,b and many others) . Thus, a multi-tracer approach takes advantages of the individual strengths of each tracer to obtain a more complete picture on catchment scale dynamics and offers a promising new direction in constraining terrestrial Ca biogeochemical cycling.

Yet, if we are to procced forward in the direction of using multiple tracers to characterize weathering systems, we need geochemical models capable of monitoring several tracers at the same time within a given system. Thus, a more fundamental understanding of the underlying mechanisms driving the fractionation of individual tracers and, importantly, the commonalities shared across tracers is required. If stable isotope and trace element tracers behave in a manner that is broadly, self-consistent, then we have an incredible opportunity in our established numerical models to link together tracers that are well developed (like $\delta^{44}Ca$ and Sr/Ca) with those that are less developed (i.e. $\delta^{88/86}Sr$) in a single, unifying fractionation framework. DePaolo (2011) was the first to propose the idea of stable isotope and trace elements behaving in an analogous and complementary manner. Under these assumptions, the SRKM model developed a central framework that can be applied to both $\delta^{44}Ca$ and Sr/Ca during steady state calcite precipitation. Additionally, recent work in the silicate literature has confirmed that $\delta^{30}Si$ and Ge/Si share common fractionation mechanisms and, thus, are powerful complements to one another during amorphous silica precipitation in free-drift settings (**Chapter 3,** Fernandez et al. *in prep*). However, whether or not $\delta^{44}Ca$ and Sr/Ca would continue to behave self-consistently in free-drift conditions remains unknown. Further, the central fractionation model developed by DePaolo and expanded upon in the form of a binary solid solution framework in the transient models (Druhan et al., 2013; Fernandez

et al., 2019) is currently unable to monitor both major (Ca) and trace (Sr) elements and their associated stable isotopes, $\delta^{44}Ca$ and $\delta^{88/86}Sr$ respectively, simultaneously within the same system. Thus, in the proposed study we seek to both (1) determine whether $\delta^{44}Ca$, Sr/Ca, and $\delta^{88/86}Sr$ share broadly consistent fractionation mechanisms during calcite precipitation under free-drift (i.e. varying solute composition) conditions; and (2) present a novel fractionation framework that is capable of describing several major and trace element tracers in the same system at the same time.

5.2 METHODS

5.2.1 Batch experiments

Calcite precipitation experiments were conducted following a "free-drift" technique adapted by Reddy and Nancollas (1970) and Nancollas and Reddy (1971). This "free-drift" methodology allows the reaction to evolve naturally from a supersaturated initial condition so that the saturation state, pH, and solute composition changes throughout the course of the experiment as a function of the approach to chemical equilibrium (Nancollas and Reddy, 1971; Wiechers et al., 1975; Inskeep and Bloom, 1985; Zhang and Dawe, 1998). These batch experiments were run using a range of initial calcite seed surface areas and starting Sr concentrations as summarized in the **Table 5.1**. The calcite seeds used in this study were pure Iceland Spar crystals (1" × 1" dimensions, Ward Scientific ®) with trace amounts of Sr (~ 45.5 ppm in a representative calcite sample, Bracco et al., 2012) that were crushed down and sieved to two separate average particle diameter sizes of 180μm and 2mm, respectively. The specific surface areas of the crushed calcite seeds were constrained using the BET (Brunauer-Emett-Teller) method, yielding values of 0.57 $m^2\ g^{-1}$ and 0.0026 $m^2\ g^{-1}$ for the "low" and "high" average particle sizes,

respectively. Initially oversaturated solutions with respect to calcite were made by first preparing 0.8 mM calcium chloride ($CaCl_2 \cdot 2H_2O$, MW = 147.02 g mol^{-1}, ACROS ®) and 20 mM sodium bicarbonate ($NaHCO_3$, MW = 74.56 g mol^{-1}, Fisher Scientific ®) solutions separately in 500mL volumetric flasks. The contents of the 20 mM sodium bicarbonate solution were added directly into the 1L HDPE batch reactor and the 0.8 mM calcium chloride solution was slowly mixed into the reactor via drop-wise addition using a 500 mL volumetric burette with stopper at base for volume output control and slow stirring. After the calcium chloride and sodium bicarbonate solution was properly mixed, the resulting calcite-supersaturated solution had an initial pH ~8.85, concentrations of Ca^{2+}_{aq} equal to 0.35 mM, overall total inorganic carbon (TIC) equal to 10mM, and Ca:CO_3 ratio of the initial solution ~0.98. At the initial pH, bicarbonate is the predominant species

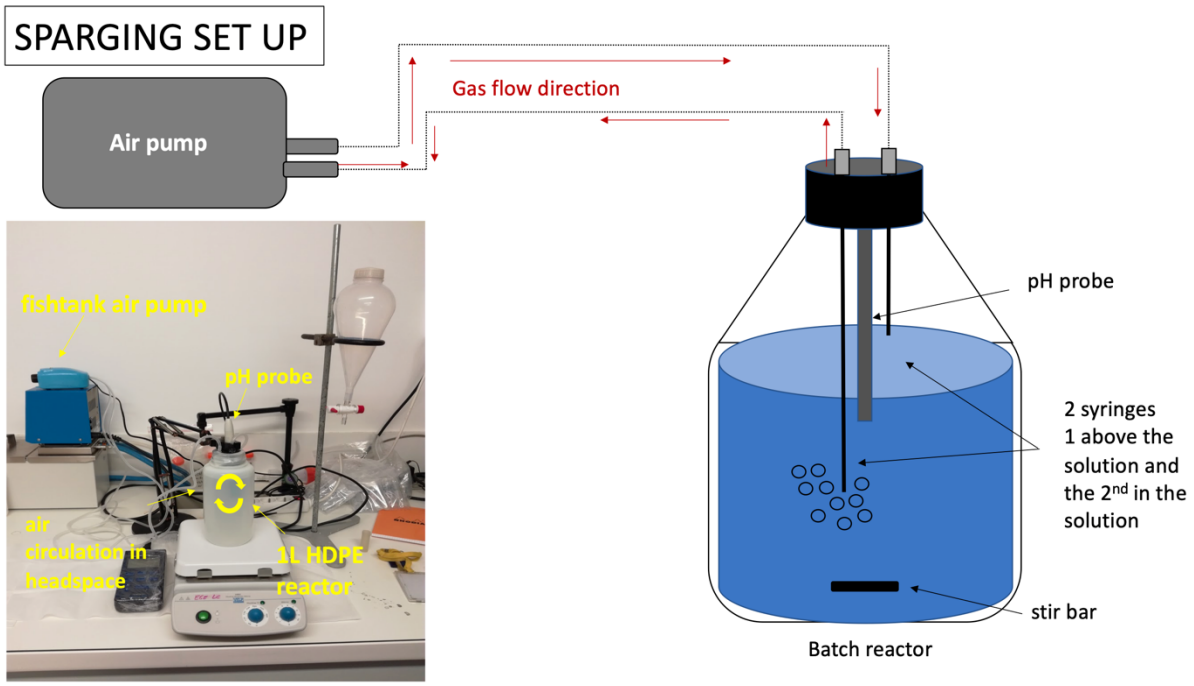

Figure 5.3 Closed system sparging setup
Experimental design for the closed system sparging technique that was implemented in the calcite precipitation batch experiments.

present with HCO_3^- representing 94% of the TIC (9.4 mM) and CO_3^{2-} as only 4% of the total TIC (~0.36 mM).

Before initiating precipitation, the oversaturated solution and its pH had to be stabilized via a closed-system sparging technique (**Fig. 5.3**) involving a continuous aeration pump (Uniclife©), which served to rapidly equilibrate the system with the pCO_2 of the headspace at 25°C (this corresponds to $CO_{2(aq)}$ ~0.003344 mmol kg^{-1}). This sparging is an important part of the procedure which was developed through the process of the experimental design. Without this initial equilibration between $CO_{2(g)}$ – $CO_{2(aq)}$ it was observed that the pH slowly drifted throughout the course of the experiment due to sluggish air-water exchange, ultimately causing slow changes in pCO_2 that make it difficult to attain meta-stable equilibrium with respect to $CaCO_3$ at the conclusion of the experiment. Once the pH has stabilized to the given value reflective of pCO_2 equilibrium (pH~8.85) for a period of approximately 30 minutes, the solution is considered stable and ready for calcite precipitation. At this point, the saturation state (log Q/K) of the initial solution was determined to be ~1.18 (**Table 5.1)**. For the Sr-doped experiments, a pure elemental 1000 ppm Sr single element standard (SPEX CertiPrep™) was used to elevate the Sr concentration in solutions to the targeted initial Sr/Ca ratios indicated in **Table 5.1**.

Table 5.1 Initial conditions for calcite precipitation experiments

Exp Cond.	Ca	Sr	Sr^{2+}_{aq}: Ca^{2+}_{aq}	Ca^{2+}_{aq} : CO_3^{2-}	$Ca_{(s)}$:$Ca_{(aq)}$	Ω[a]
	mM	μM	mol:mol	mol:mol	g:g	log (Q/K_{sp})
			High SA batches (0.57 m^2 g^{-1})			
Baseline, no Sr	0.35	0.003	8.57×10^{-6}	0.98	140	1.18
High Sr	0.35	0.720	2.06×10^{-3}	0.98	140	1.18
Medium Sr	0.35	0.147	4.20×10^{-4}	0.98	140	1.18
Low Sr	0.35	0.020	5.43×10^{-5}	0.98	140	1.18
			High SA batches (0.0026 m^2 g^{-1})			
Baseline, no Sr	0.35	0.003	8.57×10^{-6}	0.98	140	1.18
High Sr	0.35	0.720	2.06×10^{-3}	0.98	140	1.18

a. K_{sp} at 25°C for calcite = $10^{-8.40}$ (Reddy and Nancollas, 1971).

To initiate the precipitation process, 2.00 g of calcite seeds with known surface area were added to the reactor while stirring and sparging. The batch reactor was then quickly sealed to enable closed system sparging between the fluid and surrounding headspace throughout the duration of the experiment. Ports were installed for the pH probe, inlet/outlet gas connectors, and sample collection. Onset of precipitation is evidenced by a characteristic drop in pH. The completion of the kinetic portion of the experiment is indicated by a cease in pH changes (indicative of an attainment of meta-stable equilibrium), which occurs within the first ~90 minutes. The experiments were then maintained at these conditions for a week (7 days) with sampling over discrete time intervals for both Ca and Sr (~20 mL per fluid sample). Solid samples were collected at the end of experiment via vacuum filtration using Merck Millipore 0.22 μm filters and were subsequently dried at room temperature. For concentration and stable isotope analyses, portions of the solid samples were dissolved using dilute nitric acid.

5.2.2 Analytical techniques

Calcium and strontium concentrations were analyzed using an Agilent 7900 Inductively Coupled Plasma Mass Spectrometer at the Institut de Physique du Globe de Paris (IPGP) in Paris, FR. For instrumental precision, a multi-element standard for Ca and Sr along with an internal standard using Sc for correction due to matrix effects yielded precision values of $\pm$ 0.02 mM and $\pm$ 0.04 μM for Ca-44 and Sr-88, respectively. Saturation states and aqueous speciation of the initial batch reactor fluids (**Table 5.1**) were determined using the known calcite solubility constant ($10^{-8.4}$; Reddy and Nancollas, 1971) and the activity coefficients of Ca and carbonate calculated by the CrunchTope multi-component reactive transport software (Steefel et al., 2015).

The chemical purification procedure for Ca stable isotopes followed the method developed by Amsellem et al. (2017) where samples were loaded in 1N HNO_3 on 1.8 mL of pre-cleaned Eichrom DGA resin in BioRad columns to separate Ca from the solution matrix. The next step involved separating Ca from the residual Sr left over from the pass in the DGA resin by loading the sample in 3N HNO_3 on 200 μL Eichro, Sr-Specific resin (20-50 μm) in handmade Teflon® micro-columns. Due to the large interference of both ^{86}Sr and ^{88}Sr on the ^{44}Ca in the mass-spectrometer, we passed the samples two times through the Sr-Specific columns to ensure that no residual Sr remained in solution. The final purified Ca samples were then dried down and dissolved in 0.1N HNO_3 for analysis. Ca stable isotope analyses were performed on a ThermoFinnigan Neptune Plus MC-ICP-MS at the Institut de Physique du Globe de Paris. Running conditions on the machine matched the procedure described in Valdes et al. (2014). The sample introduction system used was the Apex desolvating system including a 50 μL min^{-1} Teflon® nebulizer. Measurements were conducted at medium resolution. Intensities of ^{42}Ca, ^{43}Ca, and ^{44}Ca were measured with ^{40}Ca not being analyzed as a result of the ^{40}Ar interference typical in MC-ICP-MS. Procedural blanks were below 3 mV on ^{44}Ca, which is insignificant relative to the signal attained from the samples (~2 V). Ca stable isotope compositions are reported in standard per mil notation (δ) based on blank-corrected isotope ratios calculated by a standard bracketing method using the NIST SRM 915a standard (**eq. 5.1**):

$$\delta^{i/j}Ca = \left[\frac{\left({}^{i}Ca/{}_{j}Ca \right)_{sample}}{\left({}^{i}Ca/{}_{j}Ca \right)_{SRM915a}} - 1 \right] \times 1000. \quad (5.1)$$

Where *i* and *j* correspond to either 40, 42, 43, and 44. Ca isotope compositions are presented in this paper in the form of $\delta^{44/40}$Ca relative to SRM 915a to stay consistent with previous calcite precipitation studies and, thus, converted the results from $\delta^{44/42}$Ca to the target $\delta^{44/40}$Ca via the mass-dependent fractionation law ($\delta^{44/40}Ca = -2 \times \delta^{44/42}Ca$). For a Neptune MC-ICP-MS, the long-term reproducibility determined through repeated analysis of the standard yields an uncertainty of ± 0.33‰ (2 standard deviations; Wieser et al., 2004; Tipper et al., 2016).

Strontium radiogenic and stable isotope measurements were performed on a ThermoFinnigan Neptune Plus MC-ICP-MS at the Institut de Physique du Globe de Paris. Preparation for isotope analyses involved a Sr chromatographic column setup where in fluid samples of ~ 200 ng Sr dissolved in 3N HNO_3 solution were loaded onto 200μL of pre-cleaned Sr-Specific resin (20-50 μm, Eichrom ®) in hand-made Teflon ® micro-columns. Strontium was isolated and eluted from the column using 2 mL MQ water. The pure Sr samples were then subsequently dried down at ~90°C for preservation purposes until the samples could be measured. For isotopic analysis, the dried down samples were then re-dissolved to the target acidity (0.5 N HNO_3) required for the MC-ICP-MS. Running conditions closely followed the methodology developed by Fietzke et al. (2006) involving an Apex desolvation sample introduction system and measurements conducted in high resolution. The intensities of ^{84}Sr, ^{86}Sr, ^{87}Sr, and ^{88}Sr were measured during the runs on the mass spectrometer with beam intensities for the most abundant isotopologue, ^{88}Sr, of on average roughly 7 to 8 V. Masses of Rb, 85 and 87, were also monitored to correct ^{87}Sr data in order to obtain 87/86 Sr values as well as ^{86}Kr, which is used to correct for any instrumental drift. Sr stable isotope compositions, like Ca stable

isotopes, are reported in delta notation (δ) based on blank-corrected isotope ratios calculated by a standard bracketing method using the SRM NBS987 standard as shown below (**eq. 5.2**):

$$\delta^{88/86}Sr = \left[\frac{\left({}^{88}Sr/{}^{86}Sr \right)_{sample}}{\left({}^{88}Sr/{}^{86}Sr \right)_{SRM\ NBS987}} - 1 \right] \times 1000 \qquad (5.2)$$

where the average $^{88}Sr/^{86}Sr$ ratio for the SRM NBS987 standard is 8.375209 (n = 50). Long term precision was evaluated through repeated analyses of the standard, yielding ± 0.10 ‰ (2 standard deviations).

5.3 RESULTS

5.3.1 Ca chemical and isotopic evolution through time

Measured fluid [Ca^{2+}_{aq}] and Ca stable isotope ratios (**Table 5.2**) monitored over the 1 week experimental duration are presented alongside the measured pH for high and low surface area calcite grain cases and for corresponding cases of varying initial Sr^{2+} contents present in solution (**Fig. 5.4,** referred to here as "baseline" – i.e. no Sr added, "high", "medium", and "low" Sr doped solutions). Dissolved Ca^{2+} concentrations through time for all batch experiments start at an average value of 0.35 mM and then rapidly decrease with time over the first day, followed by a period of stabilization to average values of ~0.03 mM as metastable equilibrium is achieved with respect to calcite solubility concentrations at 25°C (4.01×10^{-9} mM, Reddy and Nancollas, 1971). Neither the order of magnitude differences between seed crystal surface areas or the range of starting Sr concentrations (high Sr case = 0.72 μM, med Sr case =0.15 μM, low Sr case = 0.02 μM, and baseline case: 0.003 (high SA) – 0.0026 (low SA) μM) create obvious differences in the Ca

concentration behavior throughout the reaction timeseries (**Fig. 5.4A**). However, the content of Sr does appear to have some impact on the fluid Ca stable isotope ratios through time, most notably in the "low SA, high initial Sr" case (**Fig. 5.4B**). In the baseline – i.e. no Sr experiments, differences in the surface areas of the initial calcite crystal seeds used in the reactors appear to have negligible influence on the evolution of the fluid Ca stable isotope ratios. The largest increases in the fluid $\delta^{44/40}$Ca are observed in the "high SA, baseline" and "low SA, high initial Sr" conditions where values reach a maximum of 3.4 ± 0.73‰ and 3.04 ± 0.27‰, respectively. The pH is relatively stable throughout the course of the reaction for all batch experiments varying between 8.85 (initial) to 8.6 in the high SA baseline case as a result of the continuous closed system sparging technique (**Fig. 5. 4C**).

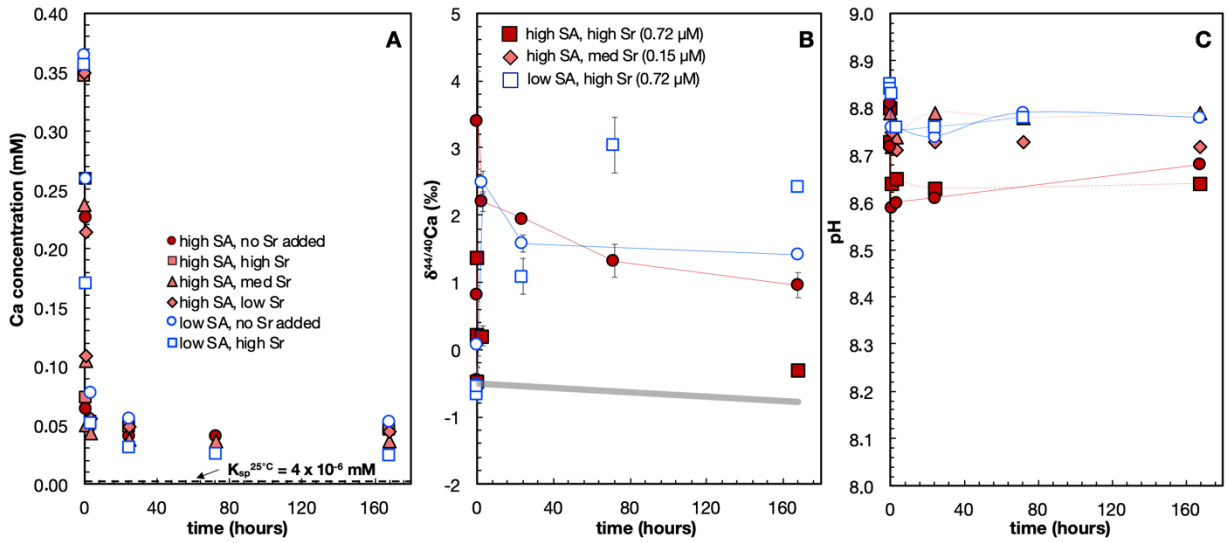

Figure 5.4 Ca batch experimental results

Ca concentration (**A**), $\delta^{44/40}$Ca (**B**), and pH (**C**) timeseries throughout the course calcite precipitation experiments beginning from oversaturated solutions and allowing 'free-drift' precipitation onto either high SA (0.57 $m^2\ g^{-1}$, red markers) to low SA (0.0026 $m^2\ g^{-1}$, blue markers) initial calcite seed crystals. seed crystals to reach equilibrium. Experimental conditions include no Sr added (circles), low Sr (diamonds), medium Sr (triangles) and high Sr (squares) added to initially oversaturated solutions with respect to calcite.

Table 5.2 Free drift calcite precipitation experimental results

	Time hours	Volume[a] L	Ω^{b} $CaCO_3$	pH	$S_{vol.corr}$[c] m^2	[Ca][d] mmoles L^{-1}	[Sr][e] µmoles L^{-1}	$N_{cumul.ppt}$ moles (10^{-4})	$N_{calcite.tot}$ moles	$N_{Sr,tot}$ moles (10^{-6})
	"High surface area (0.57 m^2 g^{-1}), baseline Sr –no added Sr" batch, T = 25°C									
1	0	1.00 ± 0.02	1.18	8.81	0.115 ± 0.015	0.35 ± 0.03	0.003 ± 0.005	–	0.0201	4.99
2	0.08	0.98 ± 0.03	0.78	8.72	0.112 ± 0.012	0.23 ± 0.02	0.005 ± 0.005	3.27	0.0204	4.98
3	0.5	0.96 ± 0.03	0.22	8.59	0.110 ± 0.012	0.06 ± 0.01	0.014 ± 0.008	7.29	0.0208	4.98
4	3	0.94 ± 0.04	0.10	8.60	0.108 ± 0.012	0.05 ± 0.01	0.030 ± 0.004	7.67	0.0208	4.96
5	24	0.92 ± 0.04	0.002	8.61	0.105 ± 0.012	0.04 ± 0.01	0.068 ± 0.012	7.90	0.0209	4.93
6	72	0.90 ± 0.05	0.003	8.67	0.103 ± 0.012	0.04 ± 0.01	0.087 ± 0.017	7.91	0.0209	4.91
7	168	0.88 ± 0.05	0.002	8.68	0.101 ± 0.013	0.05 ± 0.01	0.109 ± 0.011	7.79	0.0209	4.89
	"High surface area (0.57 m^2 g^{-1}), high Sr" batch, T = 25°C									
1	0	1.00 ± 0.02	1.18	8.80	0.115 ± 0.013	0.35 ± 0.03	0.720 ± 0.094	–	0.0201	4.99
2	0.08	0.98 ± 0.03	0.84	8.73	0.112 ± 0.011	0.26 ± 0.03	0.663 ± 0.086	2.32	0.0203	5.06
3	0.5	0.96 ± 0.03	0.29	8.64	0.110 ± 0.012	0.07 ± 0.01	0.540 ± 0.070	6.90	0.0208	5.19
4	3	0.94 ± 0.04	0.13	8.65	0.108 ± 0.012	0.05 ± 0.01	0.505 ± 0.066	7.43	0.0208	5.23
5	24	0.92 ± 0.04	0.08	8.63	0.105 ± 0.012	0.05 ± 0.01	0.488 ± 0.063	7.56	0.0208	5.26
6	168	0.90 ± 0.05	0.06	8.64	0.103 ± 0.012	0.05 ± 0.01	0.522 ± 0.068	7.62	0.0208	5.24
	"High surface area (0.57 m^2 g^{-1}), medium Sr" batch, T = 25°C									
1	0	1.00 ± 0.02	1.18	8.82	0.115 ± 0.013	0.34 ± 0.02	0.147 ± 0.023	–	0.0201	4.99
2	0.08	0.98 ± 0.03	0.45	8.79	0.112 ± 0.011	0.11 ± 0.01	0.129 ± 0.021	3.36	0.0204	5.01
3	0.5	0.96 ± 0.03	0.12	8.72	0.110 ± 0.012	0.05 ± 0.01	0.122 ± 0.019	4.72	0.0205	5.02
4	3	0.94 ± 0.04	0.04	8.74	0.108 ± 0.012	0.04 ± 0.01	0.123 ± 0.020	4.92	0.0206	5.02
5	24	0.92 ± 0.04	0.02	8.79	0.105 ± 0.012	0.04 ± 0.01	0.131 ± 0.021	5.07	0.0206	5.01
6	72	0.90 ± 0.05	0.04	8.78	0.103 ± 0.012	0.04 ± 0.01	0.135 ± 0.022	5.10	0.0206	5.01
7	168	0.88 ± 0.05	0.03	8.79	0.101 ± 0.013	0.04 ± 0.01	0.140 ± 0.022	5.14	0.0206	5.01
	"High surface area (0.57 m^2 g^{-1}), low Sr" batch, T = 25°C									
1	0	1.00 ± 0.02	1.18	8.84	0.115 ± 0.013	0.35 ± 0.04	0.020 ± 0.004	–	0.0201	4.99
2	0.08	0.98 ± 0.03	0.76	8.81	0.112 ± 0.011	0.21 ± 0.02	0.019 ± 0.004	3.49	0.0204	4.99
3	0.5	0.96 ± 0.03	0.45	8.75	0.110 ± 0.012	0.11 ± 0.01	0.022 ± 0.004	6.13	0.0207	4.99
4	3	0.94 ± 0.04	0.16	8.71	0.108 ± 0.012	0.06 ± 0.01	0.039 ± 0.008	7.43	0.0208	4.97
5	24	0.92 ± 0.04	0.08	8.73	0.105 ± 0.012	0.05 ± 0.01	0.069 ± 0.014	7.62	0.0208	4.94
6	72	0.90 ± 0.05	0.06	8.73	0.103 ± 0.012	0.05 ± 0.01	0.080 ± 0.016	7.69	0.0208	4.93
7	168	0.88 ± 0.05	0.03	8.72	0.101 ± 0.013	0.05 ± 0.01	0.095 ± 0.019	7.74	0.0208	4.92
	"Low surface area (0.0026 m^2 g^{-1}), baseline Sr –no added Sr" batch, T = 25°C									
1	0	1.00 ± 0.02	1.18	8.84	0.005 ± 0.001	0.36 ± 0.04	0.003 ± 0.001	–	0.0199	4.95
2	0.5	0.98 ± 0.03	0.84	8.76	0.005 ± 0.001	0.26 ± 0.03	0.003 ± 0.001	2.76	0.0202	4.95
3	3	0.96 ± 0.03	0.31	8.76	0.005 ± 0.001	0.08 ± 0.01	0.003 ± 0.001	7.26	0.0207	4.95
4	24	0.94 ± 0.04	0.16	8.74	0.005 ± 0.001	0.06 ± 0.01	0.009 ± 0.001	7.80	0.0207	4.95
5	168	0.92 ± 0.04	0.12	8.79	0.005 ± 0.001	0.05 ± 0.01	0.017 ± 0.003	7.89	0.0207	4.94
	"Low surface area (0.0026 m^2 g^{-1}), high Sr" batch, T = 25°C									
1	0	1.00 ± 0.02	1.18	8.85	0.005 ± 0.001	0.36 ± 0.04	0.746 ± 0.05	–	0.0201	4.99
2	0.5	0.98 ± 0.03	0.66	8.84	0.005 ± 0.001	0.17 ± 0.02	0.747 ± 0.05	4.70	0.0205	5.00
3	3	0.96 ± 0.03	0.13	8.83	0.005 ± 0.001	0.05 ± 0.01	0.742 ± 0.05	7.66	0.0208	5.02
4	24	0.94 ± 0.04	0.19	8.76	0.005 ± 0.001	0.03 ± 0.01	0.669 ± 0.07	8.15	0.0209	5.10
5	72	0.92 ± 0.04	0.09	8.78	0.005 ± 0.001	0.03 ± 0.01	0.659 ± 0.07	8.30	0.0209	5.13
6	168	0.90 ± 0.05	0.10	8.78	0.005 ± 0.001	0.03 ± 0.01	0.617± 0.07	8.33	0.0209	5.18

(Table 5.2 continued)

Exp.	log R_p	log R_p^{inst}	log R_p^{cumul}	log R_p^{mixed}	log $R_{release}^{Sr}$	log R_{uptake}^{Sr}
	mol s^{-1}	mol m^{-2} s^{-1}				
"High surface area (0.57 m^2 g^{-1}), baseline Sr –no added Sr" batch, T = 25°C						
1	–	–	–	–	–	–
2	-5.95 ± -6.43	-5.00 ± -6.09	-5.00 ± -6.09	-5.00 ± -6.09	-10.30 ± -11.66	–
3	-6.39 ± -7.17	-5.62 ± -6.46	-5.43 ± -6.33	-5.62 ± -6.46	-10.27 ± -11.18	–
4	-7.15 ± -7.94	-7.41 ± -7.70	-6.18 ± -7.11	-6.81 ± -7.11	-10.67 ± -11.45	–
5	-8.04 ± -8.84	-8.53 ± -8.73	-7.06 ± -8.01	-7.06 ± -8.00	-11.18 ± -11.89	–
6	-8.52 ± -9.31	-10.24 ± -11.14	-7.53 ± -8.48	-7.53 ± -8.47	-11.55 ± -12.24	–
7	-8.89 ± -9.68	–	-7.89 ± -8.83	-7.89 ± -8.71	-11.82 ± -12.74	–
"High surface area (0.57 m^2 g^{-1}), high Sr" batch, T = 25°C						
1	–	–	–	–	–	-
2	-6.09 ± -7.42	-5.14 ± -6.50	-5.14 ± 6.50	-5.14 ± -6.50	–	-8.67 ± -9.51
3	-6.42 ± -7.14	-5.56 ± -6.40	-5.56 ± -6.35	-5.56 ± -6.40	–	-8.99 ± -9.43
4	-7.16 ± -7.91	-7.26 ± -7.65	-6.19 ± -7.12	-6.19 ± -7.12	–	-9.68 ± -10.11
5	-8.06 ± -8.81	-8.79 ± -8.68	-7.08 ± -8.02	-7.08 ± -8.02	–	-10.53 ± -11.01
6	-8.90 ± -9.65	-9.97 ± -10.54	-7.91 ± -8.85	-7.91 ± -8.85	–	-11.40 ± -11.84
"High surface area (0.57 m^2 g^{-1}), medium Sr" batch, T = 25°C						
1	–	–	–	–	–	–
2	-5.93 ± -6.64	-4.98 ± -5.65	-4.98 ± -5.65	-4.98 ± -5.65	–	-9.20 ± -10.21
3	-6.58 ± -7.39	-6.09 ± -6.73	-5.62 ± -6.42	-6.09 ± -6.73	–	-9.82 ± -10.01
4	-7.34 ± -8.16	-7.68 ± -7.78	-6.37 ± -7.18	-6.37 ± -7.18	–	-10.57 ± -10.77
5	-8.23 ± -9.06	-8.74 ± -8.77	-7.25 ± -8.07	-7.25 ± -8.07	–	-11.55 ± -11.86
6	-8.71 ± -9.53	-9.66 ± -10.17	-7.72 ± -8.53	-7.72 ± -8.53	–	-12.03 ± -12.35
7	-9.07 ± -9.89	-10.03 ± -10.48	-8.07 ± -8.89	-8.07 ± -8.89	–	-12.42 ± -12.87
"High surface area (0.57 m^2 g^{-1}), low Sr" batch, T = 25°C						
1	–	–	–	–	–	–
2	-5.92 ± -6.44	-4.97 ± -5.51	-4.97 ± -5.51	-4.97 ± -5.51		–
3	-6.47 ± -7.17	-5.80 ± -6.42	-5.51 ± -6.34	-5.80 ± -6.42	-11.39 ± -12.95	–
4	-7.16 ± -7.94	-6.88 ± -7.49	-6.19 ± -7.12	-6.19 ± -7.12	-10.85 ± -11.49	–
5	-8.05 ± -8.83	-8.60 ± -8.66	-7.08 ± -8.01	-7.08 ± -8.01	-11.32 ± -12.11	–
6	-8.53 ± -9.31	-9.44 ± -9.86	-7.54 ± -8.48	-7.54 ± -8.48	-11.71 ± -12.51	–
7	-8.89 ± -9.67	-9.83 ± -10.38	-7.90 ± -8.84	-7.90 ± -8.84	-11.98 ± -12.80	–
"Low surface area (0.0026 m^2 g^{-1}), baseline Sr –no added Sr" batch, T = 25°C						
1	–	–	–	–	–	-
2	-6.81 ± -7.20	-4.52 ± -5.22	-4.52 ± -5.22	-4.52 ± -5.22	-10.49 ± -11.28	–
3	-7.17 ± -7.91	-5.00 ± -5.83	-4.87 ± -5.76	-5.00 ± -5.83		–
4	-8.04 ± -8.80	-6.83 ± -7.21	5.73 ± -6.66	-5.73 ± -6.66	-10.83 ± -11.49	–
5	-8.88 ± -9.65	-8.43 ± -9.14	-6.56 ± -7.50	-6.56 ± -7.50	-11.36 ± -12.01	–
"Low surface area (0.0026 m^2 g^{-1}), high Sr" batch, T = 25°C						
1	–	–	–	–	–	–
2	-6.58 ± -7.25	-4.29 ± 5.10	-4.29 ± -5.10	-4.29 ± -5.10	–	-8.83 ± -10.6
3	-7.15 ± -7.99	-5.18 ± - 6.01	-4.85 ± -5.77	-5.18 ± - 6.01	–	-9.20 ± -9.85
4	-8.03 ± -8.89	-6.88 ± -7.41	-5.72 ± -6.67	-5.72 ± -6.67	–	-9.56 ± -9.78
5	-8.49 ± -9.36	-7.74 ± -7.94	-6.18 ± -7.14	-6.18 ± -7.14	–	-9.95 ± -10.26
6	-8.86 ± -9.73	-8.81 ± -9.30	-6.53 ± -7.50	-6.53 ± -7.50	–	-10.17 ± -10.64

§ **Errors calculated through simple propagation according to the sum of squares**

Table 5.3 Ca, Sr, stable isotopes and Sr/Ca ratios for free drift calcite precipitation experiments

	Sr/Ca_{aq}	Sr/Ca_{sol}	$K_{D.Sr}^{rayl}$	$K_{D.Sr}^{evol}$	$\delta^{44/40}Ca_{fl}$	2σ	$\delta^{44/40}Ca_{inst.ppt}$	$\delta^{44/40}Ca_{cum.ppt}$	$\Delta^{44/40}Ca$				87/86 Sr	95% C.I	$\delta^{88/86}Sr_{fl}$	95% C.I	$\Delta^{88/86}Sr$		
					‰	‰	‰	‰	inst–fluid	cum–fluid	mix–fluid	calcite–fluid			‰	‰	calcite–fluid	cum–fluid	$aq_{init} - aq_{cnow}$
"High surface area (0.57 m^2 g^{-1}). baseline Sr –no added Sr" batch. T = 25°C																			
1	8.64E-06	2.48E-04	28.74	28.74	-0.45	0.18						-0.05							
2	2.10E-05	2.44E-04	11.82	11.62	0.83	0.12	-2.63	-2.63	-3.46	-3.46	-3.46	-1.47							
3	2.21E-04	2.39E-04	1.13	1.08	3.41	0.73	-0.16	-1.27	-3.56	-4.68	-3.56	-4.05							
4	6.06E-04	2.38E-04	0.41	0.39	2.20	0.15	7.13	-0.86	4.91	-3.05	-3.05	-2.84							-0.38
5	1.70E-03	2.36E-04	0.15	0.14	1.95	0.03	3.14	-0.73	1.19	-2.69	-2.69	-2.60	0.708807	0.00005	0.42	0.03	-0.04	–	-0.39
6	2.15E-03	2.35E-04	0.12	0.11	1.32	0.24	58.22	-0.66	55.27	-1.98	-1.98	-1.96	0.708805	0.00005	0.43	0.09	-0.05	–	-0.43
7	2.32E-03	2.35E-04	0.11	0.10	0.96	0.19	-1.82	-0.64	-2.78	-1.60	-1.60	-1.60	0.708010	0.00004	0.47	0.02	-0.09	–	
"High surface area (0.57 m^2 g^{-1}). high Sr" batch. T = 25°C																			
1	2.07E-03	2.48E-04	0.12	0.12	-0.47	0.10							0.708804	0.00003	0.11	0.12	0.27		-0.13
2	2.55E-03	2.49E-04	0.1	0.10	0.21	0.1	-2.34	-2.34	-3.71	-3.71	-3.71	-2.02	0.708832	0.00018	0.24	0.09	0.14	-1.36	-0.09
3	7.29E-03	2.50E-04	0.03	0.03	1.38	0.05	-0.24	-0.94	-0.44	-1.15	-0.44	-0.85	0.708804	0.00009	0.19	0.09	0.19	-0.30	
4	9.57E-03	2.51E-04	0.03	0.03	0.20	0.15	4.09	-0.58	4.09	-0.58	-0.58	-0.64							-0.04
5	1.01E-02	2.52E-04	0.02	0.02									0.708747	0.00004	0.15	0.21	0.23	-0.10	-0.14
6	1.11E-02	2.51E-04	0.02	0.02	-0.31	0.05	3.09	-0.49	3.39	-0.18	-0.18	-0.34	0.708798	0.00003	0.25	0.13	0.13	-0.40	-0.15
High surface area (0.57 m^2 g^{-1}). medium Sr" batch. T = 25°C																			
1	6.17E-04	2.48E-04	0.40	0.40	–	–	–	–	–	–	–	–	0.708817	0.00020	0.18	0.16	0.2		-0.17
2	1.22E-03	2.45E-04	0.20	0.20	–	–	–	–	–	–	–	–	0.708852	0.00025	0.34	0.12	0.04	-1.09	
3	2.40E-03	2.44E-04	0.10	0.10	–	–	–	–	–	–	–	–							-0.13
4	2.84E-03	2.44E-04	0.09	0.09	–	–	–	–	–	–	–	–	0.708793	0.00015	0.32	0.10	0.06	-0.76	
5	3.46E-03	2.43E-04	0.07	0.07	–	–	–	–	–	–	–	–	0.708723	0.00010					
6	3.65E-03	2.43E-04	0.07	0.07	–	–	–	–	–	–	–	–	0.708560	0.00014	0.33	0.10	0.05	-0.77	
7	3.85E-03	2.43E-04	0.06	0.06	–	–	–	–	–	–	–	–							0.04

(Table 5.3 continued)

"High surface area (0.57 $m^2 g^{-1}$). low Sr" batch. T = 25°C																			
1	5.69E-05	2.48E-04	4.36	4.36	–	–	–	–	–	–	–	–							0.11
2	8.86E-05	2.44E-04	2.80	2.76	–	–	–	–	–	–	–	–	0.708812	0.0001	-0.03	0.09	0.408		
3	1.98E-04	2.41E-04	1.25	1.21	–	–	–	–	–	–	–	–	0.708777	0.000013	0.11	0.03	0.27	–	0.03
4	6.92E-04	2.39E-04	0.36	0.35	–	–	–	–	–	–	–	–	0.708759	0.000005	0.07	0.02	0.31	–	-0.05
5	1.41E-03	2.37E-04	0.18	0.17	–	–	–	–	–	–	–	–							
6	1.72E-03	2.37E-04	0.14	0.14	–	–	–	–	–	–	–	–	0.708747	0.000005	0.08	0.02	0.3	–	-0.08
7	2.09E-03	2.36E-04	0.12	0.11	–	–	–	–	–	–	–	–	0.708749	0.000009	0.16	0.03	0.22	–	
"Low surface area (0.0026 $m^2 g^{-1}$). baseline Sr –no added Sr" batch. T = 25°C																			
1	7.20E-08	2.48E-04	34.50	34.50	-0.52	0.27						-0.12	0.708760	0.000005	0.04	0.01	0.34		
2	1.15E-05	2.45E-04	21.59	21.29	0.07	0.17	-1.87	-1.87	-1.94	-1.94	-1.94	-0.71	0.708757	0.000005	0.12	0.10	0.26	–	-0.38
3	3.43E-05	2.40E-04	7.24	6.99	2.48	0.17	-0.93	-1.29	-3.41	-3.78	-3.41	-3.13							
4	1.68E-04	2.39E-04	1.47	1.42	1.58	0.13	4.68	-0.88	3.09	-2.45	-2.45	-2.22							0.29
5	3.10E-04	2.38E-04	0.80	0.77	1.41	0.04	3.81	-0.82	2.39	-2.23	-2.23	-2.05	0.708747	0.00009	0.42	0.10	-0.04	–	0.12
"Low surface area (0.0026 $m^2 g^{-1}$). high Sr" batch. T = 25°C																			
0	2.10E-03	2.48E-04	0.12	0.12	-0.66	0.29						0.02	0.708817	0.00013	0.15	0.06	0.23		0.14
1	4.37E-03	2.43E-04	0.06	0.06	-0.55	0.18	-0.76	-0.76	-0.22	-0.21		-0.10	0.708798	0.00005	-0.14	0.27	0.52	15.48	0.13
2	1.45E-02	2.41E-04	0.02	0.02									0.708807	0.00007	0.04	0.08	0.34	2.55	0.00
3	2.12E-02	2.44E-04	0.01	0.01	1.09	0.02	-0.90	-0.82	-1.99	-1.91		-1.73	0.708807	0.00009	0.02	0.07	0.36	0.87	
4	2.57E-02	2.45E-04	0.01	0.01	3.04	0.27	-6.48	-0.92	-9.53	-3.96		-3.68	0.708810	0.00010	0.03	0.06	0.35	0.67	
5	2.46E-02	2.48E-04	0.01	0.01	2.41	0.42	17.10	-0.87	14.54	-3.22		-3.06	0.708799	0.00004	0.16	0.02	0.22	-0.01	
calcite_init		**2.48E-04**			**-0.51**	**0.17**							**0.708692**	**0.00009**	**0.43**	**0.15**			
calcite_final		**2.16E-04**			**-0.78**	**0.19**							**0.708524**	**0.00002**	**0.33**	**0.14**			

5.3.2 Calcite precipitation rates

Calcite precipitation rates were calculated according to a method that has been frequently applied in silicate free–drift experiments (Roerdink et al., 2015; Fernandez et al., 2019) as shown below Tang et al. (2008) as shown below (**eq. 5.3**):

$$R_p = \frac{\Delta N_{Ca}}{S \cdot \Delta t} \qquad (5.3a)$$

$$R_p^{inst.} = \frac{N_{Ca_{aq},t_I} - N_{Ca_{aq},t_{II}}}{S \cdot \Delta t} \qquad (5.3b)$$

$$R_p^{cum.} = \frac{N_{Ca_{aq}(t=0)} - N_{Ca_{aq}(t)}}{S \cdot \Delta t} \qquad (5.3c)$$

where precipitation rates (R_p), reported in units of mole m^{-2} s^{-1}, are normalized to the total available reactive surface (S, m^2) at the current time, t and the mass of Ca precipitated out of the initially oversaturated solution (ΔN_{Ca}, **eqn. 5.3a**). In chemostatic experiments like Tang et al. (2008), ΔN_{Ca} represents the total mass of Ca precipitated over the entire duration of the experiment. However, in free drift experiments the mass of Ca being removed from solution varies over the course of the experiment as a function of the proximity of the reaction to equilibrium. Thus, precipitation rates must be calculated in a different manner. There are two ways that we can characterize the ΔN_{Ca} over a given time interval, either (1) as the instantaneous (**eqn. 5.3b**) or (2) the cumulative (**eqn. 5.3c**) amount of Ca removed from solution. The instantaneous precipitation rate (log R_p^{inst}, **Table 5.2**) is calculated based on the mass of Ca precipitated out of solution over two distinct sampling times ($N_{Ca_{aq},t_I} - N_{Ca_{aq},t_{II}}$). In contrast, the cumulative precipitation rate (log $R_p^{cum.}$, **Table 5.2)** is calculated using the cumulative mass Ca precipitated out of the

initially oversaturated solution, which is determined by subtracting the initial amount of Ca ($N_{Ca(aq)}(t = 0)$) and from the Ca left in solution at the current time ($N_{Ca(aq)}(t)$).

The evolution in seed crystal reactive surface are through time is accounted for based on a volume-correction method and considering the mass of solid calcite seed crystals removed from solution as a result of sampling (Roerdink et al., 2015; Fernandez et al., 2019). Our "free-drift" experiments over the course of the reaction span the range of precipitation rates (log $R_{p,cumulative}$, **Table 5.2**) reported in previous literature for chemostatic calcite growth experiments (Lorens, 1981; Tesoriero and Pankow, 1996; Lemarchand et al., 2014; Tang et al., 2008; AlKhatib and Eisenhauer, 2017). Initial precipitation rates range from $10^{-5.41}$ ("high SA, high Sr" exp) to $10^{-4.29}$ mol m^{-2} s^{-1} ("low SA, high Sr" exp) and decrease with reaction progress to values spanning $10^{-9.97}$ ("high SA, high Sr" exp) to $10^{-6.56}$ mol m^{-2} s^{-1} ("low SA, baseline"). The average of the maximum precipitation rates determined for all six batch experiments was $10^{-4.82}$ mol m^{-2} s^{-1}, which is slightly higher than the Tang et al. (2008) value of $10^{-5.35}$ mol m^{-2} s^{-1}, and, more recently, similarly designed calcite precipitation chemostatic experiments conducted by Alkhatib and Eisenhauer (2017) ($10^{-5.12}$ mol m^{-2} s^{-1}). Using these studies as a point of reference, we show that maximum calcite precipitation rates in our free-drift experiments are faster and, notably, span the entire range of rates observed during calcite growth under chemostatic conditions in a single batch run.

5.3.3 Sr chemical and isotopic evolution through time

Measured fluid Sr, $\delta^{88/86}$Sr, and Sr/Ca ratios are shown as a function of reaction progress for all surface area and initial Sr conditions (**Fig. 5.5**). The Sr concentration evolution through time appears to differ depending on the initial amount of Sr present in solution (**Fig. 5.5A**). Batch experiments that were doped to initially high Sr (~0.72 μM) and medium Sr (0.15μM) contents show fluid Sr decreasing through time. Baseline conditions (i.e. no Sr added) and the low Sr condition where only a small amount of Sr was added into the initial solution (0.02 μM) show an inverse trend where fluid Sr actually increases through time, stabilizing to more elevated values (0.09 μM for the high SA cases, 0.02 μM

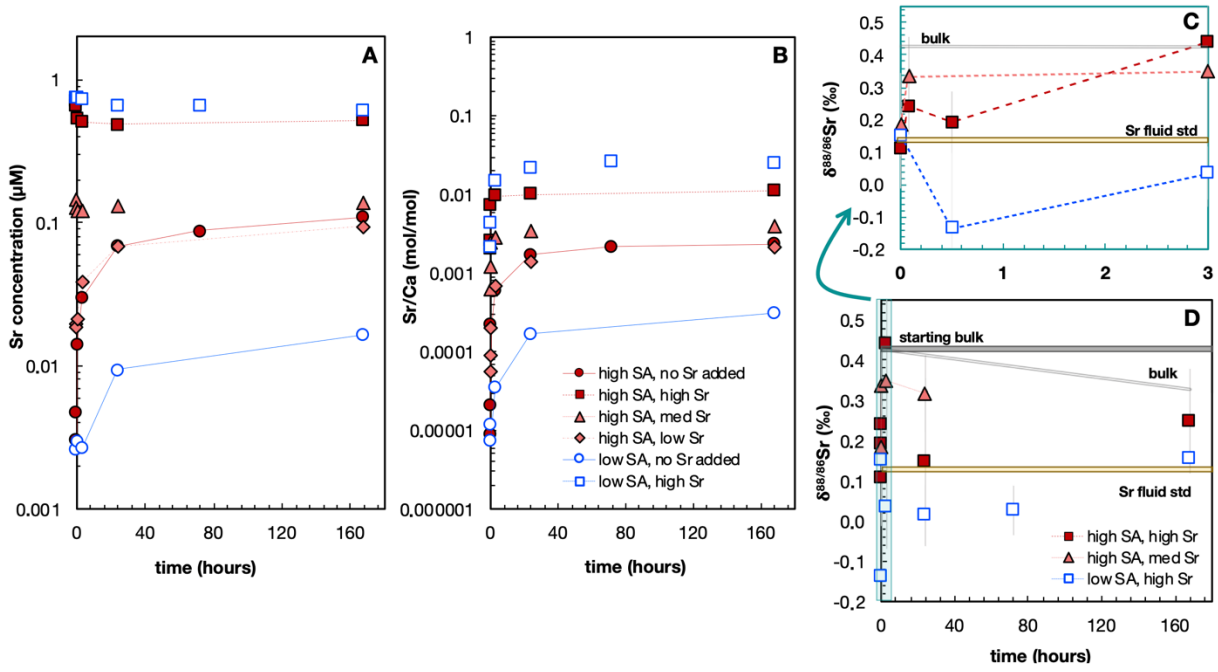

Figure 5.5 Sr batch experimental results

Sr concentration (**A**), fluid Sr/Ca ratios (**B**), and $\delta^{88/86}$Sr timeseries throughout the first 3 hours (**C**) of calcite precipitation and through the duration of the experiment (**D**) course calcite precipitation experiments beginning from oversaturated solutions and allowing 'free-drift' precipitation onto either high SA (0.57 m^2 g^{-1}, red markers) to low SA (0.0026 m^2 g^{-1} , blue markers) initial calcite seed crystals. seed crystals to reach equilibrium. Experimental conditions include no Sr added (circles), low Sr (diamonds), medium Sr (triangles) and high Sr (squares) added to initially oversaturated solutions with respect to calcite. Error bars for the Sr isotopes correspond to a 95% C.I.

for low SA, baseline case) by the end of experiment. Thus, there appear to be two regimes dependent on the amount of Sr initially in solution. One regime, defined by low initial Sr concentrations, is driven by Sr dissolution from the starting seed crystals, and the second regime, defined by high initial Sr concentrations, is driven by Sr precipitation during progressive calcite precipitation.

Fluid Sr/Ca ratios for all experiments show a general increase with time, stabilizing at elevated values, the extent of which is dictated by the amount of Sr initially in solution at the beginning of the experiment (**Fig. 5.5B**). The average fluid Sr/Ca ratios for all experiments ranges from 7.2 x 10^{-6} mol/mol (low SA, baseline case) to 0.026 mol/mol (low SA, high Sr case). The largest fluid Sr/Ca partitioning is observed in the higher Sr batch experiments (i.e. high and medium Sr batches) where the "low SA, high Sr" case appears to be lagged behind the other experiments only just starting to stabilize near ~3 days. In the case that Sr is behaving conservatively, we would anticipate fluid Sr/Ca at the end of the experiments to be ~0.0037 mole/mole and ~0.0249 mole/mole for the "high SA, med Sr" and "high/low SA, high Sr" batches, respectively. Observed fluid Sr/Ca at the end of experimental duration for the "high SA, medium Sr" (final Sr/Ca = 0.0038 mole/mole) and "low SA, high Sr" (final Sr/Ca = 0.0246 mole/mole) are very close to the conservative Sr estimated values, suggesting that the observed partitioning in these cases might be explained by conservative Sr behavior during calcite precipitation. A conservative Sr scenario is not realistic possibility for the "high SA, high Sr" experiments that arrive at final Sr/Ca values that are ~2x lower than conservative Sr estimated ratios.

Fluid Sr stable isotope ratios are also presented for the "high SA, high and medium initial Sr cases" and for the "low SA, high initial Sr" case (**Fig. 5.5C,D**). Fluid $\delta^{88/86}$Sr for these experiments start at initial values of 0.11 ± 0.03‰ reflect principally the $\delta^{88/86}$Sr

signature (0.13 ± 0.04‰) of the Sr single element standard used to dope the initial solutions. Over the course of the first 3 hours of calcite precipitation (**Fig. 5.5C**), the fluid $\delta^{88/86}$Sr of the high SA "high Sr" and "medium Sr" cases slightly increase towards maximum values of 0.44 ± 0.05‰ and 0.35 ± 0.12‰ respectively, approaching the bulk calcite value (0.43 ± 0.15 ‰). The extent of this enrichment ($\Delta^{88/86}$Sr = 0.31 ± 0.13‰, $\Delta^{88/86}$Sr = 0.22 ± 0.12‰) is minimal for these high SA experiments. The "low SA, high Sr" experiment behaves contrary to the high SA experiments where despite fluid $\delta^{88/86}$Sr exhibiting a slight decrease to a minimum value of -0.14 ± 0.27‰, remain ultimately at values close to the starting fluid (-0.05 ± 0.13, n =2). After 3 hours (**Fig. 5.5D**), "high SA, high Sr" experiment fluid $\delta^{88/86}$Sr subsequently decreases back towards the initial fluid composition (final = 0.25 ± 0.13‰). Fluid $\delta^{88/86}$Sr for the "low SA, high Sr" batch remain at values less than the initial fluid composition (0.02 ± 0.07‰, n = 2) until around 72 hours (3 days) where afterwards a slight increase in fluid $\delta^{88/86}$Sr (0.16 ± 0.02‰). The extent of Sr stable isotope fractionation in all cases appears to be much less than that observed for Ca stable isotopes (see **section 5.3.1**).

5.3.4 Fluid $\delta^{44/40}$Ca, $\delta^{88/86}$Sr, and Sr/Ca co-evolution

Fluid Ca and Sr stable isotope ratios are contrasted against fluid Sr/Ca trace element ratios for the batch experiments (**Fig. 5.6**). Fluid Ca stable isotope and Sr/Ca ratios appear to be positively correlated early in the reaction when precipitation rates are fastest (**Fig. 5.6A, B**) with fluid $\delta^{44/40}$Ca and Sr/Ca increasing with reaction progress. Then, as precipitation rates slowdown in the approach to meta-stable equilibrium, fluid $\delta^{44/40}$Ca and Sr/Ca begin to show increasing disparity in their observed behavior. This is particularly notable for the high and low SA, baseline conditions (**Fig. 5.6A**) where fluid

$\delta^{44/40}$Ca begins to re-equilibrate down towards lower values while, simultaneously, fluid Sr/Ca is continuing to increase. This decoupling between fluid $\delta^{44/40}$Ca and Sr/Ca at later times is also observed for the "high SA, high Sr" experiment, resulting in a "boomerang"-like relationship (**Fig. 5.6B**). On the other hand, "low SA, high Sr" experiment $\delta^{44/40}$Ca and Sr/Ca maintain a positive linear relationship throughout most of the duration of the experiment until the end (168 hours or 7 days) where fluid $\delta^{44/40}$Ca and Sr/Ca are observed to decrease at the same time, exhibiting none of the decoupled behavior shown for the other experiments.

The relationship between fluid $\delta^{88/86}$Sr and Sr/Ca co-evolution through time is not as apparent as $\delta^{44/40}$Ca and Sr/Ca (**Fig. 5.6C**). Specifically, fluid $\delta^{88/86}$Sr and Sr/Ca appear to be decoupled from one another throughout the entire duration of the experiment. This is particularly evident for the "low SA, high Sr" experiments where fluid $\delta^{88/86}$Sr appear to

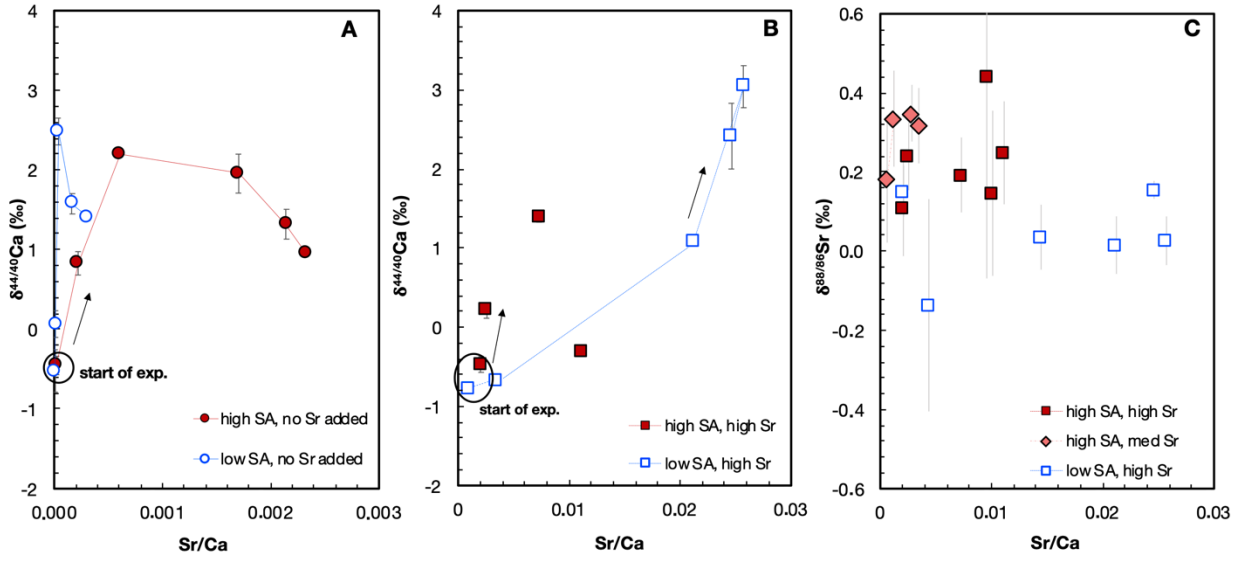

Figure 5.6 Fluid $\delta^{44/40}$Ca, $\delta^{88/86}$Sr, and Sr/Ca covariation
Fluid $\delta^{44/40}$Ca and $\delta^{88/86}$Sr vs. Sr/Ca ratios for high SA (0.57 m^2 g^{-1}, red markers) and low SA (0.0026 m^2 g^{-1}, blue open markers) baseline(**A**) and high, medium Sr (B) conditions, respectively. Error bars shown for the fluid isotope data represent 2 standard deviations.

remain at relatively constant values (reflecting very little overall fractionation) while fluid Sr/Ca are simultaneously increasing to values that are significantly higher than the high SA cases. The "high SA, high Sr" and "high SA, medium Sr" fluid $\delta^{88/86}$Sr appear to be scattered relative to the Sr/Ca values, which are increasing systematically through the course of the reaction. No distinct relationships between fluid $\delta^{88/86}$Sr and Sr/Ca are readily observed in these experiments, suggesting that these two tracers do not share similar behavior during calcite precipitation under free-drift conditions.

5.4 DISCUSSION

5.4.1 Calcite precipitation

5.4.1.1 Role of pH, growth mechanism, thermodynamic and kinetics

Calcite precipitation based on the "free-drift" design developed by Nancollas & Reddy (1971) reflects a kinetically rate limited formation of calcite according to the stoichiometry:

$$Ca^{2+}_{(aq)} + 2HCO^{-}_{3} \rightleftharpoons CaCO_{3(calcite)} + H_2O + CO_{2(aq)} \quad (5.4a)$$

and associated shifts through the attendant coupled carbonate equilibria:

$$H_2O + CO_{2(aq)} \rightleftharpoons H_2CO_{3\,(aq)} \quad (5.4b)$$

$$H_2CO_{3\,(aq)} \rightleftharpoons H^{+}_{(aq)} + HCO^{-}_{3(aq)} \quad (5.4c)$$

$$HCO^{-}_{3(aq)} \rightleftharpoons H^{+}_{(aq)} + CO^{2-}_{3(aq)} \quad (5.4d)$$

$$CO_{2(aq)} \rightleftharpoons CO_{2(g)} \quad (5.4e)$$

At the start of these experiments, the initial pH of the oversaturated solutions (pH_{init} ~8.85) leads to bicarbonate (HCO_3^-) as the predominant carbonate species (94% TIC). As a result, calcite formation follows a reaction pathway that is primarily dependent on

HCO_3^- rather than CO_3^{2-} in solution as is shown in **eq. 5.4a**. The equilibrium (K_{sp}) and kinetic rate (k_f) constants for this reaction are $10^{-8.3969}$ (Reddy and Nancollas, 1971) and $10^{-2.72}$ mol m^{-2} s^{-1} (Marty et al., 2014), respectively. This reaction follows a 1st order rate equation (Reddy and Nancollas, 1971). In this bicarbonate dependent reaction pathway, calcite precipitation produces aqueous CO_2, which in turn temporarily decreases the pH. The rates of CO_2 degassing ($CO_{2(aq)} \rightarrow CO_{2(g)}$, **eq. 5.4e**) to the surrounding pCO_2 are slow under these conditions relative to the rates of calcite formation result, which creates a slow rebound in the pH over a period of days to weeks. Slow degassing makes it relatively easy to attain equilibrium during the first few days of the experiment, but difficult to maintain this stabilized state over longer periods of time. This problem is frequently encountered in the calcite precipitation "free-drift" literature (Reddy & Nancollas, 1971; Zhang and Dawe, 1998), resulting in the establishment of temporary (24-48hrs) "metastable" equilibrium condition. This difficulty in controlling the pH and associated changes in solute composition has limited the application of "free-drift" methods for calcite growth and, thus, researchers have favored the use of more highly controlled, chemostatic experimental designs in recent years.

In this study, we have sought to improve calcite growth free-drift methods to make these techniques more viable by addressing the slow "pH-drift" problem through a modification to the experimental design. Specifically, we added a closed system sparging technique using a small air circulation pump to recycle headspace air through the reactor fluid (see further information in ***section 5.2.1***). This closed system sparging technique effectively serves to speed up the rates of CO_2 equilibration between the atmosphere and the oversaturated solution and, thus, stabilize pH quickly after the end of the kinetic portion of the reaction as is shown in the pH timeseries (**Fig. 5.4B**). Results from an initial

round of batch experiments performed without this pH control (**Appendix F**) show that without this correction to the experimental design, slow CO_2 degassing causes the pH to drop to significantly lower values at the end of the kinetic portion of the calcite precipitation reaction (pH_{min} ~ 8.2) relative to the pH-controlled experiments (pH_{min} ~ 8.6). Additionally, the pH in these preliminary batch experiments reached pH values indicative of CO_2 equilibration with the surrounding headspace (~8.8) after approximately 6 days (well after the initial calcite precipitation event). As a result of this slow increase in the pH, the Ca^{2+}_{aq} concentrations remained far from equilibrium, reaching average final concentrations of 0.13 mM (n=2), ~ 3x higher than the values attained in the pH-controlled batch runs. Notably, even Ca^{2+}_{aq} concentrations began to increase by the end of the experimental duration implying a small amount of late-stage calcite dissolution due to instability in the pH of the reactive fluid (**Appendix F**).

Thus, we confirm that pH and its evolution during calcite precipitation plays a critical role in the establishment of (metastable)equilibrium under free-drift (i.e. variable) conditions. This feedback can and does significantly impact the extent of stable isotope or trace element fractionation (as demonstrated by measured fluid $\delta^{44/40}Ca$ ratios for the preliminary set of experiments, **Appendix F**). The relationship between pH and tracer partitioning have been considered in experimental studies of Sr incorporation (Gabitov and Watson, 2007) and stable Ca isotope fractionation (DePaolo, 2011) under chemostatic, steady-state conditions. However, due to the complications of free drift, this relationship to date has not been fully explored under such conditions. The results from this study represent a first step in this regard and serve as motivation for further investigations oriented towards the behavior of trace elements and isotope ratios in dynamic systems.

For the present study, we took measures to ensure that no other calcium carbonate polymorphs were formed during the experiment, which would have obvious impacts on solute compositions and partitioning of stable isotope and trace element tracers within the system. Oversaturated solutions were prepared to reach a targeted saturation state that is well below the threshold supersaturation of amorphous calcium carbonate. This transition is generally defined by an ion activity product (IAP) and Ω ($\log Q/K_{sp}$) greater than 5.9×10^{-7} and 4.60 respectively (Clarkson et al., 1992). IAP and Ω for the starting conditions of our experiments were constrained using CrunchTope (Steefel et al., 2015) and result in values of 6.18×10^{-8} and 1.18, respectively. These values confirm that ACC was not formed during the course of the experiment. Also, these saturation states are at the lower limit of the transition between a spiral-dislocation (Burton et al., 1951) and 2D-nucleation (i.e. high order rate; Dove et al., 2008) calcite growth mechanism, which is placed at Ω ~1.0 to 1.6. Thus, our experiments can be considered to follow a classical dislocation-driven step growth rate that is linearly dependent on the oversaturation (Nielsen et al., 2012). Due to the sensitivity of stable isotope and trace element fractionation to solution stoichiometry, all batch experiments were held to the same initial Ca:CO3 ratio of 0.98 (**Table 5.1**).

5.4.1.2 Instantaneous vs. cumulative calcite precipitation rates

Calcite precipitation rates in all six batch experiments are generally observed to decrease throughout the course of the experiment (**Fig. 5.7**). Precipitation rates calculated based on the instantaneous amount of Ca precipitated between two sampling times ($\mathbf{R_p^{inst}}$, **eqn. 5.3b**) exhibit the largest drop (between 5 to 6 order of magnitude, $10^{-5} \pm 10^{-6.09}$ to $10^{-10.24} \pm 10^{-11.14}$ moles m^{-2} s^{-1}) from rates rate attained at the start to those at the finish. In comparison, cumulative precipitation rates determined from the total amount of Ca

removed from solution between the start of the experiment and a given sampling time ($\mathbf{R_p^{cumul.}}$, **eqn. 5.3c**) experience a decrease in rates between 2 to 4 orders of magnitude respectively ($10^{-5.00} \pm 10^{-6.09}$ to $10^{-7.89} \pm 10^{-8.84}$ moles m^{-2} s^{-1}). The change in the respective instantaneous and cumulative precipitation rates as a function of reaction progress follow a power law relationship (high SA batches: $R^2 = 0.9876$; low SA batches: $R^2 = 0.9598$) where instantaneous rates vary as a function of ~log $R_p^{cumul.2}$ (**Fig. 5.7**) across all free-drift experiments. Minor differences in the power law trends between the high and low SA precipitation rates could be related to either the surface area of the calcite seeds used to initiate precipitation, the initial aqueous Sr^{2+} in solution, or both. More importantly, from this comparison between these two methods of calculating the calcite precipitation rate, the use of cumulative precipitation rates for calcite growth under non-steady state conditions will both underestimate the extent of instantaneous precipitation in the early stages of the experiment and

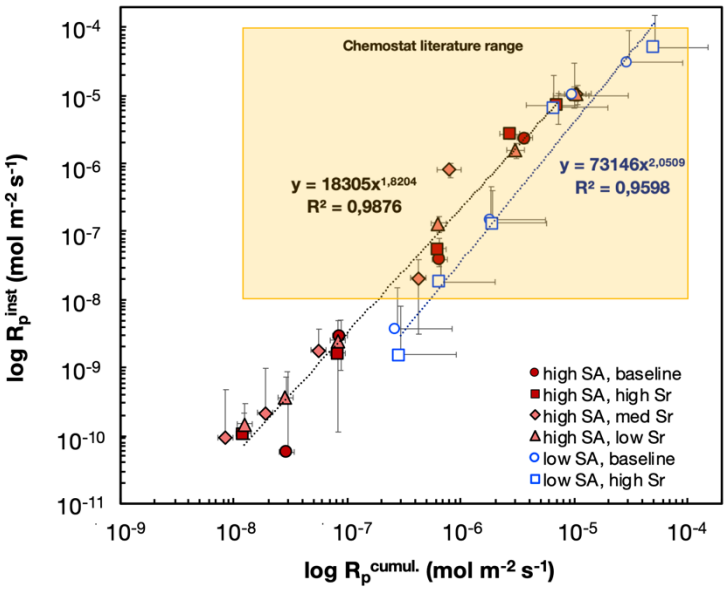

Figure 5.7 Rp^{inst} vs. $R_p^{cumul.}$ relationships
Experimentally determined instantaneous (R_p^{inst}, eq. 5.3b) calcite precipitation rates plotted against cumulative precipitation rates ($R_p^{cumul.}$, eq. 5.3c) in log–log space. All batch experiments show a consistent log-linear relationship where instantaneous rates vary approximately as a function of $R_p^{cumul^2}$. For reference, the range in steady state calcite precipitation experiments (from Tang et al., 2008 and AlKhatib and Eisenahuer, 2018) in the literature is presented here as a yellow square. Error bars correspond to one standard deviation.

overestimate rates in the approach to near-equilibrium conditions near the end of the experiment.

Thus, the instantaneous precipitation rate is a more accurate representation of the overall precipitation rate of calcite growth under free-drift conditions, particularly at early stages in the reaction when appreciable amounts of Ca are being rapidly removed from solution over short time intervals. However, the use of instantaneous precipitation rates does have some major limitations. Specifically, as less and less Ca is removed out of solution in the approach to equilibrium, the difference between the mass of Ca present between the two sample times approaches zero and the instantaneous precipitation rate breaks down as a result. In this scenario, the instantaneous precipitation rate is subject to larger uncertainty as analytical measurements might not be precise enough to quantify the trace amounts of Ca precipitated over later time intervals. Thus, the cumulative precipitation rate can be more useful at later stages in the reaction despite the fact that it generally tends to overestimate the instantaneous rate. The explicit power-law relationship shown above between cumulative and instantaneous precipitation rates can be a useful tool in this manner to estimate instantaneous rates in the approach to near-equilibrium for free-drift experiments.

5.4.1.3 Influence of surface area on calcite precipitation rates

Bulk precipitation rates (log R_p^{bulk}, **Table 5.2) ,** reported in mol s^{-1}, reflect the amount of aqueous Ca^{2+} removed over a given time interval (here defined as the change in fluid Ca^{2+} between initial and current time).When we compare bulk precipitation rates between the surface area conditions, lower surface area batch experiments exhibit overall slower rates ($10^{-6.70} \pm 10^{-7.22}$ mol s^{-1}, n = 2) compared to the higher surface area cases ($10^{-5.97} \pm 10^{-6.84}$ mol s^{-1}, n = 4) as anticipated. These results thus validate what is already well established in

the literature, namely that mineral surface area affects the rates of chemical reactions. When these values are normalized to the reactive surface areas of the given seed crystals, a somewhat counterintuitive observation of slightly faster rates when precipitation occurs on lower surface area crystal seeds is noted. This is an artificial effect in that we are dividing over a smaller total surface area relative to a high surface area case, yet not accounting for the fact that the change in saturation state at a given point in time is closer to equilibrium for the high surface area relative to the low surface area. The impact of initial Sr content on calcite precipitation rates will be addressed separately in the following section (**section 5.4.1.4**).

5.4.1.4 Presence of strontium and impacts on calcite precipitation rates

Comparison of experimentally determined precipitation rates between batch experiments of the same surface area condition, but with varying amounts of initial aqueous Sr^{2+} content in solution (ranging from ~0.003μM to ~0.72 μM), do not appear to significantly differ from one another. In the high SA case, all batch experiments show comparable initial precipitation rates around $10^{-5.00} \pm 10^{-6.03}$ mol m^{-2} s^{-1} (n = 4) that lie within the respective errors of one another. Indistinguishable precipitation rates are observed as well in the low SA batch experiments. Thus, the influence of Sr on precipitation rates is not discernable in these free-drift calcite growth experiments. These findings diverge from previous chemostatic studies investigating calcite growth under the presence of impurities like Sr^{2+} where increased impurity concentrations were shown to slow down overall calcite growth rates (Meyer 1984; Nehrke et al., 2007; Bracco et al., 2012; and others). However, it is important to note that in these prior studies the saturation state of the fluid, Ω, was held constant throughout the experimental duration. Under these steady-state conditions, the influence of Sr^{2+} on calcite growth rates can be isolated and

observed directly. In our free-drift experiments where the saturation state varies significantly through time (**Table 2)**, rate is dependent to a large extent on the overall Ω. Thus, any minor effects associated with the presence of Sr^{2+}on the observed calcite growth rates is impossible to isolate and quantify under free-drift conditions.

5.4.2 Sr partitioning during calcite formation

5.4.2.1 Sr dissolution vs. incorporation and Sr-carbonate solid solution thermodynamics

A notable observation from our calcite precipitation experiments was the existence two Sr partitioning regimes that are differentiated by the amount of Sr^{2+} initially in solution (**see section 5.3.3**). Reversible reactions like Sr-carbonate ($Sr_xCa_{1-x}CO_3$) and calcite formation are "self-correcting" by nature. This means that any significant imbalance between the concentration of reactants and products will shift the reaction to re-establish its natural solubility equilibrium values (Le Chatelier's principle). The equilibrium solubility of the $SrCO_3$ phase during calcite growth is reflective of a calcite–$SrCO_3$ solid solution where Sr^{2+} is substituted into the rhombohedral calcite crystal lattice. As rhombohedral $SrCO_3$ does not exist in nature, a hypothetical solubility for this phase is necessary to accurately describe the thermodynamics of the calcite –$SrCO_3$ solid solution. Previous studies have estimated this hypothetical $SrCO_3$ solubility to values ranging from $10^{-6.1}$ to $10^{-8.2}$ with an average of ~$10^{-7.6}$ (Bötcher, 1997; Kulik et al., 2010).

In the low and baseline Sr experiments where starting fluid Sr concentrations (0.003 μM and 0.02 μM, respectively) are lower than the solubility concentration for $SrCO_{3(s)}$ (K_{sp}~0.025μM, Kulik et al., 2010), the governing reaction $(Ca^{2+}, Sr^{2+})_{(aq)} + CO_3^{2-} \rightleftharpoons Sr_xCa_{1-x}CO_{3(s)}$ will shift to the left for Sr. Thus, Sr partitioning in this depleted aqueous Sr^{2+} regime favors the preferential dissolution of Sr from the pre-existing calcite seeds to solution as

shown by fluid Sr^{2+} concentrations increasing with time (**Fig. 5.5A**). When initial fluid Sr concentrations are higher than the Sr-carbonate solubility, as is the case for the med and high Sr experiments (0.15 μM and 0.72μM, respectively), Sr is preferentially incorporated into the growing calcite leading to a general decrease in fluid Sr^{2+} concentrations with time (**Fig. 5.5A**). Thus, the solubility with respect to $SrCO_3$ plays a major role in the behavior of aqueous Sr^{2+} during calcite formation, representing an important transition point between Sr dissolution and Sr incorporation that is well-bounded in these free-drift experiments.

Another noteworthy observation related to Sr dissolutions vs. incorporation behavior in these batch experiments is that none of the reactions ultimately reach the predicted $SrCO_3$ solubility concentration by the end of the experimental duration. Apart from the low SA experiments, which appear to still be far from (metastable) equilibrium or steady state, all batch experiments appear to reach steady state values by the end of the reaction that are distinct for each Sr condition. For example, the high SA, high Sr batch reaches fluid Sr^{2+} values of ~0.5 μM. That is roughly 4× and 5× higher than final values obtained in the high SA, med Sr (~0.14 μM) and high SA, low Sr (0.09 μM) experiments, respectively. In the experiments where Sr incorporation into the growing calcite takes place (i.e. high and med Sr cases) the final steady state appears to be strongly dependent on the initial fluid Sr^{2+} concentrations. This behavior can most likely be attributed to the relationship between the pH, carbonate speciation, and the Sr^{2+} presence in solution, which all can influence the solubility of the resulting calcite–$SrCO_3$ ($Sr_xCa_{1-x}CO_3$) solid solution.

In particular, it is well established in the literature that increasing Sr^{2+} concentrations in solution greatly enhance the overall solubility of the calcite–$SrCO_3$ solid solution as a

result of enhance solubility of the calcite end-member (Nehrke et al., 2007; Kulik et al., 2010; Nielsen et al., 2013). In an extreme case where a large quantity of Sr is incorporated, the calcite solubility could reach a point where it is no longer a thermodynamically stable solid phase, in which case Ca^{2+} dissolution would be initiated (Nielsen et al., 2013). For the experiments in this study, this behavior of subsequent calcite dissolution is not observed based on the establishment of steady state fluid Ca^{2+} concentrations towards the end of the experiment (**Fig. 5.4A**). Simultaneously, as more Sr^{2+} is being incorporated into the lattice of the growing calcite, Sr^{2+} ion detachment rates are gradually inhibited and, thus, the solid solution shifts towards the $SrCO_3$ endmember over time (Nielsen et al., 2013). All in all, Sr^{2+} incorporation has a significant influence on the balance between the calcite and $SrCO_3$ solid solution endmembers. Thus, the overall solubility of the $Sr_xCa_{1-x}CO_3$ solid solution that is ultimately established during calcite precipitation depends strongly on the amount of Sr in the fluid phase and will vary among our experiments. How this interaction ultimately controls the steady state values obtained for fluid Sr^{2+} concentrations will be discussed in further detail below (***section 4.3.4***).

5.4.2.2 Kinetics of strontium incorporation into growing calcite

Along with calcite precipitation thermodynamics, the kinetics of Sr incorporation also appear to be dictated by the amount of Sr initially present in solution. Sr uptake rates (R_{uptake}^{Sr}) were calculated according to the cumulative calcite precipitation rates described in **eqn. 3c** and are reported in mol m^{-2} s^{-1} in **Table 2**. Batch experiments with high initial fluid Sr exert the fastest overall Sr uptake rates with values of $10^{-8.67} \pm 10^{-9.51}$ and $10^{-8.83} \pm 10^{-9.16}$ mol m^2 s^{-1} for the "high SA, high Sr" and "low SA, high Sr" cases, respectively. The batch condition with medium initial fluid Sr concentration expresses the slowest Sr uptake rates with an initial value of $10^{-9.20} \pm 10^{-10.21}$ mol m^2 s^{-1}. In all cases, Sr uptake rates

are observed to decrease with time, reaching values that are on average 2 orders of magnitude less than initial rates by the end of the experiments. Among experiments of the same surface area condition, faster overall rates for the high Sr case compared to the medium Sr case imply that it is the amount of Sr initially in solution or, in other words, the distance the system is from equilibrium with respect to the respective $Sr_xCa_{1-x}CO_3$ solid solution (**section 5.4.2.1**) that dictates Sr incorporation kinetics. On the other hand, comparison of uptake rates across surface area conditions (i.e. high vs. low SA) show that the Sr incorporation rates onto higher surface area calcite seeds are enhanced relative to lower surface area grains. These results suggest that, with similar starting solute compositions, it is the available reactive surface area of the pre-existing calcite seeds that dictates Sr uptake kinetics. These observations suggest that Sr uptake kinetics during calcite precipitation under free-drift conditions are influenced by both the surface area and Sr content in the reactive fluid.

Another notable relationship that emerged from our experimental data is a clear positive correlation between Sr uptake and calcite precipitation rates for all three higher fluid Sr^{2+} initial conditions (**Fig. 5.8A**). This relationship between Sr uptake and calcite precipitation rates can be accurately characterized by a linear regression in log – log space as follows for each high Sr experiment (**eq. 5.5**):

$$\log R^{Sr}_{uptake} = 0.5403 \cdot \log R^{Ca}_{p} - 5.8863, R^2 = 0.99 \quad (5.5a)$$

$$\log R^{Sr}_{uptake} = 0.6328 \cdot \log R^{Ca}_{p} - 5.9001, R^2 = 0.99 \quad (5.5b)$$

$$\log R^{Sr}_{uptake} = 0.2930 \cdot \log R^{Ca}_{p} - 7.6990, , R^2 = 0.99 \quad (5.5c)$$

where the high Sr experiments – i.e "high SA, high Sr", "high SA, medium Sr", and "high SA are described by equations **eq. 5.5a**, **eq. 5.5b**, and **eq. 5.5c** respectively. These results

indicate that based on the calcite precipitation rate, the Sr uptake rate can be accurately approximated via a simple log linear relationship. Importantly, Sr uptake rates in all high Sr cases are always slower than overall calcite precipitation rates throughout the entirety of the reaction (**Fig. 5.8A**). Early in the reaction the difference between Sr uptake rates (average of $10^{-8.84} \pm 10^{-9.12}$ mol m^{-2} s^{-1}, n =3) are approximately 4 order of magnitude slower than calcite precipitation rates (average of $10^{-4,64} \pm 10^{-5.55}$ mol m^{-2} s^{-1}, n = 3). Yet, the difference between the rates diminishes significantly in the approach to equilibrium with Sr uptake rates only an order of magnitude slower than calcite growth rates. Thus, we can conclude based on these observations that Sr uptake kinetics are sluggish compared to overall calcite growth kinetics. Slow Sr uptake kinetics are particularly evident in the "low SA, high Sr" experiment where Sr uptake rates remain relatively elevated throughout the course of the reaction, resulting in a log-linear trendline that is shallower

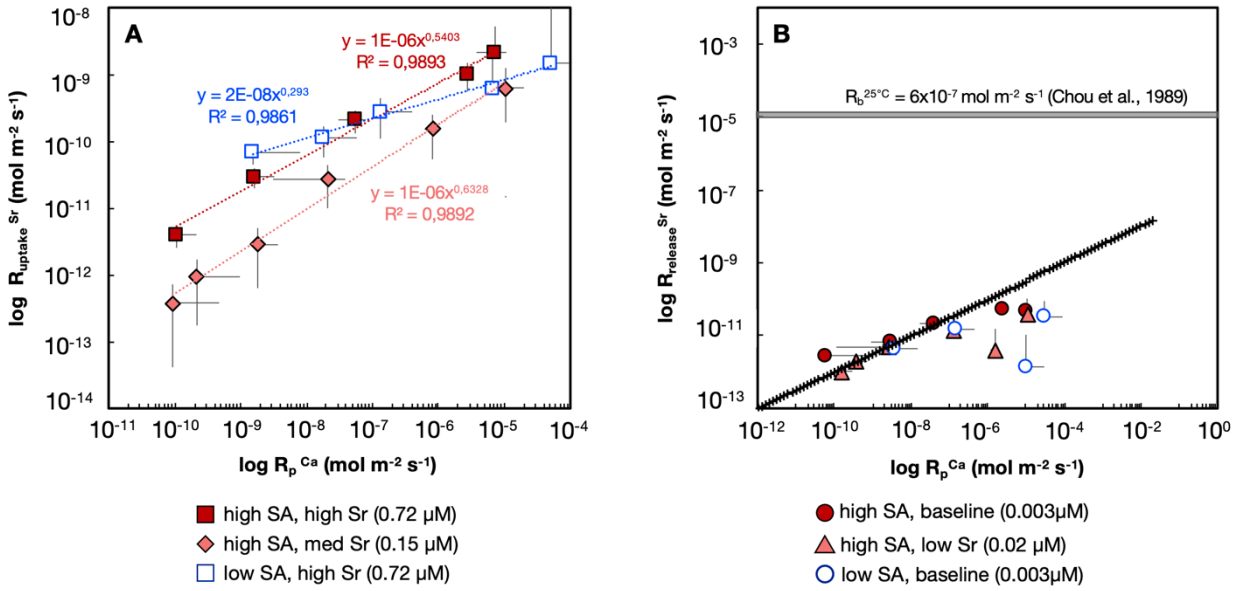

Figure 5.8 Sr uptake and release rates and their co-variation with calcite precipitation rates
Sr uptake rates (**A**) and Sr dissolution rates (**B**) vs. Cumulative calcite precipitation rates for the high SA (0.57 m^2 g^{-1}, red markers) and low SA (0.0026 m^2 g^{-1} , blue markers), respectively. DePaolo (2011) predictions for the Ca dissolution rate (R_b^{Ca}) are provided alongside the Sr dissolution rates (shown here as black crosses). Experimental conditions include no Sr added (circles), low Sr (diamonds), medium Sr (triangles) and high Sr (squares) added to initially oversaturated solutions with respect to calcite.

relative to the high SA cases. This observation along with the distinct log-linear relationships between $\log R^{Sr}_{uptake}$ and $\log R^{Ca}_{p}$ for each high Sr and surface area experiment further imply that Sr uptake rates are more sensitive to surface area and initial Sr content than the overall calcite precipitation rates.

5.4.2.3 Sr as a potential tracer of calcite dissolution rates, R_b

Just as for Sr uptake rates, Sr "release" rates were calculated following the same method as for calcite precipitation rates (**section 5.3.1**) with the sole modification that the mass of Sr^{2+} being introduced into solution from the seed crystals is tracked through time ($R_{release}^{Sr}$, **Table 5.2**). Dissolution rates were determined for the three experiments (high SA baseline, high SA low Sr, and low SA baseline conditions) in which Sr release was clearly the dominant process taking place (**Fig. 5.5A**). Overall, Sr release rates were found to be slower than calcite precipitation rates with values ranging from $10^{-10.53} \pm 10^{-11.02}$ mol m^{-2} s^{-1} (n=3) early in the experiment to $10^{-11.72} \pm 10^{-12.36}$ mol m^{-2} s^{-1}. Release rates are indistinguishable between the "low SA, baseline case" ($10^{-10.49} \pm 10^{-11.25}$ mol m^{-2} s^{-1}) and the "high SA, baseline case" ($10^{-10.30} \pm 10^{-11.66}$ mol m^{-2} s^{-1}) when the rates are normalized to the surface areas. However, when the release rates are calculated without the surface area normalization, bulk release rates (in mole s^{-1}) are much slower for the "low SA, baseline" experiment (initial rate = $10^{-12.78} \pm 10^{-13.54}$ mole s^{-1}) compared to the "high SA, baseline" rates (initial rate = $10^{-11.25} \pm 10^{-12.61}$ mole s^{-1}). These observations agree with the generally inferred positive relationship between surface area and dissolution rates where increases in available reactive surface corresponds to enhanced Sr release (and vice versa). Measured fluid Sr^{2+} concentrations with time also confirm this relationship for the high and low SA, baseline conditions where the "low SA, baseline" experiment remains at lower fluid Sr concentrations throughout most of the experiment as a result of sluggish

release kinetics analogous to slow uptake rates observed in the "low SA, high Sr" experiment (**Fig. 5.5A**).

Interestingly, despite order of magnitude differences in the starting fluid Sr^{2+} concentrations, the "low Sr" and "baseline", high SA experiment dissolution rates are quite comparable, with initial rates tightly constrained around $10^{-10.35} \pm 10^{-11.37}$ mol m^{-2} s^{-1}. Also, contrary to the Sr incorporation experiments, these two high SA experiments appear to reach similar metastable equilibrium values ($[Sr^{2+}]_{eq} \sim 0.10\ \mu M$) towards the end of the experiment. These results suggest that Sr release rates are not nearly as sensitive to initial fluid Sr contentes. Thus, this data provides a unique opportunity to gain insight into the evolution of the backward, dissolution rate (R_b) for calcite.

Describing how this R_b component of the overall or net precipitation rate varies during calcite precipitation has significant implications for calcium isotope fractionation and the extent of isotope re-equilibration. As a consequence, many studies have sought to characterize calcite dissolution rates and, importantly, how they vary as a function of overall precipitation rates (R_p). Several studies have constrained calcite dissolution rates within the range of pH implemented in this study (7.5–9) at 25°C, arriving at a value equal to $10^{-6.22}$ mol m^{-2} s^{-1} (Chou et al., 1989; Alkattan et al., 1998; LeMarchand et al., 2004; Tang et al., 2008). Recent experimental studies generally assume a constant R_b across broad ranges in net calcite precipitation rate (R_p) (Tang et al., 2008; AlKhatib and Eisenhauer, 2017), which is a reasonable assumption for their chemostatic steady state conditions. However, to account for a realistic scenario in which R_b evolves during calcite precipitation in variable, free–drift conditions, DePaolo (2011) tested a representation of this evolution through a simple relationship where R_b varies as a function of 10^{-4} $R_p^{1/2}$.

Although Sr release rates during calcite growth are not reflective of net calcite dissolution rates, they can perhaps serve as a reasonable proxy for contributions from the backward, rate (R_b) that serves as a balance to precipitation rates (R_f) in the approach to a dynamic equilibrium ($R_{net} = 0$; $R_f = R_b$). To determine if this is plausible under conditions of net calcite growth, we compare the observed relationship between calculated Sr release and calcite precipitation rates (**Fig. 5.8B**) with the values of R_b predicted according to a $10^{-4}\ R_p^{1/2}$ relation proposed by DePaolo (2011). In log–log space, Sr dissolution rates (R_b^{Sr}) are linearly correlated with calcite precipitation rates (R_p^{Ca}) as is the case for the DePaolo (2011) predicted R_b values. Remarkably, Sr release rates plot perfectly along the predicted R_b values, following the same slope of the $10^{-4}\ R_p^{1/2}$ function. This significant result shows that Sr release rates vary according to the same relationship proposed by DePaolo (2011) for the backward, calcite dissolution rate. These results represent the first time that R_b varying as a function of $R_p^{1/2}$ is actually tested against Sr release rates and validated, thereby proving that dissolution and Sr release rates are always slower than precipitation rates during calcite growth. Although we acknowledge that Sr release is not exactly R_b, these rates derived from Sr are the closest approximation we currently have to the backward, dissolution rate during calcite growth. At a minimum, Sr release rates may provide a lower bound to calcite R_b and its evolution as a function of calcite precipitation rates, characterized by a log linear relationship. Overall, the evolution of Sr release rates as a function of calcite precipitation rates represents the first key evidence of a varying R_b during calcite growth under free-drift conditions.

5.4.3 Ca/Sr trace element and Ca, Sr stable isotope fractionation during calcite formation

5.4.3.1 Calculating Ca fractionation factors in free drift conditions

The fractionation factor is a critical parameter in stable isotope geochemistry that directly quantifies the extent of fractionation between two phases. In general, the fractionation factor (α) is calculated as the isotope ratio of the instantaneous product ($R_{prod,flux}$) divided by the isotope ratio of the reactant (R_{reac}). For our purpose secondary calcite precipitate is the "product", while the "reactant" is the residual dissolved calcium in the surrounding fluid phase. Generally, the isotope fractionation between the reactant and product is reported as the measured difference between the solid and fluid phases (**eq. 5.6**):

$$\Delta_{calcite\text{-}fluid} = \delta_{calcite} - \delta_{fluid} \qquad (5.6)$$

and is related to $\boldsymbol{\alpha}$ as (**eq. 5.7**):

$$\Delta_{calcite\text{-}fluid} \approx 1000 \times \ln\alpha \qquad (5.7)$$

for calcium and strontium stable isotopes the fractionation factor is commonly reported as $\Delta^{44/40}Ca_{calcite\text{-}fluid}$.

During non-steady state calcite precipitation, Ca stable isotope fractionation occurs between the surrounding fluid and a growing mineral surface that is isotopically evolving and thus distinct from the initial, pre-existing grain. Thus, calculating the fractionation factor based on the initial isotopic ratio of the preexisting calcite upon which heterogeneous precipitation occurs is not inherently valid, and values can potentially differ substantially from the instantaneous isotopic value of the calcite most recently formed. This issue is frequently encountered in other mid-mass stable isotope systems, particularly in the silicate literature where secondary silicates form predominantly in

non-steady state conditions (Geilert et al., 2014; Roerdink et al., 2015; Fernandez et al., 2019). These studies have used classical isotope mass balance to estimate the isotope ratio of the recently precipitated solid (**$\delta^{44/40}Ca_{ppt}$**) through time and coevolution of the fluid and solid surface (**eq. 5.8**).

$$\delta^{44}Ca_{aq,I}mCa_{aq,\,I}=\delta^{44}Ca_{aq,II}mCa_{aq,\,II}+\delta^{44}Ca_{ppt}mCaCO_{3,ppt} \qquad (5.8)$$

where $\delta^{44}Ca_{aq}$ and mCa_{aq} represent the measured fluid calcium isotope ratios and dissolved Ca concentrations, respectively, between two sampling times ($\delta^{44}Ca_{aq,I/II}, mCa_{aq,I/\,II}$). $\delta^{44}Ca_{ppt}$ and $mCaCO_{3,ppt}$ represent the isotope ratio and amount of calcite precipitated during the given time interval, respectively. The $\delta^{44}Ca_{ppt}$in this case would represent the isotope ratio of precipitated calcite between times I and II, resulting in a value that we will call for the purpose of this excersise the "instantaneous" fractionation factor ($\alpha_{(inst)}$). Although, in reality, the interval between two sampling times does not represent a true "instantaneous" value, which would be established in the case where the interval between two time points approaches zero. The cumulative $\delta^{44}Ca_{ppt}$ can also be estimated by setting $\delta^{44}Ca_{aq,I}$, $mCa_{aq,I}$ in the mass balance equation equal to the initial values, resulting in a value of $\alpha_{(cum)}$. Using these two methods, the calcium isotope ratio of the precipitated calcite can be tracked throughout the reaction progress. Accordingly, the fractionation factor can now be calculated using the estimated $\delta^{44}Ca_{ppt}$ (**eq. 5.9**):

$$\alpha_{(\text{cum. or inst.})}=\frac{\left(\delta^{44}Ca_{ppt}+1000\right)}{\left(\delta^{44}Ca_{fluid}+1000\right)} \qquad (5.9a)$$

or as

$$\Delta^{44}Ca_{calcite\text{-}fluid} = \delta^{44}Ca_{ppt} - \delta^{44}Ca_{fl} \qquad (5.9b)$$

In our experiments, clear differences can be observed between the $\Delta^{44/40}Ca_{cum.ppt\text{-}fluid}$ and $\Delta^{44/40}Ca_{inst.ppt\text{-}fluid}$ as the reaction progresses with time (**Table 5.3; Fig. 5.9A**). Over the short period of time between initiation and the first sample collection, the cumulative and "instantaneous" fractionation factors are inherently identical. As stated earlier, this is due to how our "instantaneous" fractionation factor is defined, which is, in this case, between two sampling time points, t_I and t_{II}. Thus, the two measured time points used to calculate the "instantaneous" value are identical to those used to calculate the cumulative fractionation factor (i.e. the initial conditions, t=0, and the first sampling time, t_1). After the first time point measured, the cumulative and "instantaneous" fractionation factors become distinct. When precipitation rates are high and isotope fractionation is dominated by kinetic isotope effects, the fractionation factor calculated using the cumulative precipitate value is much larger (high SA, baseline ex. $\Delta^{44/40}Ca_{cum.ppt\text{-}fluid}$ = -4.68‰) than the fractionation factor calculated using the instantaneous product (high SA, baseline ex. $\Delta^{44/40}Ca_{inst.ppt\text{-}fluid}$ = -3.56‰). This ~1‰ difference between the cumulative and instantaneously calculated fractionation factors illustrates the sensitivity of the fractionation factor to how the freshly precipitated calcite isotope composition is defined. In the instantaneous approach, the $\delta^{44/40}Ca$ of the precipitated calcite essentially represents a weighted average of the calcite instantaneously precipitated over the given time period, whereas the cumulative approach is a weighted average over the entire duration from initiation to the given sampling time. During these fast, kinetic events when new and isotopically distinct layers are being generated quickly on the calcite surface, using a cumulative $\delta^{44/40}Ca$ could result in a loss of information that can be

significant and lead to an over-estimation of the kinetic fractionation. Even though the "instantaneous" approach itself inherently contains some loss of information (due to the fact that we sample the $\delta^{44/40}$Ca of the fluid and calcite formed at each instant in the reaction), calculating the $\delta^{44/40}$Ca of the precipitated calcite based on the mass balance between two measured time points can provide a better estimation of the fractionation factor for the kinetically dominated portion of the reaction (Ref silicate examples again).

On the other hand, later in the experiment as the precipitation rate decreases significantly in the approach to metastable equilibrium, the mass precipitated over two measured time points, mCa_{aq}, becomes smaller and smaller, approaching zero. This leads to unreasonable fractionation factors (e.g. for our high SA, baseline $mCaCO_{3,inst.ppt}$ = 0.001 mmoles and $\Delta^{44/40}Ca_{inst.ppt\text{-}fluid}$ = +55.27‰). Thus, calculating the fractionation factor based on instantaneously precipitated calcite is limited only to the kinetic portion of the experiment where a substantial mass of calcite is precipitated between sampling intervals. Fractionation factors based on the cumulatively precipitated calcite are more appropriate at near-equilibrium conditions. Combining the instantaneously calculated fractionation factors calculated early in the reaction with the cumulative fractionation factors for the later portion in the approach to metastable equilibrium thus returns a reasonable description of the overall behavior of the free-drift system (**Fig. 5.9B**).

The fractionation factors and precipitation rates experimentally determined in this study are compared with the Tang et al. (2008) dataset, which was formed under chemostatic conditions where the calcite was precipitated homogenously at steady state rather than onto preexisting seed crystals during free drift (**Fig. 5.9**). Additionally, we explore the overall literature range in precipitation rates and fractionation factors for

inorganic calcite (yellow box; Gussone et al., 2003; Lemarchand et al., 2004; Gussonne et al., 2005) and culture experiments (green box; Böhm et al., 2006; Gussonne et al., 2003; Gussonne et al., 2007; Langer et al., 2007; Müller et al., 2011; Kisakürek et al.,2011). Our average $\Delta^{44/40}Ca_{calcite\text{-}fluid}$ for the high SA, baseline case (-2.72 ± 0.80‰) and low SA, baseline case (-2.51 ± 0.64‰) is larger than that determined in the Tang et al.(2008) study (-1.02± 0.32‰) and other similar calcite precipitation experiments (-1.5 ± 0.25‰, Lemarchand et al., 2004; -1.01 ± 0.25‰, Gussone et al., 2005; -1.42 ± 0.18‰, Alkhatib and Eisenhauer, 2017;+ 0.4‰, Oelkers et al.,2019). However, average $\Delta^{44/40}Ca_{calcite\text{-}fluid}$ values do fall in the same range as the observed fractionation factors determined for a carbonate aquifer (-

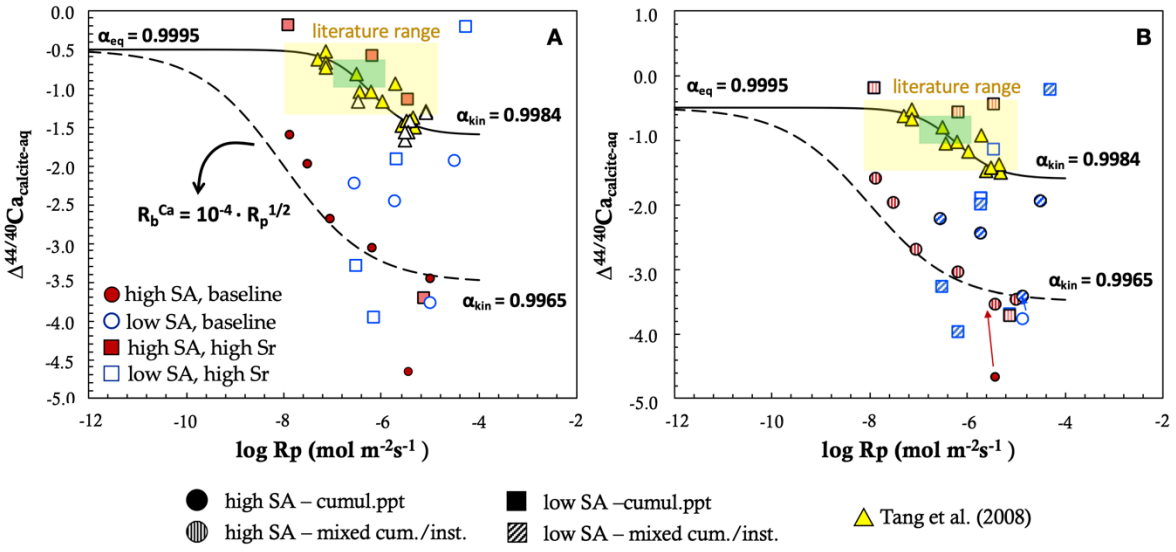

Figure 5.9 $\Delta^{44/40}Ca$ as a function of precipitation rate

The fractionation factors and precipitation rates experimentally determined in this study are compared with the Tang et al.(2008) dataset, which was formed under chemostatic conditions where the calcite was precipitated homogenously rather than onto preexisting seed crystals. (**A**) the Ca fractionation factors calculated using the cumulative solid precipitate value determined using isotope mass balance and (**B**) the Ca fractionation factor calculated using the instantaneously determined solid precipitate value for both high SA (red circles) and low SA (blue squares) baseline (no Sr added) experiments. DePaolo (2011) SRK model predictions are shown in black solid and dashed lines, respectively that were determined using the same equilibrium fractionation factor (0.9995), but different kinetic fractionation factors (0.9984 and 0.9965, respectively).

2.1‰, Jacobson and Holmden, 2008). Importantly, negligible differences between the high and low SA experiments suggests that the surface area of the seed crystals does not exert a significant control on both precipitation rates and the observed fractionation factor.

In the Tang et al. (2008) study, each point in the dataset represents a unique experiment that was conducted at a specific solute composition and saturation sate. Thus, their calculated $\Delta^{44/40}Ca_{calcite\text{-}fluid}$ values represent a steady state held at a certain distance from equilibrium along the reaction pathway. Variation in these fractionation factors as a function of precipitation rate can be modeled using the steady state, surface-reaction kinetic model (DePaolo, 2011, black solid line), an analytical solution that can predict such rate dependency in the fractionation factor based on mixed kinetic and equilibrium isotope effects. DePaolo (2011) used equilibrium and kinetic fractionation factors of 0.9995 and 0.9984, respectively and the backward, dissolution rate (R_b) was allowed to vary as a function of $R_p^{1/2}$, which has been validated as an appropriate representation of the evolution of the dissolution rate in the last section (**Section 5.1.2.3**).

This surface-reaction kinetic model has also been successfully applied to free drift experiments in Si isotope systems (Oelze et al., 2014; Geilert et al., 2015; Roedink et al.,2015; Fernandez et al., 2019), and indeed it also appears to function for our dataset using the DePaolo (2011) parameters, with the single adjustment of a kinetic fractionation factor = 0.9965. Our mixed definition of fractionation factors based on the instantaneous and cumulatively precipitated calcite for the high SA experiment provides good agreement with the model. The analytical solution developed for this surface-reaction kinetic model was solved assuming steady state mineral surface isotope ratio and, thus, might not be directly applicable to the data generated from our non-steady state

experiments. As expected, application of the "steady-state" model does not fully capture the behavior in the fractionation factor observed in our experiments, particularly for the low SA system which shows quite a bit of variability early in the reaction.

Further, a distinct feature of these free-drift experiments is the large apparent fractionation extending to $\Delta^{44/40}Ca_{calcite\text{-}aq}$ values of ~5 ‰, which is roughly 5x higher than apparent fractionation factors determined from prior steady state calcite growth experiments (Tang et al., 2008; AlKhatib and Eisenhauer, 2017). Increasing the kinetic fractionation factor from the value determined in the chemostatic literature (0.9984) to 0.9965 in order to achieve a decent characterization of the variability in the apparent Ca fractionation factor highlights a key difference between calcite growth under steady-state and non-steady state conditions. Namely, calcite growth under varying solute composition and saturation states could potentially introduce transient isotope effects associated with a fluid isotopically interacting with an evolving calcite mineral surface, forming isotopically heterogeneous newly formed mineral surfaces, which violates the derivation of the DePaolo (2011) model. However, the DePaolo (2011) model does provide an important framework in which to characterize isotopic exchange during mineral formation that has already been applied to other isotope systems. The concepts of surface exchange reactions and dynamic equilibrium provide a basis from which to develop a more suitable, transient model that can incorporate these transient isotope effects arising from calcite precipitation under non-steady state conditions.

5.4.3.2 Calculating Sr stable isotope fractionation factors in free drift conditions

Analogous to Ca stable isotopes, Sr fractionation factors are generally described according to **eq. 5. 8** and reported as $\Delta^{88/86}Sr_{calcite\text{-}fluid}$. Due to distinct starting fluid and solid $\delta^{88/86}Sr$ (-0.04 ± 0,10‰ and 0.43 ± 0.06 ‰, respectively), we also calculated Sr fractionation factors as the difference between the fluid starting and current composition ($\Delta^{88/86}Sr_{aq,0\text{-}aq,t}$). Apparent fractionation factors ($\Delta^{88/86}Sr_{cumul.ppt\text{-}fluid}$, **Table 5.3**) for the high Sr conditions where Sr incorporation took place are also calculated following the method described in the previous section to account for fractionation in non-steady state conditions (**eq. 5.9**). These apparent Sr fractionation factors as a function of precipitation rate are displayed

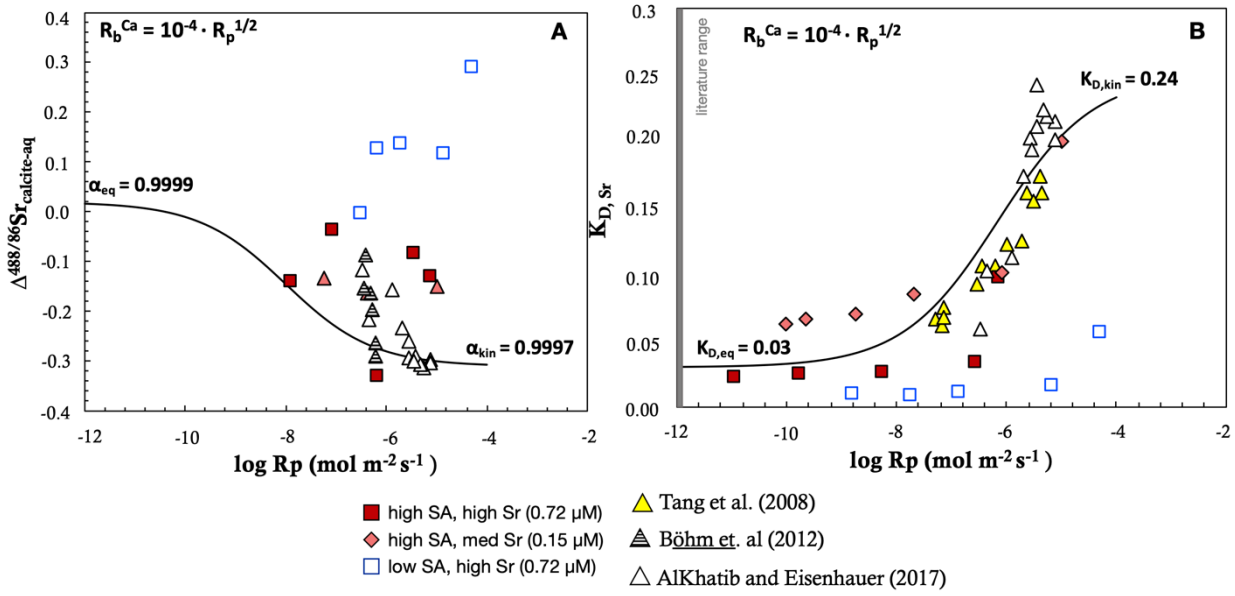

Figure 5.10 $\Delta^{88/86}Sr$ and K_D as a function of precipitation rates

Sr fractionation factors (**A**) and partition coefficients (**B**) are plotted against experimentally calculated calcite precipitation rates. Results are compared with the Tang et al.(2008) dataset (yellow triangles), Böhm et al. (2012) datset (triangles with horizontal line motif), and AlKhatib and Eisenhauer (2017) dataset (open triangles), which were generated under chemostatic conditions where the calcite was precipitated homogenously rather than onto preexisting seed crystals. DePaolo (2011) SRK model predictions are shown in black solid lines for both figures. For Sr fractionation factors, the equilibrium and kinetic fractionation factors implemented in the model were 0.9999 and 0.9997, respectively whereas the partition coefficients were estimated using equilibrium and kinetic values of 0.03 and 0.24. Experimental conditions include medium Sr (triangles) and high Sr (squares) initial conditions for high SA (0.57 m^2 g^{-1}, red markers) and low SA (0.0026 m^2 g^{-1} , blue markers).

for the high Sr, high and low SA conditions along with the high SA, medium Sr conditions in **Fig. 10A**. Fractionation factors for the "high SA, high and medium Sr" cases fall in the range observed in the literature for Sr stable isotope fractionation during calcite precipitation (Böhm et al., 2012: AlKhatib & Eisenhauer, 2017) and, outside of the "low SA, high Sr" experiment, are fairly well predicted by the DePaolo (2011) SRK model for an equilibrium fractionation factor (α_{eq}) equal to 0.9999 and a kinetic fractionation factor (α_{kin}) equal to 0.9997 (AlKhatib & Eisenhauer, 2017).

The kinetic fractionation for Sr stable isotopes appears to be muted relative to that observed for Ca stable isotopes. Yet, like Ca stable isotopes, Sr fractionation factors do appear to be slightly rate-dependent in agreement with previous observations (AlKhatib and Eisenhauer, 2017; Mavromatis et al., 2017). Thus, its plausible that muted Sr stable isotope fractionation is a consequence of slow Sr uptake kinetics, which can serve to minimize the extent of kinetic enrichment. Notably, these trends are reproduced over precisely the same range of rates used for the calcium isotopes above (**Fig. 5.9**) and thus indicate consistency between the two ratios as a function of precipitation rate.

5.4.3.3 Calculating Sr partition coefficients in free drift conditions

Sr partitioning between the fluid and growing calcite can be characterized by a partition coefficient ($K_{D,Sr}$) that is defined as the ratio between calcite and fluid Sr/Ca as shown in **eq. 5.10**:

$$K_{D,Sr} = \frac{\left(Sr/Ca\right)_{calcite}}{\left(Sr/Ca\right)_{fluid}} \qquad (5.10)$$

Calcite Sr/Ca in this definition is usually defined as the ratio of the pre-existing or "bulk" calcite. However, calcite precipitation is known to kinetically partition fluid Sr/Ca ratios

(Tang et al., 2008; AlKhatib and Eisenhauer, 2017), which results in the formation of a heterogeneous calcite surface that can influence the calcite Sr/Ca ratio and, therefore, the apparent partition coefficient. Tracking the evolution of the partition coefficient throughout the course of precipitation can be done via two methods. The first method involves the expression from Usdowski (1975) developed under the assumption of closed system Rayleigh-type Sr distillation shown as follows (**eq. 5.11**):

$$\left(\frac{[Sr]}{[Ca]}\right)_{bulkcalcite} = \left(\frac{[Sr]}{[Ca]}\right)_{aq,0} \cdot \frac{1-\left(\frac{[Ca]}{[Ca]_0}\right)_{aq}^{K_{D,Sr}}}{1-\left(\frac{[Ca]}{[Ca]_0}\right)_{aq}} \quad (5.11)$$

where $\left(\frac{[Sr]}{[Ca]}\right)_{bulkcalcite}$ represents the molar ratio (mol mol^{-1}) of the measured, bulk calcite seed at the end of the experiment, $\left(\frac{[Sr]}{[Ca]}\right)_{aq,0}$ is the molar ratio of the initial oversaturated solution, and $\left(\frac{[Ca]}{[Ca]_0}\right)_{aq}$ is the evolution of the measured fluid Ca concentration throughout the course of the reaction with respect to the starting Ca concentration ($[Ca]_0$). Partition coefficients calculated using this closed-system, Rayleigh approximation ($K_{D,Sr}^{rayleigh}$) are provided in **Table 5.3**. This method has been frequently used in the calcite experimental literature where calcite is formed homogeneously (i.e. without the use of initial crystal seeds to facilitate precipitation) under chemostatic conditions (Tang et al., 2008; AlKhatib and Eisenhauer, 2017). The second method is more applicable to calcite precipitation under variable, "free-drifting" conditions. It involves calculating the partition coefficient through the explicit tracking of the aqueous Sr throughout the course of the experiment using measured fluid and initial solid Sr concentrations as shown in the following expression (**eq. 5.12**):

$$K_{D,Sr} = \frac{\left(\frac{N^t_{Sr}}{N^t_{Ca}}\right)_{\text{evolving calcite}}}{\left(\frac{N^t_{Sr}}{N^t_{Ca}}\right)_{\text{fluid}}} \quad (5.12a)$$

$$N^t_{X,\text{evolving calcite}} = N^{\text{initial}}_{X,\text{bulk calcite}} + \Delta N^{t_0\text{-}t}_{X,\text{fluid}} \quad (5.12b)$$

where $\left(\frac{N^t_{Sr}}{N^t_{Ca}}\right)_{\text{evolving calcite}}$ is the molar ratio of the evolving bulk calcite during calcite precipitation that is calculated based on the initial amount of Ca and Sr in the bulk calcite ($N^{\text{initial}}_{X,\text{bulk calcite}}$, X = Ca, Sr) plus the cumulative amount of Ca and Sr removed from solution ($\Delta N^{t_0\text{-}t}_{X,\text{fluid}}$) between times t=0 ($N^{t_0}_{X,\text{fluid}}$) and the current sampling time ($N^t_{X,\text{fluid}}$). Results from these partition coefficients ($K^{evolv.calcite}_{D,Sr}$) are presented in **Table 5.3**. Calculating the partition coefficient using either of these two methods for the experiments in this study yields similar values. As a result, we can conclude from this exercise that: (1) the bulk calcite composition is not significantly altered as a result of calcite growth and (2) both of these methods are reasonable metrics for the evolving calcite Sr/Ca composition during precipitation under "free-drift" conditions. For the remainder of the discussion we will utilize the partition coefficients calculated using an evolving calcite Sr/Ca ratio (**eq. 5.12a & b**).

Now that the partition coefficient has been explicitly defined, we can consider the evolution of $K_{D,Sr}$ as a function of calcite precipitation rate for the high SA, high and medium Sr along with the high SA, high Sr conditions (**Fig. 5.10B**). A first observation is that $K_{D,Sr}$ does appear to be rate-dependent and generally decreases with decreasing precipitation rate. This behavior in the Sr partition coefficients can be modeled effectively

with the SRK model using an apparent equilibrium partition coefficient ($K_{D,eq}$) equal to 0.03 (Fantle and DePaolo, 2006) and a kinetic partition coefficient ($K_{D,kin}$) equal to 0.24 (DePaolo, 2011; Nielsen et al., 2013) under the assumption of a varying R_b (same as with the SRK models applied to Ca and Sr fractionation factors). Again, the behavior of the "low SA, high Sr" batch experiment remains an important outlier that the SRK model fails to fit, expressing apparent $K_{D,Sr}$ values that are significantly lower (in the range of 0.06 at fast precipitation rates to 0.01 at slow precipitation rates near the end of the experiment) than the high SA experiments. Failure of the DePaolo (2011) SRK model to fit the collective low SA, high Sr dataset including observed $\Delta^{44/40}$Ca, $\Delta^{88/86}$Sr, and $K_{D,Sr}$ variability as a function of precipitation rate could imply either erroneous data or a potentially significant outlier. To address this oddly behaving dataset, we next explore how Ca and Sr stable isotopes and Sr trace elements co-evolve during calcite precipitation under free-drift conditions. We first identify relationships between all fractionation factors and partition coefficients, and subsequently apply numerical models better suited to handle transient effects that could generate observed outlier behavior in the "low SA, high Sr" experiment.

5.4.3.4 Relationships between $\Delta^{44/40}$Ca, $\Delta^{88/86}$Sr, and $K_{d,Sr}$

A comparison of Ca and Sr fractionation factors and Sr partition coefficients across our batch experiments (**Fig. 5.11**) show behavior in all three tracers that differ drastically from the relationships observed in traditional, steady state chemostatic calcite growth experiments (Tang et al., 2008; Böhm et al., 2012; AlKhatib and Eisenhauer, 2017). Relationships between apparent $\Delta^{44/40}Ca_{ppt.cum-aq}$ and K_D^{Sr} (**Fig. 5.11A)** determined in this study exhibit no comparable relationships to that observed in the literature. The apparent Ca fractionation factor varies considerably (-3.96‰ to -0.18‰) relative to the apparent

partition coefficient, which are tightly bound to values (0.02 mole/mole to 0.10 mole/mole) that are much lower than is observed in the chemostatic studies (0.24 mole/mole to 0.06 mole/mole). The extent of the variability in the apparent $\Delta^{44/40}Ca_{ppt.cum-aq}$ is significantly greater than is observed in the chemostatic experiments where the largest fractionation observed is -1.57 ‰ (AlKhatib and Eisenhauer, 2017). Correspondingly, within the $\Delta^{88/86}Sr_{ppt.cum-aq}$ vs K_D^{Sr} relationships (**Fig. 5.11B**), the apparent Sr fractionation factor show little to no correlation with the K_D^{Sr} in any of the "high Sr" batch experiments. Also (like for $\Delta^{44/40}Ca_{ppt.cum-aq}$), our free-drift experiments express $\Delta^{88/86}Sr_{ppt.cum-aq}$ that are significantly larger and more variable than what is observed in the literature ranging from ~ 0.3 ‰ ("low SA, high Sr") to -0.3 ‰ ("high SA, high Sr"). Lastly, when the two stable isotope tracers are compared against one another (**Fig. 5.11C**),

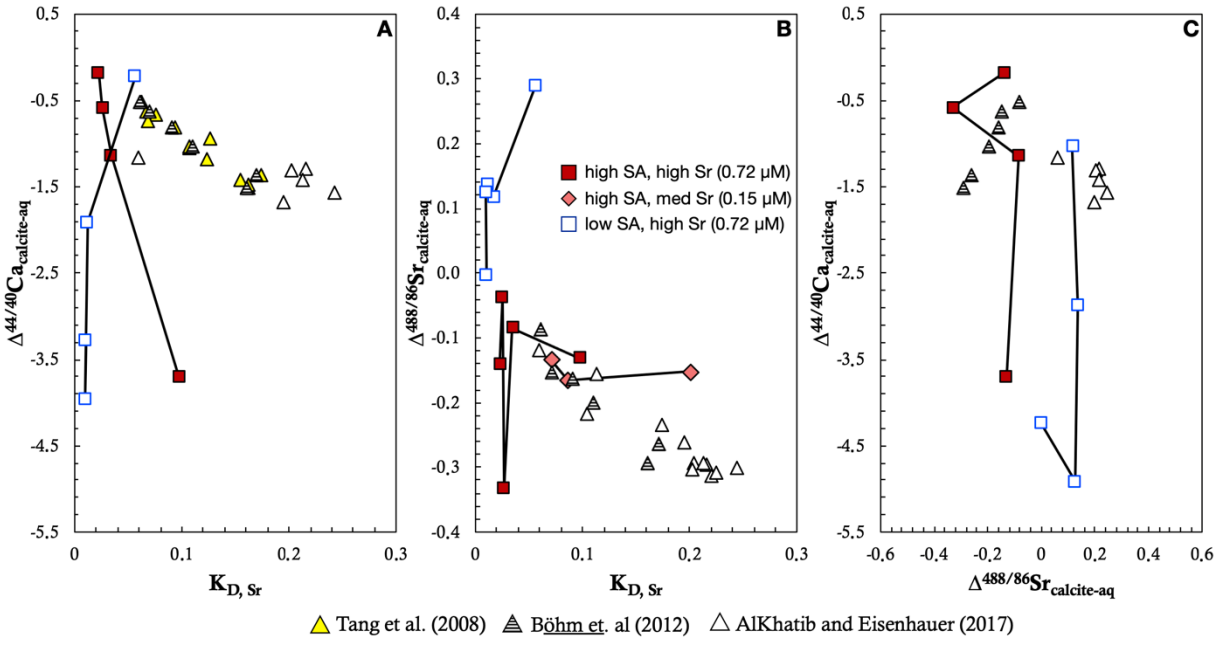

Figure 5.11 $\Delta^{44/40}Ca$, $\Delta^{88/86}Sr$, and $K_{D,Sr}$ cross correlations
Observed fractionation factors for Ca and Sr plotted against observed Sr partition coefficients (**A, B**) and plotted against each other (**C**) for medium and high Sr conditions at both high (0.057 m^2 g^{-1}) and low SA (0.0026 m^2 g^{-1}) conditions. Literature values are presented from Tang et al.(2008), Böhm et al.(2012), and AlKhatib and Eisenhauer (2017) for comparison.

$\Delta^{44/40}Ca_{ppt.cum\text{-}aq}$ exhibits a much larger fractionation range than what is observed for $\Delta^{88/86}Sr_{ppt.cum\text{-}aq}$. This disparity between Ca and Sr stable isotope fractionation gives the appearance that Sr stable isotopes are not being fractionated at all. However, the large fractionation observed in $\Delta^{88/86}Sr_{ppt.cum\text{-}aq}$ compared to fractionations observed in the literature implies that Sr is fractionating significantly during calcite growth in free-drift conditions.

As we recently showed in the previous section (**Section 5.1.3.3**), the DePaolo (2011) steady state model was able to cover most of the behavior observed in the respective tracers based on assumptions of "steady-state" conditions (**Fig. 5.9 & 5.10)**. This agreement with the steady state model implied that calcite growth under free-drift experiments behave for the most part in a manner comparable to steady state experiments and, importantly, that Ca, Sr table isotope and Sr/Ca trace element fractionation all exhibit a rate–dependence; thereby implying that all three tracers are self-consistent.

Thus, its striking that cross correlations between $\Delta^{44/40}Ca$, $\Delta^{88/86}Sr$, and $K_{D,Sr}$ show substantial disparity between free-drift vs. chemostatic conditions and, further, that the tracers do not behave systematically to one another. Based from these results, partitioning under free-drift experiments does not behave similarly to chemostatic experiments contrary to expectations based from the DePaolo (2011) model results. Disparities between the extent of Ca and Sr stable isotope fractionation, where $\Delta^{88/86}Sr_{ppt.cum\text{-}aq}$ were substantially smaller than observed $\Delta^{44/40}Ca_{ppt.cum\text{-}aq}$ imply that dependencies outside of the overall calcite precipitation rate could be driving observed fractionation. For instance, it is possible that Sr stable isotopes fractionation during calcite growth in a free-drift setting is driven more by slower, Sr uptake rates rather than overall fast, calcite precipitation rates, yielding minimized apparent $\Delta^{88/86}Sr_{ppt.cum\text{-}aq}$ as a result. Similarly,

tightly bound apparent partition coefficients, $K_{D,Sr,}$ that are skewed towards lower values relative to the chemostat literature could also be a result of this interplay between fast calcite kinetics and slow Sr incorporation, which ultimately drives fluid Sr/Ca ratios to higher values and decreases the observed $K_{D,Sr}$. Ultimately, what is clear from these cross-correlations is that the factors driving the fractionation observed in our experimental data cannot be properly accounted for in simplified, steady state models. As a consequence, we cannot determine whether or not Ca, Sr stable isotopes and Sr/Ca trace element ratios are broadly, self-consistent during calcite growth without the aid of numerical models that are capable of tracking the evolution of these tracers through time and, thereby, can properly characterize the intrinsic characteristics underlying observed behavior between $\Delta^{44/40}$Ca, $\Delta^{88/86}$Sr, and $K_{D.}$

5.4.4 Using numerical models to characterize partitioning during free-drift calcite growth

5.4.4.1 Numerical multi-component model application to trace element and stable isotopes

To properly test our hypothesis that Ca, Sr stable isotope and Sr trace elements fractionate under similar and broadly consistent mechanisms, we use the multi-component geochemical software, CrunchTope (Steefel et al., 2015), in application to the experimental dataset generated in this study. The treatment of isotope (and trace element) ratios integrated in this numerical model allow explicit and time – dependent tracking of the co-evolving fluid and solid phase isotope (or trace element) ratios through a set of coupled TST (Transition State Theory) rate laws (eq. 5.13, Druhan et al., 2013):

$$ {}^{i}R_p = {}^{i}X\,{}^{i}k_f\,A\left(\frac{{}^{i}E^{2+}_{(aq)}\cdot HCO_3^-}{{}^{i}X{}^{i}K_{EQ(calcite,SrCO3)}} - 1\right) \qquad (5.13a) $$

$$^{j}R_{p} = {}^{j}X\,{}^{j}k_{f}\,A\left(\frac{{}^{j}E^{2+}_{(aq)}\cdot HCO_3^-}{{}^{j}X{}^{j}K_{EQ(calcite,SrCO3)}} - 1\right) \qquad (5.13b)$$

$$^{i,j}X = \frac{{}^{i}E_{solid}}{{}^{i}E_{solid} + {}^{j}E_{solid}} \qquad (5.13c)$$

Where *E* represents Ca in this case and *i*, *j* refer to the respective Ca isotopologues (Druhan et al., 2013). In this formulation, each individual isotope has a respective TST rate law (R_p, **eq. 5.13a,b)** constructed using the parameters appropriate for calcite precipitation (**see section 5.4.1.1***)* that are coupled to one another through the solid mole fraction, $^{i/j}X$ (**eq. 5.13c**). This mole fraction is an important parameter that can be defined in two ways: (1) as either the mole fraction of the total solid phase calcite present in the system or (2) of the growing mineral surface (further information on the mole fraction can be found in **Chapter 2 (Fernandez et al., 2019**). Kinetic and equilibrium fractionation factors are imposed via differences in the individual kinetic rate constants (in mol m^{-2} s^{-1}) for each isotopologue ($\alpha_{kin} = {}^{j}k_f / {}^{i}k_f$) and equilibrium solubility constants for calcite or $SrCO_3$ ($\alpha_{EQ} = {}^{j}K_{eq} / {}^{i}K_{eq}$) solid solution endmembers. A subtle, but significant component in this model setup is the presence of the reactive surface area (*A*, m^2), which controls the overall rates and ultimately dictates the observed behavior and evolution of fluid and solid phase stable isotope ratios over the course of the experiment. Importantly, in this model theory the extent of stable isotope fractionation is controlled by the proximity of the reaction to equilibrium and, thus, predicts a rate-dependence for observed fractionation factors which functions like the DePaolo (2011) model for a system that is capable of isotopically evolving through time.

This model currently has not been utilized for trace element partitioning other than the results reported in Chapter 3. However, assuming that trace elements partition according

to the same mechanisms established for stable isotope fractionation, Sr can be treated in the same manner as the "rare" isotopologue in the stable isotope model design and expressed in the following equations identical to those described above for stable isotopes (**eq. 5.14**):

$$^{Sr}R_p = {}^{Sr}X\ {}^{Sr}k_f\ A\left(\frac{Sr^{2+}_{(aq)} \cdot HCO_3^-}{{}^{Sr}X\ {}^{Sr}K_{EQ,Sr_xCa_{1-x}CO_3^{2-}}} - 1\right) \qquad (5.14a)$$

$$^{Ca}R_p = {}^{Ca}X\ {}^{Ca}k_f\ A\left(\frac{Ca^{2+}_{(aq)} \cdot HCO_3^-}{{}^{Ca}X\ {}^{Ca}K_{EQ,Sr_xCa_{1-x}CO_3^{2-}}} - 1\right) \qquad (5.14b)$$

Where individual TST rate expressions are described for Sr and Ca and are coupled through the solid mole fraction ($^{Ca,Sr}X$). The kinetic rate constants ($^{Ca,Sr}k_f$) and equilibrium solubility constants ($^{Ca,Sr}K_{EQ}$) are defined individually for Sr incorporation and Ca precipitation, respectively. Kinetic and equilibrium partition coefficients are defined, like for the stable isotope fractionation factors, by the differences between $^{Sr}k_f / {}^{Ca}k_f$ and $^{Sr}K_{EQ} / {}^{Ca}K_{EQ}$. Input parameters for the CrunchTope model are presented in **Table 5.4** and **Table 5.5**. At present, the CrunchTope model is implemented in order to track two isotopes of a given element (or a trace and major element) and thus would not be appropriate to simultaneously track both Sr trace element partitioning (Sr/Ca ratios) and the fractionation of the trace element stable isotopes ($\delta^{88/86}Sr$) simultaneously. In other words, the model theory described in detail above is applicable to a two-endmember solid solution, defined either by the rare and abundant isotope (as shown in **eqn. 5.13**) or by the trace and major element (as shown in **eqn. 5.14**). Additionally, since Sr is strongly dependent on the solid solution with calcite, Sr stable isotopes cannot be simply tracked by assuming a pure $SrCO_3$ mineral endmember and then solving the coupled rate

equations of the rare and abundant isotopes as was done for the Ca stable isotopes (**eq. 5.13**). A simplified fractionation framework that is capable of monitoring several tracers at the same time will be discussed in further detail in the next section. For the remainder of this section, we focus on numerical results for Ca and its stable isotopes along with Sr trace element partitioning during calcite precipitation, which we will refer to as the "isotope model" and "trace model", respectively.

Table 5.4 Initial conditions for CrunchTope simulations

Parameters	units	values	description
reaction order		1.0	
duration	days	7	Based on experiments
timestep	hours	1.2, 5	dT
T	ºC	25	
pH		8.85	
SSA	$m^2\ g^{-1}$	0.057	High SA condition
		0.0026	Low SA condition
Ca^{2+}_{aq}[a]	mM	0.35	
$Sr^{2+}_{(aq)}$[b]	μM	0.003	High + Low SA, baseline
		0.720	High SA+ Low SA, high Sr
		0.147	High SA, med Sr
		0.020	High SA, low Sr
log $k_{f\ (calcite)}$	mol $m^{-2}s^{-1}$	-3.11	Kinetic rate constant for calcite formation
log $k_{b\ (SrCO3)}$	mol $m^{-2}s^{-1}$	-3.73	Kinetic rate constant for Sr-carbonate
log $K_{eq(calcite)}$[c]		-8.40	Calcite solubility constant
log $K_{eq\ (SrCO3)}$[d]		-7.6	Sr-carbonate solubility constant

a. Measured starting dissolved calcium concentrations.
b. Measured starting dissolved strontium concentrations from this study.
c. Reddy and Nancollas (1971).
d. Kulick et al.(2010).

5.4.4.2 Ca stable isotope simulations

We first start with numerical simulations for the fluid $\delta^{44/40}Ca$ experimental datasets from the "baseline and high Sr", "low and high SA" conditions, respectively. Ca stable isotope simulations were run using a calcite kinetic rate (log k_f^{Ca} = -3.11) constrained based on numerical model results for a strictly Ca precipitation scenario –i.e

no isotopes included. Corresponding Ca isotope model results using this kinetic rate successfully captures the fluid Ca concentration evolution through time in both high and low SA experiments **(Fig. 5.12A).** These results thus verify that the isotope model is behaving appropriately and is capable of predicting Ca concentrations through time with the same kinetic rate constant derived from the simple Ca precipitation model. After this "concentration check", the isotope model was then applied to the experimental fluid $\delta^{44/40}$Ca data.). Kinetic (α_{kin}) and equilibrium fractionation factors imposed in the model of 0.9965 and 0.9995, respectively, are based on the fit of the SRKM model (DePaolo, 2011) to the experimental results of this study (**Fig. 5.8**) and from measurements of deep ocean sediment pore fluids (Fantle and DePaolo, 2007). We show numerical simulations strictly under the "surface" scenario for two different time intervals, T = 1.2 hours and T = 5 hours respectively. These time intervals act as a proxy for the depth of newly formed mineral surface that the fluid is allowed to interact with, which is tracked throughout the

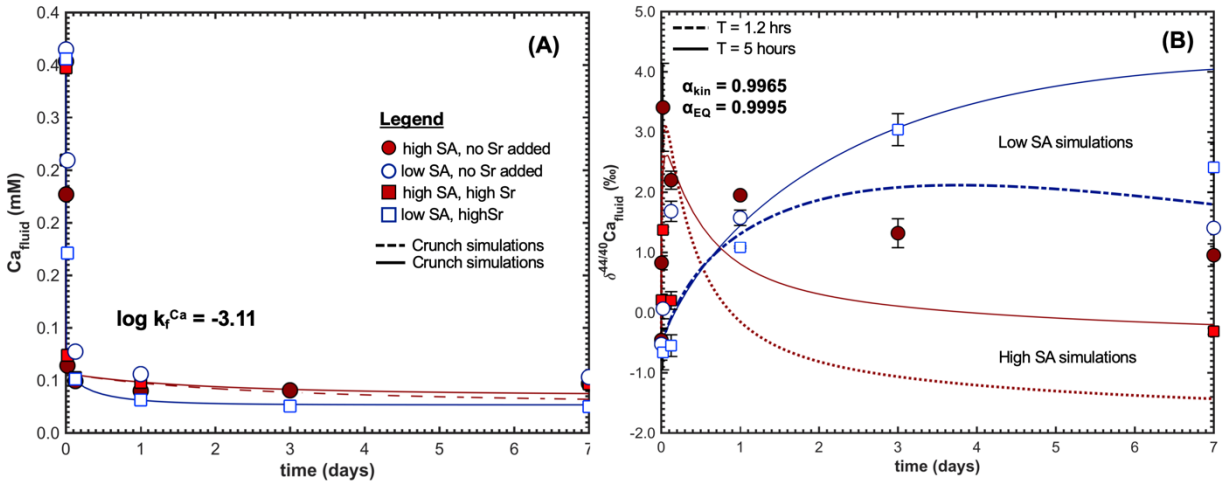

Figure 5.12 CrunchTope model simulations for Ca stable isotopes

Fluid $\delta^{44/40}$Ca Crunch model simulations using the "surface option" and a kinetic and equilibrium fractionation factor of 0.9965 and 0.9995 respectively. Numerical results for Ca concentration timeseries (**A**) were determined using a kinetic rate constant of $10^{-3.11}$ mol m^{-2} s^{-1}. Simulations of fluid $\delta^{44/40}$Ca through time (**B**) tested two running average time intervals for the surface simulations: 1.2 hrs (dashed lines) and 5 hrs (solid lines), respectively.

course of the simulation by a running average (more information on this calculation can be found in **Chapter 2**).

Overall, these isotope model "surface" simulations were able to capture a large extent of the observed fluid Ca behavior in the "baseline" and "high Sr" conditions (**Fig. 5.12B**). Generally, the time interval necessary to reproduce each experiment has been shown to depend highly on the surface area based on fractionation $\delta^{30}Si$ during opal precipitation (Fernandez et al., 2019). However, in this case, the choice in time interval between 1.2 and 5 hours does not appear to drastically change fluid $\delta^{44/40}Ca$ predictions between high and low SA conditions. For instance, high SA simulations conducted with a running average time interval of 1.2 hours and 5 hours both capture the extent of kinetic enrichment experimentally observed ($\delta^{44/40}Ca_{max}$ = 3.41 ± 0.73 ‰). The only disparities observed in the T = 1.2 hours and T = 5 hours simulations are in the subsequent re-equilibration of fluid $\delta^{44/40}Ca$ to values reflecting the portion of the mineral surface that the fluid is in contact with. In both low SA surface simulations, the timing and extent of kinetic enrichment using a time interval of 5 hours tends overpredicts the experimental data whereas a time interval of 1.2 hours appears to better capture fluid $\delta^{44/40}Ca$ behavior. But, in general these slow rates of $\delta^{44/40}Ca$ in the low SA case makes it difficult to properly determine the proper fluid–mineral surface interaction depth between the running average time intervals of 1.2 and 5 hours. Thus, these findings provide a first indication that either (1) the surface area is not as influential in these rapid carbonate precipitation systems as compared with slower silicates; or (2) the surface area does not play as large of a role in overall Ca stable isotope partitioning as is the case for other secondary mineral tracers.

5.4.4.3 Trace model simulations

We next turn to the application of the CrunchTope "trace model" to the experimental fluid Sr/Ca datasets. Importantly, this is first time that this model theory developed for stable isotope fractionation is applied to Sr trace element partitioning during calcite formation. The extent of Sr partitioning in the trace model is controlled by imposing kinetic ($K_{D,kin}$) and equilibrium ($K_{D,EQ}$) fractionation factors via the ratio of kinetic rate constants (k_f^{Sr}/k_f^{Ca}) and solubility constants (K_{sp}^{Sr}/K_{sp}^{Ca}). In these experiments, the solubility constant for the Sr-carbonate endmember in the binary $Sr_xCa_{1-x}CO_3$ solid solution is a key parameter in determining the equilibrium fractionation factor. The range in the solubility constant for Sr-carbonate (K_{sp}^{Sr}) in solid solution with calcite has been previously estimated in the literature according to a hypothetical rhombohedral crystal structure to be in the range of $10^{-6.1}$ to $10^{-8.2}$ with an average value of $10^{-7.6}$ (Kulik et al., 2010). When we implement this Sr-carbonate solubility value of $10^{-7.6}$ as predicted by equilibrium thermodynamic models along with the calcite solubility constant of $10^{-8.40}$ (Reddy and Nancollas, 1971) we obtain an intrinsic equilibrium fractionation factor ($K_{D,EQ}^{intrinsic}$) of ~6.3. This equilibrium fractionation factor is high relative to the equilibrium fractionation factor ($K_{D,EQ} = 0.03$) utilized in the application of the DePaolo (2011) model to our experimental data that derives from low observed Sr partition coefficients (ranging between 0.02 to 0.07) in deep ocean sediment pore fluids that represent (near)equilibrium conditions (DePaolo and Fantle, 2006).

There is a simple argument for justifying a higher equilibrium fractionation factor than what has been previously proposed by DePaolo (2011) and applied successfully in our steady state models (**Figure 5.10B, section 5.4.3.3**). Notably, the trace element $K_{D,EQ}^{intrinsic}$ is a true ratio of the equilibrium constants of the two endmembers of the solid solution,

which is distinct from $K_{D,EQ}$ (the apparent partition coefficient), defined as the ratio of the Sr/Ca composition of the calcite, $(Sr/Ca)_{calcite}$, over that of the fluid $(Sr/Ca)_{fluid}$ as shown in **eqn. 5.10**. To highlight these difference between "apparent" ($K_{D,EQ}$) and "intrinsic" ($K_{D,EQ}^{intrinsic}$), two trace model simulations for the high and med Sr batch experimental cases were run using the $K_{D,EQ}$ (0.035) proposed by DePaolo (2011) and the $K_{D,EQ}^{intrinsic}$ (6.3)

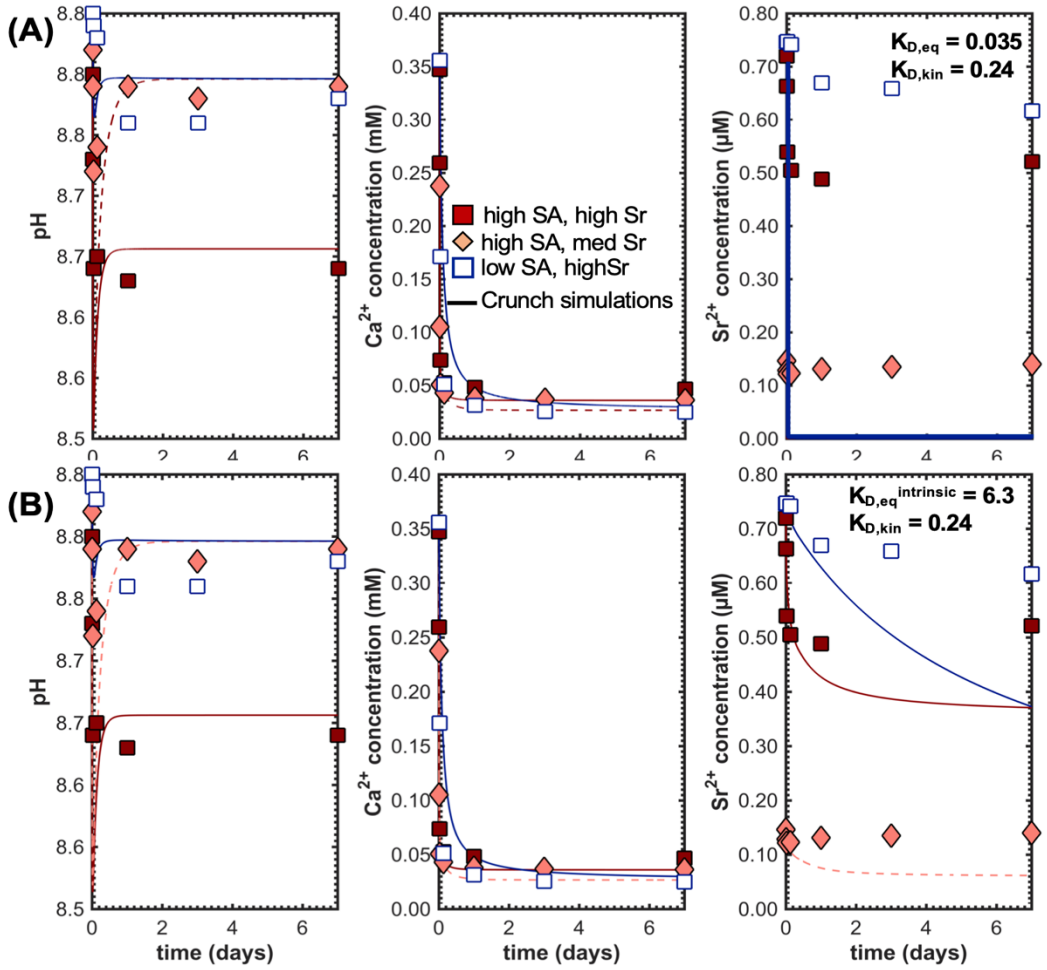

Figure 5.13 Trace model simulations for Sr incorporation batch experiments
Trace model simulations for the pH, fluid Ca and Sr concentrations (dashed lines) for the high SA med and high Sr cases along with the low SA, high Sr experiment. The results of two simulations are presented where the equilibrium fractionation factor ($K_{D,EQ}$) is set to either 0.035 reflecting the equilibrium fractionation proposed by DePaolo (2011) (**A**) or 6.3, representing the estimated solubility constant for the Sr-carbonate endmember in a $(Sr,Ca)CO_3$ solid solution (Kulik et al., 2010) (**B**), respectively. The kinetic fractionation factor ($K_{D,kin}$ = 0,24) is held constant between the two numerical runs.

based on thermodynamic calculations of the Sr-carbonate endmember in the $Sr_xCa_{1-x}CO_3$ solid solution (**Fig. 5.13)**. The kinetic fractionation factor is set to 0.24 in both simulations based on literature derived values (Gabitov and Watson, 2006; DePaolo, 2011). For an Sr-carbonate solubility constant of $10^{-9.8}$ (i.e. $K_{D,EQ}$ = 0.035) Sr fluid concentrations are predicted to decrease far below experimentally determined values for all surface area cases (**Fig. 5.13A**). These low Sr fluid concentrations (~0.15 μM to 0.01 μM) result in apparent K_D's within the range of ~0.08 to 1.24, which is higher than the observed K_D in equilibrated marine sediment pore fluids (~0.02, DePaolo and Fantle, 2006). In contrast, trace model simulation with Sr solubility constant of $10^{-7.6}$ (i.e. $K_{D,EQ}$ of 6.3) yields more accurate results for fluid Sr concentrations where good agreement is found between the experimental data and the numerical estimations (**Fig. 5.13B**). These results yield apparent Kd's at the end of the simulation that correspond well with experimentally determined Kd (**Fig. 5.10**, **Table 5.3**) with values ranging from 0.02 to 0.06. Thus, based on these numerical trace model simulations, we show that a $K_{D,EQ}^{intrinsic}$ is a more precise estimate of the Sr distribution equilibrium fractionation factor, which agrees with previous arguments put forth by Nielsen et al. (2013) for calcite formation. The resulting apparent $K_{D,EQ}$ is then in good agreement with the DePaolo (2011) model (**Fig. 5.10b**).

With the kinetic and equilibrium fractionation factors clearly defined, trace element model simulations for all the batch experimental conditions can now be presented. We start first with applying the trace model to the low fluid Sr experiments where Sr dissolution is taking place (**Fig. 5.14**). The objective for these simulations is to determine whether the trace model is capable of predicting Sr dissolution even during net carbonate precipitation through the binary solid solution framework. In this case, numerical results show that the trace model is capable of predicting a fluid that is both undersaturated with

respect to the Sr-carbonate endmember (log Q/K = -4.1967) and oversaturated with respect to calcite (log Q/K = 1.18) based on initial aqueous Ca and Sr concentrations. This result produce trace model simulations that accurately capture contemporaneous Sr dissolution and Ca precipitation for baseline and low fluid Sr experiments during net carbonate precipitation. This is the first demonstration of the mixed solubility behavior behaving appropriately for Sr:Ca in such a modeling framework. using the same kinetic rates and solubility constants as those employed for Sr incorporation (**Fig. 5.14A**). Just like for the equilibrium K_D, faster Sr release rates (log k^{Sr} = -3.73) imposed in the model reflect the "intrinsic" release rate which is a true ratio of the kinetic constants for the Ca and Sr during calcite growth and, thus, is different from the "apparent" release rates experimentally observed (**Fig. 5.8B; section 5.4.2.3**). Further, the trace model fluid Sr/Ca evolution through time agrees nicely with the experimental data, only slightly overpredicting the fluid Sr/Ca observed for the high SA, baseline and low fluid Sr cases. These findings highlight the breadth of capabilities of a binary solid solution framework for Sr trace element partitioning during calcite precipitation.

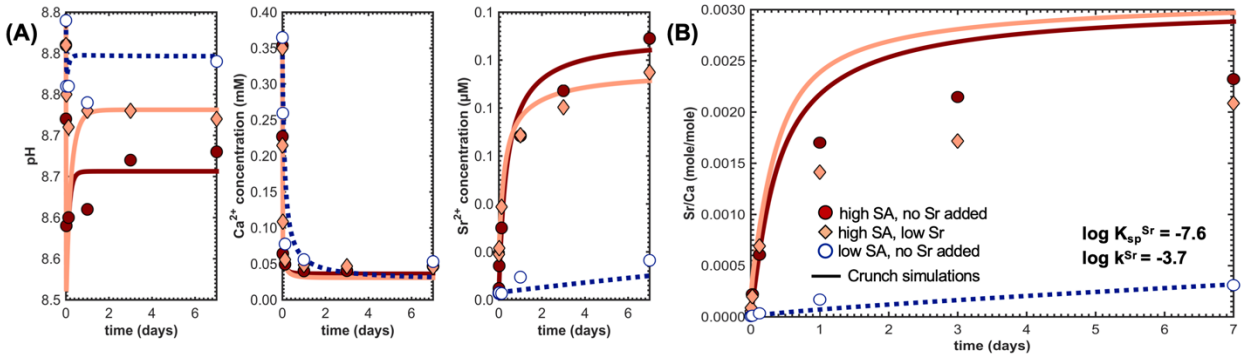

Figure 5.14 Trace model simulations of Sr release batch experiments

Trace model simulations of the baseline and low Sr, high and low SA experiments (filled and open markers) as a function of time for the pH, fluid Ca and Sr concentrations **(A),** and the fluid Sr/Ca ratios (**B**) respectively. The Crunch simulations (solid and dashed lines) were performed using kinetic rate constants of log k^{Ca} = -3.11 and log k^{Sr} = -3.7 and equilibrium constants of log K_{eq}^{Ca} = -8.4 and log K_{eq}^{Sr} = -7.6, respectively.

We now turn to trace model simulations for fluid Sr/Ca behavior during Sr incorporation under high fluid Sr conditions performed over a range of partitioning scenarios. Notably, these scenarios were originally developed to characterize stable isotope exchange between a solid and its surrounding fluid (Druhan et al., 2013; Fernandez et al., 2019). We take the opportunity to test these scenarios for the first time in application to Sr trace element incorporation to determine if trace element re-equilibrate in a manner similar to known isotopic re-equilibration. These scenarios are (1) "no back-reaction" where the fluid is not allowed to (re)equilibrate with the solid phase composition (i.e. only kinetic fractionation is imposed); (2) "bulk" exchange where the fluid equilibrates with the isotopic or trace element composition of the entirety of the available or bulk calcite and (3) "surface" or "mineral zoning" where the fluid is allowed to interact and (re)equilibrate with a small, newly-formed portion of the growing calcite mineral surface, which in this case would be concentrated in Sr relative to the rest of the bulk calcite mineral as a result of Sr incorporation during the period of calcite growth. These 'none', 'bulk' and 'surface' options were similarly used in the modeling of $d^{30}Si$ during opal formation (**Chapter 2**) and are introduced in further detail there.

These three different scenarios are shown in **Fig. 5.15** for high SA, medium and high Sr cases and the low SA, high Sr case. Under the "no back-reaction" scenario, trace model simulations do not capture the evolution of the observed fluid Sr/Ca for any of the experiments (**Fig. 5.15A**). Fluid Sr/Ca are predicted to increase rapidly to values that are around 7× to 14× higher than those measured experimentally for the high SA medium and low Sr cases, respectively. Thus, a unidirectional or "no back reaction" approach is not suitable for the experimental dataset and the model highlights the fact that kinetic partitioning alone is inaccurate to describe the behavior of Sr/Ca during carbonate

growth. The application of a "bulk" scenario incorporating both kinetic partitioning and (re)equilibration with the entirety of the mineral phase provides a much better fit to the experimental results compared to the previous approach, particularly for the high SA, medium Sr data (**Fig. 5.15B**). However, the model in this scenario predicts a turnover in the high SA, high Sr fluid Sr/Ca that is not observed and, consequently, underestimates the fluid Sr/Ca at later times during calcite precipitation. Correspondingly, the model also fails to predict the large fluid Sr/Ca partitioning in the low SA, high Sr case. These

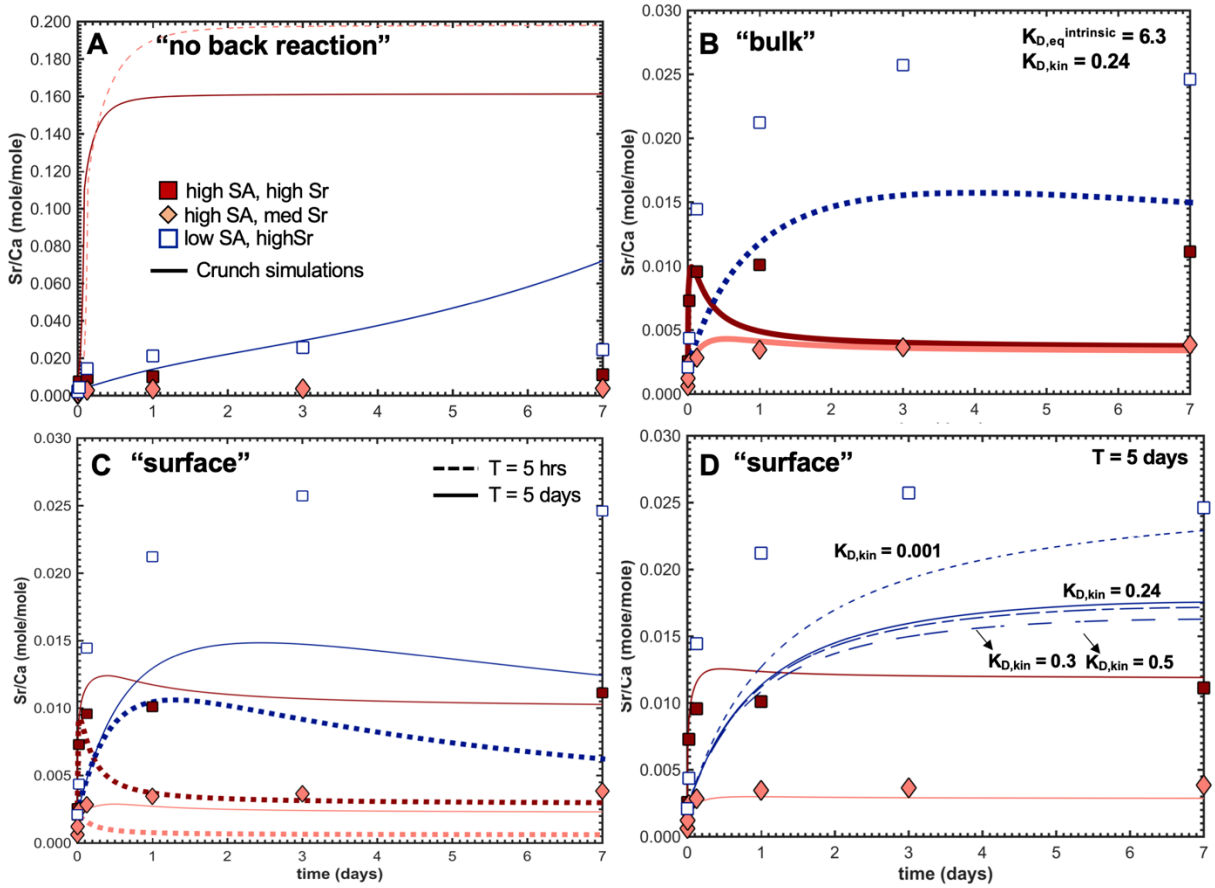

Figure 5.15 Trace model simulations of fluid Sr/Ca partitioning during Sr uptake
Crunch simulations for the Sr incorporation experiments (i.e. high Sr cases for both low and high SA). I show the three fractionation scenarios, (**A**) "none" option or "no back reaction", (**B**) "bulk" option, and (**C**) "surface" option for two different running average time intervals, T = 5 hrs (dashed lines) and T= 5 days (solid lines). Another surface option is presented in (**D**), which depicts a range of kinetic fractionation factors for the high SA, low Sr case where how the kinetic rate would need to be around log k = -6.11 to accurately reproduce the observed variability, which is 3x slower than the rate constant for calcite (log k = -3.11).

findings lead us to the final scenario where the fluid is allowed to interact with the thin, co-evolving newly formed calcite surface.

The model under the surface scenario shows the best overall reproduction of the experimental data (**Fig. 5.15C,D**). When we vary the time interval between 5 hours and 5 days in the present model, the trace model simulations return the best representation of all respective experimental datasets at a time interval of 5 days. This is notably a much larger time interval then was used in simulating fluid $\delta^{44/40}Ca$ and suggests that, like $\delta^{44/40}Ca$, fluid Sr/Ca is subject to re-equilibration as a result of fluid–mineral surface interactions. Our numerical simulations closely track the observed Sr/Ca partitioning for the "high SA, medium and high Sr" experiments (**Fig. 5.15C**). However, simulations for the "low SA, high Sr case" continue to underpredict the extent of Sr/Ca partitioning. Thus, it appears necessary to envoke a unique kinetic fractionation factor increased by 2 orders of magnitude (0.001) in order to be able to accurately replicate the low SA, high Sr experimental results. This would require suggish Sr kinetics ($\log k_f^{Sr} = -6.11$) that are 3 orders of magnitude slower than the kinetic rate constant for calcite (**Fig. 5.13D**). Based on these simulations, the origins of these potentially slow Sr incorporation kinetics can be attributed to the rate-dependence of Sr kinetic partitioning. Specifically, due to the influence of surface area on rates, overall calcite growth rates are slower when precipitation occurs on lower surface area grains. Thus, it is likely that observed "low SA, high Sr" Sr/Ca behavior reflect a combination of slow incorporation kinetics, high Sr fluid content, and relatively fast calcite precipitation rates that combined serve to enhance kinetic partitioning and lead to more elevated fluid Sr/Ca ratios compared to the other Sr incorporation experiments.

Thus, several take-a-ways can be extracted from these CrunchTope $\delta^{44/40}$Ca and Sr/Ca model simulations. First, a time interval of ~5 hours and 5 days determined for both $\delta^{44/40}$Ca and Sr/Ca "surface" simulations provide further evidence that surface area imparts only a minimal influence on both observed $\delta^{44/40}$Ca and Sr/Ca fractionation during calcite precipitation under free drift conditions characterized in this study by fast precipitation rates. This is a quite notable result and distinguishes these Ca-weathering tracers from other stable isotope and trace element systems, like the silicate weathering tracers, that are slower and apparently much more sensitive to surface area effects. Second, trace element partitioning based on a binary solid solution framework has the capacity to account for both Sr dissolution and Sr incorporation as a function of the saturation state of the system relative to the Sr-carbonate endmember. Lastly, $\delta^{44/40}$Ca and Sr/Ca partitioning do appear to behave analogously, reflecting mixed kinetic and equilibrium isotope effects and are generally influenced by similar physiochemical properties during calcite precipitation under free drifting conditions, notably in this case the presence of Sr impurities in the initial oversaturated solution. This is shown by the success in the CrunchTope "trace" and "isotope" models in characterizing $\delta^{44/40}$Ca and Sr/Ca using consistent kinetic and thermodynamic parameters. Thus, we are now poised to expand upon the binary solid solution framework currently in place within the CrunchTope model and construct a model theory that can successfully incorporate several of these self-consistent tracers (like $\delta^{44/40}$Ca and Sr/Ca) within the same model. In the next section, we test in a simplified Matlab fractionation model a 4-endmember solid solution framework that has the capability to trace $\delta^{88/86}$Sr isotopes, $\delta^{44/40}$Ca, and Sr/Ca fractionation simultaneously during calcite precipitation.

5.4.4.4 Multi-tracer model: Tracking $\delta^{44/40}Ca$, $\delta^{88/86}Sr$, and Sr/Ca partitioning simultaneously

The "multi-tracer" model builds upon the coupled rate equations developed by Druhan et al. (2013) to now account for both the partitioning of trace elements and their associated stable isotopes through a four-endmember, ternary solid solution defined by the major and minor elements and their respective stable isotope ratios. These eight, coupled linear differential equations characterized by Transition Rate Theory (TST) rate laws was originally developed by Kußner (2019) in a simple non-dimensionalized reactive transport scheme to track Sr and Ca stable isotopes fractionation across scales from a batch experiment to a small headwater catchment. Modifications that were made to the original setup involved dimensionalizing the equations (adding time for instance) and rearranging the equations for simplification purposes so that they appear in the form shown above (**eq. 5.16**):

For fluid calcium concentrations and stable isotope ratios

$$\frac{d^{40}Ca_{aq}^{2+}}{dt} = K_{eq}^{Ca}\ k_f^{Ca}\left[\frac{^{40}Ca_{solid}}{^{40}Ca_{solid}+^{44}Ca_{solid}+^{88}Sr_{solid}+^{86}Sr_{solid}} - \frac{^{40}Ca_{aq}^{2+}\cdot HCO_3^-}{K_{eq}^{Ca}}\right] \tag{16a}$$

$$\frac{d^{40}Ca_{solid}}{dt} = K_{eq}^{Ca}\ k_f^{Ca}\left[\frac{^{40}Ca_{aq}^{2+}\cdot HCO_3^-}{K_{eq}^{Ca}} - \frac{^{40}Ca_{solid}}{^{40}Ca_{solid}+^{44}Ca_{solid}+^{88}Sr_{solid}+^{86}Sr_{solid}}\right] \tag{16b}$$

For calcite calcium concentrations and stable isotope ratios

$$\frac{d^{44}Ca_{aq}^{2+}}{dt} = \alpha_{eq}^{Ca}\ K_{eq}^{Ca}\ \alpha_{kin}^{Ca}\ k_f^{Ca}\left[\frac{^{44}Ca_{solid}}{^{40}Ca_{solid}+^{44}Ca_{solid}+^{88}Sr_{solid}+^{86}Sr_{solid}} - \frac{^{44}Ca_{aq}^{2+}\cdot HCO_3^-}{\alpha_{eq}^{Ca}\ K_{eq}^{Ca}}\right] \tag{16c}$$

$$\frac{d^{44}Ca_{solid}}{dt} = \alpha_{eq}^{Ca}\ K_{eq}^{Ca}\ \alpha_{kin}^{Ca}\ k_f^{Ca}\left[\frac{^{44}Ca_{aq}^{2+}\cdot HCO_3^-}{\alpha_{eq}^{Ca}\ K_{eq}^{Ca}} - \frac{^{44}Ca_{solid}}{^{40}Ca_{solid}+^{44}Ca_{solid}+^{88}Sr_{solid}+^{86}Sr_{solid}}\right] \tag{16d}$$

For fluid strontium concentrations and stable isotope ratios

$$\frac{d^{88}Sr_{aq}^{2+}}{dt} = K_{D,kin}\, K_{eq}^{Sr}\, k_f^{Ca}\left[\frac{^{88}Sr_{solid}}{^{40}Ca_{solid}+^{44}Ca_{solid}+^{88}Sr_{solid}+^{86}Sr_{solid}} - \frac{^{88}Sr_{aq}^{2+}\cdot HCO_3^-}{K_{eq}^{Sr}}\right] \quad (16e)$$

$$\frac{d^{88}Sr_{solid}}{dt} = K_{D,kin}\, K_{eq}^{Sr}\, k_f^{Ca}\left[\frac{^{88}Sr_{aq}^{2+}\cdot HCO_3^-}{K_{eq}^{Ca}} - \frac{^{88}Sr_{solid}}{^{40}Ca_{solid}+^{44}Ca_{solid}+^{88}Sr_{solid}+^{86}Sr_{solid}}\right] \quad (16f)$$

For solid phase strontium concentrations and stable isotope ratios

$$\frac{d^{86}Sr_{aq}^{2+}}{dt} = K_{D,kin}\alpha_{eq}^{Sr}\, K_{eq}^{Sr}\, \alpha_{kin}^{Sr}\, k_f^{Ca}\left[\frac{^{86}Ca_{solid}}{^{40}Ca_{solid}+^{44}Ca_{solid}+^{88}Sr_{solid}+^{86}Sr_{solid}} - \frac{^{86}Sr_{aq}^{2+}\cdot HCO_3^-}{\alpha_{eq}^{Sr}\, K_{eq}^{Sr}}\right] \quad (16g)$$

$$\frac{d^{86}Sr_{solid}}{dt} = K_{D,kin}\alpha_{eq}^{Sr}\, K_{eq}^{Sr}\, \alpha_{kin}^{Sr}\, k_f^{Ca}\left[\frac{^{86}Sr_{aq}^{2+}\cdot HCO_3^-}{\alpha_{eq}^{Sr}\, K_{eq}^{Sr}} - \frac{^{86}Sr_{solid}}{^{40}Ca_{solid}+^{44}Ca_{solid}+^{88}Sr_{solid}+^{86}Sr_{solid}}\right] \quad (16h)$$

This model was implemented in Matlab and the code for the subsequent simulations can be found in **Kußner, 2018**. In this setup, kinetic and equilibrium fractionation factors for Sr trace element distribution and major and minor stable isotope fractionation is denoted as $K_{D,kin}$ and $K_{D,eq}$ and $\alpha_{kin}^{Ca,Sr}$ and $\alpha_{eq}^{Ca,Sr}$ respectively. The values chosen for these parameters for Sr/Ca and $\delta^{44/40}Ca$ are consistent with those used previously in the CrunchTope models in the preceding section above. Strontium stable isotope kinetic and equilibrium fractionation factors of 0.9997 and 0.9999, respectively, derive from previous experimental studies (Böhm et al., 2012; AlKhatib and Eisenhauer, 2017). Kinetic rate and solubility constants for Ca (k_f^{Ca} and $K_{eq}{}^{Ca}$) and Sr (k_f^{Sr} and $K_{eq}{}^{Sr}$) are the same as those used for the CrunchTope model (**Table 5.5**).

The simplicity of this Matlab scripted multi-tracer model limits its capability to incorporate all the aspects of a fully integrated numerical reactive transport model. As a result, Ca concentrations from the Crunch model output that inherently incorporates the variability associated with dynamic carbonate equilibria and changing pH. were input directly into the multi-tracer model. Additionally, since the multi-tracer model can only

run a simple fractionation scenario where the fluid is assumed to equilibrate with the "bulk" calcite composition, the model must be benchmarked to the "bulk" fluid Ca concentrations and stable isotope simulations run using CrunchTope. The results of this benchmark are provided in **Fig. 5.16** and overall show good agreement between the multi-tracer and CrunchTope model predictions of fluid Ca (**Fig. 5.16A**) and $\delta^{44/40}$Ca (**Fig. 5.16B**) behavior throughout the course of calcite precipitation. Thus, with this agreement between the two models, we proceeded to apply the multi-tracer model to the high Sr, low and high SA experiments including the stable isotopes of the trace strontium (**Fig.**

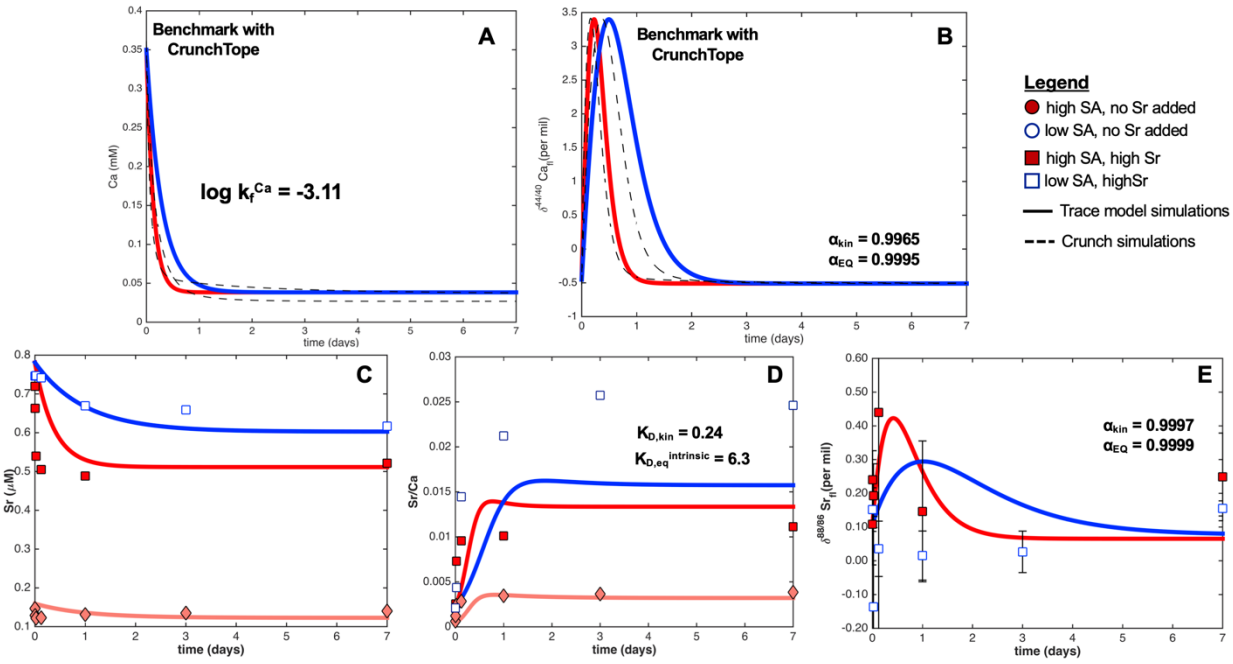

Figure 5.16 Multi-tracer model simulations for $\delta^{44/40}$Ca, Sr/Ca, and $\delta^{88/86}$Sr fractionation during calcite growth

Numerical simulations using a ternary (4-endmember) solid solution framework are shown for fluid $\delta^{44/40}$Ca (**A**), Sr/Ca (**C,D**), and $\delta^{88/86}$Sr (**D**) during calcite growth. Kinetic and thermodynamic parameters used in the model are the same as those used for our CrunchTope simulations. The multi–tracer was first benchmarked against the Crunch Ca concentration (**A**) and fluid $\delta^{44/40}$Ca output using the "bulk" fractionation scheme (**B**). Then the multi-tracer model was subsequently applied to the Sr incorporation experimental data where predicted Sr concentrations (solid lines, **C**) correspond well with observed values and produce similar results as the CrunchTope "trace model" for fluid Sr/Ca evolution through time (**D**). Novel simulations of fluid $\delta^{88/86}$Sr behavior in "high SA, high Sr" and "low SA, high Sr" (**E**) highlight the advantageous of using a 4-endmember solid solution framework.

5.16C,D,E). Multi-tracer model simulations accurately reproduce observed fluid Sr concentrations for the high and med Sr, high SA and high Sr, low SA experiments, predicting the gradual decrease and subsequent stabilization to more elevated values for the high Sr cases and lower values for the med Sr, high SA case (**Fig. 5.16C**).

Novel model results of the fluid $\delta^{88/86}$Sr evolution through time for the low and high SA, high Sr experiments (**Fig. 5.16E**) show an overall good agreement between the multi-tracer model predictions and the observed fluid $\delta^{88/86}$Sr behavior for the high SA, high Sr experiment. From this model simulation it appears as though early enrichment in the fluid $\delta^{88/86}$Sr to values of ~0.43‰ observed in the high SA, high Sr case is driven mostly by kinetic fractionation, shifting fluid $\delta^{88/86}$Sr to higher values. The subsequent turnover of fluid $\delta^{88/86}$Sr most likely represents slight re-equilibration with an isotopically light, newly formed mineral surface, giving an appearance of a departure from solid phase values as a result of disequilibrium isotope effects. On the other hand, numerical results for the low SA highlight a major discrepancy between model and measured fluid $\delta^{88/86}$Sr, which appears to exhibit behavior that is opposite to what is predicted by the model. Notably, in the early stages of calcite growth where precipitation rates along with Sr incorporation are fastest measured fluid $\delta^{88/86}$Sr are observed to decrease rapidly to a value of -0.14 ± 0.27‰. Based on the error associated with this value, it is certainly possible that this decrease is not real, and this data point is an erroneous outlier. However, if we look at the continued fluid $\delta^{88/86}$Sr trend through time for the remaining data points, it does appear as though fluid ratios decrease slightly with time and then rebound upwards to higher values at the end of the experiment (+0.16 ± 0.02‰). This behavior is simply not captured by the multi-tracer model which anticipates fluid $\delta^{88/86}$Sr

in this case to kinetically enrich and subsequently re-equilibrate similarly to the high SA, high Sr case, but at slower rates due to its smaller surface area. This could be a result of Sr rate dependence in the fluid $\delta^{88/86}$Sr, as has been proposed of similar outlier observations in fluid Sr/Ca. But this can't be confirmed from the multi-tracer model in its currently simplified form.

Overall, the successful development and application of a novel multi-tracer model that incorporates a ternary solid solution framework capable of tracking simultaneously Sr/Ca, $\delta^{44/40}$Ca, and $\delta^{88/86}$Sr during calcite precipitation under free drift conditions represents a novel step forward in our tracer modeling capabilities. The multi-tracer model as currently constituted is limited by its simplicity, which hinders its ability to model transient effects associated with physiochemical characteristics of the system and complex fluid–mineral interactions that can be accounted for in more robust multi-component geochemical models like CrunchTope. Thus, the next step would be to fully integrate the multi-tracer model framework into one of these more established geochemical modeling software so that we have the added capacity to trace numerous weathering tracers in the same system at the same time.

Table 5.5 Crunch and multi-tracer model trace element and stable isotope input parameters

Parameters	units	High SA				Low SA	
		Baseline	High Sr	Med Sr	Low Sr	Baseline	High Sr
Sr trace element							
Sr/Ca_{fluid}[a]	molar	8.64×10^{-6}	0.002	6.17×10^{-4}	5.69×10^{-5}	8.64×10^{-6}	0.002
Sr/Ca_{solid}[a]	molar	2.48×10^{-4}	2.48×10^{-4}	2.48×10^{-4}	2.48×10^{-4}	2.48×10^{-4}	2.48×10^{-4}
$K_{D,kin}$[b]		⟵ 0.24 ⟶					
$K_{D,eq}$[c]		⟵ 6.3 ⟶					
Ca stable isotopes							
$\delta^{44/40}Ca_{fluid}$[d]	‰	-0.45	-0.45	–	–	-0.45	-0.45
$\delta^{44/40}Ca_{solid}$[d]	‰	-0.51	-0.51	–	–	-0.51	-0.51
α_{kin}^{Ca}[e]		0.9965	0.9965	–	–	0.9965	0.9965
α_{eq}^{Ca}[f]		0.9995	0.9995	–	–	0.9995	0.9995
Sr stable isotopes							
$\delta^{88/86}Sr_{fluid}$[g]	‰	–	0.11	0.11	0.11	–	0.11
$\delta^{88/86}Sr_{solid}$[g]	‰	–	0.43	0.43	0.43	–	0.43
α_{kin}^{Sr}[h]		–	0.9997	0.9997	0.9997	–	0.9997
α_{eq}^{Sr}[h]		–	0.9999	0.9999	0.9999	–	0.9999

a. Measured initial fluid and calcite Sr/Ca trace element ratios.
b. Kinetic partition coefficient from DePaolo (2011) and Gabitov and Watson (2006).
c. Equilibrium partition coefficient from Fantle and DePaolo (2006).
d. Measured initial fluid and calcite Ca stable isotope ratios.
e. Kinetic fractionation factor derived from this study.
f. Equilibrium fractionation factor from DePaolo (2011).
g. Measured initial fluid and calcite Sr stable isotope ratios.
h. Kinetic and equilibrium fractionation factor from AlKhatib & Eisenhauer (2017).

5.5 CONCLUSIONS

This study is the first of its kind to investigate Ca, Sr, and Sr/Ca fractionation during calcite precipitation under free-drift conditions. A novel, closed system sparging technique is introduced that addresses the common problems associated with free-drift calcite precipitation experiments (i.e. pH-drift and sluggish CO_2 degassing) and, thus, makes these free-drift designs viable options to explore calcite precipitation under more dynamic, variable conditions. We find that under certain conditions, calcite precipitation from Sr-depleted oversaturated solutions can facilitate Sr dissolution, the extent of which

is dependent on the original calcite surface area. These Sr dissolution rates can potentially serve as lower limits on the backward, dissolution rate (R_b) for calcite that is an important component accurately characterizing Ca stable isotope fractionation but has yet to be fully constrained via prior studies. Calcite–$SrCO_3$ solid solution overall solubility and Sr uptake rates during calcite precipitation are strongly controlled by the amount of Sr initially present in the reactive fluid. A novel fractionation framework was developed and applied to Sr/Ca, $\delta^{44/40}$Ca, and $\delta^{88/86}$Sr behavior observed in the batch experiments over a range of surface areas and initial fluid Sr content. This new approach to tracking multiple tracers simultaneously in the same system offers a new path forward in the characterization of weathering tracers from the laboratory, individual reaction scale to larger dynamic hydrologic systems at the catchment scale.

CHAPTER 6

Summary

In summary, this thesis covers a broad range of metal stable isotope and trace element tracers across different spatiotemporal scales and secondary mineral formation systems. In this dissertation, a variety of different approaches and techniques were developed and applied in order to accurately capture and predict tracer behavior during weathering processes across scales from the laboratory to catchments. Metal stable isotopes and trace elements are leveraged as tracers of both silicate and carbonate weathering systems and appear to be dependent on a variety of physiochemical properties of the system such as mineral surface area, solid to fluid ratios, and fluid solute compositions. Their respective fractionation factors and partition coefficients are observed to vary with reaction progress, the extent to which is dependent on the rate of the secondary weathering. Importantly, from this dissertation we now have the foundations in place to create a new generation of reactive transport models capable of characterizing variable tracer behavior in weathering environments using a broadly consistent model theory.

In **Chapter 2**, new mineral growth onto higher surface areas seeds was found to result in rapid isotopic re-equilibration (over a period of ~2 weeks) whereas precipitation onto lower surface area grains retained a kinetic signature throughout the experimental duration. Experimental results were quantified using a modified numerical reaction network model featuring the novel capacity to explicitly treat the depth into the mineral that the fluid can chemically and isotopically exchange with through time. These numerical simulations demonstrate that the fluid-mineral surface interaction depth is

larger for low surface area seed crystals where both a larger mass of amorphous silica was formed (due to higher initial solid to fluid $SiO_{2(s)}$: $SiO_{2(aq)}$ in the lower surface area cases), and slower precipitations rates kept the reaction far from equilibrium, thereby impeding the influence of the back reaction and corresponding isotopic re-equilibration. These results highlight the significant role that water-rock interaction and, specifically, the unique isotopic signature of the growing mineral surface plays in the preservation of isotopic ratios within secondary silicate phases and surrounding pore fluids. Further, this study argues that a transient modeling approach is necessary to improve quantitative interpretations of observed isotope behavior in natural systems as in the case of these transient mineral formation experiments. This study has recently been published in *Geochimica et Cosmochimica Acta* (Fernandez et al., 2019).

In Chapter 3, building off the amorphous silica precipitation experiments conducted in **Chapter 2**, a novel Ge/Si dataset was developed providing a first glimpse into Ge behavior during secondary silicate formation. Findings from this combined experimental and numerical modeling study showed that there is a distinct lag between the onset of Ge partitioning and $\delta^{30}Si$ fractionation during active mineral growth. Ge/Si partitioning appears to be roughly 3 to 6 orders of magnitude slower than $\delta^{30}Si$ kinetic fractionation, thereby giving an appearance of conservative behavior over short experimental timescales (~30 days). This interplay between rapid $\delta^{30}Si$ fractionation and slower, continued Ge/Si partitioning over much longer timescales may provide important new insight into the progress of amorphous silica formation during and long after kinetic precipitation rates are observable. The extent to which Ge/Si equilibrates does appear to show some dependence on the mineral surface area of the pre-existing amorphous silica seeds. Notably, successful application of the numerical model initially

developed for silicon stable isotope fractionation suggests that Ge/Si does partition in a manner analogous to $\delta^{30}Si$ and can be described utilizing a common fractionation model theory.

In Chapter 4, we move away from the laboratory scale and investigate how dissolved Si concentrations and corresponding Si stable isotope ratios behave at the catchment scale using stream data during storm events, which provides a unique opportunity to explore Si geochemical behavior across a large range of discharge over a short period of time (hourly to daily timescales). Over 150 stream samples were analyzed representing seven catchments of various lithology and climates and eight distinct storm events. From this large-scale dataset arise several global observations with the most notable being the existence of a robust relationship between stream Si concentrations and corresponding $\delta^{30}Si$. On the other hand, globally observed chemostatic solute concentrations across catchments are shown to break down within individual catchments, and timescales of the respective storm events, where dissolved Si concentrations and $\delta^{30}Si$ vary considerably as a function of discharge. From these observations, two main take-a-ways can be extracted. First, evidence of a positive relationship between stream DSi and $\delta^{30}Si$ demonstrate that Si stable isotopes are effective tracers of weathering intensity. Second, complex datasets at the individual storm event timescale suggest that site-specific catchment processes and unique characteristics of a given system ultimately drive observed stream $\delta^{30}Si$ signatures. The unprecedented large-scale dataset generated from this study offers a new quantitative metric for chemical weathering reactions occurring within the weathering zone in the form of stable

isotope (R) – discharge (Q) relationships, which is argued to serve as a powerful complement to traditional C–Q relationships.

In Chapter 5, we look towards the future and begin to explore how similar concepts of physical parameters impacting environmental signatures and analogous fractionating mechanisms across tracers can be extended to systems outside those of the silicates (in this case, the carbonates). Free drift calcite precipitation experiments similar to those conducted for amorphous silica (**Chapter 2 and 3**) were run for a variety of surface areas and initial Sr contents. The results from this study suggest that mineral surface area plays a relatively minor role in overall calcite precipitation rates and associated Ca, Sr stable isotope fractionation. On the other hand, strontium fluid concentrations do show some dependence on surface area that is consistent with what was observed for Ge during amorphous silica precipitation. Model results successfully reproduces $\delta^{44/40}$Ca, $\delta^{88/86}$Sr, and Sr/Ca using the same rate parameters, thereby showing that these tracers are self-consistent. Thus, findings from these experiments highlight the need to incorporate a multi-tracer partitioning framework into established geochemical multi-component software, such as CrunchTope, which hold a great advantage over simplified batch model approaches in that it features extensive thermodynamic and kinetic databases that can fully characterize complex reactions such as calcite precipitation.

There are many future directions that stem from the research conducted in this thesis. The next envisioned steps are: (1) the continued development of multi-tracer approaches, which is the way forward in characterizing the reaction and transport processes that drive overall chemical weathering rates; (2) application of these new, experimentally calibrated multi-tracer reactive transport models to the catchment scale;

and (3) establishing high frequency stream chemistry and weathering tracer datasets that will allow us to gain better insight into the pathways of solute generation, fate, and transport that have until recently been obscured beneath coarse, low resolution monthly and annual datasets. All chapters from this thesis are intended to be submitted for publication in highly ranked journals. Chapter 2 has recently been published in *GCA* (Fernandez et al., 2019). Chapters 3, 4, and 5 will be submitted for publication in the coming months to peer-reviewed journals.

REFERENCES

Aagaard P. and Helgeson H. C. (1982) Thermodynamic and kinetic constraints on reaction rates among minerals and aqueous solutions. I. Theoretical considerations. *Am. J. Sci.* **282**, 237–285.

Abe Y. and Hunkeler D. (2006) Does the Rayleigh equation apply to evaluate field isotope data in contaminant hydrogeology? *Environ. Sci. Technol.* **40**, 1588–1596.

Aguirre A. A. (2019) Applying Ge/Si ratios to trace weathering reactions, hydrologic pathways and coal fly ash contamination in watersheds across the United States, *PhD Thesis dissertation*, Cornell University.

Aguirre A. A., Derry L. A., Mills T. J. and Anderson S. P. (2017) Colloidal transport in the Gordon Gulch catchment of the Boulder Creek CZO and its effect on C-Q relationships for silicon. *Water Resour. Res.* **53**, 2368–2383.

Andrews M. G., Jacobson A. D., Lehn G. O., Horton T. W. and Craw D. (2016) Radiogenic and stable Sr isotope ratios (87Sr/86Sr, δ88/86Sr) as tracers of riverine cation sources and biogeochemical cycling in the Milford Sound region of Fiordland, New Zealand. *Geochim. Cosmochim. Acta* **173**, 284–303.

Alexandre A., Bouvet M. and Abbadie L. (2011) The role of savannas in the terrestrial Si cycle: A case-study from Lamto, Ivory Coast. *Glob. Planet. Change* **78**, 162–169.

Alexandre A., Meunier J. D., Colin F. and Koud J. M. (1997) Plant impact on the

biogeochemical cycle of silicon and related weathering processes. *Geochim. Cosmochim. Acta* **61**, 677–682.

Alfredsson H., Hugelius G., Clymans W., Stadmark J., Kuhry P. and Conley D. J. (2015) Amorphous silica pools in permafrost soils of the Central Canadian Arctic and the potential impact of climate change. *Biogeochemistry* **124**, 441–459.

Alfieri L., Bisselink B., Dottori F., Naumann G., de Roo A., Salamon P., Wyser K. and Feyen L. (2017) Global projections of river flood risk in a warmer world. *Earth's Futur.* **5**, 171–182.

AlKhatib M. and Eisenhauer A. (2017) Calcium and strontium isotope fractionation in aqueous solutions as a function of temperature and reaction rate: I. Calcite. *Geochim. Cosmochim. Acta* **209**, 296–319.

Ameli A. A., Beven K., Erlandsson M., Creed I. F., McDonnell J. J. and Bishop K. (2017) Primary weathering rates, water transit times, and concentration-discharge relations: A theoretical analysis for the critical zone. *Water Resour. Res.* **53**, 942–960.

Anderson S. P., von Blanckenburg F. and White A. F. (2007) Physical and Chemical Controls on the Critical Zone. *Elements* **3**, 315–319.

Arnorsson, S. (1988) Germanium in Icelandic geothermal systems. *Geochim. Cosmochim. Acta* **48**(12), 2489-2502.

Arora B., Dwivedi D., Faybishenko B., Jana R. B. and Wainwright H. M. (2019)

Understanding and Predicting Vadose Zone Processes. *Rev. Mineral. Geochemistry* **85**, 303–328.

Bales R., Stacy E., Safeeq M., Meng X., Meadows M., Oroza C., Conklin M., Glaser S. and Wagenbrenner J. (2018) Spatially distributed water-balance and meteorological data from the rain-snow transition, southern Sierra Nevada, California. *Earth Syst. Sci. Data* **10**, 1795–1805.

Bao C., Li L., Shi Y. and Duffy C. (2017) Understanding watershed hydrogeochemistry: 1. Development of RT-Flux-PIHM. *Water Resour. Res.* **53**, 2328–2345.

Baronas J. J., Torres M. A., West A. J., Rouxel O., Georg B., Bouchez J., Gaillardet J. and Hammond D. E. (2018) Ge and Si isotope signatures in rivers: A quantitative multi-proxy approach. *Earth Planet. Sci. Lett.* **503**, 194–215.

Basile-Doelsch I., Meunier J. D. and Parron C. (2005) Another continental pool in the terrestrial silicon cycle. *Nature* **433**, 399–402.

Benettin P., Bailey S. W., Campbell J. L., Green M. B., Rinaldo A., Likens G. E., McGuire K. J. and Botter G. Linking water age and solute dynamics in streamflow at the Hubbard Brook Experimental Forest, NH, USA. *Water Resour. Res.* **51**, 9256–9272. Available at: https://agupubs.onlinelibrary.wiley.com/doi/abs/10.1002/2015WR017552.

Benettin P., Bailey S. W., Rinaldo A., Likens G. E., McGuire K. J. and Botter G. Young

runoff fractions control streamwater age and solute concentration dynamics. *Hydrol. Process.* **31**, 2982–2986.

Berger T. W., Swoboda S., Prohaska T. and Glatzel G. (2006) The role of calcium uptake from deep soils for spruce (Picea abies) and beech (Fagus sylvatica).

Berner R. A., Lasaga A. C. and Garrels R. M. (1983) The carbonate-silicate geochemical cycle and its effect on atmospheric carbon dioxide over the past 100 million years. *Am. J. Sci.* **283**, 641–683.

Best J. (2019) Anthropogenic Stresses on the World 's Big Rivers. *Nat. Geosci.* **12**, 1–59.

Blake Jr. M.C., Jayko A.S., McLaughlin R.J. (1985) Tectonostratigraphic terranes of the northern coast ranges, California. *Council for Energy and Mineral Resources*, **1**, 159-219.

Blecker S. W., King S. L., Derry L. A., Chadwick O. A., Ippolito J. A. and Kelly E. F. (2007) The ratio of germanium to silicon in plant phytoliths: Quantification of biological discrimination under controlled experimental conditions. *Biogeochemistry* **86**(2), 189–199.

Blecker S. W., McCulley R. L., Chadwick O. A. and Kelly E. F. (2006) Biologic cycling of silica across a grassland bioclimosequence. *Global Biogeochem. Cycles* **20**, 192-210.

Böhm F., Eisenhauer A., Tang J., Dietzel M., Krabbenhöft A., Kisakürek B. and Horn C. (2012) Strontium isotope fractionation of planktic foraminifera and inorganic calcite. *Geochim. Cosmochim. Acta* **93**, 300–314.

Van Den Boorn S. H. J. M., Vroon P. Z., Van Belle C. C., Van Der Wagt B., Schwieters J. and Van Bergen M. J. (2006) Determination of silicon isotope ratios in silicate materials by high-resolution MC-ICP-MS using a sodium hydroxide sample digestion method. *J. Anal. At. Spectrom.* **21**, 734–742.

Bouchez J., Blanckenburg F. von and Schuessler J. A. (2013) Modeling novel stable isotope ratios in the weathering zone. *Am. J. Sci.* **313**, 267–308.

Bouchez J. and Gaillardet J. (2014) How accurate are rivers as gauges of chemical denudation of the Earth surface? *Geology* **42**, 171–174.

Bouchez J., Gaillardet J. and von Blanckenburg F. (2014) Weathering Intensity in Lowland River Basins: From the Andes to the Amazon Mouth. *Procedia Earth Planet. Sci.* **10**, 280–286.

Boudon G., Komorowski J.-C., Villemant B. and Semet M. P. (2008) A new scenario for the last magmatic eruption of La Soufrière of Guadeloupe (Lesser Antilles) in 1530 A.D. Evidence from stratigraphy radiocarbon dating and magmatic evolution of erupted products. *J. Volcanol. Geotherm. Res.* **178**, 474–490.

Bracco J. N., Grantham M. C. and Stack A. G. (2012) Calcite Growth Rates As a Function of Aqueous Calcium-to-Carbonate Ratio, Saturation Index, and Inhibitor Concentration: Insight into the Mechanism of Reaction and Poisoning by Strontium. *Cryst. Growth Des.* **12**, 3540–3548.

Bullen T. D. and Bailey S. W. (2005) Identifying calcium sources at an acid deposition-impacted spruce forest: A strontium isotope, alkaline earth element multi-tracer approach. *Biogeochemistry* **74**, 63–99.

Buss H. L., Chapela Lara M., Moore O. W., Kurtz A. C., Schulz M. S. and White A. F. (2017) Lithological influences on contemporary and long-term regolith weathering at the Luquillo Critical Zone Observatory. *Geochim. Cosmochim. Acta* **196**, 224–251.

Cakmak I., Kurz H. and Marschner H. (1995) Short-term effects of boron, germanium and high light-intensity on membrane-permeability in boron deficient leaves of sunflower. *Physiologia Plantarum* **95**, 11–18.

Callot Y., Marticerona B., Bergametti G.(2000) Geomorphological approach for modeling the surface features of arid environments in a model of dust emissions: application to the Sahara desert. *Geodinamica Acta*, **13**, 245-270.

Campo J., Maass J. M., Jaramillo V. J. and Martínez Yrízar A. (2000) Calcium, potassium, and magnesium cycling in a Mexican tropical dry forest ecosystem. *Biogeochemistry* **49**, 21–36.

Capobianco C. and Navrotsky A. (1982) Calorimetric evidence for ideal mixing of silicon and germanium in glasses and crystals of sodium-feldspar composition. *Am. Mineral.* **67**, 718–724.

Capobianco C. and Watson E. B. (1981) Olivine/silicate melt partitioning of germanium:

an example of a nearly constant partition coefficient. *Geochim. Cosmochim. Acta* **46**, 235–240.

Cardinal D., Gaillardet J., Hughes H. J., Opfergelt S. and André L. (2010) Contrasting silicon isotope signatures in rivers from the Congo Basin and the specific behaviour of organic-rich waters. *Geophys. Res. Lett.* **37**.

Carey J. C. and Fulweiler R. W. (2012) The Terrestrial Silica Pump ed. S. Mozumdar. *PLoS One* **7**, e52932.

Cenki-Tok B., Chabaux F., Lemarchand D., Schmitt A.-D., Pierret M.-C., Viville D., Bagard M.-L. and Stille P. (2009) The impact of water–rock interaction and vegetation on calcium isotope fractionation in soil- and stream waters of a small, forested catchment (the Strengbach case). *Geochim. Cosmochim. Acta* **73**, 2215–2228.

Chanat J. G., Rice K. C. and Hornberger G. M. (2002) Consistency of patterns in concentration-discharge plots. *Water Resour. Res.* **38**, 22-1-22–10.

Chanda P., Gorski C. A., Oakes R. L. and Fantle M. S. (2019) Low temperature stable mineral recrystallization of foraminiferal tests and implications for the fidelity of geochemical proxies. *Earth Planet. Sci. Lett.* **506**, 428–440.

Chapela Lara M., Buss H.L., Pogge von Strandmann P.A.E., Dessert C., Gaillardet J. (2014) Controls on the Mg cycle in the tropics: insights from a case study at the Luquillo Critical Zone Observatory.*Proc. Earth and Plan. Sciences* **10**, 200-203.

Chapela Lara M., Buss H. L., Pogge von Strandmann P. A. E., Schuessler J. A. and Moore O. W. (2017) The influence of critical zone processes on the Mg isotope budget in a tropical, highly weathered andesitic catchment. *Geochim. Cosmochim. Acta*. **196**, 224-251.

Charbonnier Q., Moynier F. and Bouchez J. (2018) Barium isotope cosmochemistry and geochemistry. *Sci. Bull.* **63**, 385–394.

Chetelat B., Liu C.-Q., Zhao Z. Q., Wang Q. L., Li S. L., Li J. and Wang B. L. (2008) Geochemistry of the dissolved load of the Changjiang Basin rivers: Anthropogenic impacts and chemical weathering. *Geochim. Cosmochim. Acta* **72**, 4254–4277.

Chorover J., Derry L. A. and McDowell W. H. (2017) Concentration-Discharge Relations in the Critical Zone: Implications for Resolving Critical Zone Structure, Function, and Evolution. *Water Resour. Res.* **53**, 8654–8659.

Clarke J. (2003) The occurrence and significance of biogenic opal in the regolith. *Earth-Science Rev.* **60**, 175–194.

Clergue C., Dellinger M., Buss H. L., Gaillardet J., Benedetti M. F. and Dessert C. (2015) Influence of atmospheric deposits and secondary minerals on Li isotopes budget in a highly weathered catchment, Guadeloupe (Lesser Antilles). *Chem. Geol.* **414**, 28–41.

Cockerton H. E., Street-Perrott F. A., Barker P. A., Leng M. J., Sloane H. J. and Ficken K.

J. (2015) Orbital forcing of glacial/interglacial variations in chemical weathering and silicon cycling within the upper White Nile basin, East Africa: Stable-isotope and biomarker evidence from Lakes Victoria and Edward. *Quat. Sci. Rev.* **130**, 57–71.

Cognard-Plancq A.-L., Vincent M. and Normand M. (2003) Rôle De La Forêt Sur Les Débits Dans Des Bassins Versants Montagneux Sub-Méditerranéens : Une Approche Par Modélisation. *Études Géographie Phys.*, 43–60.

Conley D.J. (2002) Terrestrial ecosystems and the global biogeochemical silica cycle. *Global Biogeochem Cy* **16**, 1121.

Cornelis J. T., Delvaux B. and Titeux H. (2010) Contrasting silicon uptakes by coniferous trees: A hydroponic experiment on young seedlings. *Plant Soil* **336**, 99–106.

Cornelis J. T. and Delvaux B. (2016) Soil processes drive the biological silicon feedback loop. *Funct. Ecol.* **30**, 1298–1310.

Curti E., Fujiwara K., Iijima K., Tits J., Cuesta C., Kitamura A., Glaus M. A. and Müller W. (2010) Radium uptake during barite recrystallization at 23 ± 2 °C as a function of solution composition: An experimental 133Ba and 226Ra tracer study. *Geochim. Cosmochim. Acta* **74**, 3553–3570.

Curti E., Kulik D. A. and Tits J. (2005) Solid solutions of trace Eu(III) in calcite: Thermodynamic evaluation of experimental data over a wide range of pH and pCO2. *Geochim. Cosmochim. Acta* **69**, 1721–1737.

Dellinger M., Gaillardet J., Bouchez J., Calmels D., Louvat P., Dosseto A., Gorge C., Alanoca L. and Maurice L. (2015) Riverine Li isotope fractionation in the Amazon River basin controlled by the weathering regimes. *Geochim. Cosmochim. Acta* **164**, 71–93.

Delstanche S., Opfergelt S., Cardinal D., Elsass F., André L. and Delvaux B. (2009) Silicon isotopic fractionation during adsorption of aqueous monosilicic acid onto iron oxide. *Geochim. Cosmochim. Acta* **73**, 923–934.

Delvigne C., Opfergelt S., Cardinal D., Hofmann A. and André L. (2016) Desilication in Archean weathering processes traced by silicon isotopes and Ge/Si ratios. *Chem. Geol.* **420**, 139–147.

Radiogenic and Nucleosynthetic Processes. *Rev. Mineral. Geochemistry* **55**, 255–288.

DePaolo D. J. (2011) Surface kinetic model for isotopic and trace element fractionation during precipitation of calcite from aqueous solutions. *Geochim. Cosmochim. Acta* **75**, 1039–1056.

Derry L. A., Kurtz A. C., Ziegler K. and Chadwick O. A. (2005) Biological control of terrestrial silica cycling and export fluxes to watersheds. *Nature* **433**, 728–731.

Derry L. A., Pett-Ridge J. C., Kurtz A. C. and Troester J. W. (2006) Ge/Si and 87Sr/86Sr tracers of weathering reactions and hydrologic pathways in a tropical granitoid system. *J. Geochemical Explor.* **88**, 271–274.

Dessert C., Clergue C., Rousteau A., Crispi O. and Benedetti M. F. (2020) Atmospheric contribution to cations cycling in highly weathered catchment, Guadeloupe (Lesser Antilles). *Chem. Geol.* **531**, 119354.

Dialynas Y. G., Bastola S., Bras R. L., Marin-Spiotta E., Silver W. L., Arnone E. and Noto L. V. (2016) Impact of hydrologically driven hillslope erosion and landslide occurrence on soil organic carbon dynamics in tropical watersheds. *Water Resour. Res.* **52**, 8895–8919.

Ding T. P., Gao J. F., Tian S. H., Wang H. B. and Li M. (2011) Silicon isotopic composition of dissolved silicon and suspended particulate matter in the Yellow River, China, with implications for the global silicon cycle. *Geochim. Cosmochim. Acta* **75**, 6672–6689.

Dixon J. L., Heimsath A. M. and Amundson R. (2009) The critical role of climate and saprolite weathering in landscape evolution. *Earth Surf. Process. Landforms* **34**, 1507–1521.

Donat M. G., Lowry A. L., Alexander L. V, O'Gorman P. A. and Maher N. (2016) More extreme precipitation in the world's dry and wet regions. *Nat. Clim. Chang.* **6**, 508–513.

Dove P. M., Han N., Wallace A. F. and Yoreo J. J. De (2008) Kinetics of amorphous silica dissolution and the paradox of the silica polymorphs. *Proc. Natl. Acad. Sci.* **105**,

9903–9908.

Drouet T., Herbauts J., Gruber W. and Demaiffe D. (2005) Strontium isotope composition as a tracer of calcium sources in two forest ecosystems in Belgium. *Geoderma* **126**, 203–223.

Druhan J. L., Brown S. T. and Huber C. (2015) Isotopic Gradients Across Fluid–Mineral Boundaries. *Rev. Mineral. Geochemistry* **80**, 355–391.

Druhan J. L. and Maher K. (2017) The influence of mixing on stable isotope ratios in porous media: A revised Rayleigh model. *Water Resour. Res.***53**, 1101–1124.

Druhan J. L., Steefel C. I., Williams K. H. and DePaolo D. J. (2013) Calcium isotope fractionation in groundwater: Molecular scale processes influencing field scale behavior. *Geochim. Cosmochim. Acta* **119**, 93–116.

Druhan J.L., Winnick M.J., and Thullner, M. (2019) by Transport and Transformation, **85**, 239-264.

Druhan J.L. and Winnick M.J. (2019) Reactive Transport of stable isotopes, *Elements* **15**, 107-110.

Dupuis R., Benoit M., Nardin E. and Méheut M. (2015) Fractionation of silicon isotopes in liquids: The importance of configurational disorder. *Chem. Geol.* **396**, 239–254.

Durand P., Lelong F. and Neal C. (1992) Comparison and significance of annual hydrochemical budgets in three small granitic catchments with contrasting

vegetation (Mont-Lozere, France). *Environ. Pollut.* **75**, 223–228.

Eckert D., Rolle M. and Cirpka O. A. (2012) Numerical simulation of isotope fractionation in steady-state bioreactive transport controlled by transverse mixing. *J. Contam. Hydrol.* **140–141**, 95–106.

Enüstün B. V. and Turkevich J. (1960) Solubility of Fine Particles of Strontium Sulfate. *J. Am. Chem. Soc.* **82**, 4502–4509.

Epstein E. (2001) Silicon in plants: facts vs. concepts. In: Datnoff LE, Snyder GH, and Korndörfer GH (Eds). Silicon in agriculture, Amsterdam, Netherlands: Elsevier Science.

Evans M. J. and Derry L. A. (2002) Quartz control of high germanium/silicon ratios in geothermal waters. *Geology* **30**, 1019–1022.

Fantle M. S. (2015) Calcium isotopic evidence for rapid recrystallization of bulk marine carbonates and implications for geochemical proxies. *Geochim. Cosmochim. Acta* **148**, 378–401.

Fantle M. S. (2010) Evaluating the Ca Isotope Proxy. *Am. J. Sci.* **310**, 194–230.

Fantle M. S. and DePaolo D. J. (2007) Ca isotopes in carbonate sediment and pore fluid from ODP Site 807A: The Ca2+(aq)–calcite equilibrium fractionation factor and calcite recrystallization rates in Pleistocene sediments. *Geochim. Cosmochim. Acta* **71**, 2524–2546.

Fantle M. S. and Higgins J. (2014) The effects of diagenesis and dolomitization on Ca and Mg isotopes in marine platform carbonates: Implications for the geochemical cycles of Ca and Mg. *Geochim. Cosmochim. Acta* **142**, 458–481.

Fantle M.S. and Tipper E.T. (2014) Calcium isotopes in the global biogeochemical Ca cycle: Implications for development of a Ca isotope proxy. *Earth-Science Reviews* **129**, 148-177.

Farmer V. C. (2005) Forest vegetation does recycle substantial amounts of silicon from and back to the soil solution with phytoliths as an intermediate phase, contrary to recent reports. *Eur. J. Soil Sci.* **56**, 271–272.

Fernandez N. M., Zhang X. and Druhan J. L. (2019) Silicon isotopic re-equilibration during amorphous silica precipitation and implications for isotopic signatures in geochemical proxies. *Geochim. Cosmochim. Acta* **262**, 104–127.

Ferrier K. L., Kirchner J. W., Riebe C. S. and Finkel R. C. (2010) Mineral-specific chemical weathering rates over millennial timescales: Measurements at Rio Icacos, Puerto Rico. *Chem. Geol.* **277**, 101–114.

Fleming B. A. (1986) Kinetics of reaction between silicic acid and amorphous silica surfaces in NaCl solutions. *J. Colloid Interface Sci.* **110**, 40–64.

Floury P., Gaillardet J., Gayer E., Bouchez J., Tallec G., Ansart P., Koch F., Gorge C., Blanchouin A. and Roubaty J. L. (2017) The potamochemical symphony: New

progress in the high-frequency acquisition of stream chemical data. *Hydrol. Earth Syst. Sci.* **21**, 6153–6165.

Foster D. R., Fluet M. and Boose E. R. (1999) Human or natural disturbance: Landscape-scale dynamics of the tropical forests of Puerto Rico. *Ecol. Appl.* **9**, 555–572.

Frierdich A. J., Beard B. L., Thiruchelvi R. R., Scherer M. M. and Johnson C. M. (2014) Iron isotope fractionation between aqueous Fe(II) and goethite revisited: New insights based on a multi-direction approach to equilibrium and isotopic exchange rate modification. *Geochim. Cosmochim. Acta* **139**, 383–398.

Frierdich A. J., Helgeson M., Liu C., Wang C., Rosso K. M. and Scherer M. M. (2015) Iron Atom Exchange between Hematite and Aqueous Fe(II). *Environ. Sci. Technol.* **49**, 8479–8486.

Fries D. M., James R. H., Dessert C., Bouchez J., Beaumais A. and Pearce C. R. (2019) The response of Li and Mg isotopes to rain events in a highly-weathered catchment. *Chem. Geol.* **519**, 68–82.

Frings Patrick J., Clymans W., Fontorbe G., De La Rocha C. L. and Conley D. J. (2016) The continental Si cycle and its impact on the ocean Si isotope budget. *Chem. Geol.* **425**, 12–36.

Frings Patrick J, Clymans W., Fontorbe G., De La Rocha C. L. and Conley D. J. (2016) The continental Si cycle and its impact on the ocean Si isotope budget. *Chem. Geol.* **425**,

12–36.

Froelich Philip N., Blanc V., Mortlock R. A. and Chillrud S. N. (1992) River fluxes of dissolved silica to the ocean were higher during glacials: Ge/Si in diatoms, rivers, and oceans. *Paleoceanography* **7**, 739–767.

Froelich P N, Blanc V., Mortlock R. A., Chillrud S. N., Dunstan W., Udomkit A. and Peng T.-H. (1992) River Fluxes of Dissolved Silica to the Ocean Were Higher during Glacials: Ge/Si In Diatoms, Rivers, and Oceans. *Paleoceanography* **7**, 739–767.

Froelich P. N., Hambrick G. A., Andreae M. O., Mortlock R. A. and Edmond J. M. (1985) The geochemistry of inorganic germanium in natural waters. *J. Geophys. Res. Ocean.* **90**, 1133–1141.

Fruchter N., Eisenhauer A., Dietzel M., Fietzke J., Böhm F., Montagna P., Stein M., Lazar B., Rodolfo-Metalpa R. and Erez J. (2016) 88Sr/86Sr fractionation in inorganic aragonite and in corals. *Geochim. Cosmochim. Acta* **178**, 268–280.

Fulweiler R.W. and Nixon, S. (2005) Terrestrial vegetation and the seasonal cycle of dissolved silica in a southern New England coastal river. *Biogeochemistry* **74**, 115-130.

Gabitov R. I., Sadekov A. and Leinweber A. (2014) Crystal growth rate effect on Mg/Ca and Sr/Ca partitioning between calcite and fluid: An in situ approach. *Chem. Geol.* **367**, 70–82.

Gabitov R. I. and Watson E. B. (2006) Partitioning of strontium between calcite and fluid. *Geochemistry, Geophys. Geosystems* **7**, 1-12.

Gaillardet J., Braud I., Hankard F., Anquetin S., Bour O., Dorfliger N., de Dreuzy J. R., Galle S., Galy C., Gogo S., Gourcy L., Habets F., Laggoun F., Longuevergne L., Le Borgne T., Naaim-Bouvet F., Nord G., Simonneaux V., Six D., Tallec T., Valentin C., Abril G., Allemand P., Arènes A., Arfib B., Arnaud L., Arnaud N., Arnaud P., Audry S., Comte V. B., Batiot C., Battais A., Bellot H., Bernard E., Bertrand C., Bessière H., Binet S., Bodin J., Bodin X., Boithias L., Bouchez J., Boudevillain B., Moussa I. B., Branger F., Braun J. J., Brunet P., Caceres B., Calmels D., Cappelaere B., Celle-Jeanton H., Chabaux F., Chalikakis K., Champollion C., Copard Y., Cotel C., Davy P., Deline P., Delrieu G., Demarty J., Dessert C., Dumont M., Emblanch C., Ezzahar J., Estèves M., Favier V., Faucheux M., Filizola N., Flammarion P., Floury P., Fovet O., Fournier M., Francez A. J., Gandois L., Gascuel C., Gayer E., Genthon C., Gérard M. F., Gilbert D., Gouttevin I., Grippa M., Gruau G., Jardani A., Jeanneau L., Join J. L., Jourde H., Karbou F., Labat D., Lagadeuc Y., Lajeunesse E., Lastennet R., Lavado W., Lawin E., Lebel T., Le Bouteiller C., Legout C., Lejeune Y., Le Meur E., Le Moigne N., Lions J., Lucas A., Malet J. P., Marais-Sicre C., Maréchal J. C., Marlin C., Martin P., Martins J., Martinez J. M., Massei N., Mauclerc A., Mazzilli N., Molénat J., Moreira-Turcq P., Mougin E., Morin S., Ngoupayou J. N.,

Panthou G., Peugeot C., Picard G., Pierret M. C., Porel G., Probst A., Probst J. L., Rabatel A., Raclot D., Ravanel L., Rejiba F., René P., Ribolzi O., Riotte J., Rivière A., Robain H., Ruiz L., Sanchez-Perez J. M., Santini W., Sauvage S., Schoeneich P., Seidel J. L., Sekhar M., Sengtaheuanghoung O., Silvera N., Steinmann M., Soruco A., Tallec G., Thibert E., Lao D. V., Vincent C., Viville D., Wagnon P. and Zitouna R. (2018) OZCAR: The French network of critical zone observatories. *Vadose Zo. J.* **17**.

Gaillardet J., Dupré B., Louvat P. and Allègre C. J. (1999) Global silicate weathering and CO2consumption rates deduced from the chemistry of large rivers. *Chem. Geol.* **159**, 3–30.

Gaillardet J., Rad S., Rivé K., Louvat P., Gorge C., Allègre C. J. and Lajeunesse E. (2011) Orography-driven chemical denudation in the lesser antilles: Evidence for a new feed-back mechanism stabilizing atmospheric CO2. *Am. J. Sci.* **311**, 851–894.

Geilert S., Vroon P. Z., Keller N. S., Gudbrandsson S., Stefánsson A. and van Bergen M. J. (2015) Silicon isotope fractionation during silica precipitation from hot-spring waters: Evidence from the Geysir geothermal field, Iceland. *Geochim. Cosmochim. Acta* **164**, 403–427.

Geilert S., Vroon P. Z., Roerdink D. L., Van Cappellen P. and van Bergen M. J. (2014) Silicon isotope fractionation during abiotic silica precipitation at low temperatures: Inferences from flow-through experiments. *Geochim. Cosmochim. Acta* **142**, 95–114.

Georg R.B., Reynolds B. C., Frank M. and Halliday A. N. (2006) Mechanisms controlling the silicon isotopic compositions of river waters. *Earth Planet. Sci. Lett.* **249**, 290–306.

Georg R B, Reynolds B. C., Frank M. and Halliday A. N. (2006) New sample preparation techniques for the determination of Si isotopic compositions using MC-ICPMS. *Chem. Geol.* **235**, 95–104.

Georg R.B., Reynolds B. C., West A. J., Burton K. W. and Halliday A. N. (2007) Silicon isotope variations accompanying basalt weathering in Iceland. *Earth Planet. Sci. Lett.* **261**, 476–490.

Georg R. B., Zhu C., Reynolds B. C. and Halliday A. N. (2009) Stable silicon isotopes of groundwater, feldspars, and clay coatings in the Navajo Sandstone aquifer, Black Mesa, Arizona, USA. *Geochim. Cosmochim. Acta* **73**, 2229–2241.

Gíslason S. D. S. R., Arnórsson S. and Ármannsson H. (1996) Chemical weathering of basalt in Southwest Iceland: Effects of runoff, age of rocks and vegetative/glacial cover. *Am. J. Sci.* **296**, 837–907.

Goldschmidt V. M. (1926) Concerning the crystallo-chemical and geochemical behaviour of Germanium. *Naturwissenschaften* **14**, 295–297.

Goddéris Y., Schott J. and Brantley S. L. (2019) Reactive transport models of weathering. *Elements* **15**, 103–106.

Godsey, S.E., Kirchner J.W., Clow D.W. (2009) Concentration–discharge relationships

reflect chemostatic characteristics of US catchments. *Hydrol. Process.* **23**, 1844–1864. Available at: https://onlinelibrary.wiley.com/doi/abs/10.1002/hyp.7315.

Godsey S. E., Hartmann J. and Kirchner J. W. (2019) Catchment chemostasis revisited: Water quality responds differently to variations in weather and climate. *Hydrol. Process.*, 3056–3069.

Gorski C. A. and Fantle M. S. (2017) Stable mineral recrystallization in low temperature aqueous systems: A critical review. *Geochim. Cosmochim. Acta* **198**, 439–465.

Goudie A. S. and Middleton N. J. (2001) Saharan dust storms: Nature and consequences. *Earth-Science Rev.* **56**, 179–204.

Gresens R. L. (1981) The aqueous solubility product of solid solutions: 1. Stoichiometric saturation: partial and total solubility product. *Chem. Geol.* **32**, 59–72.

Griffith E. M., Schmitt A.-D., Andrews M. G. and Fantle M. S. (2020) Elucidating modern geochemical cycles at local, regional, and global scales using calcium isotopes. *Chem. Geol.* **534**, 1–13.

Guerzoni S., Molinaroli E., Rossini P., Rampazzo G., Quarantotto G., De Falco G. and Cristini S. (1999) Role of desert aerosol in metal fluxes in the mediterranean area. *Chemosphere* **39**, 229–246.

Gunnarsson I. and Anórsson S. (2000) Amorphous silica solubility and the thermodynamic properties of H4SiO°4 in the range of 0° to 350°C at Psat. *Geochim.*

Cosmochim. Acta **64**, 2295–2307.

Gussone N., Böhm F., Eisenhauer A., Dietzel M., Heuser A., Teichert B. M. A., Reitner J., Wörheide G. and Dullo W.-C. (2005) Calcium isotope fractionation in calcite and aragonite. *Geochim. Cosmochim. Acta* **69**, 4485–4494. Available at: http://www.sciencedirect.com/science/article/pii/S0016703705004795.

Hahm W. J., Riebe C. S., Lukens C. E. and Araki S. (2014) Bedrock composition regulates mountain ecosystems and landscape evolution. *Proc. Natl. Acad. Sci. U. S. A.* **111**, 3338–3343.

Hajj F., Poszwa A., Bouchez J. and Guérold F. (2017) Radiogenic and "stable" strontium isotopes in provenance studies: A review and first results on archaeological wood from shipwrecks. *J. Archaeol. Sci.* **86**, 24–49.

Halbach P. and Puteanus D. (1984) The influence of the carbonate dissolution rate on the growth and composition of Co-rich ferromanganese crusts from Central Pacific seamount areas. *Earth Planet. Sci. Lett.* **68**, 73–87.

Halicz L., Segal I., Fruchter N., Stein M. and Lazar B. (2008) Strontium stable isotopes fractionate in the soil environments? *Earth Planet. Sci. Lett.* **272**, 406–411.

Halperin S. J., Barzilay A., Carson, M., Roberts C., Lynch J., and Komarneni, S. (1995) Germanium accumulation and toxicity in barley, *J. Plant Nutr.* **18**, 1417–1426.

Handler R. M., Beard B. L., Johnson C. M. and Scherer M. M. (2009) Atom Exchange

between Aqueous Fe(II) and Goethite: An Fe Isotope Tracer Study. *Environ. Sci. Technol.* **43**, 1102–1107..

Handler R. M., Frierdich A. J., Johnson C. M., Rosso K. M., Beard B. L., Wang C., Latta D. E., Neumann A., Pasakarnis T., Premaratne W. A. P. J. and Scherer M. M. (2014) Fe(II)-Catalyzed Recrystallization of Goethite Revisited. *Environ. Sci. Technol.* **48**, 11302–11311.

Harouaka K., Eisenhauer A. and Fantle M. S. (2014) Experimental investigation of Ca isotopic fractionation during abiotic gypsum precipitation. *Geochim. Cosmochim. Acta* **129**, 157–176.

He H., Zhang S., Zhu C. and Liu Y. (2015) Equilibrium and kinetic Si isotope fractionation factors and their implications for Si isotope distributions in the Earth's surface environments. *Acta Geochim.* **35**, 15–24.

Heger T. J., Giesbrecht I. J. W., Gustavsen J., del Campo J., Kellogg C. T. E., Hoffman K. M., Lertzman K., Mohn W. W. and Keeling P. J. (2018) High-throughput environmental sequencing reveals high diversity of litter and moss associated protist communities along a gradient of drainage and tree productivity. *Environ. Microbiol.* **20**, 1185–1203.

Helgeson H. C., Murphy W. M. and Aagaard P. (1984) Thermodynamic and kinetic constraints on reaction rates among minerals and aqueous solutions. II. Rate

constants, effective surface area, and the hydrolysis of feldspar. *Geochim. Cosmochim. Acta* **48**, 2405–2432.

Hilley G. E. and Porder S. (2008) A framework for predicting global silicate weathering and CO2 drawdown rates over geologic time-scales. *Proc. Natl. Acad. Sci. U. S. A.* **105**, 16855–16859.

Hindshaw R. S., Reynolds B. C., Wiederhold J. G., Kretzschmar R. and Bourdon B. (2011) Calcium isotopes in a proglacial weathering environment: Damma glacier, Switzerland. *Geochim. Cosmochim. Acta* **75**, 106–118.

Hirabayashi Y., Mahendran R., Koirala S., Konoshima L., Yamazaki D., Watanabe S., Kim H. and Kanae S. (2013) Global flood risk under climate change. *Nat. Clim. Chang.* **3**, 816–821.

Hofmann A. E., Bourg I. C. and DePaolo D. J. (2012) Ion desolvation as a mechanism for kinetic isotope fractionation in aqueous systems. *Proc. Natl. Acad. Sci.* **109**, 18689–18694.

Hogan J. F. and Blum J. D. (2003) Tracing hydrologic flow paths in a small forested watershed using variations in 87Sr/86Sr, [Ca]/[Sr], [Ba]/[Sr] and δ18O. *Water Resour. Res.* **39**.

Holdren G. R. and Speyer P. M. (1985) Reaction rate-surface area relationships during the early stages of weathering-I. Initial observations. *Geochim. Cosmochim. Acta* **49**, 675–

681.

Holmden C. and Bélanger N. (2006) Calcium isotope fractionation in a boreal forest ecosystem. *Geochim. Cosmochim. Acta* **70**, A261.

Hornberger G. M., Scanlon T. M. and Raffensperger J. P. (2001) Modelling transport of dissolved silica in a forested headwater catchment: the effect of hydrological and chemical time scales on hysteresis in the concentration-discharge relationship. *Hydrol. Process.* **15**, 2029–2038.

Huang Y. and Fairchild I. J. (2001) Partitioning of Sr2+ and Mg2+ into calcite under karst-analogue experimental conditions. *Geochim. Cosmochim. Acta* **65**, 47–62.

Huber C., Druhan J. L. and Fantle M. S. (2017) Perspectives on geochemical proxies: The impact of model and parameter selection on the quantification of carbonate recrystallization rates. *Geochim. Cosmochim. Acta* **217**, 171–192.

Hughes H. J., Sondag F., Cocquyt C., Laraque A., Pandi A., André L. and Cardinal D. (2011) Effect of seasonal biogenic silica variations on dissolved silicon fluxes and isotopic signatures in the Congo River. *Limnol. Oceanogr.* **56**, 551–561.

Hughes H. J., Sondag F., Santos R. V, André L. and Cardinal D. (2013) The riverine silicon isotope composition of the Amazon Basin. *Geochim. Cosmochim. Acta* **121**, 637–651.

Hunsaker C. T. and Johnson D. W. (2017) Concentration-discharge relationships in headwater streams of the Sierra Nevada, California. *Water Resour. Res.* **53**, 7869–7884.

Imbert D., Rousteau A. and Labbé P. (1998) Ouragans et diversite biologique dans les forets tropicales. L'exemple de la Guadeloupe. *Acta Oecologica* **19**, 251–262.

Iler R. K. (1979) *The Chemistry of Silica: Solubility, Polymerization, Colloid and Surface Chemistry, and Biochemistry*., John Wiley & Sons.

Inskeep W. P. and Bloom P. R. (1985) An evaluation of rate equations for calcite precipitation kinetics at pCO2 less than 0.01 atm and pH greater than 8. *Geochim. Cosmochim. Acta* **49**, 2165–2180.

Jacobson A. D., Grace Andrews M., Lehn G. O. and Holmden C. (2015) Silicate versus carbonate weathering in Iceland: New insights from Ca isotopes. *Earth Planet. Sci. Lett.* **416**, 132–142.

Johnson T.M. and DePaolo D. J. (1996) Reaction-Transport models for radiocarbon in groundwater: the effects of longitudinal dispersion and the use of Sr isotope ratios to correct for water-rock interaction. *Water Resour. Res.,* **35**(7), 2203-2212.

Johnson T. M. and Depaolo D. J. (1997) Rapid exchange effects on isotope ratios in groundwater systems 1. Development of a transport-dissolution-exc. *Water Resour.* **33**, 187–195.

Johnson C. M., Skulan J. L., Beard B. L., Sun H., Nealson K. H. and Braterman P. S. (2002) Isotopic fractionation between Fe(III) and Fe(II) in aqueous solutions. *Earth Planet. Sci. Lett.* **195**, 141–153.

Joshi P., Fantle M. S., Larese-Casanova P. and Gorski C. A. (2017) Susceptibility of Goethite to Fe 2+-Catalyzed Recrystallization over Time.

Keir R. S. (1980) The dissolution kinetics of hiogenic calcium carbonates in seawater. *Geochim. Cosmochim. Acta* **44**, 241–252.

Kiczka M., Wiederhold J. G., Frommer J., Kraemer S. M., Bourdon B. and Kretzschmar R. (2010) Iron isotope fractionation during proton- and ligand-promoted dissolution of primary phyllosilicates. *Geochim. Cosmochim. Acta* **74**, 3112–3128.

Kim H., Bishop J. K. B., Dietrich W. E. and Fung I. Y. (2014) Process dominance shift in solute chemistry as revealed by long-term high-frequency water chemistry observations of groundwater flowing through weathered argillite underlying a steep forested hillslope. *Geochim. Cosmochim. Acta* **140**, 1–19.

Kim, H., Dietrich W.E., Thurnhoffer B.M., Bishop J.K., Fung I.Y. (2017) Controls on solute concentration–discharge relationships revealsed by simultaneous hydrochemistry observations of hillsope runoff and stream flow: The importance of critical zone structure. *Water Resour. Res.*, **53**, 1424-1443.

Korover, M.C., Floyd W.C., Brunsting R. (2019) Observed stream flow from seven coastal watersheds in British Columbia, Canada, Sep 2013–April 2019. Version 4.0. Hakai Institute. Dataset.

Kulik D. A., Vinograd V. L., Paulsen N. and Winkler B. (2010) (Ca,Sr)CO3 aqueous-solid

solution systems: From atomistic simulations to thermodynamic modelling. *Phys. Chem. Earth* **35**, 217–232.

Kunimatsu T., Hamabata E., Sudo M. and Hida Y. (2001) Comparison of nutrient budgets betwen three forested mountain watersheds on granite bedrock. *Water Sci. Technol.* **44**, 129–140.

Kurtz A. C., Derry L. A. and Chadwick O. A. (2002) Germanium-silicon fractionation in the weathering environment. *Geochim. Cosmochim. Acta* **66**, 1525–1537.

De La Rocha C. L., Brzezinski M. A., DeNiro M. J. and Shemesh A. (1998) Silicon-isotope composition of diatoms as an indicator of past oceanic change. *Nature* **395**, 680–683.

Landrot G., Ajo-Franklin J. B., Yang L., Cabrini S. and Steefel C. I. (2012) Measurement of accessible reactive surface area in a sandstone, with application to CO2 mineralization. *Chem. Geol.* **318–319**, 113–125.

Lara M. C., Buss H. L., Strandmann P. A. E. P. von, Dessert C. and Gaillardet J. (2014) Controls on the Mg Cycle in the Tropics: Insights from a Case Study at the Luquillo Critical Zone Observatory. *Procedia Earth Planet. Sci.* **10**, 200–203.

Laruelle G. G., Roubeix V., Sferratore A., Brodherr B., Ciuffa D., Conley D. J., Dürr H. H., Garnier J., Lancelot C., LeThiPhuong Q., Meunier J.-D., Meybeck M., Michalopoulos P., Moriceau B., Ni L., Loucaides S., Papush L., Presti M., Ragueneau O., Regnier P., Saccone L., Slomp C. P., Spiteri C. and Van C. (2009) Anthropogenic perturbations of

the silicon cycle at the global scale: Key role of the land-ocean transition. *Global Biogeochem. Cycles* **23**.

Lelong F., Dupraz C., Durand P. and Didon-Lescot J. F. (1990) Effects of vegetation type on the biogeochemistry of small catchments (Mont Lozere, France). *J. Hydrol.* **116**, 125–145.

Lemarchand D. and Gaillardet J. (2006) Transient features of the erosion of shales in the Mackenzie basin (Canada), evidences from boron isotopes. *Earth Planet. Sci. Lett.* **245**, 174–189.

Lemarchand E., Chabaux F., Vigier N., Millot R. and Pierret M. C. (2010) Lithium isotope systematics in a forested granitic catchment (Strengbach, Vosges Mountains, France). *Geochim. Cosmochim. Acta* **74**, 4612–4628.

Lemarchand E., Wasserburg G.J., Papanastassiou D.A. Rate-controleed calcium isotope fractionation in synthetic calcite. *Geochim. Cosmochim. Acta* **66**(22), 4665-4678.

Li Li., Maher K., Navarre-Sitchler A., Druhan J., Meile C., Lawrence C., Moore J., Perdrial J., Sullivan P., Thompson A., Jin L., Bolton E. W., Brantley S. L., Dietrich W. E., Mayer K. U., Steefel C. I., Valocchi A., Zachara J., Kocar B., Mcintosh J., Tutolo B. M., Kumar M., Sonnenthal E., Bao C. and Beisman J. (2017) Expanding the role of reactive transport models in critical zone processes. *Earth-Science Rev.* **165**, 280–301.

Levy-Booth D. J., Giesbrecht I. J. W., Kellogg C. T. E., Heger T. J., D'Amore D. V.,

Keeling P. J., Hallam S. J. and Mohn W. W. (2019) Seasonal and ecohydrological regulation of active microbial populations involved in DOC, CO 2 , and CH 4 fluxes in temperate rainforest soil. *ISME J.* **13**, 950–963.

Lichtner P. C. (1988) The quasi-stationary state approximation to coupled mass transport and fluid-rock interaction in a porous medium. *Geochim. Cosmochim. Acta* **52**, 143–165.

Lichtner P. C. (1985) Continuum model for simultaneous chemical reactions and mass transport in hydrothermal systems. *Geochim. Cosmochim. Acta* **49**, 779–800.

Liu F., Conklin M. H. and Shaw G. D. (2017) Insights into hyrologic and hydrochemical processes based on concentration-discharge and end-member mixing analyses in the mid-Merced River Basin, Sierra Nevada, California. *J. Am. Water Resour. Assoc.* **53**, 832–850.

Lloret E., Dessert C., Gaillardet J., Albéric P., Crispi O., Chaduteau C. and Benedetti M. F. (2011) Comparison of dissolved inorganic and organic carbon yields and fluxes in the watersheds of tropical volcanic islands, examples from Guadeloupe (French West Indies). *Chem. Geol.* **280**, 65–78.

Lloret E., Dessert C., Pastor L., Lajeunesse E., Crispi O., Gaillardet J. and Benedetti M. F. (2013) Dynamic of particulate and dissolved organic carbon in small volcanic mountainous tropical watersheds. *Chem. Geol.* **351**, 229–244.

Loomis W. D. and Durst R. W. (1992) Chemistry and biology of boron. *Biofactors* **3**, 229–239.

Lorens R. B. (1981) Sr, Cd, Mn and Co distribution coefficients in calcite as a function of calcite precipitation rate. *Geochim. Cosmochim. Acta* **45**, 553–561.

Loretta Ann Williams (2), George A. L. A., Parks G. A. and Crerar D. A. (1985) Silica Diagenesis, I. Solubility Controls. *SEPM J. Sediment. Res.* **Vol. 55**, 301–311.

Loucaide S., Cappelle P. Van and Behrends T. (2008) Dissolution of biogenic silica from land to ocean: Role of salinity and pH. *Limnol. Oceanogr.* **53**, 1614–1621.

Louvat P., Jean C. and Gre A. (1997) Present denudation rates on the island of Réunion determined by river geochemistry: Basalt weathering and mass budget between chemical and mechanical erosions. *Geochim. Cosmochim. Acta*, **61**(17), 3645-3669.

Lucas, Y. (2001) The role of plants in controlling rates and products of weathering: Importance of biological pumping. *Annu. Rev. Earth Planet. Sci.* **29**, 135-163.

Lugolobi F., Kurtz A. C. and Derry L. A. (2010) Germanium-silicon fractionation in a tropical, granitic weathering environment. *Geochim. Cosmochim. Acta* **74**, 1294–1308.

Maher K., Steefel C. I., DePaolo D. J. and Viani B. E. (2006) The mineral dissolution rate conundrum: Insights from reactive transport modeling of U isotopes and pore fluid chemistry in marine sediments. *Geochim. Cosmochim. Acta* **70**, 337–363.

Maher K. (2010) The dependence of chemical weathering rates on fluid residence time.

Earth Planet. Sci. Lett. **294**, 101–110..

Maher K. (2011) The role of fluid residence time and topographic scales in determining chemical fluxes from landscapes. *Earth Planet. Sci. Lett.* **312**, 48–58.

Maher K., Steefel C. I., White A. F. and Stonestrom D. A. (2009) The role of reaction affinity and secondary minerals in regulating chemical weathering rates at the Santa Cruz Soil Chronosequence, California. *Geochim. Cosmochim. Acta* **73**, 2804–2831.

Maher K. and Chamberlain C. P. (2014) Hydrologic Regulation of Chemical Weathering and the Geologic Carbon Cycle. *Science (80-.).* **343**, 1502–1504.

Martin C. and Didon-Lescot J. F. (2003) Fonctionnement hydrochimique des bassins versants expérimentaux du Mont-Lozère (France) et conséquences d'une coupe forestière. *Zeitschrift fur Geomorphol.* **47**, 117–140.

Mavromatis V., Bundeleva I. A., Shirokova L. S., Millo C., Pokrovksy O. S., Bénézeth P., Ader M. and Oelkers E. H. (2015) The continuous re-equilibration of carbon isotope compositions of hydrous Mg carbonates in the presence of cyanobacteria. *Chem. Geol.* **404**, 41–51.

Mavromatis V., Harrison A. L., Eisenhauer A. and Dietzel M. (2017) Strontium isotope fractionation during strontianite (SrCO3) dissolution, precipitation and at equilibrium. *Geochim. Cosmochim. Acta* **218**, 201–214.

Mavromatis V., Pearce C. R., Shirokova L. S., Bundeleva I. A., Pokrovksy O. S., Benezeth

P. and Oelkers E. H. (2012) Magnesium isotope fractionation during hydrous magnesium carbonate precipitation with and without cyanobacteria. *Geochim. Cosmochim. Acta* **76**, 161–174.

Mavromatis V., van Zuilen K., Purgstaller B., Baldermann A., Nägler T. F. and Dietzel M. (2016) Barium isotope fractionation during witherite (BaCO3) dissolution, precipitation and at equilibrium. *Geochim. Cosmochim. Acta* **190**, 72–84.

McIntosh J. C., Schaumberg C., Perdrial J., Harpold A., Vázquez-Ortega A., Rasmussen C., Vinson D., Zapata-Rios X., Brooks P. D., Meixner T., Pelletier J., Derry L. and Chorover J. (2017) Geochemical evolution of the Critical Zone across variable time scales informs concentration-discharge relationships: Jemez River Basin Critical Zone Observatory. *Water Resour. Res.* **53**, 4169–4196.

Meek K., Derry L., Sparks J. and Cathles L. (2016) 87Sr/86Sr, Ca/Sr, and Ge/Si ratios as tracers of solute sources and biogeochemical cycling at a temperate forested shale catchment, central Pennsylvania, USA. *Chem. Geol.* **445**, 84–102.

Méheut M., Lazzeri M., Balan E. and Mauri F. (2007) Equilibrium isotopic fractionation in the kaolinite, quartz, water system: Prediction from first-principles density-functional theory. *Geochim. Cosmochim. Acta* **71**, 3170–3181.

Méheut M. and Schauble E. A. (2014) Silicon isotope fractionation in silicate minerals: Insights from first-principles models of phyllosilicates, albite and pyrope. *Geochim.*

Cosmochim. Acta **134**, 137–154.

Meunier J.D., Kirman S., Strasberg D., Keller C. (2010) The output and biocycling of Si in a tropical rain forest developed on young basalt flows (La Réunion Island). *Geoderma* **159**, 431-439.

Meybeck M. (1987) Global chemical weathering of surficial rocks estimated from river dissolved loads. *Am. J. Sci.* **287**, 401–428.

Millero F. J., Feistel R., Wright D. G. and McDougall T. J. (2008) The composition of Standard Seawater and the definition of the Reference-Composition Salinity Scale. *Deep. Res. Part I Oceanogr. Res. Pap.* **55**, 50–72.

Millot R., Gaillardet J., Dupré B. and Allègre C. J. (2002) The global control of silicate weathering rates and the coupling with physical erosion: New insights from rivers of the Canadian Shield. *Earth Planet. Sci. Lett.* **196**, 83–98.

Moon S., Chamberlain C. P. and Hilley G. E. (2014) New estimates of silicate weathering rates and their uncertainties in global rivers. *Geochim. Cosmochim. Acta* **134**, 257–274.

Morris C. A., Anderson M. L., Stroud R. M., Merzbacher C. I. and Rolison D. R. (1999) Silica sol as a nanoglue: Flexible synthesis of composite aerogels. *Science (80-.).* **284**, 622–624.

Morse J. W., Arvidson R. S. and Lüttge A. (2007) Calcium Carbonate Formation and Dissolution. *Chem. Rev.* **107**, 342–381.

Mucci A. and Morse J. W. (1983) The incorporation of Mg2+ and Sr2+ into calcite overgrowths: influences of growth rate and solution composition. *Geochim. Cosmochim. Acta* **47**, 217–233.

Murnane R. J. and Stallard R. F. (1990) Germanium and silicon in rivers of the Orinoco drainage basin. *Nature* **344**, 749. Available at: https://www.nature.com/articles/344749a0.

Murphy W. M., Oelkers E. H. and Lichtner P. C. (1989) Surface reaction versus diffusion control of mineral dissolution and growth rates in geochemical processes. *Chem. Geol.* **78**, 357–380.

Murphy S. F. and Stallard R. F. (2012) Water quality and landscape processes of four watersheds in eastern Puerto Rico: US Geological Survey Professional Paper.

Nancollas G. H. and Reddy M. M. (1971) The crystallization of calcium carbonate. II. Calcite growth mechanism. *J. Colloid Interface Sci.* **37**, 824–830.

Neal C., Reynolds B., Rowland P., Norris D., Kirchner J. W., Neal M., Sleep D., Lawlor A., Woods C., Thacker S., Guyatt H., Vincent C., Hockenhull K., Wickham H., Harman S. and Armstrong L. (2012) High-frequency water quality time series in precipitation and streamflow: From fragmentary signals to scientific challenge. *Sci. Total Environ.* **434**, 3–12.

Nielsen L. C., DePaolo D. J. and De Yoreo J. J. (2012) Self-consistent ion-by-ion growth

model for kinetic isotopic fractionation during calcite precipitation. *Geochim. Cosmochim. Acta* **86**, 166–181.

Nielsen L. C., De Yoreo J. J. and DePaolo D. J. (2013) General model for calcite growth kinetics in the presence of impurity ions. *Geochim. Cosmochim. Acta* **115**, 100–114.

Noack Y., Colin F., Nahon D., Delvigne J. and Michaux L. (1993) Secondary-mineral formation during natural weathering of pyroxene: review and thermodynamic approach. *Am. J. Sci.* **293**, 111–134.

Nusko R. and Heumann K. G. (1997) Cr(III)/Cr(VI) speciation in aerosol particles by extractive separation and thermal ionization isotope dilution mass spectrometry. *Fres*

Oelkers E. H., Berninger U.-N., Pérez-Fernàndez A., Chmeleff J. and Mavromatis V. (2018) The temporal evolution of magnesium isotope fractionation during hydromagnesite dissolution, precipitation, and at equilibrium. *Geochim. Cosmochim. Acta* **226**, 36–49.

Oelkers E. H., Pogge von Strandmann P. A. E. and Mavromatis V. (2018) The rapid resetting of the Ca isotopic signatures of calcite at ambient temperature during its congruent dissolution, precipitation, and at equilibrium. *Chem. Geol.* **512**, 1–10.

Oelze M., von Blanckenburg F., Bouchez J., Hoellen D. and Dietzel M. (2015) The effect of Al on Si isotope fractionation investigated by silica precipitation experiments.

Chem. Geol. **397**, 94–105.

Oelze M., von Blanckenburg F., Hoellen D., Dietzel M. and Bouchez J. (2014) Si stable isotope fractionation during adsorption and the competition between kinetic and equilibrium isotope fractionation: Implications for weathering systems. *Chem. Geol.* **380**, 161–171.

Oliva P., Dupré B., Martin F. and Viers J. (2004) The role of trace minerals in chemical weathering in a high-elevation granitic watershed (Estibère, France): chemical and mineralogical evidence. *Geochim. Cosmochim. Acta* **68**, 2223–2243.

Oliver A. A., Tank S. E., Giesbrecht I., Korver M. C., Floyd W. C., Sanborn P., Bulmer C. and Lertzman K. P. (2017) A global hotspot for dissolved organic carbon in hypermaritime watersheds of coastal British Columbia. *Biogeosciences* **14**, 3743–3762.

Opfergelt S., Cardinal D., André L., Delvigne C., Bremond L. and Delvaux B. (2010) Variations of δ30Si and Ge/Si with weathering and biogenic input in tropical basaltic ash soils under monoculture. *Geochim. Cosmochim. Acta* **74**, 225–240.

Opfergelt S., Cardinal D., Henriet C., André L. and Delvaux B. (2006) Silicon isotope fractionation between plant parts in banana: In situ vs. in vitro. *J. Geochemical Explor.* **88**, 224–227.

Opfergelt S., Cardinal D., André L., Delvigne C., Bremond L., Delvaux B.(2010) Variations in δ^{30}Si and Ge/Si with weathering and biogenic input in tropical basaltic ash soils

under monoculture. *Geochim. Cosmochim. Acta,* **74**(1), 225-740.

Opfergelt S. and Delmelle P. (2012) Silicon isotopes and continental weathering processes: Assessing controls on Si transfer to the ocean. *Comptes Rendus Geosci.* **344**, 723–738.

Orem C. A. and Pelletier J. D. (2016) The predominance of post-wildfire erosion in the long-term denudation of the Valles Caldera, New Mexico. *J. Geophys. Res. F Earth Surf.* **121**, 843–864.

Papadimitriou S., Kennedy H., Kennedy P. and Thomas D. N. (2014) Kinetics of ikaite precipitation and dissolution in seawater-derived brines at sub-zero temperatures to 265K. *Geochim. Cosmochim. Acta* **140**, 199–211.

Parkman R. H., Charnock J. M., Livens F. R. and Vaughan D. J. (1998) A study of the interaction of strontium ions in aqueous solution with the surfaces of calcite and kaolinite. *Geochim. Cosmochim. Acta* **62**, 1481–1492.

Parks G. A. (1984) *SURFACE AND INTERFACIAL FREE ENERGIES OF QUARTZ.*,

Pearce C. R., Saldi G. D., Schott J. and Oelkers E. H. (2012) Isotopic fractionation during congruent dissolution, precipitation and at equilibrium: Evidence from Mg isotopes. *Geochim. Cosmochim. Acta* **92**, 170–183.

Peters C. A. (2009) Accessibilities of reactive minerals in consolidated sedimentary rock: An imaging study of three sandstones. *Chem. Geol.* **265**, 198–208.

Pett-Ridge Julie C., Derry L. A. and Barrows J. K. (2009) Ca/Sr and 87Sr/86Sr ratios as tracers of Ca and Sr cycling in the Rio Icacos watershed, Luquillo Mountains, Puerto Rico. *Chem. Geol.* **267**, 32–45.

Pett-Ridge Julie C, Derry L. A. and Kurtz A. C. (2009) Sr isotopes as a tracer of weathering processes and dust inputs in a tropical granitoid watershed, Luquillo Mountains, Puerto Rico. *Geochim. Cosmochim. Acta* **73**, 25–43.

Pokrovski G. S. and Schott J. (1998) Experimental study of the complexation of silicon and germanium with aqueous organic species: implications for germanium and silicon transport and Ge/Si ratio in natural waters. *Geochim. Cosmochim. Acta* **62**, 3413–3428.

Pogge von Strandmann P. A. E., Burton K. W., James R. H., van Calsteren P., Gislason S. R. and Sigfússon B. (2008) The influence of weathering processes on riverine magnesium isotopes in a basaltic terrain. *Earth Planet. Sci. Lett.* **276**, 187–197.

Pogge von Strandmann P. A. E., Opfergelt S., Lai Y.-J., Sigfússon B., Gislason S. R. and Burton K. W. (2012) Lithium, magnesium and silicon isotope behaviour accompanying weathering in a basaltic soil and pore water profile in Iceland. *Earth Planet. Sci. Lett.* **339–340**, 11–23.

Poitrasson F. (2017) Silicon Isotope Geochemistry. *Rev. Mineral. Geochemistry* **82**, 289–344. 5.

Pokrovsky O. S., Reynolds B. C., Prokushkin A. S., Schott J. and Viers J. (2013) Silicon

isotope variations in Central Siberian rivers during basalt weathering in permafrost-dominated larch forests. *Chem. Geol.* **355**, 103–116.

Pokrovski G. S. and Schott J. (1998) Experimental study of the complexation of silicon and germanium with aqueous organic species: implications for germanium and silicon transport and Ge/Si ratio in natural waters. *Geochim. Cosmochim. Acta* **62**, 3413–3428.

Porder S., Johnson A. H., Xing H. X., Brocard G., Goldsmith S. and Pett-Ridge J. (2015) Linking geomorphology, weathering and cation availability in the Luquillo Mountains of Puerto Rico. *Geoderma* **249–250**, 100–110. Available at: http://dx.doi.org/10.1016/j.geoderma.2015.03.002.

Pringle E. A., Moynier F., Savage P. S., Badro J. and Barrat J.-A. (2014) Silicon isotopes in angrites and volatile loss in planetesimals. *Proc. Natl. Acad. Sci.* **111**, 17029–17032.

Prospero J.M., Glaccum, R.A., Nees R.T. (1981) Atmospheric transport of soil dust from Africa to South America. *Nature*, **289**, 570-572.

Prospero J.M. (1996) Saharan dust transport over the North Atlantic Ocean and Mediterranean: an overview. In: Guerzoni, S., Chester, R. (Eds), The impact of desert dust across the Mediterranean. Kluwer Academic Publishing, Dordrecht, 133-151.

Prospero J.M. (1996) The atmospheric transport of particles to the Ocean. In: Ittekot, V., Schäfer, P., Honjo, S., S., Depetris, P.J. (Eds) Particle flux in the Ocean, SCOPE Report

57. John Wiley & Sons, Chichester, 19-52.

Rad S., Louvat P., Gorge C., Gaillardet J. and Allégre C. J. (2006) River dissolved and solid loads in the Lesser Antilles: New insight into basalt weathering processes. *J. Geochemical Explor.* **88**, 308–312.

Rad S., Rivé K., Vittecoq B., Cerdan O. and Allègre C. J. (2013) Chemical weathering and erosion rates in the lesser antilles: An overview in guadeloupe, martinique and dominica. *J. South Am. Earth Sci.* **45**, 331–344.

Rayleigh L. (1902) On the distillation of binary mixtures. *Phil. Mag.* **4**, 521–537.

Reddy M. M. and Nancollas G. H. (1976) The crystallization of calcium carbonate. *J. Cryst. Growth* **35**, 33–38.

Rempe D. and Dietrich W. (2014) A bottom-up control on fresh-bedrock topography under landscapes. *Proc. Natl. Acad. Sci.* **111**, 6576–6581.

Reynolds B. (2012) Silicon Isotopes as Tracers of Terrestrial Processes. In *Handbook of Environmental Isotope Geochemistry* Advances in Isotope Geochemistry. Springer, Berlin, Heidelberg. pp. 87–104.

Riebe C. S., Kirchner J. W. and Finkel R. C. (2004) Erosional and climatic effects on long-term chemical weathering rates in granitic landscapes spanning diverse climate regimes. *Earth Planet. Sci. Lett.* **224**, 547–562.

Riebe C. S., Kirchner J. W. and Finkel R. C. (2003) Long-term rates of chemical

weathering and physical erosion from cosmogenic nuclides and geochemical mass balance. *Geochim. Cosmochim. Acta* **67**, 4411–4427.

Riebe C. S., Hahm W. J. and Brantley S. L. (2017) Controls on deep critical zone architecture: a historical review and four testable hypotheses. *Earth Surf. Process. Landforms* **42**, 128–156.

Riebe C. S., Kirchner J. W. and Finkel R. C. (2003) Long-term rates of chemical weathering and physical erosion from cosmogenic nuclides and geochemical mass balance. *Geochim. Cosmochim. Acta* **67**, 4411–4427.

Riotte J., Meunier J.-D., Zambardi T., Audry S., Barboni D., Anupama K., Prasad S., Chmeleff J., Poitrasson F., Sekhar M. and Braun J.-J. (2018) Processes controlling silicon isotopic fractionation in a forested tropical watershed: Mule Hole Criti Zone Observatory (Southern India). *Geochim. Cosmochim. Acta* **228**, 301–319

Riley J. P. and Tongudai M. (1967) The major cation/chlorinity ratios in sea water. *Chem. Geol.* **2**, 263–269.

Rimstidt J. D. and Barnes H. L. (1980) The kinetics of silica-water reactions. *Geochim. Cosmochim. Acta* **44**, 1683–1699.

Roerdink D. L., van den Boorn S. H. J. M., Geilert S., Vroon P. Z. and van Bergen M. J. (2015) Experimental constraints on kinetic and equilibrium silicon isotope fractionation during the formation of non-biogenic chert deposits. *Chem. Geol.* **402**,

40–51. 5.

Safeeq M. and Hunsaker C. T. (2016) Characterizing Runoff and Water Yield for Headwater Catchments in the Southern Sierra Nevada. *J. Am. Water Resour. Assoc.* **52**, 1327–1346.

Savage P.S., Bastian Georg R., Williams H.M., Turner S., Halliday A.N., Chapell B.W.(2012) The silicon isotope composition of granites. *Geochim. Cosmochim. Acta* **92**, 184-202.

Savage P.S., Bastian Georg R., Williams H.M., Turner S., Halliday A.N., The silicon isotope composition of the upper continental crust. *Geochim. Cosmochim. Acta* **109**, 384-399.

Salve R., Rempe D. and Dietrich W. (2012) Rain, rock moisture dynamics, and the rapid response of perched groundwater in weathered, fractured argillite underlying a steep hillslope. *Water Resour. Res.* **48**, 1–25.

Sankhla, N., and Sankhla, D. (1967) Effect of germanium on growth of higher plants, *Naturwissen* **54**(23), 621.

Schmitt A.-D., Vigier N., Lemarchand D., Millot R., Stille P. and Chabaux F. (2012) Processes controlling the stable isotope compositions of Li, B, Mg and Ca in plants, soils and waters: A review. *Comptes Rendus Geosci.* **344**, 704–722.

Schmitt A. D., Stille P. and Vennemann T. (2003) Variations of the 44Ca/40Ca ratio in

seawater during the past 24 million years: Evidence from δ44Ca and δ18O values of Miocene phosphates. *Geochim. Cosmochim. Acta* **67**, 2607–2614.

Scholl M. A. and Murphy S. F. (2014) Precipitation isotopes link regional climate pattern to water supply in a tropical mountain forest, eastern Puerto Rico. *Water Resour. Res.* **50**, 4305–4322.

Shtenberg, M.V., Bychinskii, V.A., Koroleva, O.N., Korobatova, N.M., Tupitsyn, A.A., Fomichev, S.V., Krenev, V.A., 2017. Calculation of the formation enthalpies, standard entropies, and standard heat capacities of alkali and alkaline-earth germanates. *Russian Journal of Inorganic Chemistry* **62**, 1464–1468.

Scribner A. M., Kurtz A. C. and Chadwick O. A. (2006) Germanium sequestration by soil: Targeting the roles of secondary clays and Fe-oxyhydroxides. *Earth Planet. Sci. Lett.* **243**, 760–770.

Skulan J. L., Beard B. L. and Johnson C. M. (2002) Kinetic and equilibrium Fe isotope fractionation between aqueous Fe(III) and hematite. *Geochim. Cosmochim. Acta* **66**, 2995–3015.

Stack A. G. and Kent P. R. C. (2015) Geochemical reaction mechanism discovery from molecular simulation. *Environ. Chem.* **12**, 20–32.

Stallard R. F. and Edmond J. M. (1983) Geochemistry of the Amazon 2. The influence of geology and weathering environment on the dissolved load. *J. Geophys. Res.* **88**, 9671–

9688.

Steefel C. I., Druhan J. L. and Maher K. (2014) Modeling coupled chemical and isotopic equilibration rates. *Procedia Earth Planet. Sci.* **10**, 208–217.

Steefel C. I., Yabusaki S. B. and Mayer K. U. (2015) Reactive transport benchmarks for subsurface environmental simulation. *Comput. Geosci.* **19**, 439–443.

Stefansson A. and Gislason S. R. (2001) Chemical weathering of basalts, Southwest Iceland: Effect of rock crystallinity and secondary minerals on chemical fluxes to the ocean. *Am. J. Sci.* **301**, 513–556.

Steinhoefel G., Breuer J., von Blanckenburg F., Horn I. and Sommer M. (2017) The dynamics of Si cycling during weathering in two small catchments in the Black Forest (Germany) traced by Si isotopes. *Chem. Geol.* **466**, 389–402.

Stonestrom D. A., White A. F. and C. Akstin K. (1998) Determining rates of chemical weathering in soils—solute transport versus profile evolution. *J. Hydrol.* **209**, 331–345.

Street-Perrott F. A. and Barker P. A. (2008) Biogenic silica: A neglected component of the coupled global continental biogeochemical cycles of carbon and silicon. *Earth Surf. Process. Landforms* **33**, 1436–1457.

Teng H. H., Dove P. M., Orme C. A. and Yoreo J. J. De (1998) Thermodynamics of Calcite Growth: Baseline for Understanding Biomineral Formation. *Science (80-.).* **282**, 724–

727.

Teng H. H., Dove P. M. and De Yoreo J. J. (2000) Kinetics of calcite growth: surface processes and relationships to macroscopic rate laws. *Geochim. Cosmochim. Acta* **64**, 2255–2266.

Tesoriero A. J. and Pankow J. F. (1996) Solid solution partitioning of Sr2+, Ba2+, and Cd2+ to calcite. *Geochim. Cosmochim. Acta* **60**, 1053–1063.

Tang J., Köhler S. J. and Dietzel M. (2008) Sr2+/Ca2+ and 44Ca/40Ca fractionation during inorganic calcite formation: I. Sr incorporation. *Geochim. Cosmochim. Acta* **72**, 3718–3732.

Tang J., Dietzel M., Böhm F., Köhler S. J. and Eisenhauer A. (2008) Sr2+/Ca2+ and 44Ca/40Ca fractionation during inorganic calcite formation: II. Ca isotopes. *Geochim. Cosmochim. Acta* **72**, 3733–3745.

Tatzel M., von Blanckenburg F., Oelze M., Schuessler J. A. and Bohrmann G. (2015) The silicon isotope record of early silica diagenesis. *Earth Planet. Sci. Lett.* **428**, 293–303.

Thien B. M. J., Kulik D. A. and Curti E. (2014) A unified approach to model uptake kinetics of trace elements in complex aqueous – solid solution systems. *Appl. Geochemistry* **41**, 135–150.

Thompson S. D., Nelson T. A., Giesbrecht I., Frazer G. and Saunders S. C. (2016) Data-driven regionalization of forested and non-forested ecosystems in coastal British

Columbia with LiDAR and RapidEye imagery. *Appl. Geogr.* **69**, 35–50.

Tipper E. T., Galy A. and Bickle M. J. (2008) Calcium and magnesium isotope systematics in rivers draining the Himalaya-Tibetan-Plateau region: Lithological or fractionation control? *Geochim. Cosmochim. Acta* **72**, 1057–1075.

Tipper E. T., Galy A. and Bickle M. J. (2006) Riverine evidence for a fractionated reservoir of Ca and Mg on the continents: Implications for the oceanic Ca cycle. *Earth Planet. Sci. Lett.* **247**, 267–279.

Tipper E. T., Lemarchand E., Hindshaw R. S., Reynolds B. C. and Bourdon B. (2012) Seasonal sensitivity of weathering processes: Hints from magnesium isotopes in a glacial stream. *Chem. Geol.* **312–313**, 80–92.

Tipper E. T., Schmitt A. D. and Gussone N. (2016) *Global ca cycles: Coupling of continental and oceanic processes.*,

Tréguer P. J. and De La Rocha C. L. (2013) The World Ocean Silica Cycle. *Ann. Rev. Mar. Sci.* **5**, 477–501.

Tobler D. J., Shaw S. and Benning L. G. (2009) Quantification of initial steps of nucleation and growth of silica nanoparticles: An in-situ SAXS and DLS study. *Geochim. Cosmochim. Acta* **73**, 5377–5393.

Urr, Meybeck M., Hartmann J., Laruelle G. G. and Roubeix V. (2011) Global spatial distribution of natural riverine silica inputs to the coastal zone. *Biogeosciences* **8**, 597–

620.

Vázquez-Ortega A., Perdrial J., Harpold A., Zapata-Ríos X., Rasmussen C., McIntosh J., Schaap M., Pelletier J. D., Brooks P. D., Amistadi M. K. and Chorover J. (2015) Rare earth elements as reactive tracers of biogeochemical weathering in forested rhyolitic terrain. *Chem. Geol.* **391**, 19–32.

Velbel M. A. (1987) Influence of Surface Area, Surface Characteristics, and Solution Composition on Feldspar Weathering Rates. In *Geochemical Processes at Mineral Surfaces* ACS Symposium Series. American Chemical Society. pp. 615–634.

Velbel M. A. and Price J. R. (2007) Solute geochemical mass-balances and mineral weathering rates in small watersheds: Methodology, recent advances, and future directions. *Appl. Geochemistry* **22**, 1682–1700.

Walter L. M. and Morse J. W. (1985) The dissolution kinetics of shallow marine carbonates in seawater: A laboratory study. *Geochim. Cosmochim. Acta* **49**, 1503–1513.

Wang T., Campbelle, E.M., O'Neil G.A., Aitken S.N. (2012) Projecting future distributions of ecosystem climate niches: Uncertainties and management applications. *Forest Ecology and Management*, **279,** 128-140.

Wasylenki L. E., Dove P. M., Wilson D. S. and De Yoreo J. J. (2005) Nanoscale effects of strontium on calcite growth: An in situ AFM study in the absence of vital effects. *Geochim. Cosmochim. Acta* **69**, 3017–3027.

Watson E. B. (2004) A conceptual model for near-surface kinetic controls on the trace-element and stable isotope composition of abiogenic calcite crystals. *Geochim. Cosmochim. Acta* **68**, 1473–1488.

White A. F. and Blum A. E. (1995) Effects of climate on chemical_ weathering in watersheds. *Geochim. Cosmochim. Acta* **59**, 1729–1747.

White A. F., Blum A. E., Schulz M. S., Vivit D. V, Stonestrom D. A., Larsen M., Murphy S. F. and Eberl D. (1998) Chemical Weathering in a Tropical Watershed, Luquillo Mountains, Puerto Rico: I. Long-Term Versus Short-Term Weathering Fluxes. *Geochim. Cosmochim. Acta* **62**, 209–226.

White A. F., Bullen T. D., Schulz M. S., Blum A. E., Huntington T. G. and Peters N. E. (2001) Differential rates of feldspar weathering in granitic regoliths. *Geochim. Cosmochim. Acta* **65**, 847–869.

Wiche O., Székely B., Moschner C. and Heilmeier H. (2018) Germanium in the soil-plant system—a review. *Environ. Sci. Pollut. Res.* **25**, 31938–31956.

Wiederhold J. G. (2015) Metal Stable Isotope Signatures as Tracers in Environmental Geochemistry. *Environ. Sci. Technol.* **49**, 2606–2624.

Winnick M.., Wenming D. and Maher K. (2017) Snowmelt controls on concentration-discharge relationships and the balance of oxidative and acid-base weathering fluxes in an alpine catchment, East River, Colorado. *Water Resour. Res.* **53**,

Wiechers H. N. S., Sturrock P. and Marais G. v. R. (1975) Calcium carbonate crystallization kinetics. *Water Res.* **9**, 835–845.

Wiederhold J. G., Kraemer S. M., Teutsch N., Borer P. M., Halliday A. N. and Kretzschmar R. (2006) Iron Isotope Fractionation during Proton-Promoted, Ligand-Controlled, and Reductive Dissolution of Goethite. *Environ. Sci. Technol.* **40**, 3787–3793.

Wolthers M., Nehrke G., Gustafsson J. P. and Van C. (2012) Calcite growth kinetics: Modeling the effect of solution stoichiometry. *Geochim. Cosmochim. Acta* **77**, 121–134.

Yang J.-L. and Zhang G.-L. (2019) Si cycling and isotope fractionation: Implications on weathering and soil formation processes in a typical subtropical area. *Geoderma* **337**, 479–490.

Zahibo, N., Pelinovsky, E., Talipova, T., Rabinovich, A., Kurkin, A., Nikolkina, I., 2007. Statis-tical analysis of cyclone hazard for Guadeloupe, Lesser Antilles. Atmos. Res.84, 13–29.

Zapata-Rios X., McIntosh J., Rademacher L., Troch P. A., Brooks P. D., Rasmussen C. and Chorover J. (2015) Climatic and landscape controls on water transit times and silicate mineral weathering in the critical zone. *Water Resour. Res.* **51**, 6036–6051.

Zhang Y. and Dawe R. (1998) The kinetics of calcite precipitation from a high salinity water. *Appl. Geochemistry* **13**, 177–184.

Zhu, C, Blum, A E, Veblen, D R, Wanty, R B, and Seal, R R (2004) Feldspar dissolution rates and clay precipitation in the Navajo aquifer at Black Mesa, Arizona, USA: *A.A. Balkema*, **1**, 441-442.

Zhu C. and Lu P. (2009) Alkali feldspar dissolution and secondary mineral precipitation in batch systems: 3. Saturation states of product minerals and reaction paths. *Geochim. Cosmochim. Acta* **73**, 3171–3200.

Ziegler K., Chadwick O. A., Brzezinski M. A. and Kelly E. F. (2005a) Natural variations of δ30Si ratios during progressive basalt weathering, Hawaiian Islands. *Geochim. Cosmochim. Acta* **69**, 4597–4610.

Ziegler K., Chadwick O. A., White A. F. and Brzezinski M. A. (2005b) δ30Si systematics in a granitic saprolite, Puerto Rico. *Geology* **33**, 817–820.

APPENDIX A

MASS-DEPENDENT FRACTIONATION

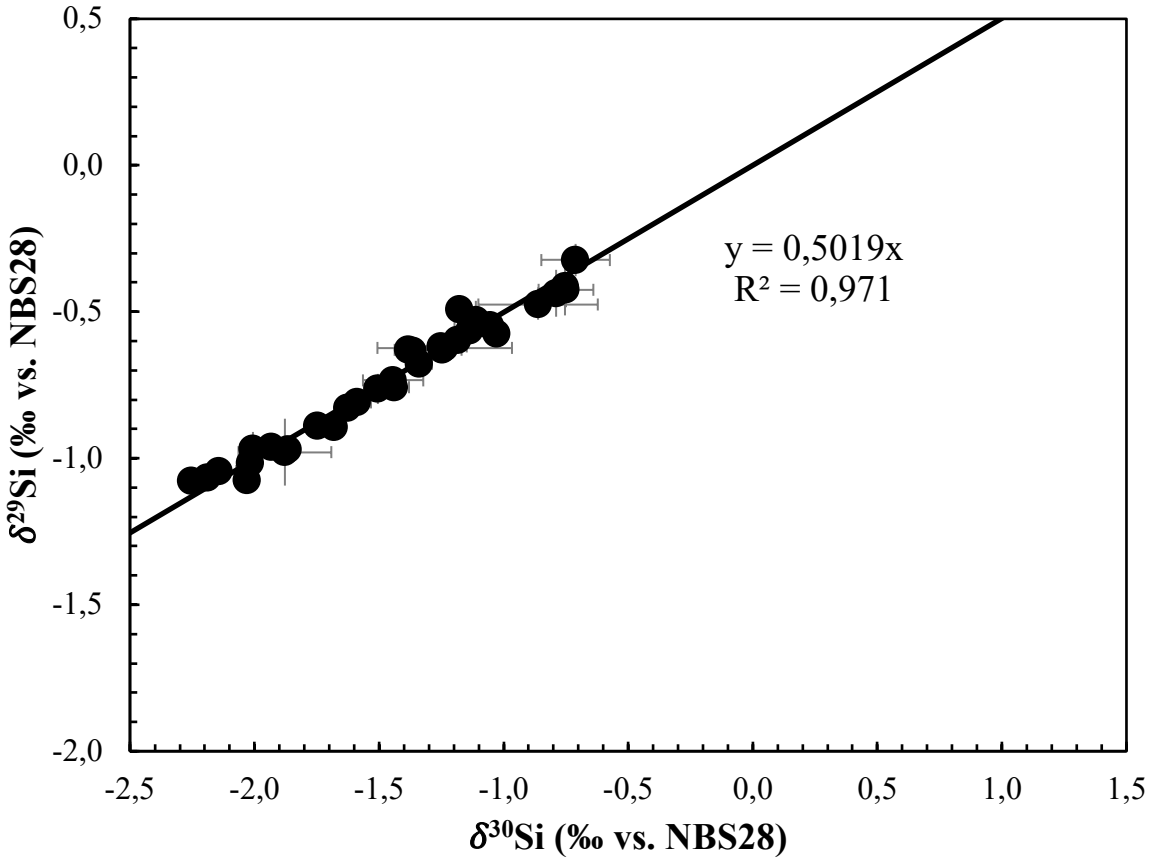

Figure A.1 Silicon three-isotope plot for mass-dependent fractionation
Three-isotope plot for all experimental samples analyzed in our amorphous silica precipitation study. Si isotope ratios are shown to follow mass-dependent equilibrium fractionation line ($\delta^{29}Si = \delta^{30}Si \times 0.5019x$, $R^2 = 0.971$).

APPENDIX B

INFLUENCE OF SURFACE AREA ON SOLUBILITY

The Freundlich-Ostwald Equation provides an relationship between surface area and solubility and can be described as follows (eq. B.1):

$$\log S' = \log S + \frac{\gamma}{2.3RTM}\left(\frac{2}{3}A\right) \qquad (B.1)$$

Where γ = surface free energy = 360 [mJ m^{-2}] (Parks, 1984 for qtz-liquid)

S = solubility of amorphous silica at 20°C = 1.75mM (Gunnarsson &Anórsson, 2000)

R = gas constant [J $mol^{-1}K^{-1}$]

T = 293 K (20°C)

M = molecular weight of SiO_2 [60.083 g mol^{-1}]

A = specific surface area [m^2 g^{-1}]

Table B.1 Calculated surface area corrected amorphous silica solubility concentrations (S′, **eq. B.1**) at 20°C for all three amorphous silica batch experiments spanning a range of surface areas.

No	SiO2(aq)	SSA	S′	Ω
	mmoles/L	m^2 g^{-1}	mmoles/L	log Q/S′
High surface area batch				
1	5.3±0.7	50±15	1.7494	0.48±0.06
2	5.1±0.5	50±7	1.7494	0.47±0.04
3	4.6±0.6	49±3	1.7494	0.42±0.06
4	4.3±0.7	48±2	1.7494	0.39±0.06
5	3.4±0.9	46±1	1.7494	0.29±0.08
6	3.3±0.1	45±1	1.7494	0.28±0.01
7	2.9±0.6	44±1	1.7494	0.22±0.05
8	2.3±0.2	43.1±0.8	1.7494	0.12±0.01
9	2.2±0.5	42.1±0.7	1.7494	0.10±0.02
10	2.2±0.4	41.1±0.7	1.7494	0.10±0.02
11	2.1±0.4	40.0 ±0.6	1.7494	0.07±0.02
Medium surface area batch				
1	5.3±0.4	0.127*	1.7493	0.48±0.04

(Table B.1 continued)

2	4.6±0.4	0.125±0.003	1.7493	0.42±0.04
3	4.1±0.4	0.123±0.002	1.7493	0.38±0.04
4	3.7±0.8	0.122±0.001	1.7493	0.33±0.08
5	3.6±0.5	0.120±0.001	1.7493	0.32±0.04
6	3.2±0.4	0.118±0.001	1.7493	0.27±0.03
7	3.1±0.7	0.117±0.001	1.7493	0.25±0.06
8	2.9±0.6	0.115±0.001	1.7493	0.23±0.05
9	3.0±0.5	0.114±0.001	1.7493	0.23±0.04
Low surface area batch				
1	5.3±0.5	0.072*	1.7493	0.48±0.05
2	4.7±0.5	0.071±0.002	1.7493	0.43±0.04
3	4.4±0.4	0.070±0.001	1.7493	0.41±0.04
4	4.2±0.6	0.070±0.001	1.7493	0.38±0.06
5	4.1±0.3	0.069±0.001	1.7493	0.37±0.03
6	3.9±0.3	0.068±0.001	1.7493	0.35±0.03
7	3.8±0.4	0.067±0.001	1.7493	0.34±0.04
8	3.6±0.5	0.066±0.001	1.7493	0.32±0.05
9	3.6±0.7	0.066±0.001	1.7493	0.32±0.06

APPENDIX C

MINERAL-FLUID INTERACTION DEPTH APPROXIMATION

Mavromatis et al. (2016, 2017) described a method for calculating the depth into the mineral that the fluid can isotopically interact with. This method is based on a simple isotopic mass balance where mass exchange between fluid and instantaneously precipitated solid phases can be approximated using Rayleigh distillation. We provide the high surface area experiment calculations as an example (**Table C.1**).

Knowledge of the solid phase crystal structure is required to determine fluid-mineral interaction depth. We approximate the crystallography of amorphous silica with that of α-quartz, which can be described as a Trigonal crystal system with a rhombic unit cell defined chemically by the formula Si_3O_6 (i.e. 3 x SiO_2). As shown in **Figure C.1**, the unit cell has a volume of ~ 113Å with an edge dimension of 5.405Å, denoted as **c** and considered in the direction perpendicular to the amorphous silica surface (Ackermann and Sorrell, 1974; Wright and Lehmann, 1981).

Figure C.1 Unit cell of quartz (modified from Nejad et al., 2017)

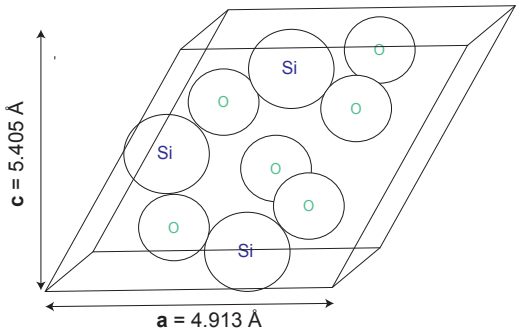

$V_{unit\ cell} = a^2c\ sin60° = 113Å$

Using these unit cell properties, the total amount of amorphous silica formed during the precipitation experiment (0.522g), and the starting reactive surface area (50 m^2/g), the amount of Si in the outermost surface layer (Si_{surf}) of the amorphous silica can be calculated:

$$A_{am.silica} = mSiO_{2,am.silica} \times rSA \qquad (C.1)$$

$$N_{\text{unit cell}} = \frac{A_{\text{am.silica}}}{A_{\text{unit cell}}} \quad (C.2)$$

$$Si_{\text{surf}} = N_{\text{unit cell}} \times \frac{3 \text{ atoms Si}}{1 \text{ unit cell}} \times \frac{1}{N_A} \times 1000 \quad (C.3)$$

where $A_{\text{am.silica}}$ (m^2) corresponds to the total area of the amorphous silica present in the reactor, $A_{\text{unit cell}}$ (2.66×10^{-19} m^2) is the area of the unit cell , $N_{\text{unit cell}}$ is the number of unit cells composing the outermost surface layer, and N_A is Avogadro's number (6.022×10^{23} atoms/mol). Following equations (C.1 – C.3), the amount of Si present within the outermost layer of the amorphous silica present in the batch reactor was determined to be 0.49 mmoles Si. This value provides an important constraint on the maximum amount of Si that can be exchanged with the fluid phase per surface layer. Thus, mass balance between fluid and solid phase δ^{30}Si values can be relied upon to determine how much of the Si present in the fluid phase at the end of the experiment derived from exchange with the amorphous silica surface.

Assuming that the freshly precipitated solid phase has a distinct isotopic composition from that of the bulk, a Rayleigh-distillation model can be used to calculate the isotopic ratio of the instantaneously precipitated amorphous silica at equilibrium using a kinetic fractionation factor, α_{kin}, of 0.9967 (**Fig. C.2**). High surface area experimental values are shown to deviate quickly from Rayleigh model predictions due to isotopic exchange with the newly formed amorphous silica surface. Fluid phase δ^{30}Si ratios reached values around -2.22 ± 0.05 ‰ (n=2) at isotopic equilibrium when roughly 83% of the starting amount of Si in solution has been precipitated as amorphous silica. This fluid phase δ^{30}Si value is significantly lighter than Rayleigh model predictions. A general trend toward lighter fluid isotopic values in the approach to equilibrium was also observed in the Mavromatis et al. (2017) study. This observed behavior in the fluid isotopic ratios was argued to derive from isotopic exchange at depth with the newly precipitated surface layers formed early in the kinetic event where isotopic signatures are preferentially lighter. If this is assumed to be the case, then the amount of Si in these freshly formed

surface layers that can be exchanged with the fluid has to be estimated in order to determine the mineral-fluid interaction depth.

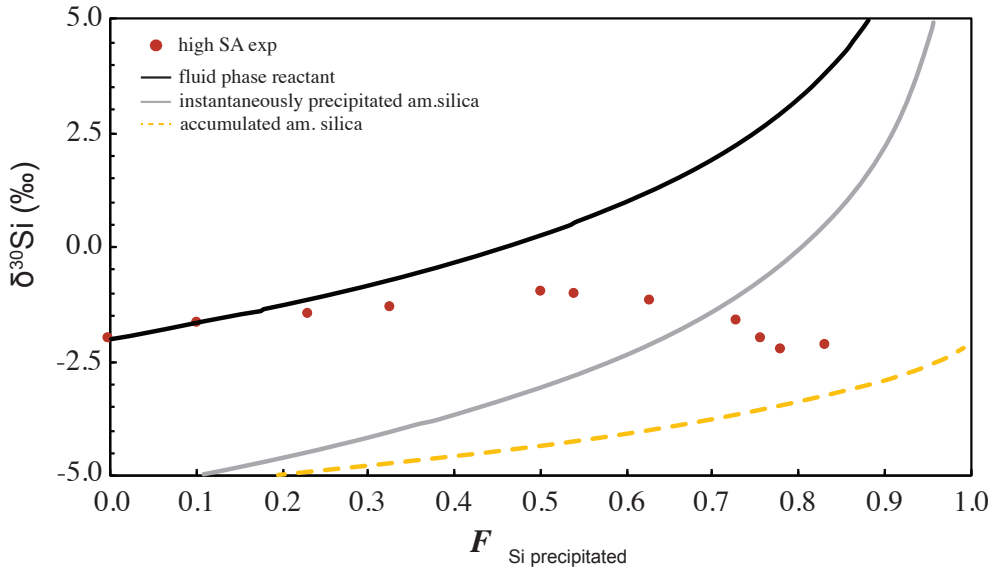

Figure C.2 Rayleigh distillation curves of $\delta^{30}Si$ isotopic evolution as a function of the fraction of aqueous Si precipitated as amorphous silica.

With our calculated equilibrium fractionation factor (α_{eq} = 1.0002, $\Delta^{30}Si_{am.silica\text{-}fluid}$ = 0.20‰) and $\delta^{30}Si$ fluid at isotopic equilibrium (-2.22 ± 0.05‰), we first determine the $\delta^{30}Si$ composition of the freshly precipitated amorphous silica surface at isotopic equilibrium (**eq. C.4**). The $\delta^{30}Si_{ppt,EQ}$ value obtained through this calculation was -2.02‰.

$$\delta^{30}Si_{ppt,EQ} = \Delta^{30}Si_{am.silica\text{-}fluid} + \delta^{30}Si_{aq,EQ} \quad (C.4)$$

Using the Rayleigh model for the instantaneously precipitated amorphous silica (**Fig. C.2**), the amount of Si precipitated as amorphous silica by the time equilibrium was reached can be calculated. A $\delta^{30}Si$ solid phase value of-2.02‰ on the instantaneously precipitated Rayleigh line corresponds to a $\mathbf{F_{Si\text{-}precipitated}}$ = 0.64, which corresponds to 0.096 mmoles of Si that was precipitated as amorphous silica. Under the assumption that all of the Si in the freshly precipitated amorphous silica surface exchanged with the fluid phase

at equilibrium, the depth into the mineral that the fluid is in direct contact with ($d_{fluid\text{-}am.silica}$) can be constrained (**eq. C.5**):

$$d_{\text{fluid-am.silica}} = \frac{Si_{ppt}}{Si_{surface}} \times l_{\text{unit cell}} \qquad (C.5)$$

where Si_{ppt} (0.096 mmoles) represents the amount of Si precipitated as amorphous silica, $Si_{surface}$ (0.49 mmoles) is the amount of Si within a single amorphous silica layer, and $l_{unit\ cell}$ corresponds to the edge length of the unit cell perpendicular to the mineral surface (5.405Å = 0.5405nm). Thus, the Mavromatis method for our high surface area experiments estimates a fluid-mineral interaction depth of **0.110nm** assuming that (1) the crystal geometry can be correctly defined by a rhombic unit cell, (2) the reaction reaches isotopic equilibrium, and (3) a Rayleigh distillation approach for calculating the isotopic composition of a growing mineral surface is appropriate.

Table C.1 High surface area batch experimental data used for the Mavromatis et al. (2016, 2017) mineral-fluid interaction depth calculation

No.	**time**	**Volume**	**S**	**SiO_2^{*} (aq)**	**$SiO_{2(inst.precip)}$**	**$\delta^{30}Si_{fluid}$**	
	days	L	m^2	mmoles	mmoles	‰	±‰ (2σ)
1	0	0.050	25	0.26	-	-2.03	0.04
2	0.02	0.049	24	0.25	0.02	-1.68	0.07
3	0.11	0.048	24	0.22	0.03	-1.51	0.05
4	0.19	0.047	23	0.20	0.02	-1.34	0.05
5	0.93	0.046	23	0.16	0.04	-1.03	0.04
6	1.00	0.045	22	0.15	0.01	-1.05	0.04
7	2.00	0.044	22	0.13	0.02	-1.19	0.04
8	8.87	0.043	21	0.10	0.03	-1.63	0.05
9	13.88	0.042	21	0.09	0.01	-2.01	0.05
10	18.95	0.041	20	0.09	0.00	-2.25	0.04
11	31.08	0.040	20	0.08	0.01	-2.19	0.05

* corrected for the mass $SiO_{2(aq)}$ removed due to sampling

REFERENCES

Ackermann R. J. and Sorrell C. A. (1974) Thermal Expansion and the High-Low Transformation in Quartz. I. High-Temperature X-ray Studies*. *J. Appl. Crystallogr.* **7**, 461–467.].

Mavromatis V., Harrison A. L., Eisenhauer A. and Dietzel M. (2017) Strontium isotope fractionation during strontianite (SrCO3) dissolution, precipitation and at equilibrium. *Geochim. Cosmochim. Acta* **218**, 201–214. Available at: http://www.sciencedirect.com/science/article/pii/S0016703717305410.

Nejad M. A., Mï¿½cksch C. and Urbassek H. M. (2017) Insulin adsorption on crystalline SiO2: Comparison between polar and nonpolar surfaces using accelerated molecular-dynamics simulations. *Chem. Phys. Lett.* **670**, 77–83..

Wright A. F. and Lehmann M. S. (1981) The structure of quartz at 25 and 590°C determined by neutron diffraction. *J. Solid State Chem.* **36**, 371–380..

APPENDIX D

SOLVING FOR THE INSTANTANEOUS PARTITION COEFFICIENT (K_D^{INST}) FROM THE RAYLEIGH-DISTILLATION DERIVATION (TANG ET AL., 2008)

The Rayleigh-distillation approach for calculating the instantaneous partition coefficient (K_d^{inst}) for Ge evolution and distribution into the growing amorphous silica crystal through time can be tracked through the following equation derived by Usdowski (1975).

$$\left(\frac{Ge}{Si}\right)_{bulk,am.silica} = \left(\frac{Ge}{Si}\right)_{aq,0} \times \frac{1-\left(\frac{Si}{Si_0}\right)_{aq}^{K_d^{inst}}}{1-\left(\frac{Si}{Si_0}\right)_{aq}} \qquad \text{(D.1)}$$

This equation was initially developed for Sr distribution with respect to calcite growth and has been used frequent in the carbonate experimental literature (Tang et al., 2008; Böhm et al., 2012; AlKhatib and Eisenhauer, 2017). We now apply this approach for the first time to Ge partitioning during amorphous silica formation.

Solving for the K_d^{inst} in this particular expression requires simple algebraic re-arrangement that will be shown step-by-step below.

First, **eqn. D.1** is re-arranged to isolate for $\left(\frac{Si}{Si_0}\right)_{aq}^{K_d^{inst}}$ so that the equation is presented as follows (**eqn. D.2**):

$$\left(\frac{Si}{Si_0}\right)_{aq}^{K_d^{inst}} = 1 - \left[\frac{\left(1-\left(\frac{Si}{Si_0}\right)_{aq}\right)\times\left(\frac{Ge}{Si}\right)_{bulk,am.silica}}{\left(\frac{Ge}{Si}\right)_{aq,0}}\right] \qquad \text{(D.2)}$$

Then, following the logarithm power rule that states $\log_b(X^y) = y \cdot \log_b(X)$ we take the log base 10 of both sides of **eqn. D.2** as shown below:

$$K_d^{inst} log_{10}\left(\frac{Si}{Si_0}\right)_{aq} = log_{10}\left(1 - \left[\frac{\left(1-\left(\frac{Si}{Si_0}\right)_{aq}\right)\times\left(\frac{Ge}{Si}\right)_{bulk,am.silica}}{\left(\frac{Ge}{Si}\right)_{aq,0}}\right]\right) \qquad \text{(D.3)}$$

Finally, K_d^{inst} is solved for by moving $log_{10}\left(\frac{Si}{Si_0}\right)_{aq}$ over to the right hand side of the **eqn. D.3** giving the final expression (**eq. D.4**):

$$K_d^{inst} = \frac{log_{10}\left(1-\left[\frac{\left(1-\left(\frac{Si}{Si_0}\right)_{aq}\right)\times\left(\frac{Ge}{Si}\right)_{bulk,am.silica}}{\left(\frac{Ge}{Si}\right)_{aq,0}}\right]\right)}{log_{10}\left(\frac{Si}{Si_0}\right)_{aq}} \quad \text{(D.4)}$$

APPENDIX E

STORM EVENT C–Q AND R–Q RELATIONSHIPS FOR EACH SITE

Table E.1 Stream water major cation chemistry corrected for atmospheric input

(a) storm event runoff (q) normalized to the annual runoff (**eqn. 4.3**)

(b) stream major cation chemistry corrected for atmospheric or rain input using Cl- concentrations and respective sodium elemental ratios (**eqn. 4.1**): 0.859 (Na/Cl), 0.019 (K/Cl), 0.097 (Mg/Cl), and 0.019 (Ca/Cl) (Riley and Tongudai, 1967; Stallard 1980; Gaillardet et al., 1999)

(c) Weighted average (WTAVG) calculated in terms of runoff through the following equation: $\frac{\sum q_i X_i}{\sum q_i}$ where X corresponds to respective variable.

I.D	Sample time	Q	q	q*(a)	Na*b	% rain input	K*(b)	% rain input	Ca*(b)	% rain input	Mg*(b)	% rain input	Sr*(b)	% rain input	Cl-
		$m^3 s^{-1}$	mm day^{-1}		µM		µM		µM		µM		µM		µM
Sapine															
SE3-03	12/10/2016 16:50	0.0004	0.07	0.02	28.3	16%	3.8	16%	19.6	4%	9.2	30%	0.05	11%	39.9
SE3-15	13/10/2016 04:50	0.0027	0.43	0.14	24.7	8%	7.8	8%	17.5	4%	7.7	32%	0.06	10%	37.9
SE3-21	13/10/2016 10:50	0.0033	0.52	0.17	18.6	8%	8.6	8%	14.1	5%	8.4	33%	0.06	10%	42.4
SE3-27	13/10/2016 16:50	0.0039	0.63	0.20	18.8	8%	8.7	8%	13.7	5%	8.1	33%	0.06	10%	40.9
SE3-31	13/10/2016 20:50	0.0067	1.07	0.35	23.5	7%	8.7	7%	14.0	5%	8.9	28%	0.06	8%	35.2
SE3-33	13/10/2016 22:50	0.0181	2.90	0.95	22.6	5%	13.0	5%	13.7	4%	8.3	28%	0.06	8%	34.0
SE3-35	14/10/2016 00:50	0.0209	3.35	1.09	22.1	6%	10.6	6%	12.7	5%	8.1	30%	0.06	9%	35.2
SE3-36	14/10/2016 01:50	0.0300	4.80	1.56	20.7	6%	10.6	6%	12.9	5%	8.3	28%	0.06	9%	33.8
SE3-38	14/10/2016 03:50	0.0251	4.01	1.31	17.6	6%	11.2	6%	12.7	5%	8.2	30%	0.06	9%	35.8
SE3-42	14/10/2016 07:50	0.0221	3.53	1.15	21.1	7%	9.4	7%	11.8	5%	7.5	31%	0.06	9%	35.3
SE3-46	14/10/2016 12:00	0.0522	8.35	2.72	25.8	10%	5.8	10%	16.8	4%	10.3	25%	0.05	10%	35.8
SE3-47	14/10/2016 16:00	0.0297	4.75	1.55	14.6	6%	10.5	6%	12.1	5%	7.4	32%	0.05	11%	36.6
SE3-49	15/10/2016 00:00	0.0223	3.56	1.16	18.2	8%	8.1	8%	12.8	5%	7.8	32%	0.05	11%	37.2

(Table E.1 continued)

SE3-51	15/10/2016 08:00	0.0205	3.28	1.07	18.7	10%	7.1	10%	13.0	6%	7.8	33%	0.05	11%	40.5
SE3-59	16/10/2016 16:00	0.0261	4.17	1.36	19.3	14%	4.7	14%	13.0	5%	8.0	32%	0.06	11%	39.6
SE3-61	17/10/2016 00:00	0.0286	4.58	1.49	19.7	14%	4.6	14%	12.7	5%	7.8	33%	0.05	11%	39.3
SE3-65	17/10/2016 16:00	0.0308	4.93	1.61	22.3	15%	4.2	15%	14.4	5%	8.2	32%	0.05	11%	39.6
Max		***0.052***	***8.354***	***2.72***	***28.32***	***16%***	***13.00***	***16%***	***19.61***	***6%***	***10.28***	***33%***	***0.06***	***11%***	***42.45***
Min		***0.0004***	***0.069***	***0.02***	***14.59***	***5%***	***3.84***	***5%***	***11.83***	***4%***	***7.39***	***25%***	***0.05***	***8%***	***33.78***
AVG		***0.020***	***3.232***	***1.05***	***20.99***	***9%***	***8.07***	***9%***	***13.98***	***5%***	***8.24***	***31%***	***0.06***	***10%***	***37.59***
WTAVG[(c)]		-	-	-	***20.66***	***9%***	***7.94***	***9%***	***13.59***	***5%***	***8.32***	***30%***	***0.05***	***10%***	***36.96***
I.D	**Sample time**	**Q**	**q**	**q***	**Na*[b]**	**% rain input**	**K*[C]**	**% rain input**	**Ca*[d]**	**% rain input**	**Mg*[e]**	**% rain input**	**Sr*[f]**	**% rain input**	**Cl-[(H)]**
		$m^3 s^{-1}$	**mm day^{-1}**		**µM**		**µM**		**µM**		**µM**		**µM**		**µM**
La Jara															
NMS 1887	13/03/2017 18:00	0.03	0.76	0.61	89.8	2%	36.0	2%	189.0	0.4%	35.0	9%	0.5	1%	37.49
NMS 1888	14/03/2017 06:00	0.03	0.69	0.55	108.8	2%	35.3	2%	219.6	0.3%	35.7	10%	0.5	1%	40.52
NMS 1916	17/03/2017 19:00	0.06	1.68	1.35	89.1	2%	40.3	2%	226.1	0.4%	38.0	10%	0.5	1%	42.25
NMS 1950	24/03/2017 10:00	0.11	2.89	2.31	61.5	2%	38.7	2%	187.5	0.4%	34.5	10%	0.5	1%	38.39
NMS 1975	28/03/2017 19:00	0.09	2.42	1.94	72.9	2%	36.2	2%	190.0	0.4%	38.6	9%	0.4	1%	38.37
NMS 1976	29/03/2017 10:00	0.09	2.33	1.87	71.8	2%	33.3	2%	174.3	0.4%	34.5	10%	0.4	1%	38.12
NMS 1981	30/03/2017 10:00	0.08	2.13	1.70	67.6	2%	33.8	2%	157.1	0.5%	34.9	10%	0.4	1%	38.89
NMS 1985	30/03/2017 17:00	0.08	2.20	1.76	69.3	2%	35.2	2%	156.5	0.5%	35.2	9%	0.4	1%	37.71
NMS 1986	31/03/2017 08:00	0.08	2.06	1.65	112.9	2%	33.4	2%	169.2	0.4%	34.7	10%	0.4	2%	39.94
NMS 1993	01/04/2017 17:00	0.07	1.93	1.55	83.7	2%	32.3	2%	216.1	0.3%	34.3	9%	0.4	1%	36.2
NMS 1994	02/04/2017 08:00	0.07	1.73	1.39	77.6	2%	32.8	2%	162.5	0.4%	35.0	10%	0.4	1%	38.27
NMS 2001	02/04/2017 17:00	0.07	1.96	1.57	79.4	2%	33.5	2%	167.2	0.4%	33.9	10%	0.4	2%	37.81

(Table E.1 continued)

NMS 2002	03/04/2017 08:00	0.07	1.77	1.42	73.8	2%	32.3	2%	175.4	0.4%	34.0	10%	0.4	1%	38.06
NMS 2036	09/04/2017 08:00	0.07	1.92	1.54	74.7	2%	32.7	2%	180.1	0.4%	36.8	9%	0.4	1%	35.54
NMS 2037	09/04/2017 17:00	0.08	2.10	1.69	76.9	2%	34.5	2%	182.6	0.3%	37.0	8%	0.4	1%	33.93
NMS 2114	21/04/2017 17:00	0.12	3.26	2.62	70.8	2%	33.5	2%	152.4	0.3%	31.3	8%	0.4	1%	27.39
NMS 2119	23/04/2017 17:00	0.11	2.96	2.37	78.7	1%	34.5	1%	159.4	0.3%	31.1	8%	0.4	1%	27.34
NMS 2120	24/04/2017 08:00	0.11	2.80	2.24	81.8	2%	30.9	2%	161.4	0.3%	30.5	8%	0.4	1%	28.76
I.D	**Sample time**	**Q**	**q**	**q***	**Na*[b]**	**% rain input**	**K*[C]**	**% rain input**	**Ca*[d]**	**% rain input**	**Mg*[e]**	**% rain input**	**Sr*[f]**	**% rain input**	**Cl-(H)**
		$m^3 s^{-1}$	**mm day^{-1}**		**µM**		**µM**		**µM**		**µM**		**µM**		**µM**
NMS 2145	27/04/2017 17:00	0.09	2.35	1.88	74.8	1%	30.8	1%	165.3	0.3%	30.3	7%	0.4	1%	24.3
NMS 2146	28/04/2017 10:00	0.09	2.32	1.86	75.5	2%	29.4	2%	161.2	0.3%	30.4	7%	0.4	1%	23.93
NMS 2147	28/04/2017 17:00	0.08	2.21	1.77	80.0	1%	30.0	1%	154.6	0.3%	30.0	7%	0.4	1%	23.99
NMS 2148	29/04/2017 10:00	0.08	2.12	1.70	90.2	2%	28.4	2%	154.3	0.3%	29.8	8%	0.4	1%	25.28
NMS 2149	29/04/2017 17:00	0.08	2.04	1.63	80.5	1%	29.5	1%	157.2	0.3%	29.5	7%	0.4	1%	23.79
NMS 2206	08/05/2017 17:00	0.07	1.75	1.41	84.6	1%	32.9	1%	137.1	0.3%	21.4	9%	0.3	1%	21.88
NMS 2211	10/05/2017 08:47	0.07	1.91	1.53	79.1	1%	31.6	1%	134.2	0.3%	20.9	10%	0.3	1%	23.5
NMS 2226	12/05/2017 17:00	0.07	1.70	1.36	81.6	1%	32.9	1%	132.9	0.3%	20.1	10%	0.3	1%	22.63
NMS 2227	13/05/2017 17:00	0.06	1.68	1.34	70.1	2%	31.5	2%	133.4	0.5%	19.6	14%	0.3	2%	34.16
NMS 2228	14/05/2017 17:00	0.06	1.62	1.30	84.3	1%	30.6	1%	133.3	0.3%	22.5	8%	0.3	1%	21.5
NMS 2231	18/05/2017 10:40	0.06	1.52	1.22	75.6	1%	26.8	1%	144.1	0.3%	27.4	6%	0.4	1%	19.56
Max		***0.12***	***3.26***	***2.62***	***113***	***2%***	***40***	***2%***	***226***	***0.5%***	***39***	***14%***	***0.5***	***2%***	***42***
Min		***0.03***	***0.69***	***0.55***	***62***	***1%***	***27***	***1%***	***133***	***0.3%***	***20***	***6%***	***0.3***	***1%***	***20***

(Table E.1 continued)

AVG		*0.08*	*2.03*	*1.63*	*80*	*2%*	*33*	*2%*	*167*	*0.4%*	*31*	*9%*	*0.4*	*1%*	*32*
WTAVG[c]		-	-	-	*80.05*	*2%*	*33.20*	*2%*	*168.18*	*0.4%*	*31.63*	*9%*	*0.40*	*1%*	*31.84*
Elder Creek															
EC-01	01/05/2017 17:30	1.95	9.93	2.08	200.1	8%	13.0	8%	246.6	0%	132.1	4%	1.1	1%	59.29
EC-05	07/01/2017 05:20	1.71	8.71	1.82	192.3	8%	12.8	8%	246.1	0%	131.8	4%	1.3	1%	62.45
EC-07	07/01/2017 13:46	2.29	11.66	2.44	179.7	8%	12.3	8%	216.6	0%	116.1	4%	1.0	1%	53.71
EC-09	07/01/2017 16:57	2.35	11.95	2.50	184.0	7%	12.8	7%	221.7	0%	118.5	4%	1.0	1%	53.00

I.D	Sample time	Q	q	q*	Na*[b]	% rain input	K*[C]	% rain input	Ca*[d]	% rain input	Mg*[e]	% rain input	Sr*[f]	% rain input	Cl-[(H)]
		$m^3 s^{-1}$	mm day^{-1}		µM		µM		µM		µM		µM		µM
EC-11	08/01/2017 05:40	2.83	14.39	3.01	181.2	7%	12.9	7%	219.1	0%	116.6	4%	0.9	1%	55.66
EC-12	08/01/2017 10:40	4.98	25.33	5.30	198.5	5%	15.2	5%	221.8	0%	118.6	3%	1.0	1%	44.08
EC-15	08/01/2017 19:10	9.51	48.36	10.11	124.5	7%	10.1	7%	115.4	1%	60.4	6%	0.5	1%	41.24
EC-19	09/01/2017 11:30	6.74	34.25	7.16	163.9	7%	13.7	7%	185.7	1%	100.2	5%	0.7	1%	52.40
EC-23	09/01/2017 23:30	6.60	33.53	7.01	161.6	6%	13.4	6%	181.8	1%	98.3	5%	0.7	1%	48.80
EC-25	10/01/2017 08:15	8.83	44.90	9.39	147.2	6%	13.8	6%	161.9	1%	86.5	5%	0.6	1%	47.01
EC-28	10/01/2017 17:30	32.00	162.63	34.01	118.0	4%	18.5	4%	131.3	1%	69.2	5%	0.6	1%	38.19
EC-33	11/01/2017 11:25	9.09	46.20	9.66	137.5	6%	15.5	6%	162.9	1%	86.4	5%	0.7	1%	49.82
EC-38	12/01/2017 08:45	6.34	32.24	6.74	149.2	7%	13.5	7%	176.9	1%	95.4	5%	0.8	1%	52.00
Max		*32.00*	*162.63*	*34.01*	*200.10*	*8%*	*18.47*	*8%*	*246.58*	*1%*	*132.09*	*6%*	*1.25*	*1%*	*62.45*
Min		*1.71*	*8.71*	*1.82*	*118.04*	*4%*	*10.06*	*4%*	*115.36*	*0%*	*60.40*	*3%*	*0.46*	*1%*	*38.19*
AVG		*7.33*	*37.24*	*7.79*	*164.44*	*7%*	*13.65*	*7%*	*191.36*	*1%*	*102.32*	*5%*	*0.85*	*1%*	*50.59*
WTAVG[c]		-	-	-	*143.80*	*6%*	*15.06*	*6%*	*162.00*	*1%*	*86.29*	*5%*	*0.71*	*1%*	*45.52*

(Table E.1 continued)

Quiock Creek															
QC1	06/10/2015	0.0002	0.25	0.16	-29.7	112%	2.8	69%	6.5	49%	-5.3	120%	0.00	97%	333.7
QC2	07/10/2015	0.0002	0.23	0.15	-28.4	111%	-0.1	101%	6.8	48%	-4.7	117%	0.01	82%	333.1
QC3	08/10/2015	0.0002	0.23	0.15	-28.7	111%	0.2	96%	6.8	48%	-4.8	117%	0.01	87%	336.5
QC4	09/10/2015	0.0002	0.25	0.16	-39.7	115%	0.1	98%	7.4	47%	-5.5	119%	0.02	73%	350.4
QC5	10/10/2015	0.0003	0.36	0.23	-33.3	113%	3.2	66%	7.2	46%	-4.1	115%	0.01	80%	326.4
QC6	11/10/2015	0.0004	0.45	0.29	-44.3	118%	2.1	75%	6.4	49%	-5.4	120%	0.01	86%	331.8
QC7	12/10/2015	0.0002	0.23	0.15	-41.8	117%	1.2	84%	6.7	48%	-5.4	120%	0.01	86%	335.2
QC8	13/10/2015	0.0002	0.16	0.10	-41.7	117%	1.4	82%	6.9	47%	-5.1	119%	0.01	84%	327.5
QC9	14/10/2015	0.0020	2.18	1.40	-26.5	110%	0.9	87%	5.3	54%	-5.3	120%	0.01	90%	327.7
QC10	15/10/2015	0.0005	0.51	0.33	-16.7	107%	2.2	73%	7.6	44%	-2.8	110%	0.03	68%	316.7
QC11	16/10/2015	0.0019	2.07	1.33	-23.9	110%	0.2	98%	5.8	51%	-4.1	116%	0.01	88%	318.7
QC12	17/10/2015	0.0040	4.29	2.75	-14.6	106%	-0.8	116%	6.3	48%	-1.8	107%	0.02	77%	306.8
QC13	18/10/2015	0.0009	0.93	0.60	-25.3	110%	-1.2	125%	6.0	50%	-3.4	112%	0.01	86%	321.1
QC14	19/10/2015	0.0005	0.54	0.35	-18.2	107%	-0.7	114%	7.0	47%	-2.6	109%	0.02	72%	325.2

I.D	**Sample time**	**Q**	**q**	**q***	**Na*[b]**	**% rain input**	**K*[C]**	**% rain input**	**Ca*[d]**	**% rain input**	**Mg*[e]**	**% rain input**	**Sr*[f]**	**% rain input**	**Cl-[(H)]**
		$m^3 s^{-1}$	**mm day^{-1}**		**µM**		**µM**		**µM**		**µM**		**µM**		**µM**
QC15	20/10/2015	0.0004	0.46	0.30	-22.6	109%	-0.9	117%	6.2	50%	-3.1	111%	0.01	86%	326.0
QC16	21/10/2015	0.0003	0.36	0.23	-17.8	107%	-0.7	114%	6.6	48%	-3.2	111%	0.01	82%	326.3
QC17	22/10/2015	0.0004	0.43	0.28	-18.9	107%	0.1	98%	7.1	47%	-3.4	112%	0.02	70%	327.6
QC18	23/10/2015	0.0004	0.42	0.27	-12.6	105%	0.4	94%	6.4	49%	-3.1	111%	0.00	94%	329.6
QC19	24/10/2015	0.0003	0.36	0.23	-14.9	106%	-0.4	106%	6.6	49%	-2.7	109%	0.01	84%	330.5
QC20	25/10/2015	0.0247	26.64	17.08	7.3	96%	0.6	88%	6.6	39%	0.1	99%	0.02	67%	225.8
QC21	26/10/2015	0.0021	2.30	1.47	-9.7	104%	-1.2	128%	5.7	49%	-2.2	108%	0.01	81%	296.8
Max		***0.02***	***26.64***	***17.08***	***7.33***	***118%***	***3.17***	***128%***	***7.60***	***54%***	***0.11***	***120%***	***0.03***	***97%***	***350.38***
Min		***0.0002***	***0.16***	***0.10***	***-44.31***	***96%***	***-1.22***	***66%***	***5.33***	***39%***	***-5.50***	***99%***	***0.00***	***67%***	***225.80***
AVG		***0.0019***	***2.08***	***1.33***	***-23.91***	***109%***	***0.44***	***97%***	***6.57***	***48%***	***-3.72***	***114%***	***0.01***	***82%***	***321.59***
WTAVG[(c)]	-	-	-	***68.16***	***-3.50***	***101%***	***0.30***	***95%***	***6.46***	***43%***	***-1.22***	***104%***	***0.02***	***73%***	***6.06***
Hakai															
111	16/09/2017 14:36	0.22	2.39	2.01	5.7	92%	1.1	57%	9.7	13%	1.5	84%	0.02	37%	80.06
125	17/09/2017 05:00	0.19	2.10	1.77	5.8	93%	1.2	57%	10.0	14%	2.1	80%	0.02	38%	85.55
110	17/09/2017 07:00	0.19	2.16	1.82	3.9	95%	1.2	56%	9.8	14%	1.3	87%	0.02	36%	83.75

(Table E.1 continued)

326	17/09/2017 09:00	0.21	2.31	1.94	5.3	93%	1.8	47%	11.1	13%	2.5	77%	0.03	30%	84.01
253	17/09/2017 11:00	0.50	5.53	4.65	1.7	98%	1.1	60%	10.6	14%	1.6	84%	0.03	34%	88.77
130	17/09/2017 13:00	0.61	6.76	5.69	2.7	97%	1.2	57%	9.5	15%	1.3	86%	0.02	37%	88.11
252	17/09/2017 15:00	0.53	5.93	4.99	4.8	94%	1.5	49%	8.8	15%	1.3	86%	0.02	37%	79.87
142	17/09/2017 17:00	0.50	5.57	4.69	2.8	96%	1.4	52%	8.5	16%	0.8	91%	0.02	41%	83.12
141	17/09/2017 19:00	0.43	4.74	3.99	-6.0	107%	0.5	79%	15.3	11%	2.0	83%	0.03	37%	104.1
256	17/09/2017 21:00	0.37	4.13	3.47	3.2	96%	1.6	48%	9.0	14%	1.3	86%	0.03	35%	81.38
260	17/09/2017 23:00	0.34	3.80	3.20	4.0	95%	1.2	59%	10.7	14%	3.1	74%	0.03	31%	91.25

I.D	**Sample time**	**Q**	**q**	**q***	**Na*[b]**	**% rain input**	**K*[C]**	**% rain input**	**Ca*[d]**	**% rain input**	**Mg*[e]**	**% rain input**	**Sr*[f]**	**% rain input**	**Cl-[(H)]**
		$m^3 s^{-1}$	**mm day^{-1}**		**µM**		**µM**		**µM**		**µM**		**µM**		**µM**
349	18/09/2017 01:00	0.32	3.50	2.95	0.6	99%	1.8	47%	8.9	15%	0.7	92%	0.02	38%	86.59
339	18/09/2017 03:00	0.30	3.31	2.79	3.2	96%	1.7	50%	9.7	15%	2.3	79%	0.03	34%	91.21
114	18/09/2017 05:00	0.29	3.16	2.66	-11.8	116%	1.6	54%	16.3	10%	0.2	98%	0.02	42%	101.2
350	18/09/2017 09:00	0.26	2.93	2.47	1.6	98%	1.8	46%	9.6	14%	0.7	92%	0.02	39%	81.73
251	18/09/2017 13:00	0.25	2.79	2.35	3.6	95%	1.6	50%	7.7	17%	0.9	90%	0.02	39%	83.37
302	18/09/2017 19:00	0.23	2.60	2.19	7.6	90%	1.4	53%	9.5	14%	2.8	74%	0.03	30%	82.62
113	19/09/2017 01:00	0.22	2.45	2.06	6.8	91%	1.6	49%	10.8	12%	2.6	76%	0.03	31%	81.62
Max		***0.61***	***6.76***	***5.69***	***7.64***	***116%***	***1.82***	***79%***	***16.30***	***17%***	***3.09***	***98%***	***0.03***	***42%***	***104.10***
Min		***0.19***	***2.10***	***1.77***	***-11.77***	***90%***	***0.53***	***46%***	***7.74***	***10%***	***0.24***	***74%***	***0.02***	***30%***	***79.87***
AVG		***0.33***	***3.68***	***3.09***	***2.54***	***97%***	***1.41***	***54%***	***10.31***	***14%***	***1.62***	***84%***	***0.03***	***36%***	***86.57***
WTAVG[(c)]		**-**	**-**	**-**	***2.20***	***97%***	***1.38***	***55%***	***10.27***	***14%***	***1.55***	***85%***	***0.03***	***36%***	***87.02***

(Table E.1 continued)

123	16/09/2017 14:36	0.22	2.39	2.01	5.7	92%	1.1	57%	9.7	13%	1.5	84%	0.02	37%	80.06
292	14/10/2017 09:30	0.15	1.71	1.44	3.1	97%	1.8	51%	9.0	17%	1.2	89%	0.02	41%	99.74
280	14/10/2017 12:30	0.27	2.98	2.51	-8.2	109%	1.5	58%	15.0	13%	-0.9	109%	0.02	49%	114.3
120	14/10/2017 15:30	0.31	3.40	2.87	6.4	92%	1.3	55%	8.9	15%	2.2	78%	0.03	32%	82.56
329	14/10/2017 18:30	0.40	4.46	3.76	4.6	94%	1.2	57%	8.0	16%	1.4	84%	0.02	39%	81.23
129	14/10/2017 21:30	0.65	7.25	6.10	4.0	95%	1.2	55%	7.7	16%	1.2	87%	0.02	38%	80.88
307	15/10/2017 00:30	0.63	6.94	5.84	3.9	95%	1.0	61%	9.2	15%	2.4	78%	0.03	33%	85.64
261	15/10/2017 03:30	0.50	5.52	4.65	-50.1	171%	0.4	86%	33.2	7%	-4.4	148%	0.02	58%	140.4

I.D	Sample time	Q	q	q^{*}	Na*[b]	% rain input	K*[C]	% rain input	Ca*[d]	% rain input	Mg*[e]	% rain input	Sr*[f]	% rain input	$Cl^{-(H)}$
		$m^3 s^{-1}$	mm day^{-1}		µM		µM		µM		µM		µM		µM
131	15/10/2017 06:30	0.41	4.50	3.78	3.4	96%	1.2	58%	9.6	14%	2.3	78%	0.03	32%	86.56
331	15/10/2017 09:30	0.38	4.22	3.55	4.4	95%	0.9	67%	9.7	16%	3.3	75%	0.03	34%	98.53
291	15/10/2017 12:30	0.99	10.96	9.23	-27.0	132%	0.6	79%	21.4	10%	-0.7	106%	0.03	44%	128.1
284	15/10/2017 15:30	1.56	17.24	14.51	-17.3	122%	1.0	68%	13.5	13%	-0.1	101%	0.02	46%	110.4
276	15/10/2017 18:30	1.08	12.01	10.11	-5.1	107%	1.2	58%	13.2	11%	0.3	96%	0.02	43%	88.22
135	15/10/2017 21:30	0.91	10.06	8.47	26.1	87%	5.7	40%	9.5	28%	-4.0	126%	0.01	76%	199.2
285	16/10/2017 00:30	0.86	9.49	7.98	6.3	92%	1.1	59%	10.1	13%	2.0	80%	0.03	35%	83.14
320	16/10/2017 03:30	1.00	11.08	9.33	20.2	89%	4.0	47%	10.5	26%	-3.9	126%	0.01	71%	191.1
306	16/10/2017 06:30	1.81	20.05	16.88	-8.4	110%	1.1	64%	17.3	10%	1.5	87%	0.03	36%	105.0

(Table E.1 continued)

345	16/10/2017 09:30	5.34	59.20	49.83	2.1	97%	1.2	58%	10.9	13%	2.7	76%	0.03	33%	89.10
139	16/10/2017 12:30	4.13	45.76	38.52	-6.6	109%	1.4	56%	13.7	11%	0.4	96%	0.02	43%	93.73
278	16/10/2017 15:30	2.89	32.02	26.95	0.5	99%	1.4	54%	8.3	17%	1.5	85%	0.02	40%	88.01
259	16/10/2017 18:30	2.75	30.42	25.61	9.5	90%	1.5	54%	10.1	15%	3.1	75%	0.03	33%	95.94
127	16/10/2017 21:30	3.14	34.77	29.27	8.7	89%	1.3	55%	8.2	16%	1.8	81%	0.02	36%	82.42
134	17/10/2017 00:30	3.59	39.80	33.50	8.0	91%	2.9	38%	7.8	19%	0.7	93%	0.02	42%	95.58
138	17/10/2017 09:30	2.53	28.05	23.61	6.5	91%	1.3	52%	7.5	16%	1.9	80%	0.02	37%	78.00
140	17/10/2017 12:30	2.23	24.67	20.77	6.8	91%	1.3	54%	9.1	14%	1.8	81%	0.03	34%	80.90
250	17/10/2017 15:30	1.90	21.09	17.75	2.7	96%	1.9	44%	9.8	13%	1.4	85%	0.03	34%	80.80

I.D	Sample time	Q	q	q^{*}	Na*[b]	% rain input	K*[c]	% rain input	Ca*[d]	% rain input	Mg*[e]	% rain input	Sr*[f]	% rain input	$Cl^{-(H)}$
		$m^3\ s^{-1}$	mm day^{-1}		µM		µM		µM		µM		µM		µM
286	17/10/2017 18:30	1.63	18.04	15.19	-2.2	103%	2.1	46%	8.8	17%	1.2	88%	0.03	36%	93.17
301	17/10/2017 21:30	1.41	15.66	13.18	-2.4	103%	2.5	38%	10.8	13%	0.5	94%	0.02	38%	82.79
303	18/10/2017 00:30	1.25	13.87	11.68	8.4	90%	0.9	64%	9.5	15%	3.8	69%	0.04	28%	87.52
311	18/10/2017 03:30	1.18	13.06	10.99	3.0	96%	2.1	44%	7.4	18%	1.4	85%	0.03	32%	86.63
325	18/10/2017 06:30	1.72	19.01	16.00	8.0	88%	1.5	46%	6.6	17%	2.5	73%	0.03	31%	69.91
340	18/10/2017 09:30	2.40	26.56	22.36	7.3	89%	2.6	33%	9.2	12%	2.2	75%	0.02	32%	67.85
346	18/10/2017 12:30	1.75	19.35	16.29	5.7	93%	1.3	55%	7.5	17%	1.6	83%	0.02	36%	81.98
248	18/10/2017 17:00	1.36	15.08	12.70	7.4	90%	1.3	52%	6.9	17%	2.2	76%	0.02	34%	73.98

(Table E.1 continued)

333	18/10/2017 23:00	1.26	13.96	11.75	8.2	89%	1.2	54%	7.9	15%	1.9	80%	0.02	34%	76.42
277	19/10/2017 11:00	1.19	13.13	11.05	6.5	92%	0.8	66%	9.3	15%	2.5	77%	0.03	33%	87.73
337	19/10/2017 17:00	1.08	11.95	10.06	5.6	93%	1.1	60%	9.4	15%	3.2	73%	0.03	32%	88.09
304	19/10/2017 23:00	1.16	12.80	10.78	5.7	93%	1.4	55%	7.8	18%	1.5	86%	0.02	40%	92.52
309	20/10/2017 05:00	1.25	13.85	11.65	17.9	87%	4.3	38%	7.9	25%	-0.4	103%	0.02	53%	141.32
290	20/10/2017 11:00	1.41	15.59	13.12	-10.5	113%	1.2	62%	12.9	13%	0.6	95%	0.03	41%	104.8
324	20/10/2017 17:00	1.10	12.13	10.21	8.4	89%	1.2	56%	9.2	14%	3.0	72%	0.03	32%	79.38
299	20/10/2017 23:00	0.95	10.48	8.82	7.5	90%	1.4	52%	8.0	16%	2.0	80%	0.02	38%	80.92
279	21/10/2017 05:00	0.85	9.38	7.90	8.3	88%	1.5	48%	5.1	21%	1.4	83%	0.02	38%	72.44
282	21/10/2017 11:00	0.79	8.77	7.39	8.2	89%	1.4	52%	7.1	17%	2.1	78%	0.02	36%	78.12

I.D	Sample time	Q	q	q*	Na*[b]	% rain input	K*[C]	% rain input	Ca*[d]	% rain input	Mg*[e]	% rain input	Sr*[f]	% rain input	Cl-[(H)]
		$m^3 s^{-1}$	mm day^{-1}		µM		µM		µM		µM		µM		µM
335	21/10/2017 17:00	0.83	9.16	7.71	9.2	88%	1.0	60%	8.8	15%	3.0	72%	0.03	30%	80.86
123	21/10/2017 23:00	1.16	7.71	6.49	9.6	88%	0.9	63%	8.6	15%	2.9	73%	0.03	31%	79.78
Max		***5.34***	***59.20***	***49.83***	***26.09***	***171%***	***5.67***	***86%***	***33.22***	***28%***	***3.84***	***148%***	***0.04***	***76%***	***199.23***
Min		***0.15***	***1.71***	***1.44***	***-50.13***	***87%***	***0.42***	***33%***	***5.12***	***7%***	***-4.43***	***69%***	***0.01***	***28%***	***67.85***
AVG		***1.47***	***16.16***	***13.60***	***2.76***	***98%***	***1.58***	***55%***	***10.22***	***16%***	***1.29***	***87%***	***0.02***	***39%***	***94.80***
WTAVG[(c)]		-	-	-	***3.12***	***97%***	***1.62***	***53%***	***9.98***	***15%***	***1.46***	***85%***	***0.03***	***38%***	***91.99***
Providence Creek															
2018- 452	08/01/2018 12:24	0.010	0.65	0.85	133.3	11%	28.0	1%	91.5	0%	21.9	8%	0.5	1%	19.78
2018- 453	08/01/2018 13:24	0.014	0.90	1.17	114.5	14%	29.5	1%	98.5	0%	21.2	9%	0.5	1%	21.26

(Table E.1 continued)

2018- 454	08/01/2018 14:24	0.024	1.59	2.07	108.1	15%	33.6	1%	88.4	0%	20.7	10%	0.4	1%	22.55
2018- 455	08/01/2018 15:24	0.034	2.22	2.88	104.8	17%	34.5	1%	95.4	0%	20.0	11%	0.5	1%	24.71
2018- 456	08/01/2018 16:24	0.033	2.19	2.84	98.5	18%	30.9	2%	80.3	1%	18.7	12%	0.6	1%	25.37
2018- 457	08/01/2018 17:24	0.031	2.06	2.67	104.6	17%	31.5	2%	86.9	1%	19.5	11%	0.5	1%	25.82
2018- 458	08/01/2018 18:24	0.028	1.82	2.37	105.3	17%	31.1	2%	82.2	1%	20.7	11%	0.5	1%	25.35
2018- 459	08/01/2018 19:24	0.025	1.65	2.14	104.9	17%	29.8	2%	91.3	1%	19.3	11%	0.5	1%	24.58
2018- 460	08/01/2018 20:24	0.027	1.74	2.26	103.9	17%	30.5	1%	91.2	1%	19.2	11%	0.5	1%	24.72
2018- 461	08/01/2018 21:24	0.027	1.75	2.27	132.5	14%	30.2	1%	143.4	0%	19.4	11%	0.4	1%	24.18
2018- 462	08/01/2018 22:24	0.024	1.54	2.00	119.1	14%	29.7	1%	94.6	0%	19.9	10%	0.5	1%	23.32
2018- 463	08/01/2018 23:24	0.021	1.37	1.79	107.3	20%	29.0	2%	93.4	1%	19.0	14%	0.5	1%	31.26
2018- 464	09/01/2018 00:24	0.019	1.24	1.61	113.5	15%	28.3	2%	89.4	0%	20.0	10%	0.3	1%	23.53

I.D	Sample time	Q	q	q^*	Na*[b]	% rain input	K*[c]	% rain input	Ca*[d]	% rain input	Mg*[e]	% rain input	Sr*[f]	% rain input	$Cl^{-(H)}$
		$m^3\ s^{-1}$	mm day^{-1}		μM		μM		μM		μM		μM		μM
2018- 465	09/01/2018 01:24	0.018	1.15	1.49	106.0	16%	27.7	2%	83.9	1%	20.0	11%	0.5	1%	24.26
2018- 466	09/01/2018 02:24	0.016	1.03	1.34	114.4	15%	27.1	2%	84.5	1%	19.9	11%	0.5	1%	24.38
2018- 467	09/01/2018 03:24	0.014	0.90	1.17	129.8	13%	30.2	1%	102.0	0%	30.0	7%	0.8	0%	23.47
2018- 468	09/01/2018 04:24	0.012	0.82	1.06	109.1	16%	25.7	2%	86.5	1%	20.2	10%	0.6	1%	24.15
2018- 469	09/01/2018 05:24	0.011	0.75	0.97	110.2	15%	25.5	2%	83.4	1%	20.4	10%	0.5	1%	22.99
2018- 470	09/01/2018 06:24	0.011	0.69	0.90	111.9	16%	25.9	2%	86.0	1%	20.5	10%	0.5	1%	24.57

(Table E.1 continued)

2018- 471	09/01/2018 07:24	0.010	0.65	0.85	105.1	15%	23.3	2%	72.6	1%	19.5	10%	0.5	1%	22.44
Max		***0.03***	***2.22***	***2.88***	***133.33***	***20%***	***34.51***	***2%***	***143.36***	***1%***	***30.03***	***14%***	***0.80***	***1%***	***31.26***
Min		***0.01***	***0.65***	***0.85***	***98.47***	***11%***	***23.26***	***1%***	***72.61***	***0%***	***18.73***	***7%***	***0.34***	***0%***	***19.78***
AVG		***0.02***	***1.34***	***1.73***	***111.84***	***16%***	***29.10***	***2%***	***91.27***	***1%***	***20.51***	***10%***	***0.51***	***1%***	***24.13***
WTAVG(c)		**-**	**-**	**-**	***110.38***	***16%***	***29.94***	***2%***	***92.29***	***1%***	***20.20***	***11%***	***0.50***	***1%***	***24.49***
Rio Icacos															
PR12-IC 06	28/05/2012 11:00	2.44	64.54	0.017	41.8	76%	11.6	20%	62.5	4%	30.4	33%	0.05	-	156.23
PR12-IC 07	28/05/2012 11:39	1.89	50.06	0.013	1.6	99%	8.8	25%	44.8	6%	12.3	56%	0.05	-	160.46
PR12-IC 08	28/05/2018 12:10	1.39	36.7	0.009	20.6	85%	9.1	22%	43.1	6%	12.8	51%	0.05	-	135.36
PR12-IC 09	28/05/2018 13:05	1.07	28.22	0.007	-54.5	100%	7.2	37%	39.3	10%	3.4	86%	0.05	-	223.21
PR12-IC 10	28/05/2018 17:24	0.58	15.23	0.004	-40.9	100%	8.0	33%	42.8	8%	6.6	75%	0.05	-	206.85
		2.44	***64.54***	***0.02***	***41.82***	***100%***	***11.63***	***37%***	***62.46***	***10%***	***30.38***	***86%***	***0.05***	***-***	***223.21***
Max		***0.58***	***15.23***	***0.00***	***-54.48***	***76%***	***7.18***	***20%***	***39.29***	***4%***	***3.44***	***33%***	***0.05***	***-***	***135.36***
Min		***1.47***	***38.95***	***0.01***	***-6.29***	***92%***	***8.92***	***27%***	***46.51***	***7%***	***13.10***	***60%***	***0.05***	***-***	***176.42***
AVG		**-**	**-**	**-**	***7.05***	***89%***	***9.48***	***25%***	***49.39***	***6%***	***16.66***	***53%***	***0.05***	***0.00***	***167.05***
WTAVG(c)	28/05/2012 11:00	2.44	64.54	0.017	41.8	76%	11.6	20%	62.5	4%	30.4	33%	0.05	-	156.23

Table E.2 Stream Si concentrations and stable isotope ratios

(a) storm event runoff (q) normalized to the annual runoff (**eqn. 4.3**).
(b) Si stable isotopes measured in this study.
(c) Si fractionation factors defined as $\Delta_{diss-rock} = \delta_{stream} - \delta_{bedrock}$.
(d) Weighted average (WTAVG) calculated in terms of runoff through the following equation: $\frac{\sum q_i X_i}{\sum q_i}$ where X corresponds to respective variable.
(e) Savage et al., (2012); (f) tonalite, Rio Icacos ; Ziegler et al.(2005) ; (g) Savage et al. (2011) ; (h) Opfergelt et al.(2012) ; (i) measured Elder Creek bedrock.

I.D	Sample time	Q	q	q*(a)	Si	Al	$\delta^{29}Si$(b)	2σ	$\delta^{30}Si$(b)	2σ	$\Delta_{diss-rock}$(c)	1σ
		$m^3\ s^{-1}$	mm day^{-1}		µM	µM	‰	‰	‰	‰	‰	‰
Sapine												
SE3-03	12/10/2016 16:50	0.0004	0.07	0.02	58.10	0.44	0.25	0.09	0.55	0.03	0.78	0.15
SE3-15	13/10/2016 04:50	0.0027	0.43	0.14	49.56	0.70	0.22	0.05	0.38	0.04	0.61	0.16
SE3-21	13/10/2016 10:50	0.0033	0.52	0.17	46.17	0.90	0.20	0.06	0.37	0.06	0.60	0.16
SE3-27	13/10/2016 16:50	0.0039	0.63	0.20	44.94	0.98	0.10	0.08	0.40	0.07	0.63	0.17
SE3-31	13/10/2016 20:50	0.0067	1.07	0.35	45.82	0.98	0.21	0.05	0.49	0.10	0.72	0.18
SE3-33	13/10/2016 22:50	0.0181	2.90	0.95	45.14	1.10	0.19	0.08	0.37	0.09	0.60	0.17
SE3-35	14/10/2016 00:50	0.0209	3.35	1.09	42.34	1.36	0.26	0.03	0.52	0.10	0.75	0.18
SE3-36	14/10/2016 01:50	0.0300	4.80	1.56	40.94	1.56	0.23	0.10	0.45	0.08	0.68	0.17
SE3-38	14/10/2016 03:50	0.0251	4.01	1.31	39.24	1.84	0.26	0.09	0.47	0.14	0.70	0.20
SE3-42	14/10/2016 07:50	0.0221	3.53	1.15	41.24	1.46	0.23	0.16	0.43	0.11	0.66	0.19
SE3-46	14/10/2016 12:00	0.0522	8.35	2.72	52.18	1.08	0.08	0.04	0.17	0.08	0.40	0.17
SE3-47	14/10/2016 16:00	0.0297	4.75	1.55	49.16	1.46	0.01	0.04	0.02	0.13	0.25	0.20
SE3-49	15/10/2016 00:00	0.0223	3.56	1.16	53.07	1.05	0.02	0.03	0.04	0.01	0.27	0.15
SE3-51	15/10/2016 08:00	0.0205	3.28	1.07	55.22	0.86	0.05	0.12	0.11	0.07	0.34	0.16
SE3-59	16/10/2016 16:00	0.0261	4.17	1.36	58.85	0.66	0.07	0.04	0.22	0.08	0.45	0.17
SE3-61	17/10/2016 00:00	0.0286	4.58	1.49	60.18	0.65	0.08	0.00	0.16	0.09	0.39	0.17
SE3-65	17/10/2016 16:00	0.0308	4.93	1.61	61.13	0.45	0.14	0.07	0.29	0.06	0.52	0.16
Max		***0.052***	***8.354***	***2.72***	***61.13***	***1.84***	***0.26***	***0.09***	***0.55***	***0.03***	***0.78***	***0.15***
Min		***0.0004***	***0.069***	***0.02***	***39.24***	***0.44***	***0.01***	***0.04***	***0.02***	***0.13***	***0.25***	***0.20***
AVG		***0.020***	***3.232***	***1.05***	***49.61***	***1.03***	***0.15***	***0.07***	***0.32***	***0.08***	***0.55***	***0.17***
WTAVG(d		-	-	-	***50.26***	***1.11***	***0.13***	***ing***	***0.27***	***0.09***	***0.50***	***0.17***
La Jara												
NMS 1887	13/03/2017 18:00	0.03	0.76	0.61	288.20	0.47	0.37	0.05	0.69	0.04	0.85	0.06
NMS 1888	14/03/2017 06:00	0.03	0.69	0.55	306.80	0.45	0.33	0.04	0.64	0.05	0.80	0.07

(Table E.2 continued)

NMS 1916	17/03/2017 19:00	0.06	1.68	1.35	318.80	0.47	0.37	0.05	0.67	0.06	0.83	0.07
NMS 1950	24/03/2017 10:00	0.11	2.89	2.31	376.10	0.34	0.42	0.04	0.74	0.10	0.90	0.11
NMS 1975	28/03/2017 19:00	0.09	2.42	1.94	484.40	4.95	0.23	0.03	0.55	0.13	0.71	0.14
NMS 1976	29/03/2017 10:00	0.09	2.33	1.87	477.80	1.34	0.28	0.05	0.65	0.09	0.81	0.10

I.D	Sample time	Q	q	q^*	Si*[b]	Al	$\delta^{29}Si$	2σ	$\delta^{30}Si$	2σ	$\Delta_{diss-rock}$	1σ
		$m^3\ s^{-1}$	mm day^{-1}		µM	µM	‰	‰	‰	‰	‰	‰
NMS 1981	30/03/2017 10:00	0.08	2.13	1.70	467.70	3.44	0.30	0.06	0.69	0.12	0.85	0.13
NMS 1985	30/03/2017 17:00	0.08	2.20	1.76	473.90	1.98	0.31	0.03	0.65	0.15	0.81	0.16
NMS 1986	31/03/2017 08:00	0.08	2.06	1.65	470.20	1.23	0.38	0.07	0.81	0.11	0.97	0.12
NMS 1993	01/04/2017 17:00	0.07	1.93	1.55	451.80	1.40	0.44	0.03	0.83	0.03	0.99	0.05
NMS 1994	02/04/2017 08:00	0.07	1.73	1.39	461.20	1.45	0.43	0.05	0.87	0.09	1.03	0.10
NMS 2001	02/04/2017 17:00	0.07	1.96	1.57	406.70	1.35	0.44	0.03	0.86	0.03	1.02	0.05
NMS 2002	03/04/2017 08:00	0.07	1.77	1.42	458.00	1.26	0.43	0.05	0.87	0.09	1.03	0.10
NMS 2036	09/04/2017 08:00	0.07	1.92	1.54	371.60	1.83	0.43	0.05	0.87	0.09	1.03	0.10
NMS 2037	09/04/2017 17:00	0.08	2.10	1.69	372.10	1.84	0.45	0.05	0.86	0.12	1.02	0.13
NMS 2114	21/04/2017 17:00	0.12	3.26	2.62	328.30	1.39	0.39	0.05	0.73	0.11	0.89	0.12
NMS 2119	23/04/2017 17:00	0.11	2.96	2.37	339.60	1.42	0.45	0.05	0.87	0.10	1.03	0.11
NMS 2120	24/04/2017 08:00	0.11	2.80	2.24	324.90	1.43	0.40	0.06	0.81	0.11	0.97	0.12
NMS 2145	27/04/2017 17:00	0.09	2.35	1.88	319.70	1.40	0.45	0.05	0.84	0.13	1.00	0.14
NMS 2146	28/04/2017 10:00	0.09	2.32	1.86	315.60	1.30	0.51	0.04	0.94	0.09	1.10	0.09
NMS 2147	28/04/2017 17:00	0.08	2.21	1.77	326.30	1.26	0.43	0.10	0.82	0.07	0.98	0.08
NMS 2148	29/04/2017 10:00	0.08	2.12	1.70	324.80	1.22	0.43	0.08	0.82	0.13	0.98	0.14
NMS 2149	29/04/2017 17:00	0.08	2.04	1.63	321.80	1.24	0.44	0.05	0.83	0.13	0.99	0.14
NMS 2206	08/05/2017 17:00	0.07	1.75	1.41	916.00	0.32	0.31	0.08	0.68	0.13	0.84	0.13
NMS 2211	10/05/2017 08:47	0.07	1.91	1.53	943.00	0.50	0.31	0.07	0.61	0.08	0.77	0.09
NMS 2226	12/05/2017 17:00	0.07	1.70	1.36	928.00	0.30	0.33	0.10	0.63	0.10	0.79	0.11

(Table E.2 continued)

NMS 2227	13/05/2017 17:00	0.06	1.68	1.34	917.00	0.31	0.35	0.08	0.70	0.10	0.86	0.11
NMS 2228	14/05/2017 17:00	0.06	1.62	1.30	1035.00	0.38	0.38	0.09	0.70	0.08	0.86	0.09
NMS 2231	18/05/2017 10:40	0.06	1.52	1.22	294.00	0.34	0.39	0.12	0.76	0.13	0.92	0.14
Max		***0.12***	***3.26***	***2.62***	***1035***	***5***	***0.51***	***0.04***	***0.94***	***0.09***	***1.10***	***0.09***
Min		***0.03***	***0.69***	***0.55***	***288***	***0***	***0.23***	***0.03***	***0.55***	***0.13***	***0.71***	***0.14***
AVG		***0.08***	***2.03***	***1.63***	***477***	***1***	***0.39***	***0.06***	***0.76***	***0.10***	***0.92***	***0.11***
WTAVG[(d)]		-	-	-	***464***	***1.53***	***0.39***	***0.06***	***0.77***	***0.10***	***0.93***	***0.11***
Elder Creek												
EC-01	01/05/2017 17:30	1.95	9.93	2.08	362.90	0.066	0.66	0.14	1.34	0.08	1.73	0.10

I.D	**Sample time**	**Q**	**q**	**q***	**Si*[b]**	**Al**	**δ^{29}Si**	**2σ**	**δ^{30}Si**	**2σ**	**$\Delta_{diss-rock}$**	**1σ**
		$m^3\ s^{-1}$	**mm day^{-1}**		**μM**	**μM**	**‰**	**‰**	**‰**	**‰**	**‰**	**‰**
EC-05	07/01/2017 05:20	1.71	8.71	1.82	355.46	0.048	0.69	0.15	1.28	0.06	1.67	0.09
EC-07	07/01/2017 13:46	2.29	11.66	2.44	336.16	0.124	0.64	0.06	1.21	0.19	1.60	0.20
EC-09	07/01/2017 16:57	2.35	11.95	2.50	333.30	0.123	0.68	0.09	1.25	0.06	1.64	0.08
EC-11	08/01/2017 05:40	2.83	14.39	3.01	336.09	0.100	0.60	0.04	1.21	0.16	1.60	0.17
EC-12	08/01/2017 10:40	4.98	25.33	5.30	340.07	0.282	0.60	0.14	1.12	0.10	1.51	0.11
EC-15	08/01/2017 19:10	9.51	48.36	10.11	279.11	0.273	0.50	0.08	0.98	0.06	1.37	0.09
EC-19	09/01/2017 11:30	6.74	34.25	7.16	336.42	0.143	0.55	0.13	1.06	0.08	1.45	0.10
EC-23	09/01/2017 23:30	6.60	33.53	7.01	327.51	0.118	0.60	0.08	1.16	0.05	1.55	0.08
EC-25	10/01/2017 08:15	8.83	44.90	9.39	297.37	0.216	0.52	0.07	1.07	0.10	1.46	0.11
EC-28	10/01/2017 17:30	32.00	162.63	34.01	259.78	0.375	0.47	0.18	0.87	0.16	1.26	0.17
EC-33	11/01/2017 11:25	9.09	46.20	9.66	334.14	0.134	0.57	0.07	1.10	0.02	1.49	0.06
EC-38	12/01/2017 08:45	6.34	32.24	6.74	364.36	0.098	0.57	0.04	1.13	0.14	1.52	0.16
Max		***32.00***	***162.63***	***34.01***	***364.36***	***0.37***	***0.69***	***0.15***	***1.34***	***0.08***	***1.73***	***0.10***
Min		***1.71***	***8.71***	***1.82***	***259.78***	***0.05***	***0.47***	***0.18***	***0.87***	***0.16***	***1.26***	***0.17***
AVG		***7.33***	***37.24***	***7.79***	***327.90***	***0.16***	***0.59***	***0.10***	***1.14***	***0.10***	***1.53***	***0.12***
WTAVG[(d)]		-	-	-	***303.00***	***0.24***	***0.54***	***0.12***	***1.03***	***0.11***	***1.42***	***0.13***
Quiock Creek												
QC1	06/10/2015	0.0002	0.25	0.16	88.9	2.1	0.16	0.06	0.32	0.14	0.55	0.16
QC2	07/10/2015	0.0002	0.23	0.15	89.9	2.0	0.15	0.08	0.33	0.16	0.56	0.18
QC3	08/10/2015	0.0002	0.23	0.15	91.2	2.1						
QC4	09/10/2015	0.0002	0.25	0.16	88.2	2.5	0.17	0.1	0.34	0.13	0.57	0.16
QC5	10/10/2015	0.0003	0.36	0.23	82.7	3.4	0.10	0.04	0.23	0.18	0.46	0.20
QC6	11/10/2015	0.0004	0.45	0.29	79.6	3.4	0.13	0.07	0.24	0.06	0.47	0.11
QC7	12/10/2015	0.0002	0.23	0.15	86.1	4.0	0.23	0.12	0.45	0.14	0.68	0.17
QC8	13/10/2015	0.0002	0.16	0.10	83.1	3.0	0.14	0.12	0.29	0.10	0.52	0.13

(Table E.2 continued)

QC9	14/10/2015	0.0020	2.18	1.40	82.2	3.3	0.05	0.05	0.10	0.12	0.33	0.15
QC10	15/10/2015	0.0005	0.51	0.33	80.9	4.9	0.13	0.08	0.28	0.08	0.51	0.12
QC11	16/10/2015	0.0019	2.07	1.33	78.6	3.8	0.05	0.02	0.09	0.09	0.32	0.13
QC12	17/10/2015	0.0040	4.29	2.75	69.1	3.8	0.06	0.04	0.12	0.05	0.35	0.10
QC13	18/10/2015	0.0009	0.93	0.60	77.4	1.8	0.10	0.11	0.26	0.34	0.49	0.35
QC14	19/10/2015	0.0005	0.54	0.35	86.7	1.8	0.10	0.08	0.21	0.23	0.44	0.25
QC15	20/10/2015	0.0004	0.46	0.30	90.5	2.6	0.07	0.07	0.14	0.11	0.37	0.14
QC16	21/10/2015	0.0003	0.36	0.23	92.3	1.8	0.15	0.09	0.27	0.12	0.50	0.15
QC17	22/10/2015	0.0004	0.43	0.28	90.6	2.3	0.08	0.07	0.16	0.13	0.39	0.16
QC18	23/10/2015	0.0004	0.42	0.27	92.4	2.6	0.17	0.14	0.37	0.24	0.60	0.26
QC19	24/10/2015	0.0003	0.36	0.23	97.5	2.2	0.02	0.11	0.39	0.07	0.62	0.12
QC20	25/10/2015	0.0247	26.64	17.08	61.4	8.0	-0.12	0.04	-0.21	0.09	0.02	0.13
QC21	26/10/2015	0.0021	2.30	1.47	73.0	2.1	-0.12	0.15	-0.22	0.21	0.01	0.23
Max		***0.02***	***26.64***	***17.08***	***97.53***	***7.97***	***0.23***	***0.12***	***0.45***	***0.14***	***0.68***	***0.17***
Min		***0.0002***	***0.16***	***0.10***	***61.45***	***1.77***	***-0.12***	***0.04***	***-0.22***	***0.21***	***0.01***	***0.23***

I.D	**Sample time**	**Q**	**q**	**q^***	**Si*[b]**	**Al**	**$\delta^{29}Si$**	**2σ**	**$\delta^{30}Si$**	**2σ**	**$\Delta_{diss-rock}$**	**1σ**
		$m^3\ s^{-1}$	**mm day^{-1}**		**μM**	**μM**	**‰**	**‰**	**‰**	**‰**	**‰**	**‰**
AVG		***0.0019***	***2.08***	***1.33***	***83.93***	***3.01***	***0.09***	***0.08***	***0.21***	***0.14***	***0.43***	***0.17***
WTAVG[(d)]	-	-	-	***68.16***	***68.16***	***6.06***	***-0.05***	***0.05***	***-0.09***	***0.10***	***0.14***	***0.14***
Hakai												
111	16/09/2017 14:36	0.22	2.39	2.01	25.3	6.1	0.33	0.09	0.55	0.12	0.78	0.19
125	17/09/2017 05:00	0.19	2.10	1.77	25.7	6.3	0.27	0.11	0.58	0.11	0.81	0.19
110	17/09/2017 07:00	0.19	2.16	1.82	28.8	7.2	0.26	0.08	0.55	0.11	0.78	0.19
326	17/09/2017 09:00	0.21	2.31	1.94	34.5	8.7	0.28	0.04	0.50	0.04	0.73	0.15
253	17/09/2017 11:00	0.50	5.53	4.65	40.5	8.5	0.24	0.03	0.50	0.08	0.73	0.17
130	17/09/2017 13:00	0.61	6.76	5.69	32.8	7.3	0.29	0.17	0.52	0.11	0.75	0.18
252	17/09/2017 15:00	0.53	5.93	4.99	24.7	5.8	0.31	0.07	0.58	0.12	0.81	0.19
142	17/09/2017 17:00	0.50	5.57	4.69	29.6	6.9	0.20	0.07	0.38	0.09	0.61	0.17
141	17/09/2017 19:00	0.43	4.74	3.99	47.9	9.9	0.26	0.11	0.49	0.08	0.72	0.17
256	17/09/2017 21:00	0.37	4.13	3.47	27.0	7.3	0.24	0.08	0.54	0.14	0.77	0.21
260	17/09/2017 23:00	0.34	3.80	3.20	43.5	10.8	0.23	0.06	0.52	0.09	0.75	0.17
349	18/09/2017 01:00	0.32	3.50	2.95	31.3	7.8	0.29	0.11	0.54	0.13	0.77	0.20
339	18/09/2017 03:00	0.30	3.31	2.79	38.3	10.1	0.21	0.05	0.42	0.18	0.65	0.24
114	18/09/2017 05:00	0.29	3.16	2.66	30.6	6.4	0.22	0.08	0.43	0.07	0.66	0.16

(Table E.2 continued)

350	18/09/2017 09:00	0.26	2.93	2.47	30.4	7.7	0.31	0.15	0.57	0.20	0.80	0.25
251	18/09/2017 13:00	0.25	2.79	2.35	30.1	6.8	0.32	0.09	0.56	0.15	0.79	0.21
302	18/09/2017 19:00	0.23	2.60	2.19	36.0	9.0	0.30	0.14	0.57	0.15	0.80	0.21
113	19/09/2017 01:00	0.22	2.45	2.06	37.4	9.7	0.32	0.12	0.60	0.13	0.83	0.20
Max		***0.61***	***6.76***	***5.69***	***47.94***	***10.76***	***0.33***	***0.09***	***0.60***	***0.13***	***0.83***	***0.20***
Min		***0.19***	***2.10***	***1.77***	***24.74***	***5.83***	***0.20***	***0.07***	***0.38***	***0.09***	***0.61***	***0.17***
AVG		***0.33***	***3.68***	***3.09***	***33.03***	***7.91***	***0.27***	***0.09***	***0.52***	***0.12***	***0.75***	***0.19***
WTAVG[(d)]		-	-	-		***7.87***	***0.27***	***0.09***	***0.51***	***0.11***	***0.74***	***0.19***
123	16/09/2017 14:36	0.22	2.39	2.01	32.2	8.8	0.34	0.13	0.66	0.14	0.89	0.21
292	14/10/2017 09:30	0.15	1.71	1.44	31.7	7.3	0.17	0.12	0.37	0.16	0.60	0.22
280	14/10/2017 12:30	0.27	2.98	2.51	34.0	9.1	0.16	0.14	0.33	0.23	0.56	0.28
120	14/10/2017 15:30	0.31	3.40	2.87	29.9	5.8	0.29	0.05	0.69	0.11	0.92	0.19
329	14/10/2017 18:30	0.40	4.46	3.76	26.4	5.6	0.29	0.05	0.54	0.10	0.77	0.18

I.D	Sample time	Q	q	q^*	Si*[b]	Al	$\delta^{29}Si$	2σ	$\delta^{30}Si$	2σ	$\Delta_{diss-rock}$	1σ
		$m^3\ s^{-1}$	mm day^{-1}		μM	μM	‰	‰	‰	‰	‰	‰
129	14/10/2017 21:30	0.65	7.25	6.10	35.0	9.5	0.22	0.11	0.47	0.15	0.70	0.21
307	15/10/2017 00:30	0.63	6.94	5.84	29.5	6.9	0.25	0.04	0.45	0.07	0.68	0.17
261	15/10/2017 03:30	0.50	5.52	4.65	36.1	9.7	0.28	0.11	0.59	0.12	0.82	0.19
131	15/10/2017 06:30	0.41	4.50	3.78	44.4	10.3	0.25	0.15	0.51	0.08	0.74	0.17
331	15/10/2017 09:30	0.38	4.22	3.55	40.3	9.4	0.32	0.01	0.54	0.02	0.77	0.15
291	15/10/2017 12:30	0.99	10.96	9.23	32.6	7.8	0.23	0.05	0.43	0.10	0.66	0.18
284	15/10/2017 15:30	1.56	17.24	14.51	30.0	7.3	0.27	0.14	0.51	0.07	0.74	0.17
276	15/10/2017 18:30	1.08	12.01	10.11	37.6	7.0	0.29	0.04	0.56	0.18	0.79	0.23
135	15/10/2017 21:30	0.91	10.06	8.47	38.0	6.8	0.26	0.11	0.49	0.13	0.72	0.20
285	16/10/2017 00:30	0.86	9.49	7.98	39.6	7.0	0.26	0.04	0.45	0.12	0.68	0.19
320	16/10/2017 03:30	1.00	11.08	9.33	43.5	10.8	0.11	0.12	0.24	0.12	0.47	0.12
306	16/10/2017 06:30	1.81	20.05	16.88	39.0	10.2	0.23	0.15	0.43	0.06	0.66	0.16
345	16/10/2017 09:30	5.34	59.20	49.83	30.5	6.8	0.23	0.04	0.46	0.13	0.69	0.20

(Table E.2 continued)

139	16/10/2017 12:30	4.13	45.76	38.52	33.2	6.9	0.19	0.12	0.40	0.12	0.63	0.12
278	16/10/2017 15:30	2.89	32.02	26.95	42.6	11.0	0.21	0.06	0.37	0.02	0.60	0.15
259	16/10/2017 18:30	2.75	30.42	25.61	33.9	7.1	0.10	0.11	0.22	0.20	0.45	0.25
127	16/10/2017 21:30	3.14	34.77	29.27	33.3	6.9			0.32	0.04	0.55	0.15
134	17/10/2017 00:30	3.59	39.80	33.50	30.3	6.7	0.16	0.10	0.39	0.10	0.62	0.18
138	17/10/2017 09:30	2.53	28.05	23.61	29.4	6.7	0.20	0.03	0.43	0.13	0.66	0.20
140	17/10/2017 12:30	2.23	24.67	20.77	30.9	7.8	0.23	0.13	0.52	0.11	0.75	0.19
250	17/10/2017 15:30	1.90	21.09	17.75	33.2	8.3	0.27	0.09	0.44	0.09	0.67	0.18
286	17/10/2017 18:30	1.63	18.04	15.19	29.5	7.4	0.23	0.09	0.47	0.17	0.70	0.22
301	17/10/2017 21:30	1.41	15.66	13.18	46.1	10.6	0.25	0.18	0.39	0.05	0.62	0.16
303	18/10/2017 00:30	1.25	13.87	11.68	33.9	7.2	0.18	0.16	0.39	0.07	0.62	0.16
311	18/10/2017 03:30	1.18	13.06	10.99	30.4	6.8	0.20	0.18	0.37	0.09	0.60	0.18
325	18/10/2017 06:30	1.72	19.01	16.00	29.2	7.1	0.21	0.07	0.39	0.13	0.62	0.20

I.D	Sample time	Q	q	q^*	Si^{*b}	Al	$\delta^{29}Si$	2σ	$\delta^{30}Si$	2σ	$\Delta_{diss-rock}$	1σ
		$m^3\ s^{-1}$	mm day^{-1}		μM	μM	‰	‰	‰	‰	‰	‰
340	18/10/2017 09:30	2.40	26.56	22.36	32.5	7.1	0.20	0.13	0.42	0.15	0.65	0.21
346	18/10/2017 12:30	1.75	19.35	16.29	31.2	7.1	0.24	0.02	0.46	0.16	0.69	0.22
248	18/10/2017 17:00	1.36	15.08	12.70	26.2	6.2	0.23	0.15	0.39	0.15	0.62	0.21
333	18/10/2017 23:00	1.26	13.96	11.75	44.6	9.2	0.20	0.18	0.43	0.10	0.66	0.18
277	19/10/2017 11:00	1.19	13.13	11.05	42.8	10.1	0.23	0.14	0.50	0.14	0.73	0.21
337	19/10/2017 17:00	1.08	11.95	10.06	32.3	7.0	0.28	0.16	0.44	0.17	0.67	0.23
304	19/10/2017 23:00	1.16	12.80	10.78	37.0	7.3	0.24	0.24	0.47	0.13	0.70	0.20
309	20/10/2017 05:00	1.25	13.85	11.65	33.6	8.4	0.26	0.12	0.60	0.16	0.83	0.22
290	20/10/2017 11:00	1.41	15.59	13.12	35.3	8.9	0.30	0.14	0.46	0.12	0.69	0.19
324	20/10/2017 17:00	1.10	12.13	10.21	33.4	6.9	0.24	0.04	0.51	0.13	0.74	0.20
299	20/10/2017 23:00	0.95	10.48	8.82	30.4	6.9	0.26	0.08	0.27	0.10	0.50	0.18

(Table E.2 continued)

279	21/10/2017 05:00	0.85	9.38	7.90	32.2	7.2	0.13	0.12	0.19	0.04	0.42	0.15
282	21/10/2017 11:00	0.79	8.77	7.39	35.8	9.4	0.09	0.01	0.59	0.13	0.82	0.20
335	21/10/2017 17:00	0.83	9.16	7.71	34.2	9.4	0.30	0.04	***0.69***	***0.11***	***0.92***	***0.19***
123	21/10/2017 23:00	1.16	7.71	6.49	***46.12***	***11.02***	***0.34***	***0.13***	***0.19***	***0.04***	***0.42***	***0.15***
Max		***5.34***	***59.20***	***49.83***	***26.21***	***5.56***	***0.09***	***0.01***	***0.45***	***0.12***	***0.68***	***0.19***
Min		***0.15***	***1.71***	***1.44***	***34.39***	***7.95***	***0.23***	***0.10***	***0.42***	***0.1***	***0.65***	***0.18***
AVG		***1.47***	***16.16***	***13.60***	***34.37***	***7.95***	***0.21***	***0.10***	***0.42***	***0.11***	***0.65***	***0.18***
WTAVG[(d)]		-	-	-	***32.2***	***8.8***	0.34	0.13	0.66	0.14	0.89	0.21
Providence Creek												
2018- 452	08/01/2018 12:24	0.010	0.65	0.85	465	2.03	1.09	0.04	1.78	0.07	2.01	0.17
2018- 453	08/01/2018 13:24	0.014	0.90	1.17	441	2.07	1.03	0.04	1.48	0.11	1.71	0.19
2018- 454	08/01/2018 14:24	0.024	1.59	2.07	510	1.91	1.02	0.10	1.74	0.06	1.97	0.16
2018- 455	08/01/2018 15:24	0.034	2.22	2.88	486	3.05	1.03	0.05	1.91	0.11	2.14	0.18
2018- 456	08/01/2018 16:24	0.033	2.19	2.84	391	2.60	1.02	0.10	2.02	0.07	2.25	0.17
2018- 457	08/01/2018 17:24	0.031	2.06	2.67	355	2.98	1.10	0.06	2.27	0.09	2.50	0.18
2018- 458	08/01/2018 18:24	0.028	1.82	2.37	431	3.46	0.97	0.06	1.91	0.13	2.14	0.20
2018- 459	08/01/2018 19:24	0.025	1.65	2.14	382	2.43	0.98	0.03	1.95	0.19	2.18	0.24

I.D	Sample time	Q	q	q^*	Si*[b]	Al	$\delta^{29}Si$	2σ	$\delta^{30}Si$	2σ	$\Delta_{diss-rock}$	1σ
		$m^3\ s^{-1}$	mm day^{-1}		μM	μM	‰	‰	‰	‰	‰	‰
2018- 460	08/01/2018 20:24	0.027	1.74	2.26	344	2.95	1.04	0.04	2.13	0.07	2.36	0.17
2018- 461	08/01/2018 21:24	0.027	1.75	2.27	500	3.14	1.09	0.04	2.01	0.11	2.24	0.19
2018- 462	08/01/2018 22:24	0.024	1.54	2.00	512	2.68	1.12	0.11	2.03	0.12	2.26	0.19
2018- 463	08/01/2018 23:24	0.021	1.37	1.79	497	3.09	1.05	0.05	2.02	0.23	2.25	0.27
2018- 464	09/01/2018 00:24	0.019	1.24	1.61	394	2.82	0.99	0.03	2.00	0.09	2.23	0.18
2018- 465	09/01/2018 01:24	0.018	1.15	1.49	479	2.74	1.04	0.11	1.99	0.08	2.22	0.17
2018- 466	09/01/2018 02:24	0.016	1.03	1.34	550	2.88	1.06	0.04	1.90	0.16	2.13	0.22
2018- 467	09/01/2018 03:24	0.014	0.90	1.17	405	2.86	1.09	0.03	2.02	0.12	2.25	0.19
2018- 468	09/01/2018 04:24	0.012	0.82	1.06	504	2.55	1.03	0.04	1.94	0.14	2.17	0.20

(Table E.2 continued)

2018- 469	09/01/2018 05:24	0.011	0.75	0.97	522	2.78	0.98	0.01	1.79	0.06	2.02	0.16
2018- 470	09/01/2018 06:24	0.011	0.69	0.90	522	2.42	0.94	0.04	1.71	0.08	1.94	0.17
2018- 471	09/01/2018 07:24	0.010	0.65	0.85	477	2.53	0.95	0.03	1.70	0.08	1.93	0.17
Max		***0.03***	***2.22***	***2.88***	***549.89***	***3.46***	***1.12***	***0.11***	***2.27***	***0.09***	***2.50***	***0.18***
Min		***0.01***	***0.65***	***0.85***	***343.94***	***1.91***	***0.94***	***0.04***	***1.48***	***0.11***	***1.71***	***0.19***
AVG		***0.02***	***1.34***	***1.73***	***458.36***	***2.70***	***1.03***	***0.05***	***1.92***	***0.11***	***2.15***	***0.19***
WTAVG[(d)]		-	-	-	***448.61***	***2.76***	***1.04***	***0.06***	***1.95***	***0.11***	***2.18***	***0.19***
Rio Icacos												
PR12-IC 06	28/05/2012 11:00	2.44	64.54	0.017	129.72	0.89	0.42	0.06	0.75	0.09	0.95	0.13
PR12-IC 07	28/05/2012 11:39	1.89	50.06	0.013	121.18	1.59	0.28	0.06	0.57	0.09	0.77	0.13
PR12-IC 08	28/05/2018 12:10	1.39	36.7	0.009	123.02	1.57	0.35	0.07	0.60	0.12	0.80	0.15
PR12-IC 09	28/05/2018 13:05	1.07	28.22	0.007	127.68	2.97	0.32	0.03	0.62	0.04	0.82	0.11
PR12-IC 10	28/05/2018 17:24	0.58	15.23	0.004	221.28	1.44	0.67	0.06	1.30	0.19	1.50	0.22
		2.44	***64.54***	***0.02***	***221.28***	***2.97***	***0.67***	***0.06***	***1.30***	***0.19***	***1.50***	***0.22***
Max		***0.58***	***15.23***	***0.00***	***121.18***	***0.89***	***0.28***	***0.06***	***0.57***	***0.09***	***0.77***	***0.13***
Min		***1.47***	***38.95***	***0.01***	***144.58***	***1.69***	***0.41***	***0.06***	***0.77***	***0.11***	***0.97***	***0.15***
AVG		-	-	-	***133.13***	***1.54***	***0.38***	***0.06***	***0.70***	***0.10***	***0.90***	***0.14***
WTAVG[(d)]		***2.44***	***64.54***	***0.017***	***129.72***	***0.89***	0.42	0.06	0.75	0.09	0.95	0.13
Bedrock composition												
granite[(e.f)]									-0.23	0.15		
									-0.20	0.10		
rhyolite[(g)]									-0.16	0.04		
andesite[(h)]									-0.23	0.09		
shale[(i)]									-0.39	-0.06		

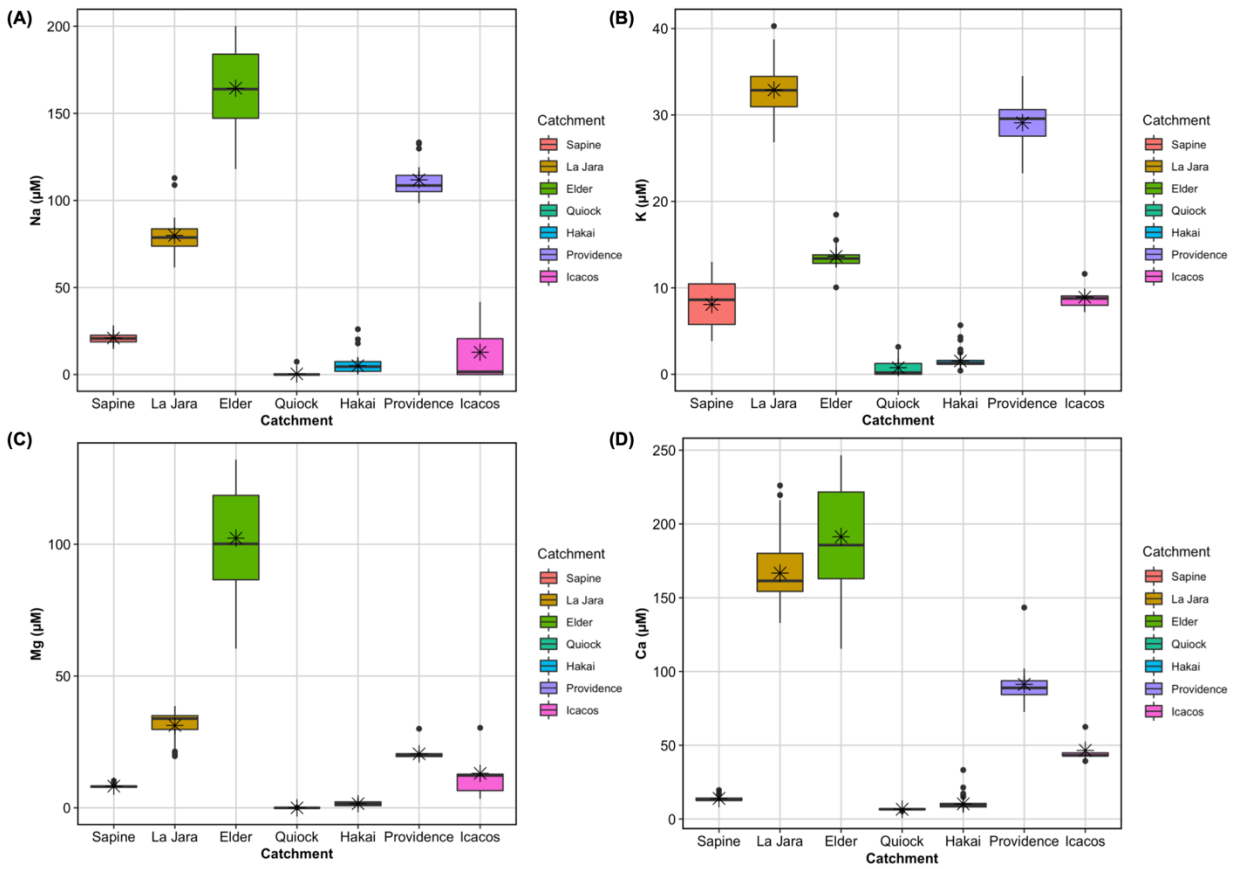

Figure E.1 Box-and-whisker plots of seawater-corrected major cations of flood events

SILHOUETTE SCORE TO DETERMINE OPTIMAL K FOR KMEANS CLUSTER ANALYSIS

Choosing the optimal number of clusters to separate the dataset is the most important step in this KMeans cluster analysis approach. The most common method used to determine this optimal number of clusters is through the **"Silhouette score" (Fig. E.2).** Silhouette scores near +1 indicate that the sample is far away from the neighboring clusters. A value of 0 indicates that the sample is on or very close to the decision boundary between two neighboring clusters and negative values indicate that those samples might have been assigned to the wrong cluster.

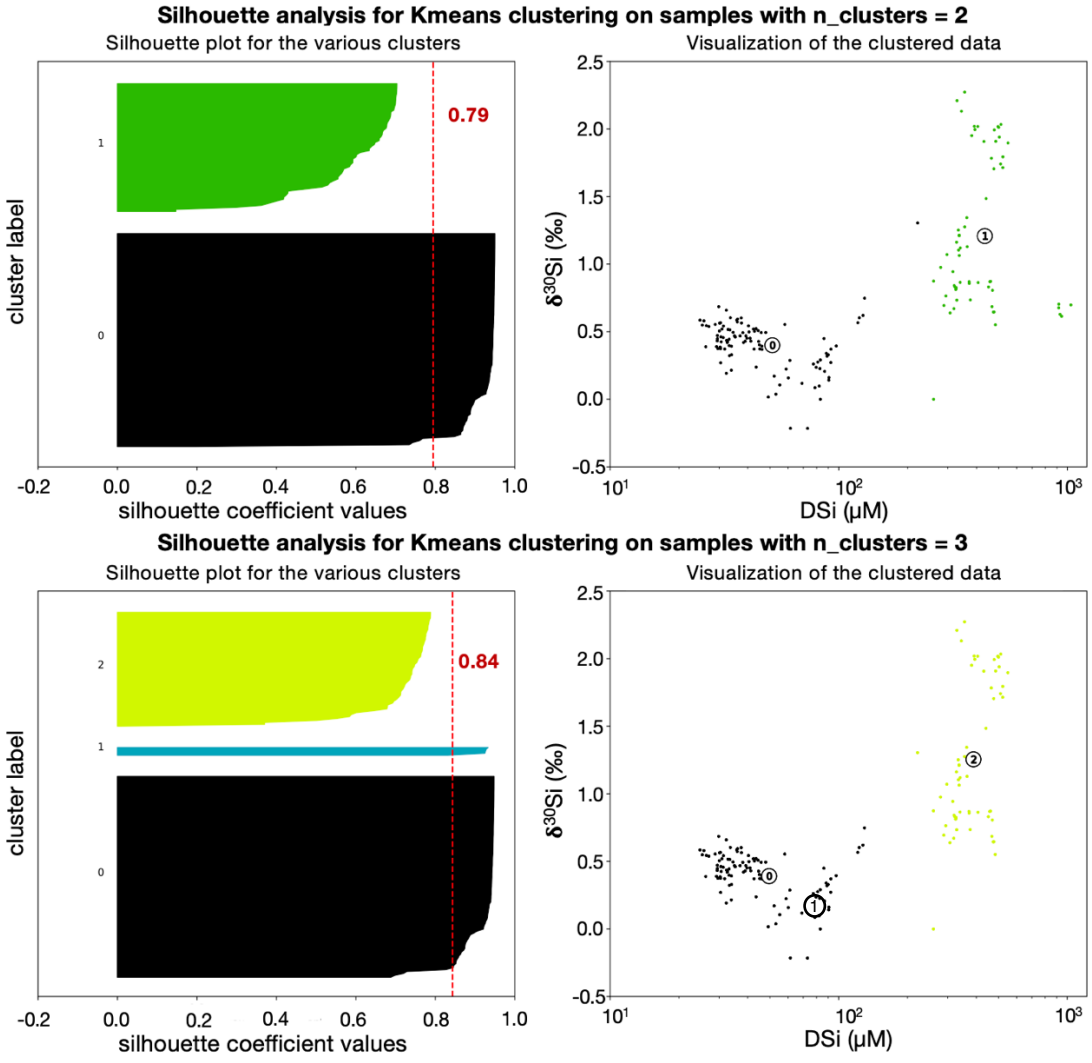

Figure E.2 Silhouette analysis for KMeans clustering

(Figure E.2 continued)

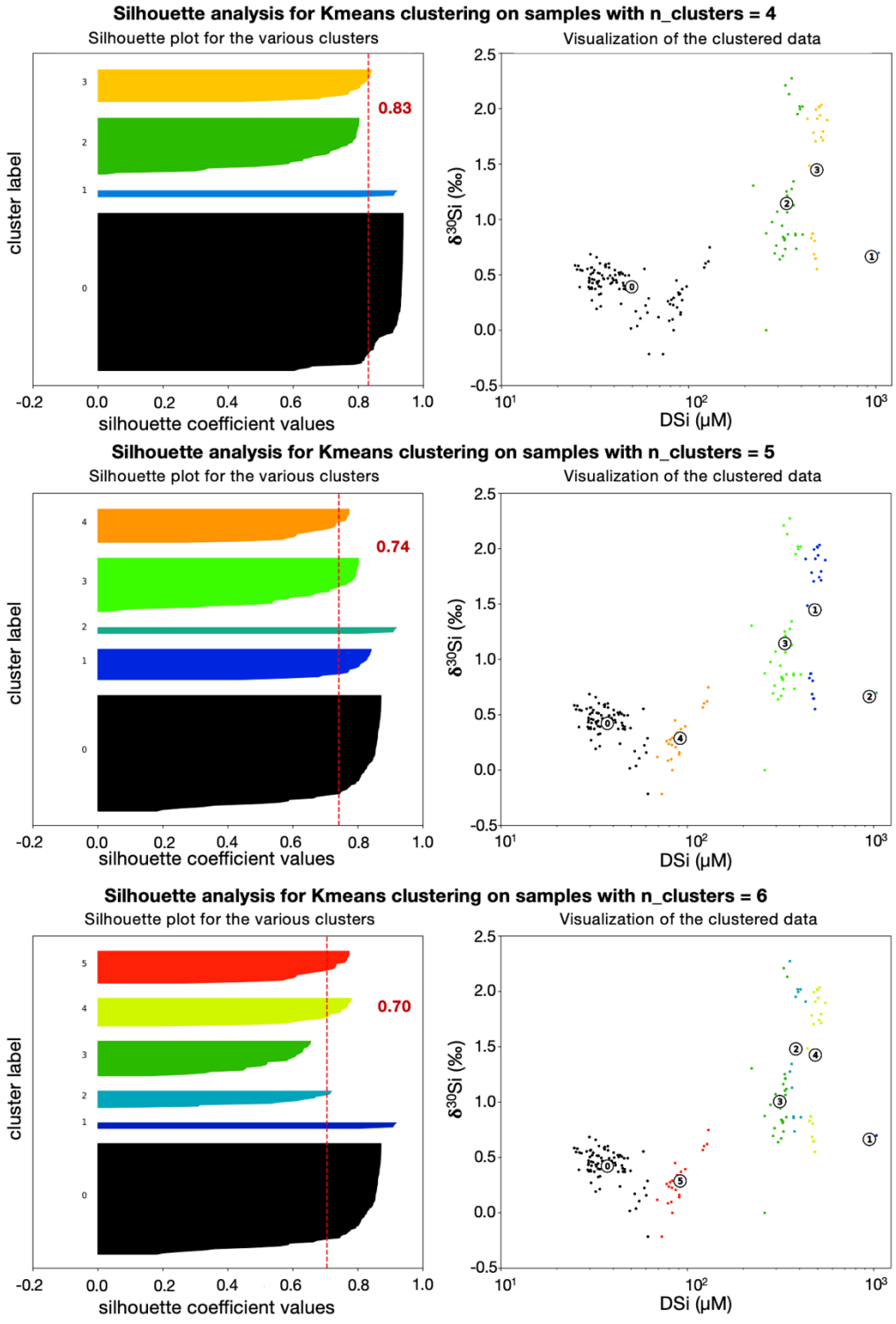

APPENDIX F

CALCITE PRECIPITATION EXPERIMENTS WITH NO PH-DRIFT CONTROL

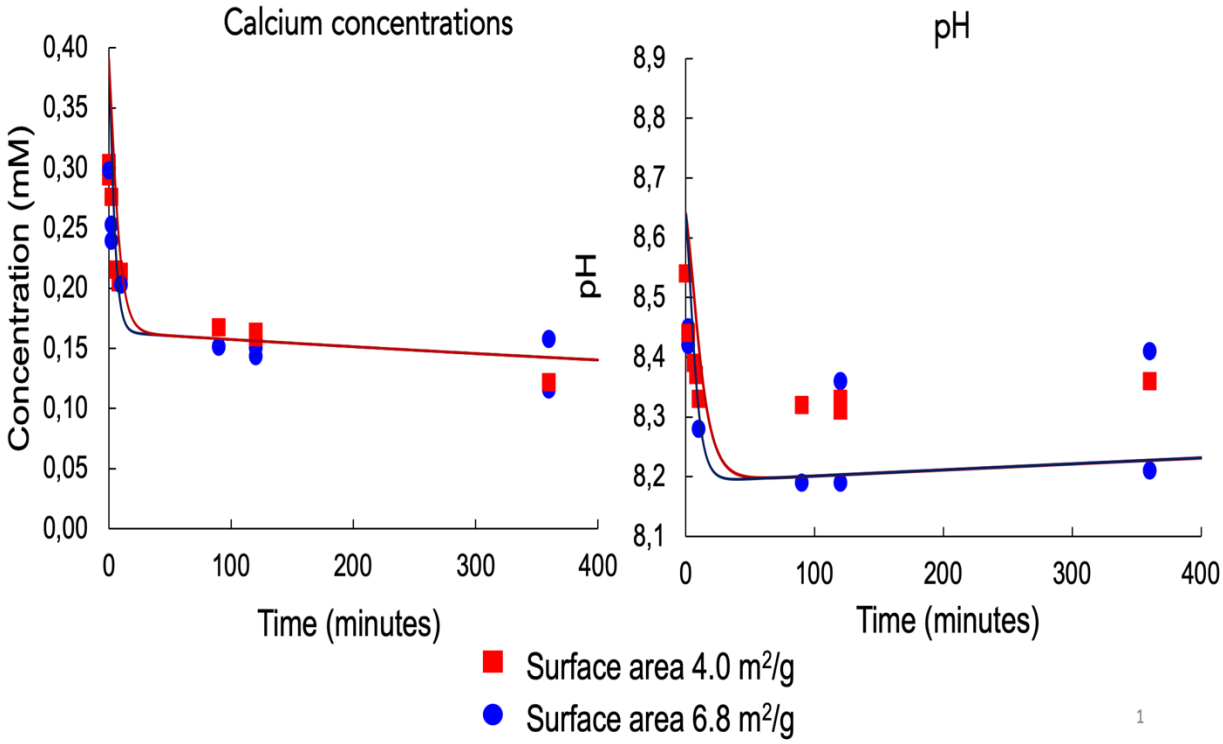

Figure F.1 pH variability and influence on the attainment of equilibrium

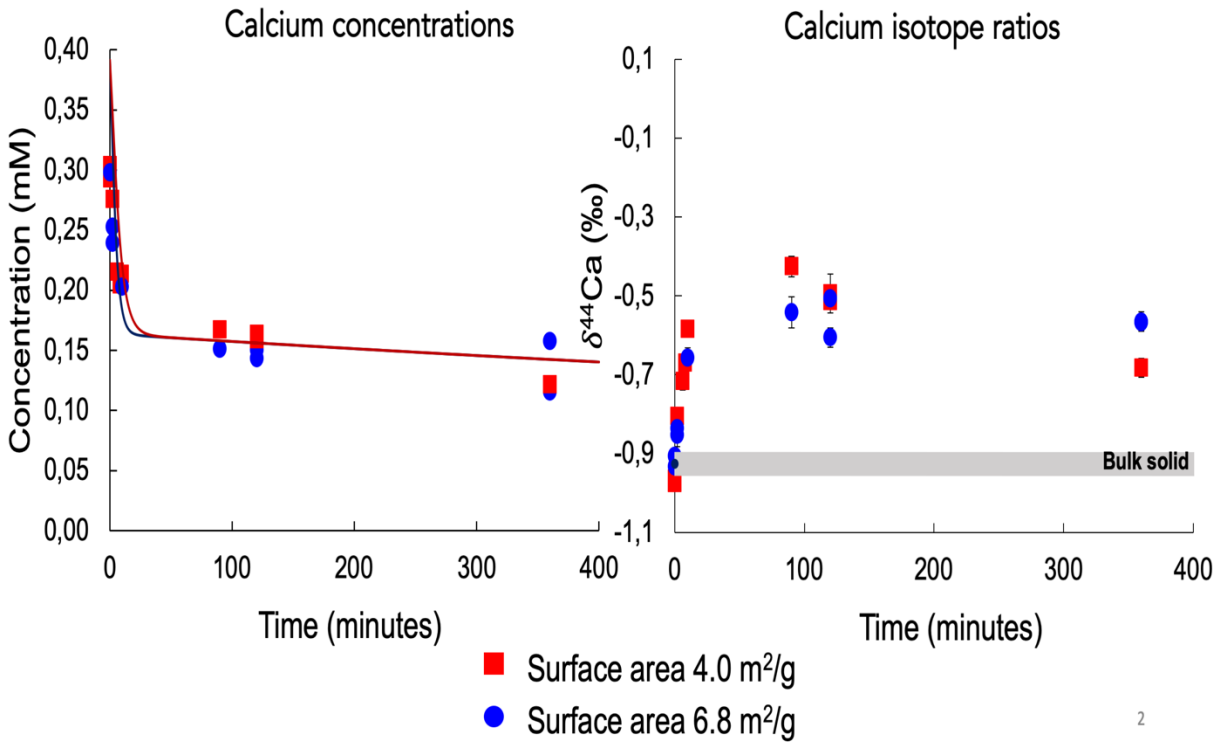

Figure F.2 Influence of pH drift on fluid Ca stable isotopes